Microstructural investigation of biomineralization

in cement-based materials

Ali Amiri

Submitted in accordance with the requirements for the degree of

Doctor of Philosophy

The University of Leeds

School of Civil Engineering

February 2024

The candidate confirms that the work submitted is his own and that appropriate credit has been given where reference has been made to the work of others.

Abstract

Many factors affecting the durability and integrity of concrete structures can be related to micro-cracks. Due to its brittle characteristics, the cracks can be induced in concrete elements under different stresses. Recent studies [1], [2] confirm the possibility of microbial induced calcium carbonate precipitation with self-healing ability. This ability of micro-crack healing can be achieved via different methods and one of the recent novel methods for this purpose is the biomineralization in cement-based materials. In this method, the calcium carbonate precipitates as a result of the biochemical process of the microorganisms. There are different studies to evaluate the self-healing in cement-based materials for the purpose of compressive strength recovery and durability of the structures. However, there is not enough information regarding the effects of biomineralization on the hydration process and its products. To fill the knowledge gap in the literature, this study aims to investigate the effect of biomineralization and calcium carbonate precipitation on possible changes in cement hydration products due to biomineralization as well as the effect of superplasticizer on this process.

This work aims to understand the biomineralization process in cement-based materials by using different testing methods such as ^{29}Si NMR, ^{27}Al NMR, XRD and SEM-EDX analysis. In the current work, the *Sporosarcina pasteruii* strain has been used for bacterial induced calcium carbonate precipitation and it has been cultivated in corn steep liquor medium with the addition of calcium nitrate as a calcium ion source. The cement paste samples and bacterial cement paste samples used in the study have been treated in water and nutrient media respectively until the testing age.

Based on the collected results, it can be concluded that the addition of S*. pasteurii* bacterial strain has a minor effect on the C-S-H and its polymerisation. However, the ^{27}Al NMR findings show a major change in the AFt and AFm phases and their transitions. Furthermore, the XRD results did not indicate any major changes to calcium carbonate content in bacterial cement paste samples but the STA analysis clearly indicated a higher amount of calcium carbonate in the same samples. As such, the presence of poorly crystalline calcium carbonate in the bacterial samples is concluded. The presence of calcium carbonate in cement based materials such as cement paste, mortar and concrete is considered to increase the density resulting decrease in porosity and increase in mechanical properties under compression. /this confirms the increase in strength correlated with biomineralization in cement based materials observed through literature review.

Dedication

This thesis is dedicated to my late father who passed away during this project.

Acknowledgment

First and most, I want to appreciate my supervisor Prof. Ian G. Richardson for his guidance and invaluable advice throughout my research. I also would like to acknowledge the support from the University of Leeds and the financial support provided.

I am deeply grateful to members of the Civil Engineering department of the University of Leeds. I want to thank Victoria Leadley, Lucy Leonard and Leslie Arkless for their help and technical support.

I acknowledge Dr. Samuel Aduawankah and Pojhan Moktar for their guidance and help for quantitative X-ray analysis. I am thankful of my colleagues Xiaohon Zhu and Sumanjani Vinnakota who provided mental support during my hard times.

In addition to all the foregoing, I highly appreciate my patient wife Katharina for all the help and support she provided. Especial thanks to my parents who dedicated their lives to me and supported my decisions.

Table of Contents

Contents

List of Tables

List of Figures

List of abbreviations

Cement clinker and hydrate phases

Alite / C_3S	$3CaO.SiO_2$
Belite / C_2S	$2CaO.SiO_2$
Tricalcium Aluminate / C_3A	$3CaO.Al2O_3$
Tetracalcium aluminoferrite /C_4AF	$4CaO.Al_2O_3.Fe_2O_3$
Gypsum	$CaSO_4.2H_2O$
Portlandite	$Ca(OH)_2$ / CH
Calcium Silicate Hydrate	C-S-H
Ettringite / AFt	$3CaO.Al_2O_3.3CaSO_4.32H_2O$
Aluminate ferrite monosulfate/AFm	$3CaO.Al_2O_3.CaSO_4.12H_2O$
Calcium carbonate	$CaCO_3$
Calcium hydroxide/CH	$Ca(OH)_2$

Cement chemistry terminology

A	Al_2O_3
C	CaO
F	Fe_2O_3
H	H_2O
K	K_2O
M	MgO
N	N_2O
S	SiO_2
Ca/Si	Calcium to silicon atomic ratio
Al/Si	Aluminium to silicon atomic ratio

Other abbreviations

wPC	White Portland cement
SP	Superplasticizer
CSL	Corn steep liquor
UCSL	Urea corn steep liquor

Bac	Bacteria
MICP	Microbial induced calcium carbonate precipitation
ACC	Amorphous calcium carbonate
CFU	Colony forming units
LML	Lactose mother liquor
LWA	Lightweight aggregate
UYE	Urea-Yeast extract
w/b	water/binder ratio
w/c	water/cement ratio

Techniques

ICC	Isothermal conduction calorimetry
STA	Simultaneous thermal analysis
DTA	Differential thermal analysis
TGA	Thermogravimetric analysis
MAS NMR	Magic angle spinning nuclear magnetic resonance
XRD	X-ray diffraction
EDX	Energy dispersive X-ray
SEM	Scanning electron microscopy
BSE	Back scattered electron

Chapter 1
Introduction

This chapter will provide an understanding of the common durability related concerns in the field of construction materials and then will carry on to the conventional methods of concrete repairs. After introducing the self-healing in cement based materials, the most recent innovations of self-healing application with biomineralization in cementitious materials and then the focus of the current study will be discussed.

1.1 Cracks

The inexpensive and most reliable materials used in construction are cement based materials. Concrete is considered as one of the most widely used construction materials [3]. During its production process, cement based materials can have adverse effects on environment. The energy consumption of industry and greenhouse gas emission related to the cement production is relatively high because of the large scale of Portland cement production and required transportation. According to available statistics, almost 7% of the carbon dioxide emission is related to cement production and construction industry [4]. Extending the service life of cementitious materials can be one of the efficient actions to reduce the whole life cost and amount of cement-based materials used and its production resulting with a decrease in CO_2 emission.

The durability of concrete structures is related to a variety of factors such as proper structural design, material selection, environmental exposure conditions and etc. Cracks in concrete structures and cement-based materials are

inevitable [5]. Although small cracks may seem negligible, they play an important role in decreasing the durability of the cementitious materials and steel reinforcement by providing pathways for harmful chemical attacks. These cracks can be the result of an external or internal stresses induced such as normal loading and shrinkage. The crack initiation and propagation can decrease the strength of concrete material as well as its durability. These cracks can decrease service life by providing internal access to aggressive materials throughout the concrete matrix (e. g. chloride ingress, carbonation [6]). There are variety of methods used for surface crack treatment such as epoxy injection, coating, sealants, etc. to remediate the cracks[7], [8]. However, mentioned methods not only require time and cost for concrete structure maintanance but also can be deficient in different applications where the cause of crack has not been investigated properly.

1.2 Autogenous and autonomous healing

Concrete has a natural reaction to crack occurrences called the autogenous healing. This mechanism relies on four factors and can seal cracks by triggering a series of chemical and/or mechanical reactions inside cracks. These four main factors (see Fig. 1.1) are; (1) further hydration of the unreacted cementitious material; (2) transported impurities or sedimentation of the fractured pieces making crack walls to swell; (3) transported impurities or sedimentation of the fractured pieces clogging the cracks; (4) $CaCO_3$ formation through the carbonation of calcium hydroxide (CH)[9].

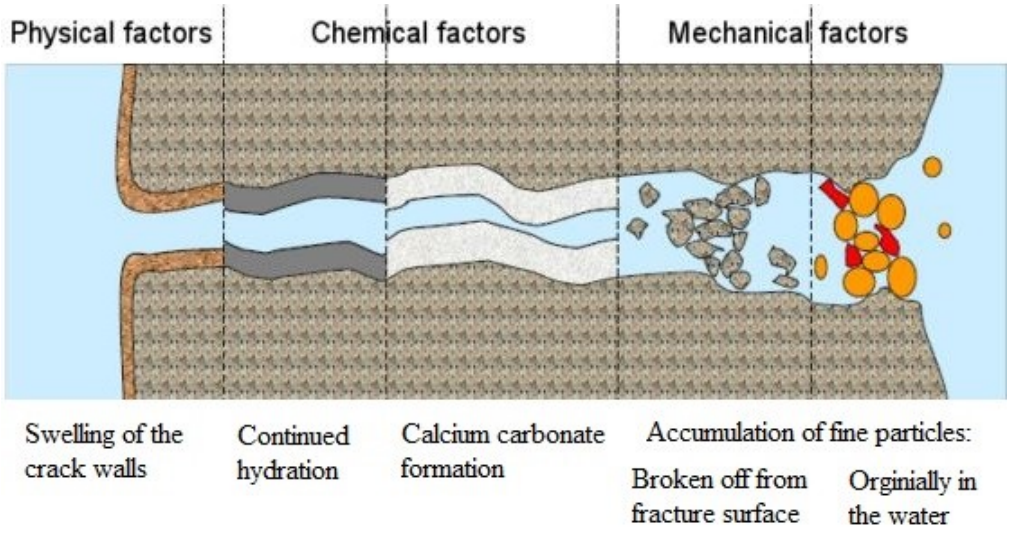

Figure 1-1 Factors triggering the autogenous healing of cracks in concrete [9]**.**

The main limitation for autogenous healing in cement-based materials can be the width of cracks, according to previous works, this type of self-healing can only occur in cracks which have a width of 10 μm to 300 μm [10], [11].

The autonomous healing in cement-based materials involves external intervention by means of introducing a healing agent. Current self-healing applications have progressed with various research methods to achieve a more stable, controllable and predictable mechanism. Recent works in the field of cement-based materials show that particular strains of microorganisms with the ability of biomineralization could be used to trigger self-healing in cement-based materials. The mineral precipitation induced by the microorganism known as biomineralization is a series of complex biochemical reactions triggered by the introduction of the biological agent (cultivated bacteria) [12].

Microbial induced calcium carbonate precipitation (MICP) is the result of biomineralization in cement-based materials which is the formation of calcium carbonate precipitation stimulated by metabolic activity of the bacteria.

There are different species of microorganisms with the natural ability of biomineralization processes. However, the survival of bacteriain cement-based materials is the main obstacle to achieve MICP in cement-based materials [13]. The alkali environment in cement-based materials with a high pH of up to 13 can be one of the leading problems for microorganism survival in this environment [14]. Moreover, the hydration and hardening process in cementitious materials can induce physio-chemical stresses on the bacterial cells resulting in the adverse effect on bacterial metabolic activity and growth rate [15]. Furthermore, there will be a nutrient reduction for bacteria after the process of hardening and restrictive access to outside [16].

Considering the influential parameters affecting microorganism viability, growth, and precipitation of calcium carbonate, choosing the suitable species of bacteria for biomineralization in the cementitious material can be a challenge when the bacteria is directly added to the cement-based materials during the mixing process.

The most commonly used species in cement-based materials is *Sporosarcina pasteurii* (*S. pasteurii,* formally known as *Baciullus pasteurii)*, which is a non-pathogenic, alkaliphilic and endospore-forming soil microorganism[17]. Moreover, there are also numerous strains of bacteria that could encourage biomineralization in cement-based materials such as; *Bacillus megaterium* [18], *Bacillus cohnii* [19]*, Bacillus subtilis* [20], *Bacillus alkalinitriculus* [18], *Shewanella* [21].

An early approach was merely incorporating endospores rather than vegetative cells (metabolically active) [22]. In this method, spore forming bacteria culture is prepared to the required concentration and sporulation to produce

dormant bacteria cells is triggered by changes to the environmental parameters such as pH. The dormant bacteria cells are then added to the concrete or mortar mix.

The endospore forming bacteria were found to be in vegetative state for up to 4 months without any protection [12]. The concerns relating to the viability of the endospore formed by bacteria within the limiting environment of cement-based materials and high values of pH for this material have led studies to suggest encapsulation for the bacteria. The encapsulation methods consist of embedding the endospores in a protective covering, e.g., inorganic lightweight porous aggregates [23] polymeric membrane [24], microcapsules [25] and hydrogels [26].

Amongst all these approaches, lightweight porous aggregates [23] and hydrogels have proven to be the best developments for the viability of the bacteria. However, both of these approaches decrease the compressive strength of mortar and increase the cost. On the other hand, previous studies have shown that with the proper selection of species and incorporation of nutrients, the vegetative cells could survive in cement paste without any encapsulation up to 11 months [27].

Even though the bacteria cells could stay viable without any encapsulation, use of the nutrients in the cement paste mix have some drawbacks in the application [22]. Generally, the yeast extract is being used in the bacterial cultures which affects the fresh and hardened properties of the mix [28]. Studies have proven that the yeast extract has a negative impact on setting time and compressive strength. Yeast extract is one of the most expensive constituents of nutrient medium. Almost more than 50% of the total cost of the bacterial culture

is due to use of yeast extract [29]. Thus, it was necessary to find a low cost replacement for yeast extract, which also provides similarly efficient results in bacterial growth and biomineralization reactions.

Limited research on biomineralization in cement based systems has shown promising results and suggested that $CaCO_3$ could seal the micro-cracks and lead to a decrease in permeability and an increase in the strength [30]. While, the latest works show the possibility of an alternative nutrient media such as corn steep liquor (CSL) and its effect on biomineralization, strength, and durability of precipitated material under different natural exposures such as weather conditions, there are uncertainties about the hydration products and microstructural changes due to use of biomineralization.

1.3 Gap in the literature

Despite all efforts on self-healing applications, one of the gaps in the literature is the uncertainty regarding the effects of bacteria on the hydration products. It is necessary to evaluate the possible effects and also the factors controlling these effects. By understanding the behaviour of the cement hydration at early ages when enhanced with biomineralization, we will be able to achieve better engineered smart materials. This understanding could also identify any possible side effects of biomineralization on the durability of the cementitious element at later ages.

Previous works have shown that the bacteria in biomineralization applications affect the hydration products. According to Skevi et.al. [31] and Hoffmann et.al. [32], bacterial cells regardless of their viability status could alter the hydration kinetics and the chemical interaction between cement clinker and

the bacteria would result in altered hydration products. As such the effects of bacteria on cement hydration require more in-depth evaluation.

The ultimate goal of this study is the characterization of hydration products affected by MICP application. Since the addition of bacteria and the required nutrient for MICP application can change the ion concentrations in the pore solution and introduce new chemical components, it is likely to affect the hydration process and C-S-H formation. To achieve this goal following objectives have been investigated:

- C-S-H structure, phases and Ca/Si ratio at an early age; noting that the added bacterial culture will impact the amount of calcium ion present and increase the calcium carbonate.
- Influence of bacterial culture and nutrient on the hydration products such as AFm and AFt phases with a focus on the transformation between AFm and AFt.
- Effect of Superplasticizer, incorporated with biomineralization on microbial induced calcium carbonate and its crystallinity.

These evaluations would help to understand the nature of biomineralization in cement-based materials and changes in microstructure of the hydration products. As such, a clarification of the biomineralization process in cementitious materials and its impact on cement hydration will be achieved.

Chapter 2
Literature Review

2.1 Portland cement

Cement as the binding material in concrete, sets and hardens when combined with water as a result of the hydration process [33]. This section will provide the detail of available phases within cement clinker and their relevant chemical reactions during hydration.

Portland cement production is the end result of a mixture of limestone, clay or shale heated to up to 1450 °C. The energy consumption for the formation of clinker through the wet or dry process is about 1750 KJ/Kg [34]. The calcium carbonate-containing components such as limestone or chalk are the main source of calcium oxide (CaO) whereas shale or clay are the sources of Aluminium oxide (Al_2O_3), silica (SiO_2) and iron (Fe_2O_3).

The heating process for raw materials results in free water evaporation known as the drying zone (at 100 °C), bound water removal from clay known as the preheating zone (at 750 °C), dissociation of calcium carbonate known as the calcining zone (between 750 °C – 1000 °C) and materials combining to form C_2S and C_3S known as the fusion (between 1000 °C – 1400 °C) [35].

Afterwards, the cooling process results in crystallisation and calcium aluminate and calcium alumino ferrite formation. The resultant material and 5% gypsum will be grounded to produce cement [36].

Alite (C_3S), Belite (C_2S), Tricalciumaluminate (C_3A) and Tetracalciumaluminoferrite (C_4AF) are 4 major phases within cement clinker.

Tricalcium silicate (C_3S) an orthosilicate exhibiting three triclinic (T), three monoclinic (M) and one rhombohedral (R) forms have been investigated by XRD and DTA [37].

Portland cement is sub-categorised to type I, Type II, Type III, Type IV, and Type V. Type I cement is a general-purpose cement including 95-100% clinker suitable for most construction projects, providing adequate strength and durability. Type II cement has 65-94% clinker that contains no more than 8% tricalcium aluminate offering moderate sulfate resistance. Type II also includes additional pozzolans or limestones. Type III cement with 95-100% clinker boasts high early strength due to high amounts of tricalcium aluminate up to 15%. Type IV cement with 40-50% clinker is designed for low heat of hydration by significantly reducing tricalcium aluminate to below 7%. Lastly, Type V cement using 90-95% clinker exhibits high sulfate resistance due to low amounts of tricalcium aluminate (<5%).

P.D. Tennis e al. [38], carried out a comprehensive survey of commercially available cements as per ASTM C150. This work showed the actual chemical composition and potential phase composition summarised in Table 2-1 and mortar strength summarised in Table 2-2 for 4 types of Portland cement.

Table 2-1 Chemical and phase composition, surveyed by P.D. Tennis et.al. [38]

Cement type*	Chemical composition, %						Loss on ignition, %	Na_2O eq.	Potential phase composition, %				Blaine fineness, m^2/kg
	SiO_2	Al_2O_3	Fe_2O_3	CaO	MgO	SO_3			C_3S	C_2S	C_3A	C_4AF	
I—mean	**20.17**	**5.07**	**2.66**	**63.23**	**2.51**	**3.26**	**1.52**	**0.70**	**56.9**	**14.8**	**8.9**	**8.2**	**384**
SD**	**0.66**	0.54	0.44	1.04	1.02	0.62	0.48	0.26	4.57	3.71	1.81	1.37	19.3
maximum	21.84	6.06	3.61	65.18	4.50	4.40	2.69	1.20	65.4	21.3	12.1	11.0	431
minimum	18.99	3.95	1.96	61.57	0.78	2.04	0.74	0.16	45.4	6.4	5.7	6.0	334
II—mean	**20.85**	**4.62**	**3.32**	**63.66**	**1.98**	**2.91**	**1.39**	**0.56**	**56.5**	**17.1**	**6.7**	**10.1**	**377**
SD	0.52	0.37	0.40	0.84	0.92	0.39	0.40	0.26	3.93	3.48	0.88	1.20	20.0
maximum	22.46	5.50	4.40	65.61	4.47	3.98	2.67	1.20	68.1	25.2	8.2	13.4	461
minimum	20.01	3.82	2.60	61.28	0.61	2.11	0.50	0.17	48.0	7.6	4.3	7.9	305
III—mean	**20.38**	**4.84**	**2.86**	**63.33**	**2.21**	**3.60**	**1.51**	**0.61**	**56.2**	**16.2**	**7.8**	**8.8**	**556**
SD	0.70	0.64	0.59	0.93	0.93	0.55	0.41	0.27	4.13	3.91	2.14	1.80	55.5
maximum	22.08	7.30	4.16	64.90	4.29	4.94	2.89	1.20	65.9	27.1	12.1	12.7	711
minimum	18.64	3.38	1.34	61.55	0.83	2.59	0.70	0.11	47.7	8.3	1.9	4.1	387
V—mean	**21.61**	**3.80**	**3.87**	**63.85**	**2.18**	**2.34**	**1.29**	**0.45**	**57.7**	**18.4**	**3.5**	**11.8**	**389**
SD	0.67	0.35	0.67	0.66	0.91	0.28	0.44	0.12	3.47	3.93	1.17	2.03	42.5
maximum	22.82	4.85	5.79	65.22	4.50	2.85	2.27	0.63	63.7	26.8	4.9	17.6	541
minimum	20.27	3.27	3.20	62.32	0.82	1.99	0.52	0.26	46.9	12.5	0.0	9.7	312

*See Table 1 for groupings of cement types.
**SD=Standard deviation

Table 2-2 Mortar strength of Portland cement, surveyed by P.D. Tennis et.al. [38]

Cement type	1 day	3 days	7 days	28 days
I—mean	**15.7**	**26.3**	**33.0**	**41.4**
SD*	2.82	2.40	2.48	3.55
maximum	21.0	30.9	40.9	50.5
minimum	8.7	20.8	28.1	34.8
II—mean	**14.9**	**25.2**	**32.4**	**42.9**
SD	2.57	2.62	2.86	3.64
maximum	22.5	32.2	39.1	50.2
minimum	7.6	15.7	21.5	30.8
III—mean	**25.0**	**34.9**	**41.2**	**49.3**
SD	3.39	3.61	3.81	4.44
maximum	32.6	42.1	48.7	58.0
minimum	16.2	26.3	32.0	39.9
V—mean	**12.8**	**23.3**	**30.9**	**43.6**
SD	1.83	3.23	4.20	4.66
maximum	15.9	27.6	36.2	50.2
minimum	7.4	12.9	17.5	31.9

*SD=Standard deviation

2.1.1 C_3S

The stability of C_3S lies between 1200 °C and 1850 °C and this can be maintained in room temperatures by the addition of other impurities such as

Mg^{2+}, Al^{3+}, Fe^{3+} with lower amounts of K^{+}, Na^{+}, SO_3 [37]. This form of C_3S with impurities is known as alite.

Alite ranges from 50%-80% in Portland cement clinker and its early rapid hydration results in the start of the induction stage controlling the development of early age strength

Upon mixing alite with water, the ions (such as OH^{-} and Ca^{2+}) are dissolved from the surface of the crysta and CH and amorphous C-S-H are formed. It has been proposed that alite hydration can have two-step reaction, a fast initial hydration and a slow diffusion controlled hydration [39].

Eq. 2.1.1 $$\mathrm{C_3S} + (3 - \mathrm{x} - \mathrm{y})\mathrm{H} \rightarrow \mathrm{C_xSH} + (3 - \mathrm{x})\mathrm{CH}$$

The shape and size of CH yielded from this reaction will be dependent on the available space for its growth.

Parameters such as foreign ions can affect the grain structure of C_3S and influence its hydraulic activity.

When in close contact with H_2O, C_3S will have a quick initial reaction but very rapidly it starts to slow down. Depending on the type of constitueents available within cement, there will be a period of inactivity (1-4 hours). This dormancy period is directly related to alite polymorph [40]. There are reports pointing out the effects of MgO, Al_2O_3 and Fe_2O_3 [41], [42]. It is possible to assume that the oxides tend to modify early reaction rates. It has been known that magnesium, aluminium and iron can affect C-S-H[43], [44]. According to Richardson et al [45], Al can also substitute the silicon in bridging sites of calcium silica hydrates (see section 2.3.1).

During the first initial reaction, there is a thick layer formation around the C_3S grains[46]. Further, C-S-H formation will then erode the initial protective layer. This protective membrane can restrict the water and ion mobility to and from particle and maintain such restriction until it is destabilised[47]. After the erosion of the initial membrane, there will be an acceleration of the C_3S reaction rate [39].

2.1.2 C_2S

Dicalcium silicate (C_2S) or Ca_2SiO_4 is also an orthosilicate which can have a different structure depending on the temperature. one of which is known as belite in cement clinker [48]. The belite is a naturally available mineral form of C_2S. There is extensive work on belite hydration [49], [50].

The four main structures are known as Ɣ, β, α and α' where α' has two different forms, α'_L and α'_H. The high temperature forms of C_2S are also stabilised in the same fashion by the substitution of ions. This stabilised form of C_2S is known as belite which can have ions such as Al^{3+}, Fe^{3+}, Mg^{2+}, K^+, SO_4^{2-}. According to previous works, β, α and α' are present in commercial clinkers[51].

The Ɣ form, compared to other polymorphs, has a lower hydration rate and non hydraulic nature which can be the main reason for the rare occurrence of Ɣ-C_2S in commercial cement [52].

Around 15%- 30% of the commercial clinker is belite. The C_2S mixed with water results with the same products as C_3S but with a slow rate of hydration.

Eq. 2.1.2 $$C_2S + (2 - x + y)H \rightarrow C_xSH + (2 - x)CH$$

The belite hydration happens with a slower rate compared to the alite but it is also dependant on the polymorphs [52], [53]. Other finding show a faster

initial reaction rate for α- C_2S where the degree of hydration can be better than the alite but the rate drops after 5 hours [54].

Since the β- C_2S is a principal form of belite present in cement, the hydration mechanism of it has been thoroughly investigated. As seen from Eq. 2.1.2, the end result of C_2S hydration is the formation of C-S-H and calcium hydroxide. The composition of C-S-H and CH content undergo a major variations from early ages of hydration [53], [54]. Initially, calcium ions evolved in the solution will increase the concentration in initial 10 minutes and then dropped and will become stable after 30 minutes. Also, Ca/Si ratio will also follow the same trend. Considering these facts and low Si levels in pores solution[55], the calcium ion concentration can have the most influential effect on controlling silicate dissolution. According to Nicoleau et al. [53], presence of saturated lime solution depressed the belite hydration and it was favoured by removal of calcium ions from solution.

It has been confirmed that the presence of calcium ions generally reduce the silicate dissolution [56], [57] and the belite dissolution in ordinary cement does not happen until such time when the calcium ion concentration has dropped.

2.1.3 C_3A

On the contrary to alite and belite, tricalcium aluminate (C_3A) does not have different polymorphs [58], [59]. There is no phase transition for C_3A and it is cubic in its pure form.

The reaction of C_3A with water along with added gypsum is strong during the first few hours of hydration[60]. Gypsum ($C\bar{S}H_2$) allows a slow reaction process. The

absence of gypsum will result in a flash setting during the initial reaction. C_3A mixed with gypsum and water results in unstable phases which then convert to AFt ($C_6A\bar{S}_3{\bullet}H_{32}$). Formed AFt builds up a layer on the C_3A and prevents further rapid reaction.

When gypsum is available:

Eq. 2.1.3 $$C_3A + 3C\bar{S}H_2 + 26H \rightarrow C_3A \bullet 3C\bar{S} \bullet H_{32}$$ (AFt)

When insufficient gypsum is available the reaction changes to:

Eq. 2.1.4 $$C_3A \bullet 3C\bar{S} \bullet H_{32} + 2C_3A + 4H \rightarrow 3(C_3A \bullet C\bar{S} \bullet H_{12})$$

The AFt (see section 2.5) exists as long hexagonal needles. It is converted into calcium aluminate monosulphate ($C_4A\bar{S}H_{12}$) via Eq 2.1.4 when sulfate ion supply becomes insufficient. Monosulphate has hexagonal shape crystals. It should be noted that in presence of carbonate ions mono-carboaluminate one form of AFt is formed instead of another form of AFt known as monosulphate (see section 2.5) [61].

2.1.4 C_4AF

Ferrites and aluminates are closely mixed together in cement clinker due to similarities in cell parameters resulting in aluminoferrite. The composition of aluminoferrite in Portland cement is fairly consistent and shows that there is very little to no substitution for Ca^{2+}[34]. C_4AF does not have polymorphs but aluminium and iron can substitute in the octahedral and tetrahedral sites. Mn^{3+} can replace all Fe^{3+} or up to sixty percent of Al^{3+} [34].

According to Beaudoin et al. [62] hydration and strength development from C_4AF can exceed compared to alite in the initial week of hydration. However, the main debate on C_4AF hydration is the destination of iron following the dissolution of C_4AF. The aluminates can get involved in C-S-H, ettringite or AFm phase formation while calcium might end up as CH or calcium silica hydrates.

Without gypsum:

Eq. 2.1.5 $$C_4AF + 13H \rightarrow C_4(A,F)H_{13}$$

With gypsum:

Eq. 2.1.6 $$C_3AF + C\bar{S}H_2 + 12H \rightarrow C_4(A,F)C\bar{S}H_{12}$$

2.2 Hydration kinetics

Cement hydration has a series of complex exothermic reactions which occur over time and have different compositions and crystallinity for hydration products depending on the hydration rate [63]. Measurements of cement hydration evolution have shown that there are three main peaks with increase in heat during the cement hydration.

The kinetics of cement hydration in conventional Portland cement are fairly understood[34], [64]. Portland cement hydration includes a series of endothermic and exothermic reactions and there is general agreement regarding these kinetics of the hydration [56], [65]. However, there are some disagreements over the mechanisms responsible for the induction and further stage(s) of hydration of Portland cement.

The main hydration products can be listed as C-S-H, CH, AFm and AFt. The most important and abundant product is C-S-H which can have various

compositions. C-S-H exists as an amorphous or very poor crystal with a mean Ca/Si ratio of 1.7-1.8[66]. The chemical composition and microstructure of C-S-H depend on cement composition, water to binder ratio, the temperature of hydration and etc. The hydration of cement has been studied by the kinetics of hydration in relation to heat evolution[35].

Figure 2-1 and Figure 2-2 show the different stages in cement hydration corresponding to the main microstructural development and heat evolution during the hydration process. Stage I in Figure 2-1 shows the highest heat produced due to clinker dissolution. Stage II is the induction or dormant phase shown as a valley. Stage 3, the acceleration period is where a very large heat evolution can be seen due to the dissolution of C_3A, $CaSO_4$ and C_3S [67].

The range within Stage III is known as the acceleration period where the cement starts setting and hardening and stage IV is known as the deceleration period. After this stage, the long-term hydration period starts and compared to other peaks is less intense and is due to the formation of AFm [68].

Table 2-3 Stages of hydration.

Stage	Phase	hydration process	Effect
I	Initial hydrolysis	Initial hydrolysis, dissolution of ions	
II	Dormant stage	Continued dissolution	Initial set
III	Acceleration	Initial formation of hydrates	Final set and initial strength
IV	Deceleration	Continued formation of hydrates	Early strength
V	Steady state	Slow formation of hydrates	Later strength

At the early age hydration, the initial primary reaction improves the heat evolution and a fast reaction increases the temperature. This is marked as stage II in Figure 2-1 and corresponds to Figure 2-2b. Aluminate and ferrite react with calcium sulphate in solution during this phase, resulting in the production of an amorphous alumina/silica rich gel on the surface. $CaSO_4$ prevents the aluminate phase from reacting quickly with water, preventing a "flash set."

The formation of AFt is due to C_3A reacting with $CaSO_4$ and water and it builds up as a layer on C_3A preventing the rapid hydration. Almost after 10 minutes of hydration, rod shaped AFt forms at the edge of the gel. The water to binder ratio is the main factor affecting the amount of AFt formed in initial hours.

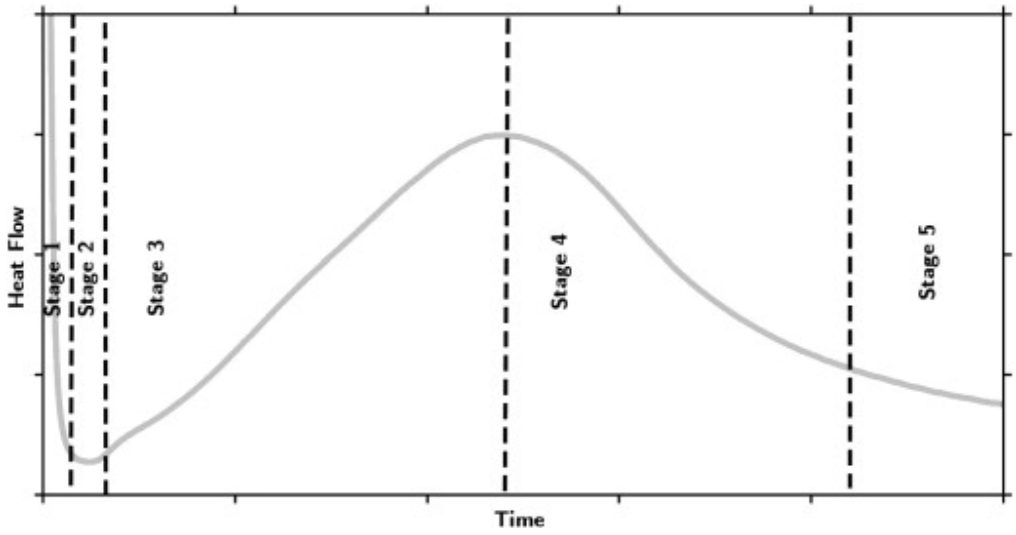

Figure 2-1 Rate of heat evolution in hydration of Portland cement[69].

The formation of C-S-H and CH can only be seen during the stage III and it contributes to an increase in strength. This is when the evolution of heat is maximum.

The hydration of alite resulting in the formation of C-S-H is the main parameter for heat evolution. The C-S-H formed is called outer product C-S-H (OP)

which grows on AFt rods in the spaces initially filled with water. C-S-H formation is the main reason for setting and binding.

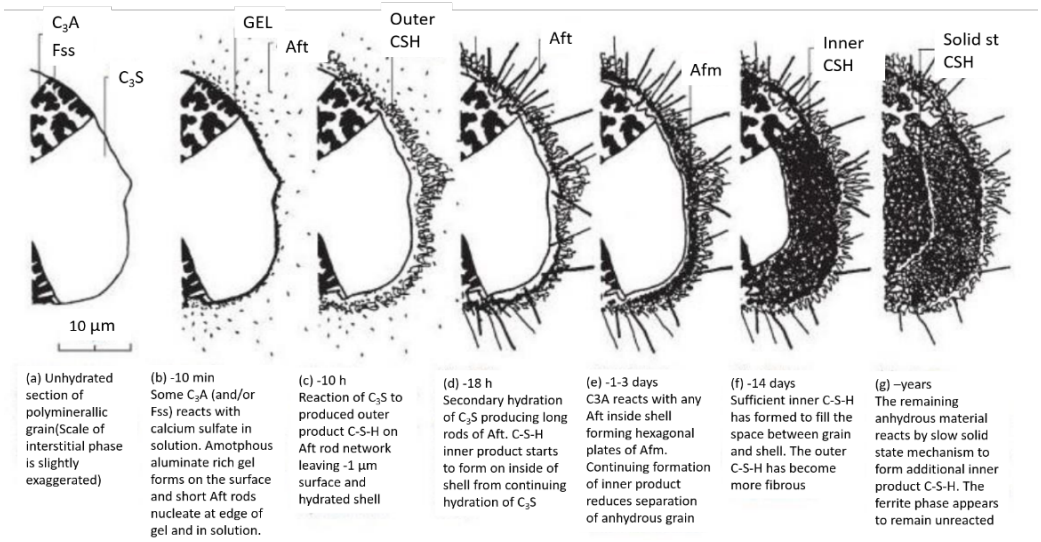

Figure 2-2 Microstructural development in a cement grain [35]**.**

As a result of secondary hydration of the aluminate phase with the formation of monosulfates, AFt develops in long rods (Figure 2-2d) after around 16 hours of hydration (AFm). C-S-H begins to grow on the interior of the shell as the inner product C-S-H after this stage. The late hydration only starts at 1 – 3 days and hexagonal AFm plates can be seen forming inside the shell (Figure 2-2e) as a result of the reaction of C_3A and AFt. The area between the anhydrous grain and the shell gradually fills up as the inner product forms over time. (Figure 2-2f). The outer product is gradually filled with C-S-H and CH (Figure 2-2g). The ferrite phase, on the other hand, remains unreacted throughout. As the hydration process progresses, belite begins to react, forming large plates of AFm at the expense of AFt [70].

2.3 Model structure for C-S-H

Le Chatelier first hypothesised that C-S-H is the primary binding phase of cement in 1919, and many other researchers have since investigated the structure of C-S-H[71]. Poor crystallinity and variable composition of C-S-H hinder the determination of its structure. When the XRD patterns of the C-S-H found in cement are compared to the patterns of natural minerals tobermorite and jennite, a few structural similarities emerge [72] and for that reason, different models have been developed based on these minerals. The natural type of tobermorite is the 1.4nm tobermorite with a Ca/Si ratio of 0.83.

2.3.1 Tobermorite and Jennite groups

Figure 2-3 illustrates the structure of 1.4 nm tobermorite which has a crystalline layered structure. The 1.4 nm structure would result in 1.1 nm tobermorite when heated to 55 °C and 0.9nm tobermorite when heated to 300 °C. The 1.4nm tobermorite has a general formula of $Ca_5Si_6O_{16}(OH)_2 \bullet 8H_2O$ and when heated would lose interlayer water and form less hydrated structures. The interlayer distance is described by the prefix. The existence of water molecules is clearly shown to have a direct relationship with the interlayer distance.

Despite the fact that C-S-H only has a single-chain dreierketten and limited chain length, several pieces of evidence have proven that the structure of 1.4 nm tobermorite is acceptable for C-S-H gel at low Ca/Si ratios [66]. Tobermorite has chains attached on both sides and a central layer of CaO sheets with silicate dreierketten (silicate tetrahedra repeating in a group of three tetrahedra). The negative charge is balanced by the presence of water molecules and Ca^{2+} ions in the space between the layers. Two forms of calcium polyhedra, one coupled to six oxygen atoms and an OH group, and the other bonded to six oxygen

atoms and a water molecule, form up the primary layers. Silicate tetrahedra are divided into two types: paired tetrahedra and bridging tetrahedra. The paired tetrahedra are held together by four oxygen atoms, two of which are shared with the centre layer. Three oxygens and one OH group are linked to the bridging tetrahedra.

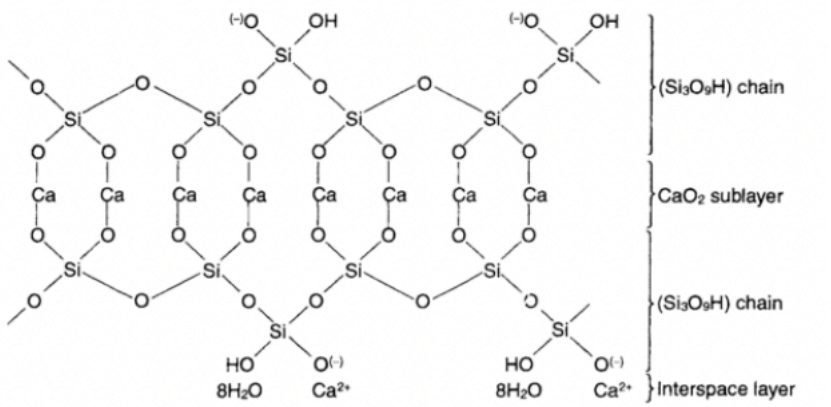

Figure 2-3 Schematic representation for the structure of 1.4nm tobermorite [63]

The structure of jennite with a general formula of $Ca_9(Si_6O_{18})(OH)_6 \cdot 8H_2O$ is shown in Figure 2-4. It has a layered structure and, like tobermorite, can undergo lattice shrinkage when heated to 70–90 °C, culminating in the creation of metajennite due to the loss of water. The structure of jennite with a Ca/Si ratio of 1.5 consists of a core layer of CaO with dreierketten units of silicate on sides [73], [74]. The differences between tobermorite and jennite could be listed as:

- Jennite has both Ca-OH and Ca-O bonds in the main calcium layer whereas tobermorite contains only Ca-O bonds.
- The CaO layers in jennite are more corrugated than that of 1.4 nm tobermorite.

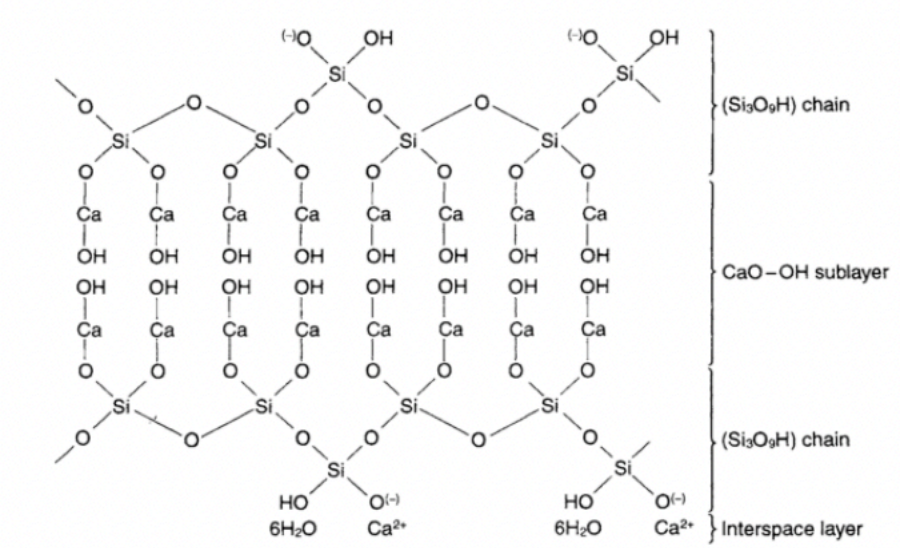

Figure 2-4 Schematic representation for the structure of jennite [63]

2.3.2 Calcium/silica ratio

Calcium silica hydrate as the main hydration product of the Portland cement significantly impacts the physical and chemical properties of cement based materials. This poorly crystalline gel has a variable amount of calcium, silica and hydrates. The layering of the C-S-H can be roughly illustrated as calcium oxide layer sandwiched between dreierketten chain structures in a repeating three silica tetrahedra. Two of these silica units known as pairing tetrahedra are linked to a layer of calcium oxide. The third silica unit links both of the pairing tetrahedra and is known as bridging tetrahedra[75].

The reactions between calcium and silicate ions in aqueous media at normal temperatures result in semi crystalline phases. The most known of these phases are C-S-H(I) and C-S-H(II) which are imperfect forms of tobermorite and jennite respectively. As noted in in section 2.3.1, the Ca/Si ratios calculated for 1.4 nm tobermorite are higher than the idealized structures. The Ca/Si ratio of C-S-H(I) and C-S-H(II) are higher than that of 1.4 nm tobermorite and jennite [34].

The Ca/Si ratio in C-S-H is mainly determined by the composition of cement. In ordinary Portland cement with a Ca/Si ratio average of ~1.7, silica chains in interlayer space consist of dimers and calcium hydroxide[76]. The Ca/Si ratio in cement paste is higher than that of jennite and 1.4 nm tobermorite [34].

The decrease in Ca/Si ratio has been linked to increase in dreierketten chain length and the interlayer spacing. In the presence of aluminium, these chains are much longer and the spacing is larger. As such, at low Ca/Si ratio, the aluminium is positioned in bridging chains as aluminium tetrahedra and increase the mean chain length. Whereas, increase in Ca/Si ratio, results in octrahdrally structured aluminium and amorphous aluminate hydrates[75]. According to Pelisser et. al. [77] changes in Ca/Si ratio affects the nature of intralamellar interactions and between nanocrystallites. They have concluded that an increase in the Ca/Si ratio reduces the interplanar distance, promoting increased strength and density.

2.4 C-S-H model development

2.4.1 Powers

The model suggested by Powers describing C-S-H as cement gel dates to the year 1958 and does not represent a nanostructured model. This cement gel consists of mostly fibrous particles and gel pores. The fibre particles with straight edges on a network of cross links. It is estimated that the C-S-H gel has a porosity of 28% [78]. When cement is in contact with water it will form this cement gel as well as calcium hydroxide and the remaining of the initial water particle. As a result of cement paste hardening, this matrix will form cross linked gel particles with various cavities called capillary pores.

This theoretical model was also used by Powers to explain deformation (i.e. drying shrinkage) and mechanical characteristics. Powers hypothesised that the main strength in C-S-H gels came from physical bonds between particles in this paradigm.

2.4.2 Feldman and Sereda

Feldman and Sereda's model [79] which also did not represent a nanostructure, suggested a layered structure of C-S-H gel relying on the deformation behaviour, weight, and Young's modulus of cement paste during absorption and desorption with relative humidity. Young's modulus remained stable after absorbing up to 50% RH, then grew dramatically until it reached 100% RH. However, after desorption, the Young's modulus stayed constant until a very low RH value, after which it significantly fell. They irreversibly proposed a tobermorite layered structure with interlayer water particles.

2.4.3 Taylor

Taylor's C-S-H model is based on the tobermorite and jennite structure, in which the bulk of the disordered layers are associated with structurally imperfect jennite and the minor proportions are related to 1.4 nm tobermorite with silica-tetrahedra removed. In this model, the lowest and maximum Ca/Si values are 0.83 and 2.25, respectively [80]. In this model, a finite silicate chain with a chain length of 3n-1 (where n is an integer) is utilised resulting in 2,5,8,.. chains (see section 2.8.7 for detail on Q units). Taylor hypothesized that each bridgin tetrahedron only carries one hydrogen atom, and when one of these tetrahedra is omitted, just one of the radicals is terminated by a hydrogen atom. The removing of all the bridging tetrahedra is consistent with experimental findings showing that the Ca/Si ratio of C-S-H differs from that of tobermorite and jennite. Because the lack of the bridging tetrahedra results in the presence of enough H^+

ions, the quantity of interlayer Ca remains constant, keeping the net charge unaltered.

According to Taylor, structural units derived from the structure of tobermorite are the first to nucleate, resulting in a C-S-H gel with a reduced Ca/ Si ratio initially, followed by the development of both tobermorite and jennite dimers when the Ca/Si ratio rises to 1.25 to 2.25. Jennite pentamers develop over time with a Ca/Si ratio of 1.8, similar to C-S-H gels.

2.4.4 Richardson and Groves

Richardson and Groves based their general model on TEM, EDX, and NMR experiments. Based on this model, C-S-H consists of a highly disordered dreierketten layered structure with changing quantities of calcium hydroxide and finite length silicate chains by (3n-1) [81]. T/CH (tobermorite/calcium hydroxide) (equation 1) and T/J (tobermorite/jennite) (equation 2) are two alternative perspectives on C-S-H in the suggested model. this model provides a more flexible Ca/Si ratio(0.67 and 2.5 for minimum and maximum respectively)than Taylor's model(0.83 and 2.25).

The most significant distinction between T/J and T/CH is the location of Ca^{2+} ions, which is in the CH layer of tobermorite-like structure for T/CH or connected to jennite dreierketten as the formation of Si-O-Ca-OH for T/CH. This concept is useful for linking the composition and structure of the C-S-H phase. The following is the general formula for T/CH viewpoint:

Eq. 2.4.1 $$[Ca_xH_{(6n-2x)}Si_{(sn-1)}O_{(9n-2)}] \bullet zCa(OH)_2 \bullet mH_2O$$

Where,

X: (6n-w)/2; Ca^{2+} ions required to charge balance the silicate chain

z: (w+n(y-2))/2

n: 1, 2, 3…… (number of units)

m: number of water molecules bound

(3n-1): silicate mean chain length

The general formula for T/J viewpoint is given by:

Eq. 2.4.2 $[Ca_{2n}H_wSi_{(3n-1)}O_{(9n-2)}] \bullet (OH)_{w+n(y-2)} \bullet Ca_{n.y/2} \bullet H_2O$

Where,

n: 1, 2, 3…… (number of units)

w: number of silanol groups

w/n: degree of protonation

(3n-1): silicate mean chain length

This model is fairly adaptable, and the index values may be determined experimentally. The silicate MCL: (3n-1) is determined using ^{29}Si NMR, and the Ca/Si ratio is determined using TEM – EDX. The degree of protonation (w) has range of values limited to maintain the layer structure and neutrality.

$0 \leq y \leq 2$: $n(2-y) \leq w \leq 2n$

$2 \leq y \leq 4$: $0 \leq w \leq 2n$

$4 \leq y \leq 6$: $0 \leq w \leq n(6-y)$

The T/J and T/CH views can be adapted to accommodate the other components when certain substitution ions take the place of Si ions in a C-S-H gel [82]. This is a typical occurrence in cement samples including SCMs, where the Al ions

produced by SCMs can replace the Si in the C-S-H silicate chain to generate C-A-S-H.

2.4.5 Pellenq

Pellenq developed a molecular model based on the Ca/Si ratio and density to characterise the structure of C-S-H, ignoring earlier layer theories based on structurally imperfect tobermorite and jennite [83]. It is based on the deformation of a monoclinic periodic computational cell of tobermorite with a Ca/Si ratio of 1 and an interlayer spacing of 1.1 nm. This model predicts the key structural aspects, fundamental physical properties, and certain mechanical properties of C-S-H gel with a chemical composition of $(CaO)_{1.65}(SiO_2)(H_2O)_{1.75}$. Ca-O lengths calculated by this model deviate from known distances for crystalline C-S-H phases, according to Richardson [84]. He also noted that the formation of calcium atoms with five, four, or 3- coordination is implausible since calcium atoms in most calcium silicates have a six or sevenfold coordination.

2.4.6 Richardson's model structure for C-(A)-S-H (I)

Richardson [66] has presented a novel model structure for C-(A)-S-H based on clinotobermorite. Normally, the model structure of C-S-H is derived from orthotobermorite, which has an orthorhombic sub-cell [71]. However, Richardson discovered that if the starting structure is orthotobermorite, it is impossible to generate a structural model for a dimer that is crystal-chemically consistent with known crystalline phase of the known structure of crystalline calcium silicate hydrates and related phases. As a result, a more credible model was built using clinotobermorite rather than orthotobermorite. The C-S-H structure is produced from single-chain clinotobermorite in this paradigm, as illustrated by the following general expression:

Eq. 2.4.2 $\mathrm{Ca_4\left[Si_{1-f-v}Al_f\square_vO_{3-2v}\right]6H_{2i}Ca_{1-i}(Ca,Na_2,K_2)_{3f}H_2O}$

Where,

$\square$: Vacant tetrahedral site

v : Fraction of tetrahedral sites that are vacant

f : Fraction that are occupied by Al

d : represents the fraction of double chain structure i.e. 0 < d < 1

Where, d = 0 describes that the structure is entirely single chain

d = 1 describes that the structure is entirely double chain

i : reflects the extent to which the net charge is balanced by protons or Ca^{2+} ions.

The Ca/Si ratio of Al free C-S-H (I) is:

$$\mathrm{Ca/Si} = (6-i)/6(1-v)$$

Also, the maximum Ca/Si ratio is obtained when the net charge is balanced by Ca^{2+} ions (i = 0).

$$(Ca/Si)max = 1/(1-v)$$

2.5 AFt and AFm phases

AFt (AL_2O_3-Fe_2O_3-tri) or calcium sulfoaluminate hydrate phase is a hydration product of cementitious materials and one of the most known phases of it is called ettringite. Initial reaction between C_3A and $CaSO_4$ form AFt and this early formation of AFt on the surface of the particles has been accepted to be the reason for reduced reaction rate [34]. Ettringite is the most important form of the AFt. According to Taylor [34],the AFt phases have the general constitutional

formula of $[Ca_3(Al,Fe)(OH)_6 \bullet 12H_2O]_2 \bullet X_3 \bullet xH_2O$ where X denotes one formula unit of doubly charged or two formula of a singly charged anion.

Minard et. al. [85] has proposed that the reduced reactivity is the resultant of the sulphate absorption on reactive sites. Secondary formation of AFt can be observed after the depletion of sulphate source. Further depletion of sulphate at later ages from several days results in the transition of AFt phase to monosulfate or AFm. Generally the amount of AFT and monosulfate formed depends on the degree of hydration and could be observed in outer product regions respectively as thin hexagonal shape needles and irregular large plates [44], [86].

AFm (Al_2O_3-Fe_2O_3-mono) phases are formed when the ions they contain are in an appropriate condition in an aqueous system. AFm phases are formed under similar conditions to AFt phases only at a lower CaX to $C_3(A,F)$ ratios. Majority of the AFm phases form during the cement hydration are poorly crystalline and mixed with calcium silicate hydrates[34].The AFm family have have the general formula of $[Ca_2(Al,Fe)(OH)_6] \bullet X \bullet xH_2O$ where X represents one formula of a singly charged anion or half a formula unit of a doubly charged unit [34]. They have a layered structure based on CH by the order replacement of Ca^{2+} and three by Al^{3+} or Fe^{3+}.Anions are used to balance the positive charge of this layer. Many different anions can be placed as X. These anions are either monovalent, e.g., OH^-, Cl^-, or divalent, e.g., CO_3^{2-}, SO_4^{2-}, etc. The number of interlayer anion are dependent on the charge balance. The AFm is also affected by the size and polarization of these anions. Hence, they control the interlayer water contents and directly control the layer stacking sequence [87].

According to Balonis et al. [88], introducing calcium nitrate or calcium nitrite into the mix results in displacing sulfate from AFm forming nitrate AFm or nitrite

AFm. The reaction is much more complex than a simple ion exchange and displaced sulfate increases the volume of solids in ettringite. Furthermore, Balonis et. al. observed that introducing nitrate and nitrite where carbonate containing phases are present resulted in the replacement of carbonate ions with nitrate and nitrite form nitrate/nitrite AFm. The freed carbonate ions from this interaction were observed to form calcite.

Wang et al.[89] has observed that in presence of nitrates, ageing of the samples promotes transition of the nitrate-AFt to nitrate bearing AFm. According to Ramachandran [90], nitrite AFm is formed when calcium nitrite reacts with the Al_2O_3 bearing phases of cement, and it can also crystallise when aqueous sodium nitrite reacts with C_3A in the presence of calcium hydroxide, but its water content is less sensitive to humid conditions. The AFm/AFt balance can be altered by presence of nitrate. The formation of nitrate-AFm in self-healing process in cement-based materials requires further investigations.

2.6 Microbially induced calcium carbonate precipitation in cement based materials

This section discusses bacterial induced precipitation of calcium carbonate in cement-based materials focusing on the following aspects:

- Biomineralization
- Types of bacteria (ureolytic, non-ureolytic)
- MICP mechanism for ureolytic bacteria
- Delivery systems of bacteria
- Selection of nutrient media
- Source of calcium ions

The scope of the current work is limited to the introduction of the ureolytic and viable *S. Pasteruii* cells into cement paste samples using a calcium nitrate medium.

2.6.1 Biomineralization in cementitious materials

Micro-cracks in the concrete matrix can provide pathways for the chemicals and water to penetrate. While there are conventional methods for micro-crack repair, the sealing agent might not be able to fully penetrate. In such a case, autogenous healing could be a method to solve the problem.

Recent works in this field showed the possibility of developing smart self-healing cement-based materials using biomineralization that could trigger an autogenous self-healing [2], [91]. Biomineralization is a series of complex bio-chemical reactions in which the microorganisms produce mineral precipitation [12]. In this particular case, the microorganisms stimulate the formation of $CaCO_3$, which is also known as MICP [12]. MICP is the product of a series of bacteria's metabolic reactions occurring at the same time.

Hoffmann et.al. [32] describes the bacteria induced mineral precipitation as a mineral precipitation when the ion concentration exceeds the solubility limits and reaches a degree of supersaturation. The metastable forms of these minerals take place in the nucleation sites where the crystal growth happens either homogeneously or heterogeneously. In MICP the bacteria triggers the reaction by modulating relevant parameters such as the ion concentration, pH and nucleation sites. Also, the large surface area of the bacteria compared to its volume makes them an ideal site for a crystal nucleation [32]. Furthermore, the bacteria's surface properties could also influence the morphology of the

precipitation and their type. It has been observed that the dead bacteria cells can also act as nucleation sites which was corroborated by Skevi et.al. [31]. The by-products of the bacterial metabolic activity also affect the pH of the environment which in returns contributes to the availability of the ions.

The anion concentration is also directly related to pH and dissociation of carbonates and this high pH results in the deprotonation of carbonate species and producing bicarbonate and carbonates. As such the bacteria have a direct influence on the increase and likelihood of crystal precipitation.

Microbial calcium carbonate precipitation may be caused, regulated, or influenced by microorganisms. Microbially induced precipitation occurs as a direct result of microbial activity, which creates biochemical conditions that favour the precipitation [2]. microbially mediated precipitation, on the other hand, is the product of cellular activity directing the nucleation and development of minerals [23].

It is still unclear if the calcium carbonate precipitated by microorganisms in cement-based materials is due to urea hydrolysis by the microorganisms, electrostatic attraction between the microorganisms' negative surface charge and ions in the pore solution, or interactions of extracellular substances formed by the microorganisms[92], [93].

2.6.2 Ureolytic and non-ureolytic bacteria

For the ureolytic bacteria, calcium carbonate precipitation strictly relies upon the urease enzyme activity of the cells. The urease enzyme controls the hydrolysis of available urea in the nutrient media initiating the metabolic reactions. As a result, high urease enzyme activity, which catalyses the hydrolysis of urea into carbonate and ammonia, is needed for microbial induced

calcium carbonate precipitation to occur. *S.pasteurii* and *Bacillus sphaericus* are two of the commonly used ureolytic bacteria strains. The previous work carried out by this researcher focused on the impact of ureolytic bacteria on the mechanical properties of cement based materials, is the main reason to use ureolytic bacteria in current work. The comparison of these works will provide a better understanding of ureolytic bacteria used in cement based materials.

For non-ureolytic bacteria, calcium carbonate precipitation relies on the degradation of organic calcium compounds and requires the introduction of an organic calcium source into the mix. Bacteria acting as a catalyst decomposes calcium source into calcium, carbon dioxide and H_2O providing them with a source of energy and building blocks for their growth. Furthermore, the decomposed carbon dioxide could turn into CO_3^{2-} and reacts with calcium ions to form calcium carbonate due to the high pH nature of the cement-based mix. *Bacillus cohnii*, *Bacillus pseudofirms* and *Bacillus alkalinitrilicus* are the typical strains in this category.

2.6.3 Mechanism of MICP

Biomineralization could naturally take place due to the unique surface structure of the microorganism and functional units on the bacterial cell wall. It also could be achieved through the metabolic activities of bacterial cells. There are many ways to achieve biomineralization process if the provided conditions are suitable for the bacteria. Heterotrophic bacteria can induce mineral precipitation via nitrogen or sulphur cycles. Nitrogen cycles can be simply explained by ammonification of amino-acids, degradation of urea and reduction of nitrates [94].

Among the abovementioned methods relevant to MICP, the degradation of urea has been commonly used in cement-based materials due to possibility of effective control measures to adjust the chemical reactions involved. In this case, bacteria possessing urease enzyme can degrade urea into ammonia and carbon dioxide . This is followed by an increase in pH and if dissolved calcium [Ca^{2+}] is present in the environment, then this pH increase triggers MICP [95].

$$CO(NH_2)_2 + H_2O \xrightarrow{urease} 2NH_3 + CO_2$$

$$NH_4^+ \leftrightarrow NH_3 + H^+$$

$$H_2CO_3 \leftrightarrow HCO_3^- + H^+$$

$$HCO_3^- \leftrightarrow CO_3^{2-} + H^+$$

These reactions lead to calcium carbonate precipitation:

$$CaCO_3 \leftrightarrow Ca^{2+} + CO_3^{2-}$$

Here, the primary nitrogen source is ammonia and it is consumed directly by the bacteria. While urease–active microorganisms can decompose urease ammonia and dissolved inorganic carbon (DIC), their surface charge can attract positively charged calcium ions acting as a heterogeneous nucleation site for MICP. There are several factors influencing these physio-chemical reactions such as microorganism type, [Ca^{2+}] and DIC concentration, pH of the environment and availability of nucleation sites [96], [97]. These factors not only influence the rate of precipitation, but they also play a crucial role in changing the morphology of $CaCO_3$ precipitate.

Three known polymorphs of $CaCO_3$ are Calcite, vaterite, and aragonite. Other known forms of hydrated calcium carbonate are ikaite and monohydrocalcite. Another known form of calcium carbonate is amorphous calcium carbonate (ACC). ACC in its pure form is known to be very unstable but some microorganisms can produce a stable form of ACC which is a transition point to form more stable forms of crystalline calcium carbonate. According to Addadi et. al [98], biomineralization could result in an unhydrated transient form of ACC which is stable.

Among the known three morphologies, calcite and aragonite are the most stable polymorphs. In the case of MICP, calcite and vaterite are the most commonly observed polymorphs [15], [98].

Mortensen et al. [99] evaluated environmental factors affecting MICP by using suspended *S.pasteurii* cells in both freshwater and seawater. The investigation to understand the effect of different factors on MICP was conducted by the authors to evaluate the different ammonium and oxygen concentrations, as well as the viability of cells. It was concluded that uniform MICP was achievable in many different environments and ureolytic microorganisms were able to remain viable in different salinity conditions. Ureolytic microorganism could be capable even in the high level of ammonium concentration and limited oxygen availability in cultural environments[99].

According to L. Addadi et al.[98], for most of the biological amorphous $CaCO_3$ precipitation, the result of infrared spectra is similar. He also, evaluated samples collected from sea organisms such as *Pyura pachydermatina* and *Orchestia cavimana*. However, it was found that the significant difference between the various amorphous $CaCO_3$ is the possibility of their transformation

during a period of time to the more stable phase of crystalline structure [98]. This concept could be useful for explaining the unusual nature of infrared spectroscopy in biogenic $CaCO_3$ production. ACC has absorption peaks at 866 cm^{-1} and 710 cm^{-1}, whereas, well-formed calcite crystal has a sharp peak at 713 cm^{-1} and the absence of 713 cm^{-1} peaks in an infrared spectrum shows well-ordered calcite is not present in the material [98].

2.6.4 Delivery systems

One of the commonly used techniques involves using microcapsules containing the bacteria directly embedded in the matrix of the cementitious material. With this method, the bacteria and nutrient medium only get released when there is a crack crossing the microcapsules and the potential for affecting early age properties of the cement hydration products is very low [100].

The encapsulation approach consists of immobilizing the endospores of the bacteria in a protective encapsulation, such as inorganic lightweight porous aggregates [101], polymeric membranes [102], hydrogels [26] and microcapsules [25].

According to Wang et al. [26] use of a biocompatible hydrogel encapsulation for self-healing in cement-based materials resulted in a high rate of viability for *Bacillus sphaericus* within the cement paste matrix and the microorganisms were able to perform MICP and seal the cracks smaller than 0.5 mm in width and decrease water permeability. However, this study did not investigate the strength recovery of the self-healing for mortar samples. Further on, series of tests to investigate the self-healing performance of *B. sphaericus* endospores were conducted by Wang et al. [102]. In this study, glass tubes embedded in mortar were used to introduce encapsulated bacteria by micro

silica gel and polyurethane membranes. Regarding strength recovery and reduction in permeability, the results confirmed that polyurethane membranes have a higher self-healing efficiency compared to silica gels [102].

Another method developed to initiate the biomineralization is the use of lightweight aggregates with embedded immobilized bacteria cells. Huynh et. al. [103] used *Bacillus subtilis Natto* encapsulated in lightweight porous aggregates with their nutrient source and calcium lactate. This approach extends the viability of the microorganisms; however, the use of lightweight porous aggregates significantly decreased the compressive strength of the samples. One of the objectives of Wiktor and Jonkers [23]study was to evaluate the time dependency bacterial viability by immobilization of bacteria inside the expanded clay. As a result, the capability of lightweight porous aggregates increased the functionality of self-healing from 7 days to 100 days.

The introduction of the viable bacterial strain directly into the fresh mix is one of the cost effective methods for biomineralization in cement-based materials. Recent studies have been aiming at developing a self-healing material by actual incorporation of the cells in mortar or concrete. An early approach by Jonkers et al. [19] was to use *Bacillus pseudofirmus* and *Bacillus cohnii* endospores suspended in water used for mixing mortar. With this approach, crack sealing was observed due to robust mineral precipitation but the permeability of the mortar after self-healing was not investigated. These endospores without protection were found to be viable after four months; however, samples cast with bacteria showed a decrease in 28day compressive strength due to increase in pore size [19].

The use of viable cells directly mixed into the fresh concrete without any encapsulation or immobilization is considerably inexpensive and a pragmatic approach in real life with fewer preparation steps required. This method is the main focus of the current study and some of the recent studies in the literature are presented in Table 2-4.

Table 2-4 Bacteria strains directly incorporated into concrete/mortar without protection measures*

*There is a lack of studies in the literature regarding incorporation of bacteria strain in cement paste.

Strain	**Concentration (cells/mL)**	**Findings**	**Reference**
Bacillus subtilis	$x10^8$	Decrease in porosity, Increase in compressive strength	[104]–[107]
Bacillus sphaericus	$X10^3$, $x10^5$, $x10^7$	Best compressive strength results with $x10^5$ concentration, improve in all mechanical properties	[108], [109]
Bacillus pasteurii	$x10^5$, $x10^6$, $x10^7$	Enhanced mechanical properties, Max increase in strength was 22%	[108], [110]
Bacillus megaterium	$x10^3$, $x10^4$, $x10^5$, $x10^6$, $x10^7$	Maximum compressive strength at $x10^5$ concentration, Enhanced mechanical properties	[111], [112]
Bacillus subtilis	$x10^8$	Increased compressive strength by 12%	[106]

2.6.5 Microorganism selection

There is an extensive list of bacterial strains that can result in biomineralization and some are presented in Table 2-4. However, considering a variety of factors affecting the bacterial culture, viability, and $CaCO_3$ precipitation, it is essential to choose the right type of bacteria for biomineralization in cement-based materials.

It is necessary to choose a microorganism which can tolerate a high level of alkalinity and shear stress because of the complex environmental conditions in cement-based materials and mixing procedure, as well as a high tolerance for limited access to nutrients. In particular, alkaliphilic and endospore-forming microorganisms can tolerate the stresses induced within cement-based materials.

B. megaterium was used by Achal et al, [18] and they stated that it is another alkaliphilic, endospore-forming bacterial strain that can also decompose urea. However, the urease enzyme activity can be suppressed by increasing ammonium and nitrogen concentrations, which is a major disadvantage of this microorganism. Ghosh et al. [21] used a modified medium (pH 7.5) to grow one strain of *Shewenella* species, then suspended the bacteria in mixing water to achieve seven different cell concentrations ranging from 10 to 10^7 per mL. The porosity of mortar with and without bacteria was tested at 28 days using mercury penetration porosimeter (MIP). The findings showed that the cubes with 10^5 CFU/mL had substantial reductions in porosity for the *Shewenella* microorganism. While the authors attributed the porosity decline to the addition of the *Shewenella* microorganism, no reason was offered as to why the

specimens with the 10^5 CFU/mL composition had the greatest reduction in porosity.

Bacillus species, according to Dickson and Koohmaraie[113], have a relatively wide surface area as compared to other strains that may be used in biomineralization. Since the total surface charge of the. bacteria rises with an increase in surface area, which means that the calcium ions and *S. pasteurii* strains have a strong bonding ability.

Sporosarcina pasteurii is one of the possible strains for biomineralization application in cement-based materials which has a high tolerance for the harsh environment of cement hydration and limited access to nutrient medium [114]. However, according to Bundur et al. [114], air-entraining agents used in concrete industries can decrease the viability of *S. pasteurii* in concrete over time. Furthermore, these microorganisms can cause calcite precipitation by acting as nucleation sites, which occur when a negatively charged surface attracts positively charged calcium ions [27].

2.6.6 Nutrient medium selection

Factors such as microorganism type, nucleation sites, viable cell concentration and selection of an efficient nutrient source are essential for MICP application, bacterial viability, and its metabolic activities.

To achieve MICP through urea hydrolysis, nitrogen and carbon source are vital for the microorganisms. Bio-chemical reaction mentioned in Section 2.6.3, shows that microorganisms use urea as the prime source of nitrogen. Urea decomposition under the urease enzyme of microorganisms results in the production of ammonium cation (NH_4^+) and then consumed by the bacterial cells.

In most of the previous studies, yeast extract was used as the primary source of carbon for cells. Yeast extract contains many amino acids and vitamins required for microorganism viability [18]. However, high sugar content and other carbohydrates in yeast extract cause a significant extension for the induction period of cement-based materials during the hydration process [115].

Besides the fact that yeast extract has an adverse effect on cement paste setting time, its high price is the main reason for finding an alternative nutrient for bacterial growth. The possible alternative for yeast extract should have a less cost value which could also have to provide the same efficiency in bacterial growth and biomineralization process.

According to Achal et al.[116], one of the alternative carbon sources could be lactose mother liquor (LML), which is a by-product of the dairy industry. Theuse of LML in the nutrient medium resulted in a better performance in bacterial growth and MICP compared to nutrient media containing nutrient broth or yeast extract.

Another feasible nutrient for biomineralization is the use of Corn steep liquor (CSL), as a waste by-product of the corn milling industry, which is low in cost and a sustainable alternative nutrient. Achal et al. [117] showed a significantly lower total cost by using CSL as a nutrient source for *S. pasteurii.* Moreover, as the main concern, the use of CSL in bacterial growth improved the urease enzyme activity and also calcite precipitation of *S. pasteurii* cells [117], [118].

The CSL used in the current study was purchased through a bait and fish food company (AABaits) at a current price of £8.99/L in comparison to the current price of yeast extract for £64.90 per 250g (Sigma Aldrich). The amount used in the bacterial growth medium is roughly similar for both CSL and yeast extract which makes the CSL a very cheap replacement.

Previously, Amiri et al. [118], conducted a series of experimental trials on the use of CSL and chemical admixtures in the self-healing application. According to this study, the replacement of yeast extract by CSL shows a significantly lower initial setting time of cement paste. This change in setting time was correlated to lower amounts of carbohydrates and sugar in CSL compared to yeast extract [118], [119]. The early age compressive strength of samples cast with CSL was higher than samples with yeast extract. Meanwhile, due to the unknown composition of CSL used in this study, the possible effects on cement hydration and its products could require further investigation.

Fahmi et.al.[120] also showed that the use of CSL as a nutrient medium for bacterial growth is a cost effective material to achieve biomineralization in sand stabilization. They also concluded that calcium nitrate is the preferred calcium ion source for ureolytic activity. Furthermore, Amini et.al.[121] reported a higher compressive strength and lower water absorption characteristics for a mortar that included bacteria and CSL nutrient medium. Based on these previous works, it has been proven that the useof CSL nutrient medium for ureolytic bacteria is effective.

Another extensive research on use of CSL for ureolytic bacteria has been conducted by Sumit et.al.[122]. Their work shows that the *Bacillus sp.CT5.* strains and CSL medium directly incorporated in cement-based materials

resulted in higher compressive strength compared to nutrient broth medium. They also concluded that the use of CSL as a nutrient medium has the lowest effect on setting time and fresh properties of the mix and this is the result of low carbohydrates and nitrogen present in CSL compared to yeast extract.

2.6.7 Influence of Ca^{2+} source on biogenic calcium carbonate:

Available calcium ion in the nutrient environment has a significant effect on the MICP and the mineral morphology. Muynck et. al [8] reported that using calcium acetate as a calcium ion source instead of calcium chloride, resulted in favouring precipitation of vaterite over calcite. Calcium ion source can be available in cement-based materials, although, additional calcium sources are often added for biomineralization applications [21], [123].

The main calcium sources used in previous studies within literature can be summarized as; calcium chloride($CaCl_2$), calcium lactate ($CaC_6H_{10}O_6$) and calcium nitrate($Ca(NO_3)_2$ [23], [123]. According to Wiktor and Jonkers [23], the use of calcium lactate did not have any negative effect on the compressive strength of cement-based mortar. Even though $CaCl_2$ worked more efficiently in MICP application, $CaCl_2$ [123] could cause corrosion for reinforcement steel inside the concrete. The addition of calcium chloride would also mean that a percentage of chloride ions will bind with the hydration products such as calcium aluminium silicate hydrate, ferric oxide and monosulfate (AFm) phases[124].

2.7 MICP application in cement-based materials

The feasibility of MICP against shear stress in a non-cohesive environment has been shown in earlier works [30], [125]. Furthermore, MICP

application has been investigated for micro-crack in cement-based materials [126], [127].

. The procedure for crack healing in cement-based cubes and beams proposed by Ramachandran et al. [126] was to fill the cracks with sand and *S. pasteurii* cells. This research was conducted by microorganism injection with urea-$CaCl_2$ solution into the cracks at different concentrations (10^7-10^8cells/cm^3). The outcome showed the possibility of biomineralization in cement-based materials for surface and interior micro-cracks. Meanwhile, the efficiency of self-healing was limited by the crack width. Also, biomineralization was more effective in crack healing than compressive strength.

Bang et al.[24], conducted another study by using immobilized *S. pasteurii* microorganism in glass beads for crack remediation. Bacterial cells were immobilized in glass beads and injected with nutrient media and calcium chloride into the samples. This research showed a decrease in the compressive strength and stiffness of samples containing bacteria when compared to control samples.

One of the possible reasons for the strength decrease can be related to the protein degradation of nutrient medium and endospores available in samples and creating voids in the matrix [128]. Then, problems with the limiting and high pH environment of cement-based materials gave another direction for self-healing applications; most commonly known as bacterial encapsulation[26], [129].

According to Amiri et al. [130], the aim of self-healing application in cement-based materials is to seal the early age cracks. Considering this fact, the use of encapsulation methods can only increase the cost of the application with a slight change in the self-healing efficiency.

Meanwhile, a recent study by Reeksting et al. [131] focusing on environmental bacteria and their ability to produce calcium carbonate precipitation revealed that urease enzyme activity is not an essential characteristic for biomineralization applications. However, this makes the MICP process faster. This study showed that the environmental bacteria produces the same amount of precipitation with a larger crystal volume and more organic components[131].

Up-to-date, most of the self-healing approaches in cement-based materials are designed to seal cracks induced after 28-days of hydration, which is considered to be an early age application for cement-based materials. In such a case, it is not necessary to encapsulate the bacterial culture. According to the literature, with a proper selection of the microorganism and nutrient medium, at least 2% of the initial bacterial inoculum remains viable for 11 months in the cement-based materials [27]. The inoculated *S. pasteurii* cells were able to precipitate $CaCO_3$ within the cement paste and remediate internal micro-cracks [28].

2.8 Characterization techniques

2.8.1 Isothermal conducting calorimetry (ICC)

The constituent phases of clinker in contact with water react in different ratios and speed to form various hydration products. Each of these reactions often include dissolution at initial step followed by precipitation and condensation of hydrate polymers [36], [132], [133].

Calorimetry is the quantitative measurement technique to record the heat required or evolved during a chemical or physical process which has been proven to be very effective [134], [135]. It has thermally insulated chambers in which the reaction system can take place and the energy exchange between the system and environment can be recorded. Its operation involves the conversion of the collected temperature differences from the sample of interest and reference into a different voltage by Seebeck coefficient. The ratio of the thermal conductivity of calorimeter and the Seebeck coefficient is taken from the heat rate for every voltage output which is dependent of the equipment and is known as calibration coefficient [136]. The calibration coefficient, baseline and the time constant will determine the heat flow which can be computed from voltage. It has been suggested to consider the influence of calibration coefficient and baseline if the data of concern is 7 days of reaction and to consider the influence of time constant for early age tests [136].

2.8.2 Fourier transform-infrared spectroscopy (FT-IR)

Infrared spectroscopy (IR) can be used for determining the molecule structure, different chemical species and quantitative and qualitative measurements. FT-IR technique is used to evaluate matter in gas, liquid and solid phases. Changes in the intensities of electromagnetic radiation passing through a sample are measured using FT-IR techniques. Since molecules absorb electromagnetic energy at frequencies that correlate to the frequency of vibrations amongst atomic bonds, measuring changes in intensity at specific wavenumbers in the infrared spectrum allows the recognition of the units present in the substance.

Theoretically, placing a molecule in an electromagnetic field such as light will initiate an energy transfer from field to the present molecule when Bohr frequency condition is met. The IR beam passes through the presented sample with higher refractive index and penetrates into the materials. The penetrated beam then reflects from the internal surface and produces the evanescent wave. The generated evanescent wave projects into the sample which is in contact with the detector. The reflected waves then get collected by the detector. The differences between optical path signals are recorded and translation of the differences by Fourier transform takes place. The peaks provided by different vibration characteristics of each chemical bond are due to the adsorption of the IR beam[137], [138].

2.8.3 Simultaneous thermal analysis (STA)

STA is a combination of two techniques: Thermogravimetry analysis (TG) and Differential thermal analysis (DTA) or Differential scanning calorimetry (DSC).

The changes in the sample mass in relation to temperature are recorded as TG. The weight changes are the result of material decomposition due to the heating process and gas release. DTA is the result of the heating process for both samples of interest and reference samples and the differences between the two temperatures. Whereas, DSC is the difference of required heat for the temperature increase of the sample and the reference sample measured as a temperature function. Both the reference and sample should be kept at a similar temperature throughout the test. Determination of the different phases present and phase transitions can be investigated by STA analysis.

The changes of a thermal treatment for a substance can be monitored by STA as a function of thermal analysis. The samples are heated at a consistent and same rate. In DTA/DSC plot, peaks and valleys are known as exothermic

and endothermic reactions respectively [138]. STA can be used to quantify the available phases in a sample.

The heating of cement-based materials results in physical or chemical changes like mass change or phase transition. The DTA/DSC curve shows these changes as a function of temperature, a peak marking an exothermal change and a valley marking and endothermal changes.

The heating and the temperature increase will result in dehydration of hydrated phases and decarbonation of carbonate phases. The mass loss due to dehydration and carbonation occurs within a range of the temperature for every different phases rather than a single change point. The mass changes in cementitious materials due to heating occurs when the sample is heated to 1000 °C. However, the decomposition of these phases is not restricted to these temperatures. For instance, the decomposition temperature of all carbonate phase is depending on their carbonate phase and crystal size [139].

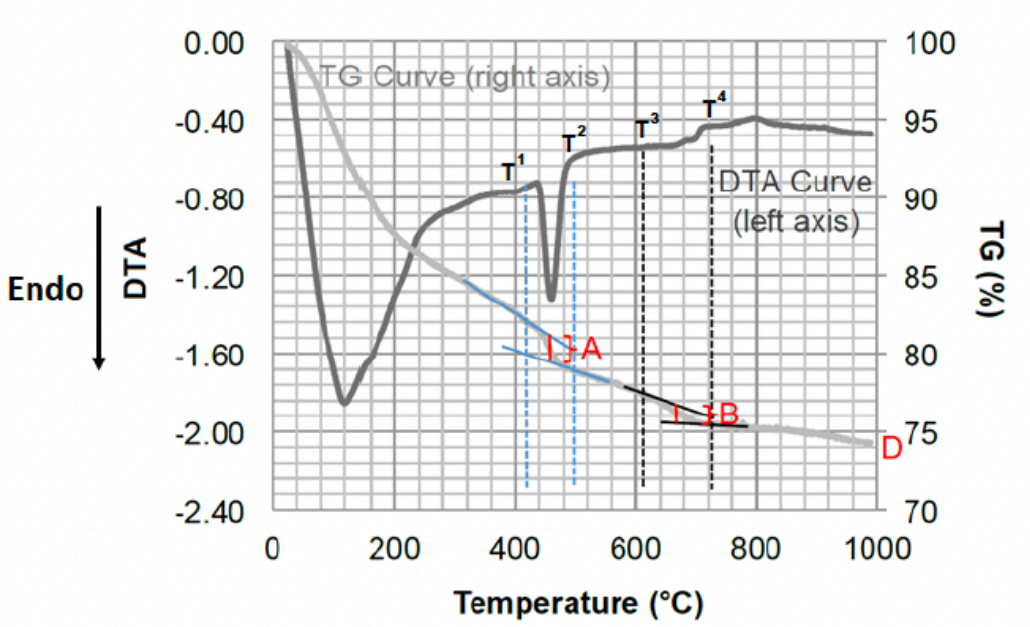

Figure 2-5 STA data for a cement paste with carbonation[140].

Figure 2-5shows TG curve and DTA curve (light grey and dark grey) of a sample heated to 1000 °C. It is also representing the temperature changes in which mass variations occur respectively due to dehydration and decarbonation of phases present in the sample such as hydrate and carbonate. The percentage of CH and carbonate can be calculated from the TG curve using the tangent method [141]. The points T1, T2, T3 and T4 are identified as a mass loss and tangents are drawn. A vertical line is drawn passing through the middle point of each point and joining the tangents. The length of this vertical line is marked as % mass loss.

A- Weight loss due to dehydration of CH.

B- Weight loss due to decarbonation of $C\bar{C}$.

Both A and B are calculated using the TG curve and tangent method.

$$Ca(OH)_2 \rightarrow CaO + H_2O \text{ (Dehydration)}$$

Mol wt. 74 g/mol 56 g/mol 18 g/mol

$$CaCO_3 \rightarrow CaO + CO_2 \text{ (Decarbonation)}$$

Mol wt. 100 g/mol 56 g/mol 44 g/mol

From dehydration equation, 1 mole of CH (74 g/mol) decomposes to give 1 mole of H_2O (18 g/mol).

$$\% \text{ CH} = (74/18)*A$$

From decarbonation equation, 1 mole of CC (100 g/mol) decomposes to give 1 mole of CO_2 (44 g/mol).

$$\% \ C\bar{C} = (100/44)*B$$

The % CH and % $C\bar{C}$ referred to are determined using the formula are:

$$\% \text{ CH} = [\{(74/18)*A\}/D]*100$$

$$\% \ C\bar{C} = [\{(100/44)*B\}/D]*100$$

D - % residual mass at the end of 1000 °C.

2.8.4 X-ray diffraction (XRD)

XRD analysis has been developed based on X-radiation technique which has been discovered by Wilhelm Conrad Roentgen which showed that the X-rays can penetrate solid materials [142].

X-ray diffraction analysis is suitable to get information of lattice constant, structure and orientation. These measurements can be done because of their wavelength order in a range of several angstroms which is the same as lattice constants. X-rays also can be useful to evaluate the present phases in a sample

and quantity determination of these phases producing a unique diffraction pattern. An X-ray photon can be scattered, diffracted, reflected or adsorbed by an atom. If the X-rays reflected by different atoms placed on separate planes happen to be in the same phase is known as diffraction. This explanation is also known as Bragg's law [138]:

$$n\lambda = 2d\ sin\theta$$

n: order of diffraction

λ: x-ray wavelength

d: interplanar spacing

θ: incident angle measured from reflecting the plane

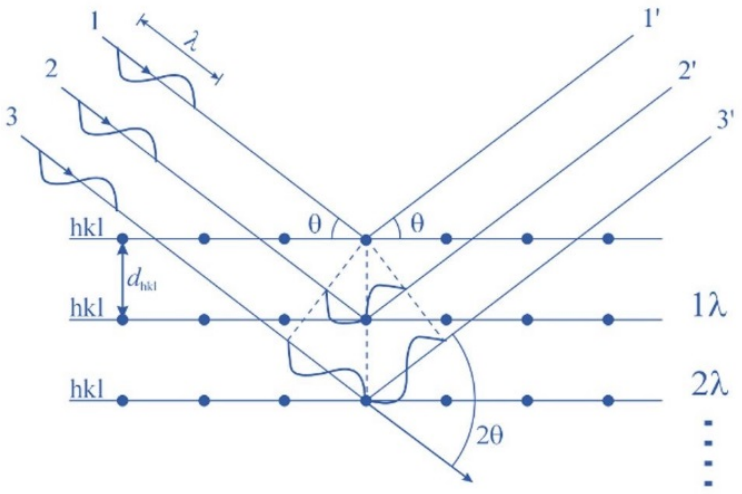

Figure 2-6 Schematic representation of Bragg's law in real space [143]**.**

Figure 2-6 is a showing the of Bragg's law. Electron bombarding a metals result with x-ray emission due to the excess energy of the atom. The interaction

of these X-ray emission with the crystal structure of the samples will have X-ray collision with the crystalline plane electrons. This collision results in diffracted X-rays [138]. Every crystal structure have characteristic peak related to a typical diffraction pattern and each one of these peaks refer to a group of planes in crystalline structure.

By changing incident angel and different inter-planar spacing in polycrystalline materials, the Bragg's law is satisfied. characteristic patterns of a sample could be plotted by the intensities of the diffracted beam versus 2θ.

Comparison of these spectrums with a database can be used to identify the phases available in a sample and their degree of crystallinity. This is due to presence of sharper peaks when using a well-defined crystal and the broad peaks when the deformation and/or the sizes of crystallites are not uniform, implying the presence of more amorphous phases.

2.8.5 Rietveld method

The Rietveld refinement method is an optimized method to minimise the difference between the experimental pattern and the simulated pattern. The widely used Rietveld Refined XRD in cement-based materials provides a quantitatively analysis of XRD results [144]–[146]. Each crystalline material's XRD pattern is distinct. The basic idea behind Rietveld analysis is to compare an experimental pattern with a pattern simulated using assumed quantities, crystal parameters, and equipment parameters of a known phase mixture. By using least square fitting, all of these parameters can be modified to reduce the discrepancy between the experimental and simulated patterns.

The amount of the phases present in a Rietveld analysis is always normalised to 100%. As a result, all of the phases present, as well as their established crystal structures, must be entered. The numbers of crystalline phases determined by the experiment would be higher than the true amounts present if amorphous or unknown phases are present. A known quantity of a reference standard phase can be added to solve this.

The background can be fitted by interpolation or another predefined functions and accurately determined phases available in anhydrous and hydrated clinker relies on the mix model of all formations. [147]–[149]. McCusker et al. [150] has suggested to adopt a predefined function for background for polycrystalline material. The refinement factors affecting the background and the calculation of amorphous phases have been investigated by Jansen et al [151] and he suggested that no amorphous phases exists in ordinary Portland cement by optimizing the background.

The phases and structures could be evaluated by the relative intensity method [152], [153], internal and external reference [147][154], [155] methods. The internal reference analysis uses a known material which is not available in the target sample, could be mixed and analysed with the target sample. Scrivener et al [149] used 10% of corundum as internal standard which was mixed with sample prior to the hydration and this has been proven to change the hydration kinetics [156]. Therefore, recent studies use corundum as an internal standard by mixing after the hydration.

Internal reference method assumes all the phases in the target sample are crystalline which is often not true and a correction factor should be implemented for any amorphous structures available[157], [158].

The external reference method overcomes the gaps of internal reference method [159] where a scan of the reference sample is separately obtained in a similar condition to the sample of interest. Afterwards, the absorption coefficient differences between reference and the objective sample should be considered and based on the scale factor and unit cell volume of the reference, the factor of calibration could be found.

The method used in this study requires an internal reference for quantitative XRD analysis of the sample. A 10% reference to sample ratio of Corundum (Al_2O_3) has been used as the internal reference.

The structures are listed in Table 3-1 (ICSD) and the Bruker search-match programme EVA was used to identify phases. Once phases have been established, they can be quantified using Rietveld refinement method, which was accomplished with the help of TOPAS software.

Table 2-5 Structures list for QXRD

Phase name	ICSD number	Reference
Anhydrite	1956	Morikawa et al. 1975
Belite	81096	Mumme et al. 1995
Brownmillerite	9197	Colville et al. 1971
Cubic C3A	1841	Mondal et al. 1975
Calcite	80869	Maslen et al., 1995
Ettringite	155395	Goetz-Neunhoeffer et al. 2006
Portlandite	43433	Henderson et al. 1962

The residual weighted pattern known as Rwp is the goodness of the fit and is defined through equation below [160], [161]:

$$Rwp = \sqrt{\frac{\sum w(Y_O - Y_C)^2}{\sum w(Y_O)^2}}$$

Y_O is the observed pattern and Y_C is the simulated pattern.

The G factor generated by the reference can be calculated as:

$$G = S_{cor}\frac{\rho_{cor}V_{cor}^2\mu_{cor}}{w_{cor}}$$

Where,

S_{cor} stands for the Rietveld scale factor of corundum;

ρ_{cor} stands for the density of corundum;

V_{cor} stands for the unit-cell volume of corundum;

W_{cor} stands for weight fraction of corundum;

μ_{cor} stands for the mass attenuation coefficient (MAC) of corundum.

General equation for determination of the phase fractions in hydrated cement-based materials is:

$$C_j = \frac{S_j(ZMV)_j}{\sum_{i=1}^{n} S_i(ZMV)_i}$$

Where,

C_j stands for the weight fraction of phase j;

S_j stands for the scale factor of phase j;

Z stands for the number of formula units per unit cell;

M stands for the mass of the formula unit;

V stands for unit-cell volume.

In this approach the scale factor of corundum is calculated through software and the MAC and G factor of corundum is identified. Then the scale

factor of phase j and MAC of each sample is determined and the phase fraction is rescaled. Figure 2-7is a representative for Rietveld method used for QXRD

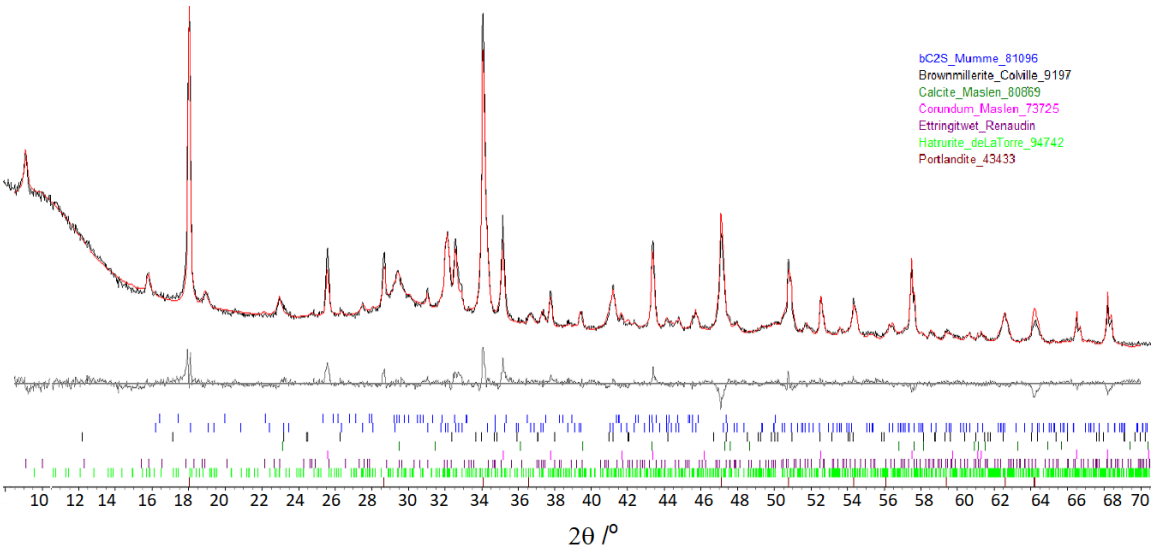

Figure 2-7 Rietveld method used for quantitative XRD analysis for NO1 at 7 days. Experimental pattern (Black), Fit (Red) and residue (Grey).

And representing the experimental, fit and residue pattern. QXRD fits for all the samples are available in Appendix G.

2.8.6 Scanning electron microscope (SEM-EDX)

SEM technique uses electron beam interaction with the surface of the sample to capture the images. The image of sample in a SEM is constructed by scanning across the sample surface by an electron beam. The lens system used in SEM to focus the beam on the sample has a probe size of 30 to 60 Å. SEM can be used to collect data on morphology of the sample, as well as topographical information, element compositions and electronic characteristics of materials. The excitation in a sample can be ranged between 0.5 and 3 μm from

its surface, and the ejection of electron or proton can be detected by the SEM. The source of signals can be:

- Backscattered electron: electrons from electron beam of excitation are shot after many impacts in all the excitement volume of the sample. The energy range of backscattered electrons can vary from 50e V to the energy level of the source and located 1-2μm of the surface. Collected data can identify composition (atomic number), crystallography and topography.
- Secondary electron: electrons knocked out due to collision with the excitation beam or backscattered electrons are known as secondary electrons with the energy level below 50e V. They can be used to get topographic information.
- Auger electrons: auger electrons are the result of excitation beam creating vacancies in the core shell of the atoms and outer shell electrons occupying these vacancies with transmitting part of their energy to another electron to leave the atom. Auger electrons have the constant energy level of 10 to 2000e V. Their information is suitable for element investigation.
- Characteristic X-ray: They are originated at 2-5μm of the sample surface. They are used for providing quantitative and qualitative analysis of target sample composition and elemental distribution.
- Visible light (cathodoluminescence): It can be used for providing analysis on the optical and electronic properties.

In most of the studies, backscattered electron and secondary electrons were used for cementitious materials imaging[162], [163]. The backscattered imaging of the polished flat surface were used primarily for quantification of the phases and porosities available in the target sample by assignment of a gray shade to every one of the phases and porosities and measuring the area that relates to each of them. [164]. Brightness and contrast could be set so that all the information required is available in a histogram for grey scale. Multiple images need to be analysed to obtain meaningful data, as each image may correspond to a small area of the sample that may not be representative. Secondary electron imaging is primarily used for characterization of the crystal structure on the fracture surface.

2.8.7 Nuclear magnetic resonance (NMR)

NMR uses the splitting, caused by a strong external magnetic field, of the energy degeneration levels of nuclei with none-zero nuclear spin for example ^{29}Si, ^{27}Al, ^{17}O or ^{1}H. At the same time, if the material is exposed to a RF pulse, conversions from on energy level to another could be perceived as absorption of photonic resonant. Chemical shifts are the frequencies at which absorption occurs and are dependent on the chemical environment of the nuclei, so NMR can be used to describe the chemical environment of specific atomic species in a sample.

Chemical shifts (differences in the resonance frequency of sample and reference) are recorded in ppm as the ratio of a change in Hz to the resonant frequency in MHz to render comparable data from different results and remove effects of the intensity of the magnetic field. [37]. Because of this, it could only be

used on liquids before it was discovered that spinning a sample at an angle of 54° 74' to the magic field resolved the spectrum. [144], [165]. Since NMR data does not require long range order, it is especially useful in understanding C-S-H, which is nanocrystalline.

The basics of NMR technique take advantage of the fact that different nuclei have different specific spins (I). Some nuclei can have integral spin (I = 1,2,3,…), others can have fractional spin (I = 1/2,3/2, …) and some with no spin (I = 0). Due to presence of a strong magnetic field on a nucleus with a non-zero spin, there will be an energy transfer resulting with an energy difference. This energy difference is between the energy states called Zeeman splitting [144], [165].

The nucleus then will be disturbed by a radio frequency pulse generating electronic transitions between each energy level. Then the nucleus will remove the disturbance by either absorbing or emitting a photon and it will be measured as a chemical shift [166], [167]. Since the chemical shift is proportional to magnetic field, it is measured in parts per million (ppm).

2.8.8 ^{29}Si and ^{27}Al MAS NMR

The silicate anion structure in C-S-H is studied using ^{29}Si DP MAS NMR (Direct pulse magic angle spinning nuclear magnetic resonance). Since the amplitude of the spectrum is directly related to their concentration due to the fact that the NMR spectrum is the total of all the signals of each Si nuclei, the deconvolution of the NMR spectrum can be used to quantify silicate structures. The condensation of the silicon-oxygen tetrahedral determines the chemical changes of silicate compounds. The different silicate species give typical

chemical shifts in the ranges defined in Table 3.2 in the case of cement-based materials.

Table 2-6 NMR shifts for silicon in cement.

Type of silicate	Designation	Chemical shift(ppm)
Monomers	Q^0	-66 to -74
End chain groups	Q^1	-75 to -82
Middle chain groups	Q^2	-85 to -89
Chain branching sites	Q^3	-95 to -100
Three-dimensional network	Q^4	-103 to -115

The different tetrahedral species are known as Q^n and Q is representing silicate tetrahedron where n denotes the connectivity of silicate tetrahedron by oxygen. The value of n is limited to the valency of oxygen (n range: $0 \leq n \leq 4$). Figure 2-8shows the schematic representation of Q^n tetrahedra. Q^1 is denoting end chain groups with a chemical shift in a range of -75 ppm to -82 ppm. Q^2 is related to middle chain group with silicon occupied neighbouring tetrahedra and having a chemical shift between -85 ppm and -89 ppm. Q^3 is for branching sites with a chemical shift of -95 ppm to -100 ppm and Q^4 is for cross linking sites in a 3 dimensional frame having a chemical shift of -103 ppm to -115 ppm.

The Q^n(mAl) is denoting middle chain sites where the neighbouring tetrahedra has been substituted by Aluminium ions [168]. Q^2(1Al) denotes

middle chain groups with a chemical shift around - 82 ppm. There is also a peak presenting from - 70 ppm and - 75 ppm indicating the presence of $Q^0(H)$ groups related to a hydrated monomer. The number of silicon and aluminium atoms surrounding the SiO_4 tetrahedra determines the local environment of silicon atoms.

It has been established that by increase in age of the sample, the mean chain length (MCL) will also increase and it is due to further polymerisation [169]. Another factor affecting the MCL is the temperature which can increase the chain length [170].

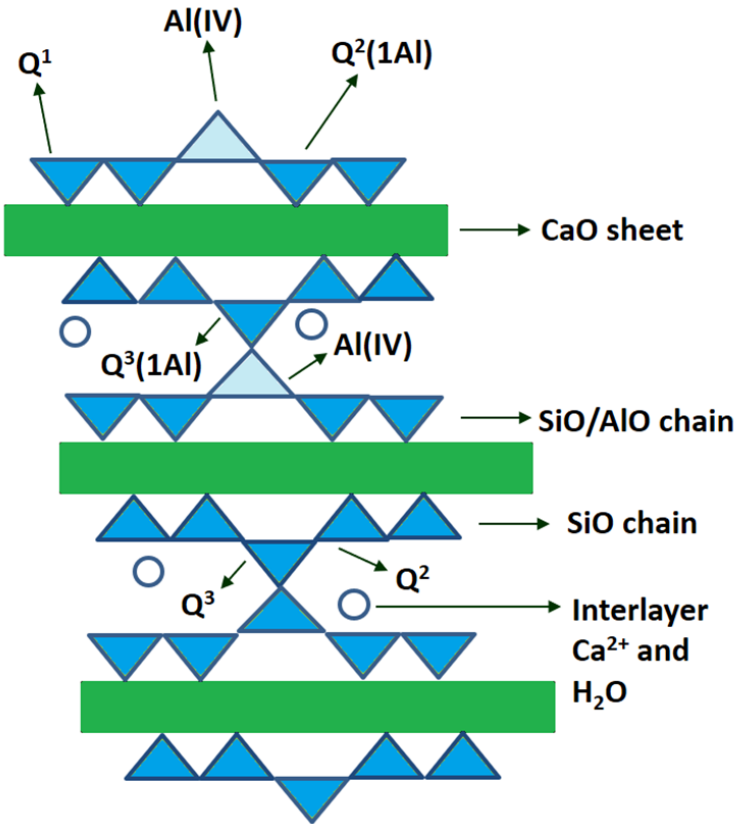

Figure 2-8 Schematic representing the Q^n sites[171].

Previous works have indication of $Q^2(1Al)$ presence in cement samples but no evidence of $Q^1(1Al)$ meaning that the aluminium incorporation in silicate

chains is a result of aluminium substitution for silicon only on the bridging tetrahedral sites [172], [173].

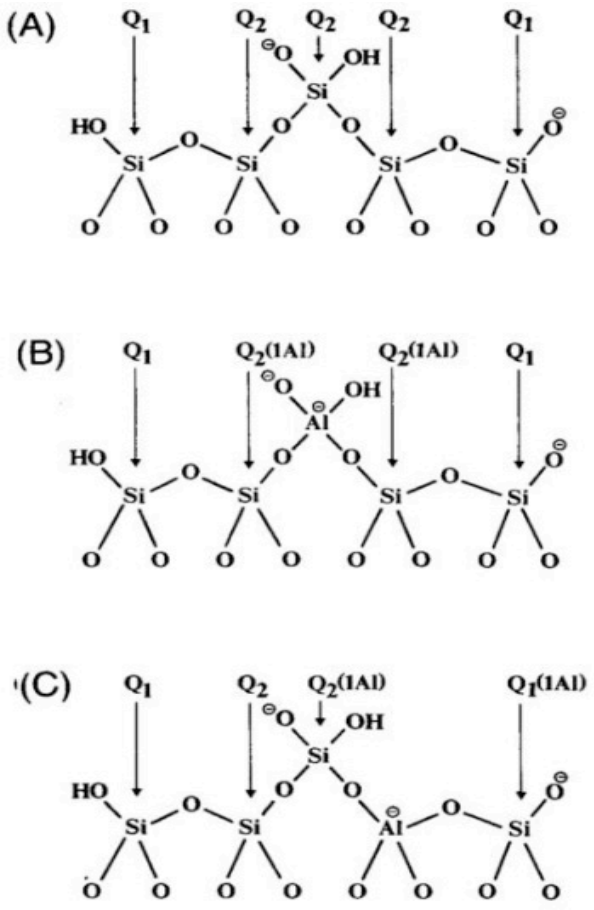

Figure 2-9 (A) Schematic presentation of pentameric silicate chain, (B) with Al substitution for silicon in bridging site, (C) with Al substitution for silicon in non-bridging site [173]**.**

Figure 2-9is representing the Al substitution for Si in different sites. The Al substitution in bridging sites (Figure 2-9(b)) will contribute to the presence of Q^1 and Q^2(1Al) whereas, this substitution for Si in non-bridging sites (Figure 2-9 (C)) would result in Q^1(1Al) groups.

As mentioned in literature: “Monomers are present in alite and belite, while C-S-H generally presents Q^1 and Q^2 groups indicating that it has a single linear chain.” [174]. The polymerization of C-S-H gel to yield Q^3 and Q^4 sites can

happen in old pastes due to carbonation [175]. Aside from the percentage of silicate species, quantification of the DP spectrum will reveal specific information such as the mean alumino silicate chain length, Al/Si ratio, and degree of hydration.

The hydrated phases can be studied using ^{29}Si-^{1}H CP NMR (cross polarization), method. The resonance condition for ^{29}Si arises in the cross polarisation mode due to the transfer of energy from 1H, so the technique detects Si atoms in close proximity to H atoms, i.e. hydrated phases. According to Tong et al.[176], βC_2S comparison of DP and cross polarization spectrum showed that cross polarization spectrum is missing the anhydrous peak usual for Q^0 sites at -71.3 ppm, where it is marked as βC_2S.

In ^{29}Si NMR, with the assumption of the Q^3 absence, it has been proven that the mean chain length of silicate and hydration degree could be calculated as[177]:

$$\text{Mean silicate chain length } (\text{MCL}_{\text{Si}}) = 2(1 + \text{Q2}/\text{Q1})$$

$$\text{Degree of hydration} = \frac{\text{Q1} + \text{Q2}}{\text{Q0} + \text{Q1} + \text{Q2}}$$

For C-S-H the mean silicate chain length normally increases with ageing or hydration degree [72] and decreases when Ca/Si ratio increases[178].

Another possible use of NMR is for chemical evaluation of the environment of available elements. ^{27}Al MAS NMR is useful for investigation of octahedral or tetrahedral structures to identify Al is substituting Si [179].

^{27}Al MAS NMR is a useful technique for cement analysis and Al^{3+} is a common ion which is responsible for substitution of Si^{4+} and has been proven to be present in C-S-H structure. ^{27}Al spins with an I = 5/2 and its natural abundance is 99.99% which will make it faster to be analysed with MAS NMR. One of the drawbacks for ^{27}Al MAS NMR is that any spin rate greater that ½ will result in broad spectral lines making it difficult for distinctions in the local environments.

^{27}Al MAS NMR can differentiate the tetrahedral and octahedral coordination[179]. Another disadvantage of ^{27}Al MAS NMR is in the interpretation of the collected spectra as it will be affected by the quadrupolar interaction and will result in side bands and peak broadening. The solution for this broad peak is increased spinning speed of the sample which will push the side bands away from the centre band.

Chapter 3
Experimental methods

3.1 Work Programme

This chapter aims to illustrate the experimental programme of the current work. The outlined objectives of this study in section 1.3 focus on the effects of bacteria and biomineralization on cement hydration products. As such, presented flowchart in Figure 3-1 shows the different characterisation techniques used to investigate the changes in:

- Hydration kinetics
- Hydration products
- Detection of calcium hydroxide and calcium carbonate
- Investigation of calcium carbonate morphology and the amount present in sample.

Section 2.6 illustrates the studies carried out in the field of MICCP in cement based materials and observed changes in cement hydration and it properties such as; delayed setting time, changes in density, compressive strength and permeability. All the above point out to a systematic change in hydration process and its final product. In order to understand the impact of MICCP in cement based materials, the work programme has been tailored to focus on hydration kinetic, products and chemical composition of deposits within hydration products.

Triplicate samples have been used for each test method at each age equating to at least 9 samples prepared per sample type per test, except for NMR, XRD and SEM-EDX test. This was due to long test running time, limited access to

equipment and limitations in available budget. Additionally, the final phase of this study coincided with the start of Covid-19 pandemic.For evaluation of bacterial culture, after achieving the bacterial growth curve for *S. pasteurii* cells cultivated in CSL, the first step would be to evaluate the $CaCO_3$ morphology in different environments. For this purpose, two different types of samples were investigated; (1) bacterial medium without any additives, (2) bacterial growth containing superplasticizer (SP). These samples also contained $Ca(NO_3)_2$ as the Ca^+ source for MICP.

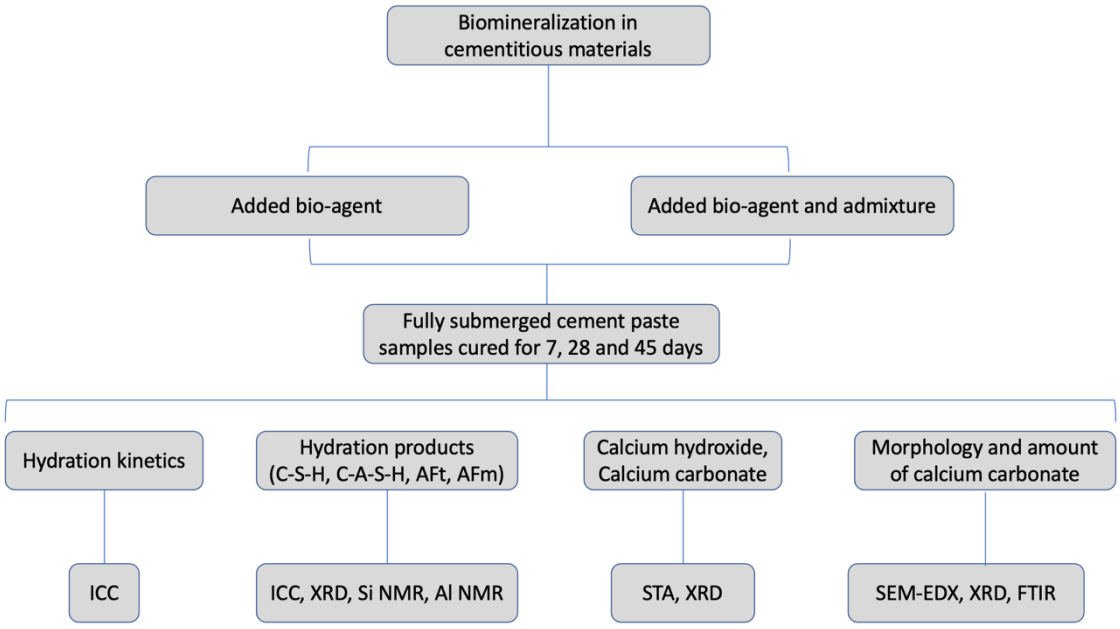

Figure 3-1 Work program of the experimental methods and techniques used in the study

3.2 Materials:

A list of all materials used in this study is presented in Table 3-1. It should also be noted that for the purpose of investigation of samples with NMR techniques, white Portland cement was used as the high amount of iron in

ordinary Portland cement can interfere with NMR results. Remaining constituents have been chosen specifically to collect a comparable data with the researcher's previous work. Additionally, all the ratios and dosages are chosen in line with the manufacturer/providers guidance. This includes all the relevant dosages required for bacterial culture growth instructed by Leibniz Institute-DSMZ GMbH.

Table 3-1 List of materials and their commercially available brands used in the study

Materials	**Commercially available**
White Portland cement	Cemex - White PC
Main's water	NA
Superplasticizer	BASF MasterGlenium 51
Bacteria	*S. Pasteruii* strain, Leibniz DSMZ33
Corn Steep Liquor	AABAITS(Fish food and baits) CSL
Urea	Sigma-Aldrich Bio-Urea 99%
Calcium source	Sigma-Aldrich Calcium Nitrate >99%
Tris base	Sigma-Aldrich Trizma base
Agar	Sigma-Aldrich Agar

3.3 Mix design and sample preparation

The white Portland cement was used to cast cement paste samples. Samples were consistent in w/c ratio of 0.5 to produce the maximum porosity in hardened cement paste matrix accommodating the viability of bactera. The

material composition of the used white Portland cement is presented in Table 3-2. The *Sporosarcina pasteurii* bacteria grown in CSL media was added as the biological agent and calcium nitrate $Ca(NO_3)_2$ to trigger the $CaCO_3$ precipitation. Neat cement paste samples were reference specimens for bacterial cement past samples.

Table 3-2 XRF result for elemental composition of white Portland cement used in this study as percentage.

SiO_2%	Al_2O_3%	Fe_2O_3%	CaO%	SO_3%	MgO%	Na_2O%	K_2O%	P_2O_5%
24.49	2.09	0.30	68.08	1.94	0.59	0.25	0.09	0.27

Control samples were prepared with w/c ratio of 0.5 and samples requiring calcium source and superplasticizer contained calcium nitrate (40g/l instructed by DSMZ) and BASF MasterGlenium (data sheet provided in appendix E) superplasticizer (0.1% of cement weight instructed by the manufacturer) respectively.

For bacterial samples, the required amount of water was replaced by the bacterial solution consisting of bacterial cells and CSL as nutrient. Samples requiring calcium source and superplasticizer contained calcium nitrate (40g/l of mix water) and BASF MasterGlenium superplasticizer (0.1% of cement weight added to mix water) respectively.

The used mixes are designed to only introduce 1 new addition (i.e. calcium source, superplasticizer, bacterial culture) to cement paste for clarity in data comparison represented in Table 3-3.

Table 3-4 Cement paste description, WPC is white Portland cement, SP is superplasticizer.

	Mix	WPC	$Ca(NO_3)_2$	Bacterial cell(CFU/mL)	SP
N01	Neat paste	✓	-	-	-
N02	Neat paste-SP	✓	-	-	✓
NC1	Neat paste	✓	✓	-	-
NC2	Neat paste-SP	✓	✓	-	✓
B01	Bacterial paste	✓	-	$\times 10^8$	-
B02	Bacterial paste-SP	✓	-	$\times 10^8$	✓
BC1	Bacterial paste	✓	✓	$\times 10^8$	-
BC2	Bacterial paste-SP	✓	✓	$\times 10^8$	✓

Table 3-5 represents the prepared mix design used for each mixe. For bacterial samples, the mix water was replaced by the same amount of bacterial growth medium. All constituents were weighed prior to mixing and where superplasticizer was required, the admixture was added to the mix water or bacterial growth medium. The calcium source was added to the samples prior to the addition of mix water.

Table 3-5 Mix design detail for neat and bacterial samples**.**

Sample	Cement (g)	Water (g)	Bacterial growth medium (g)	Superplasticizer (g) *	Calcium nitrate (g) *
Neat	100	50	NA	0.1	2
Bacterial	100	NA	50	0.1	2

*Admixture or calcium source added to samples where needed (see Table 3-4).

The prepared samples after 48 hours were then submerged in their respective solution. As such, the bacterial samples were submerged in CSL nutrient medium and neat samples were only submerged in water until the testing date. For samples required for FTIR an artificial 0.5mm width cut was introduced on the surface of each sample prior to curing in their solution.

3.4 Microorganism and nutrient medium

Leibniz Institute- German Collection of Microorganisms and Cell Cultures: *S. pasteurii* (DSMZ 33) was used in this study. This particular species can be easily obtained from the soil and it is a non-pathogenic strain. The *S.pasteurii* has been frequently used in biomineralization studies due to its high urease enzyme activity and its negative surface charge [180]. The *S. pasteurii* can withstand high alkalinity, survive the mixing phase, and thrive in environments with minimal nutrient availability [181].

In particular, the alkaliphilic and endospore forming microorganisms can tolerate the stresses induced within the cement based materials during the mixing process. The bacteria used in this study were grown aseptically under specified batch cultivation conditions (see Section 2.5). Then, these cultures

were kept at a -80˚C stock culture in glycerol solutions (filled in 1.5 mL sterile vials).

Urea corn steep liquor (UCSL) medium was used as the nutrient for bacterial cultivation [117], [130]. is the culture was composed of tris base, urea and CSL with distilled (DI) water. UCSL culture was realised by addition of Tris base (15g), urea (10g) and CSL (15g) to a litre of DI water. The medium was adjusted to pH 9 by adding approximately 0.1M HCl after the Tris base was added to 1L of DI water.

The CSL was provided in liquid-paste form which is commercially offered product by fish food industry. The chemical composition of CSL was not specified by the manufacturer. Then this media was sterilized in an autoclave at a temperature of 120 °C and 100 kPa[182], [183].

The agar plate was prepared by addition of the agar to the solution and placed in petri dishes. Then *S. pasteurii* was added to the sterilized nutrient medium and cultivated at 30 °C. The microorganisms were inoculated in 300 mL of UCSL with a shaking condition of 190 rpm at 30 °C. Periodically, aliquots of these media were taken and plated on agar plates.

The viable plate counts were performed on serially diluted samples (10^0 - 10^{-7}), and the cell concentration was calculated using viable plate counts and expressed as colony forming units (CFU/mL) [99], [184]. Hourly samples were taken from the culture and then diluted with DI water and each container was shaken for homogeneous results and then spread on agar plates. Bacterial growth curves were developed in terms of CFU/mL vs. time. The growth experiment was conducted in triplicates.

Calcium nitrate- $Ca(NO_3)_2$ (40 g/l) was also added as the calcium source when required. The amount of added calcium nitrate is calculated to have 0.167 M calcium [Ca^{2+}] [9].

The precipitates were collected by a centrifuge at 6300rpm for 15 min and analysed by XRD and SEM techniques to confirm the effect of environment charge and pH level on $CaCO_3$ morphology. It could be beneficial to monitor the precipitation in different pH environments.

The data collection method can affect the quality of the XRD scan. Some of the critical factors affecting the XRD scan are: the diffractometer's geometry, emission and its wavelength, alignment of the instrument and preparation method for samples. Literature provides appropriate guidelines for preparation of the samples and collection of the data [161], [185].

The count is determined by the powder volume of the sample and it is affected by the slits, sample and the particle size. The population of crystal phases per unit volume of a sample and the absorption of X-rays are determined by particle size. This error could be avoided by using wider slits or reducing the particle size. [186]. Meanwhile, in order to have homogeneity in particle grinding, it is better to grind the sample in a solvent [187]. But the main problem with grinding in a solvent is that some phases can be affected especially in the hydrated system.

The preferred orientation of the crystals, which can occur when inserting the ground sample into the holder, is another aspect that influences the XRD pattern. The front fill process and pressing with a glass slide will amplify this effect, which tends to increase cleavage for some crystal planes.. This method

can increase the intensity of affected phases. The increase in preferred orientation can be prevented by back loading of powder.

3.4.1 Laboratory work on bacterial incubation

The nutrient media was prepared in line with the detail provided in section 3.4. Figure 3-2 shows the 600 mL bacterial cultures after introduction of the bacteria and addition of the calcium ion source.

Each bacterial culture was then incubated aerobically by shaking for 3 days at 30 °C and samples were taken periodically and serially diluted from 10^0 – 10^{-7} and plated on agar plates for viability counts. Each agar plate was sealed with parafilm and stored at 30 °C for 2-3 days until the colonies formed were visible for counting process (Figure 3-3). Due to possible human errors during the plating process with streak plate method[7], some of the agar plates were showing dense colonies and impossible to count the colonies formed in each cultures.

Figure 3-2 *S. pasteruii* cultures prepared for agar plate count and precipitation collection after addition of calcium source.

Hence, for each of the triplicate results, multiple attempts of agar plate viability counts were conducted. For the purpose of agar plate count and measuring colony formed per unit in each of the cultures, agar plate counts were conducted to cover t = 0 hour to t = 72 hours for serially diluted (10- 10^{-7}) bacterial culture samples. Considering the laboratory access time during the day, 8 hours of each 72 hours pattern were conducted on daily basis to cover 72 hours of viability measurements.

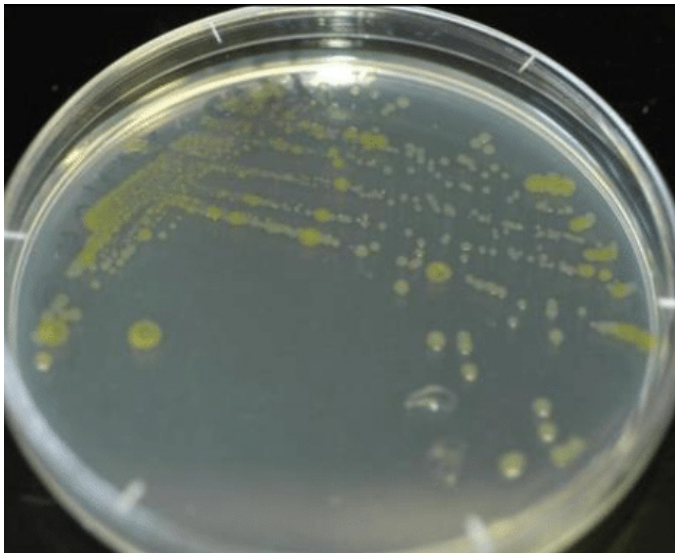

Figure 3-3 Agar plate from a diluted *S. pasteruii* culture after 48 hours of plating.

3.5 Test methods

3.5.1 Isothermal calorimetry

In this work, a TAM air calorimeter with 8 twin channels was used to measure the heat generation during the hydration of samples. 3 samples per age were tested resulting in 9 samples per mix. The water(DI water)/bacterial culture was mixed with 15 g of cement was in the designated containers with a w/c ratio of 0.5. The ampoule was then shaken on a shaker for 2 minutes at ~100 rpm.

Before starting the baseline acquisition, the ampoules were immediately placed in the samples channel of the instrument and a quartz paste sample was placed in the reference channel. For samples with superplasticizer a dosage of 0.1g admixture was added to the mix and after hand mixing the containers were placed into the ICC system. The samples were tested for 72 hours at 20°C.

The target samples were combined as defined previously and then inserted into channels using a stainless steel hook to ensure that the stability conditions were met. After placing the samples inside the calorimetry channels, the signals were considered accurate after 45 minutes and the data collection continued for 3 days.

The kinetics of the exothermic reactions of cement hydration can be followed by isothermal conducting calorimetry. Inside the twin channel instrument, the heat evolved during hydration reaction can be recorded in parallel with a reference sample. Since the main reason for using a reference sample is to eliminate external factors causing the noise to signal, both sample of interest and reference samples should hold a similar thermal properties Quartz with specific heat capacity of 0.8 J/gK is a suitable reference for cement which has a specific heat capacity of 0.75 J/gK.

The heat of reaction curve will present the first peak, a dormant period, the peak for main reaction, a shoulder next to main peak and a steady stage.

The initial peak is attributed to the water getting in contact with particles. According to Jansen et al. [188], [189] the peak for main reaction is related to silicate dissolution and the next shoulder can indicate the aluminate reaction.

3.5.2 STA

Three samples per age were tested resulting in 9 samples per mix. At the time of testing, samples were removed from casting tubes and pulverized with a pestle and mortar into fine powder. Since there is a possibility of a carbonate phase related to the hydration stopping process, none of the samples was hydration stopped. Instead, Each sample was grounded at the exact time of testing and then 15-20 mg of the powder was put into the crucible and placed in the instrument.

The fine powder was analysed by NETZSCH 1500 STA equipment which can track the loss of weight for the sample when weight the temperature is increasing from 20°C to 1100°C with a rate of 10°C/min. N_2 flow through the heat chamber prevents any further oxidation of sample during the heating process.

The loss of weight caused by decomposition of calcium hydroxide and calcium carbonate to $CaO + H_2O$ and $CaO + CO_2$ respectively, and the molecular weight of the phases were traced back to quantify the portlandite and calcium carbonate available in samples [190].

DTA peaks can represent particular phases available in the sample:

- 150-300 °C: Endothermal peak for gypsum, ettringite, C-S-H and carboaluminate hydrates
- 450-550° C: Endothermal peak for dehydration of CH
- 600-900° C: Decarbonation of calcium carbonate

Using the reactions where CH is involved and assuming all the carbonates are caused by CH carbonation, the calcium hydroxide in a sample can be quantified by TG curve.

The weight loss for dehydration and decarbonation should be calculated to obtain the amount of CH. The onset and the end of these weight losses can be measured by a derivative curve of TG plot.

Knowing that the dehydration of 74 g of CH yield 18 g of H_2O and from the carbonation and decarbonation process 74 g of CH give 44 g of carbonate and the amount of CH can be calculated (see section 2.8.3 for further detail).

3.5.3 XRD

The XRD used for this analysis is D8 Bruker operated with Cu Kα radiation at 10 mA and 30 kV, over a range of 5-70° 2Θ .

One sample per age was tested equating to 3 total samples. XRD data was obtained from freshly powder samples grounded with mortar and pestle. This was important to achieve a good signal to noise ratio and minimise preferred orientation effects. Preferred orientation is seen when there is the presence of a large amount of needle or plate like crystals in the sample being analysed. This arises because crystals packed onto the sample holder tend to orient the same way, resulting in peaks with unusually high intensities. Finely ground powders were then packed to a flat surface onto a sample holder. If the powder is not packed evenly or if the sample holder is filled too high or too low with the sample, there is always an error which results in shift of peak positions thus making the interpretation difficult.

For QXRD analysis, corundum (Al_2O_3) was introduced in the samples at the grinding and preparation stage. Rapid scanning data was acquired under following conditions: step size of 0.05, between 2θ range of 5-70°.

The C-S-H phase present in cement based materials has very poor crystal structure causing indexing problems by showing broad peaks known as

amorphous humps. These humps can overlap with other present peaks and affect the position and intensity of crystal phases. Also, the crystal size effect shows an influence on the XRD analysis. Crystals having crystal size less than 100 nm the peaks appear as broad peaks on pattern which obscure other phases as X-ray cannot achieve complete destructive interference in scattering[191].

3.5.4 NMR

Using a solid state NMR for the cement studies, a comprehensive understanding of the silicate anion structure and the coordination of aluminium in C-S-H can be achieved. The NMR works by taking advantage of the fact that some nuclei of an element have a physical spin not equal to zero.

Different experiments in NMR are considered to characterize cement samples: ^{29}Si DP (Direct Pulse) NMR provides information on the coordination of silicate tetrahedra in local environments, ^{27}Al NMR provides information about the incorporation and coordination of aluminium present in the sample and ^{29}Si CP (Cross Polarization) provides data on the hydrates[192].

As described in section 2.8.7, the basics of the NMR technique use the fact that different nuclei have different specific spins (I), and some nuclei can have integral spin (I = 1,2,3,…), while others can have fractional spin (I = 1/2,3/2, …) and some with no spin (I = 0). When the samples are tested by NMR, they will be affected by the presence of the strong magnetic field of the instrument and the nuclei will produce different levels of energy and these levels depend on nuclei spin.

^{29}Si in silicon has a magnetic moment and also spin (I) = ½ which will require a longer experimental time to obtain high quality spectra on NMR.

Another factor affecting the experimental time of ^{29}Si nuclei is the long relaxation time which will need long recycle delays. ^{29}Si has a natural abundance less than 5%.

One samples per age were tested resulting in 9 samples per mix. All the NMR data presented were collected by Bruker Advance III HD with a 9.4 T WB magnet with operational frequencies of 74.49 MHz for ^{29}Si and 104.26 MHz for ^{27}Al. For ^{29}Si, the spectra was acquired over 2000 scans using a spin rate of 6 kHz, a delay for pulse recycling of 0.4s, pulse duration of 5.5 μs and an acquisition time of 40 ms.

For ^{27}Al MAS NMR, the spectra was acquired over 7000 scans with a spin rate of 14 kHz, delay for pulse recycling of 0.2s, pulse duration of 1 μs and acquisition time of 10 ms.

For ^{29}Si a 7 mm zirconia rotor with KEL – F cap was used and for ^{27}Al a 2.5 mm zirconia rotor with Vespal cap is used.

3.5.5 Igor fitting

Collected data from NMR was transferred into Igor software as a binary file. These data uploaded to Igor Pro were examined as a single experiment and fitted by already developed macros in software (codes presented in appendix A).

Step 1: The NMR spectrum transfered into Igor Pro using the written macros. At this step, the baseline for transferred spectrum was modified to have a symmetric baseline about the centre band.

Step 2: Introduction of the anhydrous WPC spectrum as a background signal to the software. This background was used to perform background subtraction to avoid problems with alite peaks.

Step3: Baseline fitting to a cubic polynomial. After baseline fitting, each individual peak was fitted a Voigt line shape, using the shift, intensity and shape width, specific to that peak.

Step 4: Defining areas of each peak. The aim was to calculate the mean alumina silicate chain length(MCL), Al/Si ratio and the percentage of each of the hydrate peaks[66].

$$MCL = \frac{2}{\left(\frac{Q^1}{Q^1 + Q^2 + \frac{3}{2}Q^2(1Al)}\right)}$$

$$\frac{Al}{Si} = \frac{\frac{1}{2}Q^2(1Al)}{Q^1 + Q^2 + Q^2(1Al)}$$

$$\%B = \frac{Q^2(1Al)}{2/3Q^2 + Q^2(1Al)}$$

In order to achieve the most correct deconvolution of ^{29}Si NMR spectrum, a raw white Portland cement sample was tested and the spectrum was used as background. The use of this background wave insured that the subtraction of any anhydrous alite and belite from the deconvolution was possible, hence the final result only showed the hydrated silica chains.

Next step included introduction of multiple function coefficients in order to control the shape, width and intensity of each peak assigned to specific units. For the purpose of peak fitting, initial values of shape, width or intensity were

kept constant when needed and after achieving the best fit, they were relaxed. The final curve fitting process was use to get the fitted pattern and quantification calculation were performed based on the final values.

3.5.6 SEM-EDX

SEM EVO15 ZEISS was used to investigate the cement paste samples following the specific curing periods and systems. One samples per age was tested resulting in 3 samples per mix. For SEM, after the hydration was stopped, aslice of each sample was resin impregnated and then cut to 13 mm height. Each resin impregnated sample was polished by polish machine, which was set to a rotation of 80rpm. Samples were polished to Grit 2400 by SiC paper and then to a quarter micrometre by using diamond paste. After every round of polishing, samples were examined under an optical microscope to check the surface to avoid scratch. Then the samples were carbon coated and investigated under SEM. The working distance of the instrument was set to 8.5 mm and an acceleration voltage of 20 kV was used for BSE image collection. Carbon maps and intensities were collected by using Oxford instrument.

The elemental characterization done by EDX in SEM has limitation in applications for hydrated cementitious materials focused on the analysis of C-S-H in. This is caused by the point that the interface volume of the samples used in SEM are larger compared to when C-S-H is presented with no ad-mixture with other phases. Hence, usually the Ca/Si ratio calculated through this technique is not demonstrative of the phase but for all phases mixed. This behaviour could be investigated through Al/Ca plotted versus Ca/Si and noting that the result is following the known trends of other phases.

3.5.7 FTIR

FTIR spectroscopy in this work was used for further analysis of the calcium carbonate precipitation in bacterial cement paste. The samples were casted and after hardening, micro cuts were introduced into samples where the opening width was limited to 0.5 mm. 3 samples per age were tested resulting in 9 samples per mix. The prepared samples were then cured in Corn steep liquor medium for biomineralization precipitation. After 45 days of curing period the samples were taken and the precipitated calcium carbonate was removed from crack surface and tested by Nicolet™ iS™ 10 FT-IR.

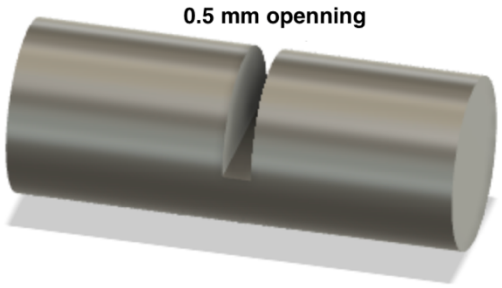

Figure 3-4 Presentation of the introduced gap in samples.

Chapter 4
Results and discussion

4.1 Bacterial growth

The bacterial growth in UCSL was evaluated by the cultivation of *s. pasteurii* in 600 mL of UCSL medium at 30 °C. The growth profile of the bacterial strain averaged from triplicate samples, is presented in Figure 4-1.

As shown in the growth profile of the bacteria, there was a substantial bacterial growth in UCSL ($x10^9$ CFU/mL). Corn steep liquor as a nutrient source for bacteria is composed of carbon, nitrogen, amino acids and vitamins which can stimulate bacterial growth. According to previous research, it has been shown that the *S.pasteurii* strain has higher urease activity when cultivated in CSL media [183].

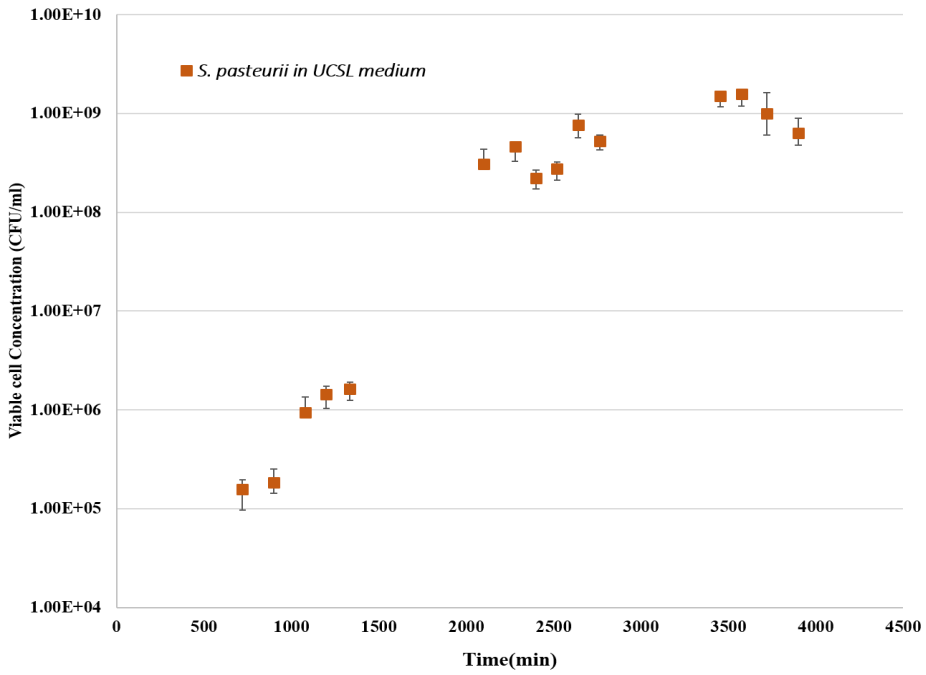

Figure 4-1 Bacterial growth profile for *S. pasteurii* (DSMZ 33) in UCSL averaged from triplicate of viable plate counts (cell concentration vs. time); error bars represent the standard deviation based on these trials.

Corn steep liquor is a low-cost carbon source compared to peptone and yeast extract. However, the variable composition of CSL could have a disadvantage in terms of nutrition dosages, thus it is necessary to predetermine the C : N ratio prior to its use [183].

Another one of the parameters which can affect the microbial induced calcium carbonate precipitation (MICP) is the Ca^{2+} ions and calcium source. There have been extensive investigations on the effect of different calcium sources such as $C_6H_{10}CaO_6$ (calcium lactate) $CaCl_2$ (calcium chloride) and $Ca(NO_3)_2$ (calcium nitrate) [125], [130], [193].

Considering the negative effects of calcium lactate and calcium chloride on cement-based materials, this work is only focusing on the use of calcium nitrate. Furthermore, the dosage of calcium source can also change the

morphology of the precipitation, Ogino et al [194] suggested that an increase in calcium ions will favour the vaterite formation and prevent the alteration of vaterite crystals to calcite.

To investigate the effect of superplasticizer on biomineralization in cement-based materials, superplasticizer (0.1% of cement weight) was added to the *S. pasteurii* bacterial culture after cultivation for 7 hours in 200 mL liquid medium (UCSL) with the presence of calcium nitrate (40 g / L). Then after 17 hours of incubation, the precipitation was collected by centrifuge (Figure 4-2).

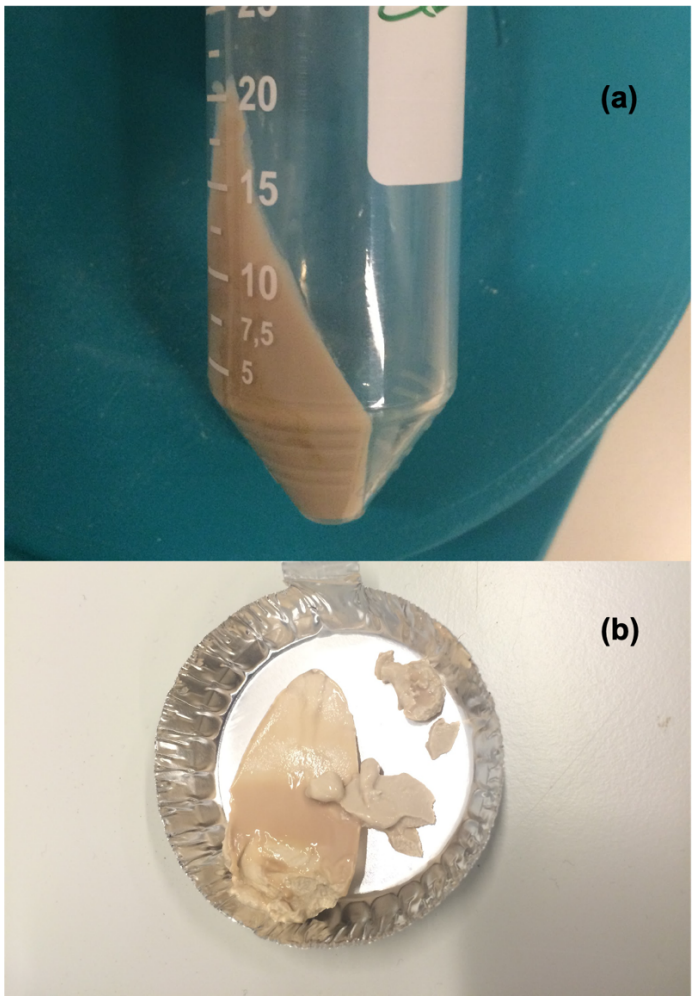

Figure 4-2 Collected bacterial precipitation after centrifuge.

The collected samples were then dried at 35 °C overnight and the powder was tested by X-ray diffraction technique.

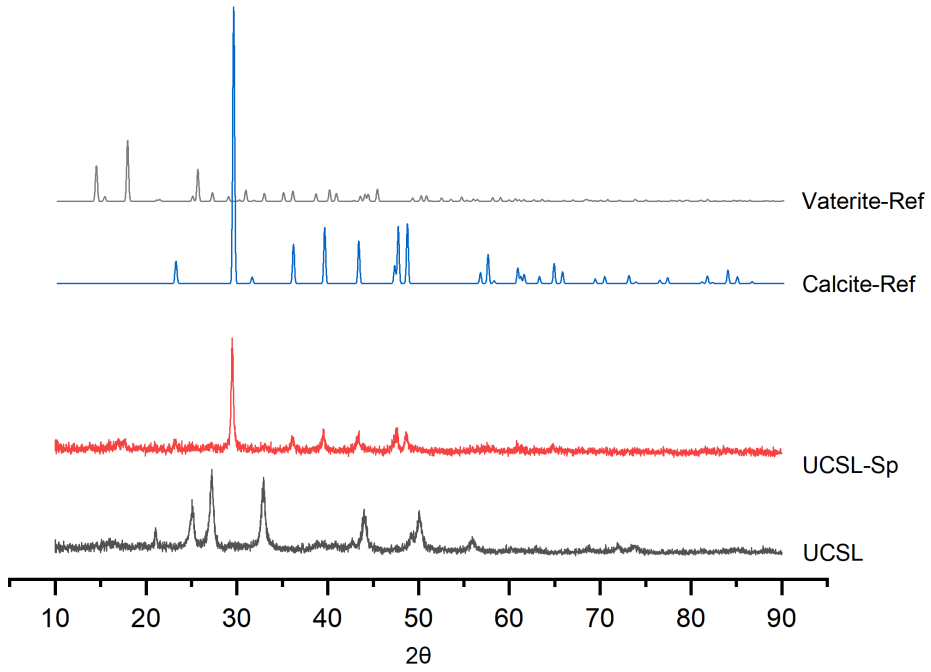

Figure 4-3 XRD pattern for collected precipitation from bacterial culture. UCSL (Urea corn steep liquor), Sp (Superplasticizer).

Figure 4-3 is presenting the X-ray diffraction pattern for two media with and without a superplasticizer. The incorporation of superplasticizer and bacteria did result in the formation of calcite crystals whereas the precipitation collected from the medium with no admixture was only showing vaterite formation.

This change in morphology of the precipitated calcium carbonate is due to the presence of the superplasticizer and the possible changes to the surface charge of the bacteria (previously recorded by Amiri et al.[130]).

4.2 Isothermal calorimetry

Isothermal conduction calorimetry was used to evaluate the degree and speed of hydration for each system. The heat evolution rate for all the samples were measured for 3 days. Figure 4-4 is representing the heat evolution rate for four control systems. NO1 and NC1 systems appeared to have their alite hydration main peak between 9-11 hours, which then were followed by a peak for aluminate signifying secondary ettringite (Aft) formation [195].

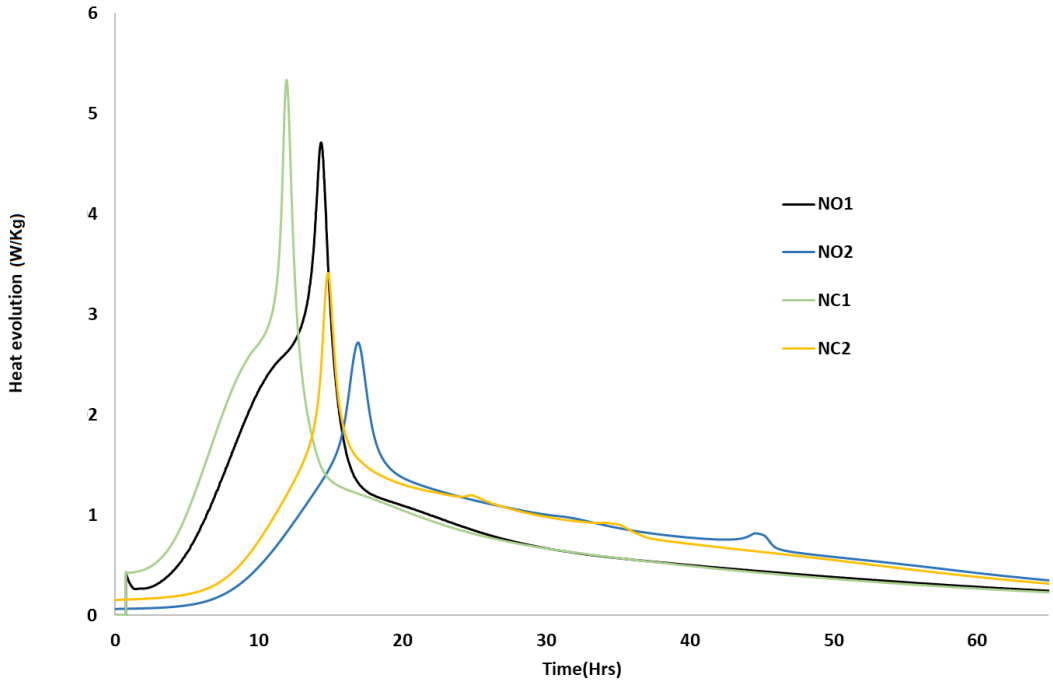

Figure 4-4 Heat evolution rate of neat samples; N (wPC), O (No calcium source), 1 (No superplasticizer), C (Calcium source), 2(Superplasticizer).

Both these systems showed low broad peaks after 20 hours representing the formation of calcium monosulfoaluminate (AFm).

For NO2 and NC2 systems, which had the superplasticizer added in the mix, there was a pronounced delay of their main alite peak between 15-18 hours. According to the literature, the addition of superplasticizer can reduce the ettringite crystal size and calcium hydroxide which can be attributed to long lasting adsorption of plasticizer particles on the surface of crystals [196], [197]. However, the addition of the calcium source (calcium nitrate) in NC1 had a similar trend as NO1.

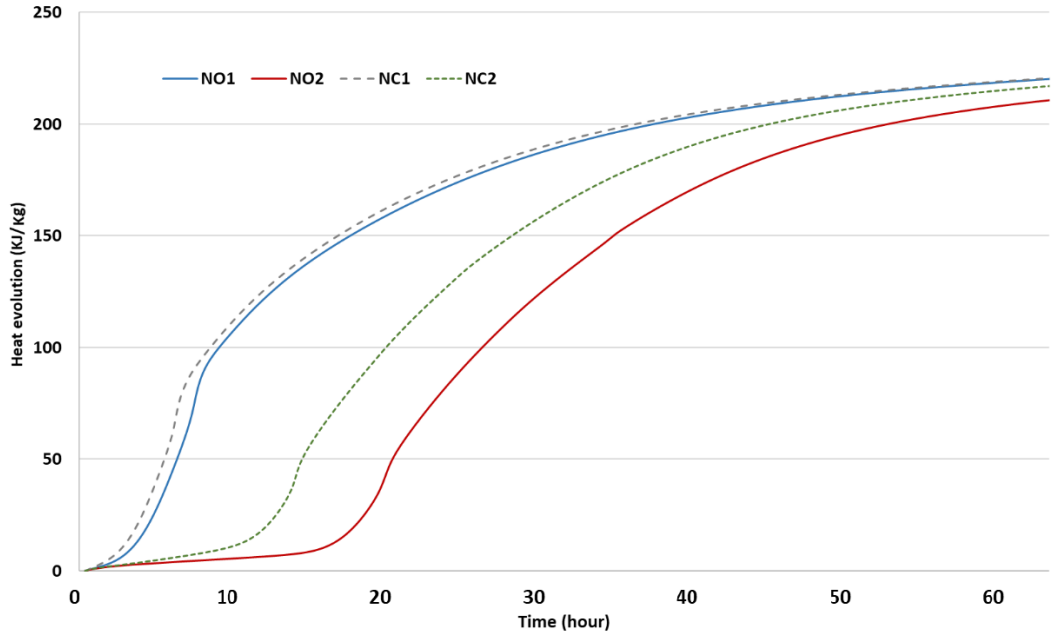

Figure 4-5 Total cumulative heat evolution of neat samples; N (wPC), O (No calcium source), 1 (No superplasticizer), C (Calcium source), 2(Superplasticizer).

The maximum heat rate comparison of all control samples indicated that NO2 and NC2 had lower heat evolution for alite peak.

Figure 4-5 s showing the total heat evolution for control systems. All four samples had reached the same overall degree of hydration after three days. However, the delay of the induction period was long in samples containing superplasticizer (NO2 and NC2). This delay was more pronounced in the control sample with the superplasticizer and no calcium nitrate source.

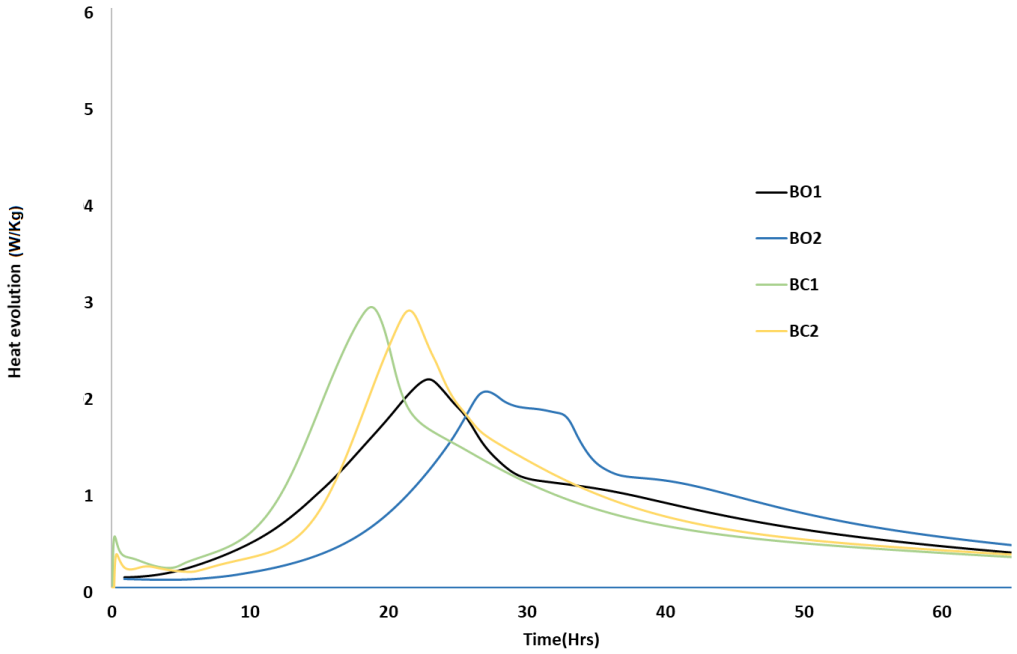

Figure 4-6 Heat evolution rate of neat samples; B (Bacterial), O (No calcium source), 1 (No superplasticizer), C (Calcium source), 2(Superplasticizer).

Figure 4-6 shows the heat evolution rate for four bacterial samples conducted for 3 days. As expected, the addition of bacterial culture and urea corn steep liquor extended the induction period for all four bacterial samples causing a 15 hours delay for alite peak. This delay can be related to the corn steep liquor content of the culture which can act as a retarder due to high volume of sugar and carbohydrate content in CSL [118], [183].

Comparison of alite peak for all bacterial systems showed the expected delay in samples containing superplasticizer. Meanwhile, the addition of calcium

nitrate as a calcium ion source proved to be beneficial for acceleration of the hydration for bacterial systems (NC1 and NC2).

The bacterial samples also experienced a change in the formation of AFt. The AFt formation is also delayed and resulted with a shorter and broader peak during heat evolution.

Figure 4-7 shows the total heat evolution for bacterial systems. The total heat evolution reached the same level for all control systems after 3 days.

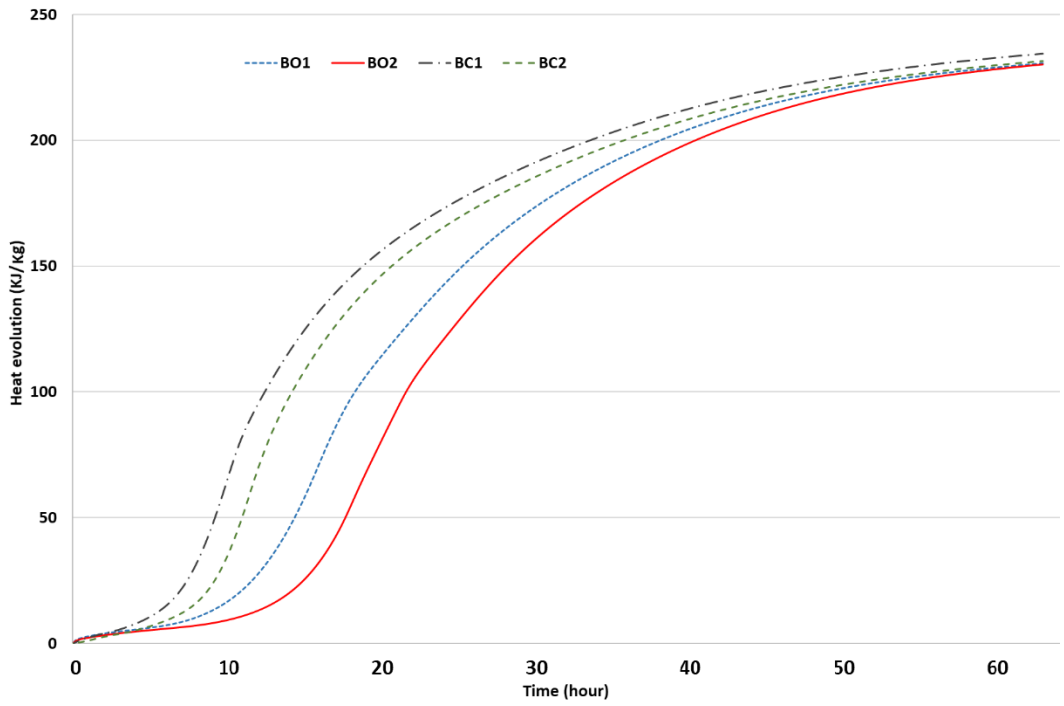

Figure 4-7 Total cumulative heat evolution of neat samples; B (Bacterial), O (No calcium source), 1 (No superplasticizer), C (Calcium source), 2(Superplasticizer).

According to Basaran *et al.*, [27] both nutrient media and the bacteria can extend the dormant period in cement hydration. Nutrient solution does not only

consist of corn steep liquor that may interfere with hydration process. Mwaluwinga et al. [198] suggested that the addition of urea in concrete can decrease the heat of hydration and retard the initial setting time. However, this effect was not observed by Basaran *et al*. [27]. Moreover, addition of Tris into the mix may affect the acceleration and deceleration stage.

Besides the effect of corn steep liquor as a retarder, use of CSL medium would increase the ionic concentration from the generation of ammonium, carbonates, and hydroxyl ions.

4.3 7 day samples

4.3.1 STA

Since vegetative cells and their nutrients were introduced into the cement paste, the possibility of the MICP inside the cement paste was investigated. As described in Section 4.4, TGA/DSC and DTG curves were obtained.

Figure 4-8 is representing TGA data for control samples at 7 days age. According to TG and emission curves all 4 samples have a range of CH content below 15% and an indication of a very small amount of calcium carbonate ranging from 0.25% - 0.65%. The highest amount CC% in control samples was related to NC1-7 and NC2-7 which had the initial calcium nitrate source added during the mix. The calcium nitrate was added to the reference samples to introduce a comparison baseline for bacterial samples and eliminate all the possible changes in the CC% due to the calcium nitrate source.

The TGA data for bacterial samples at 7days age in Figure 4-9 is showing the TG and emission curves suggesting that the CH content present in the

samples was in a range of 6% - 14%, whereas, the amount of calcium carbonate available in the samples was in the range of 2.5% - 3%. The highest amount CC% in 7 day old bacterial samples was related to BC2-7 which had the initial calcium nitrate source added during the mix. It is also possible to conclude that the samples with higher amount of calcium carbonate are showing lower amount of calcium hydroxide.

Overall comparison of 7 day samples showed a significant increase in calcium carbonate content of bacterial samples indicating the early start of biomineralization in cement paste even before 7 days and reaching to a maximum value of 3% in the sample containing bacteria culture incorporated with calcium ion source.

Considering the calcium hydroxide content in 7 day samples, the reference samples with added calcium nitrate were showing a small increase in CH content. This increase in the CH content of reference samples is due to the presence of excessive amounts of calcium ions contributing to the formation of calcium hydroxide. However, the TGA analysis for bacterial samples showed a drop in CH content which is following the trend related to calcium nitrate usage. Bacterial sample with no addition of calcium nitrate experienced a slightly lower amount of calcium hydroxide available and the addition of calcium source to samples resulted in a higher percentage of calcium carbonate and a lower drop in CH content percentage.

Further comparison of the STA, and XRD analysis are presented in section 5.6.2.

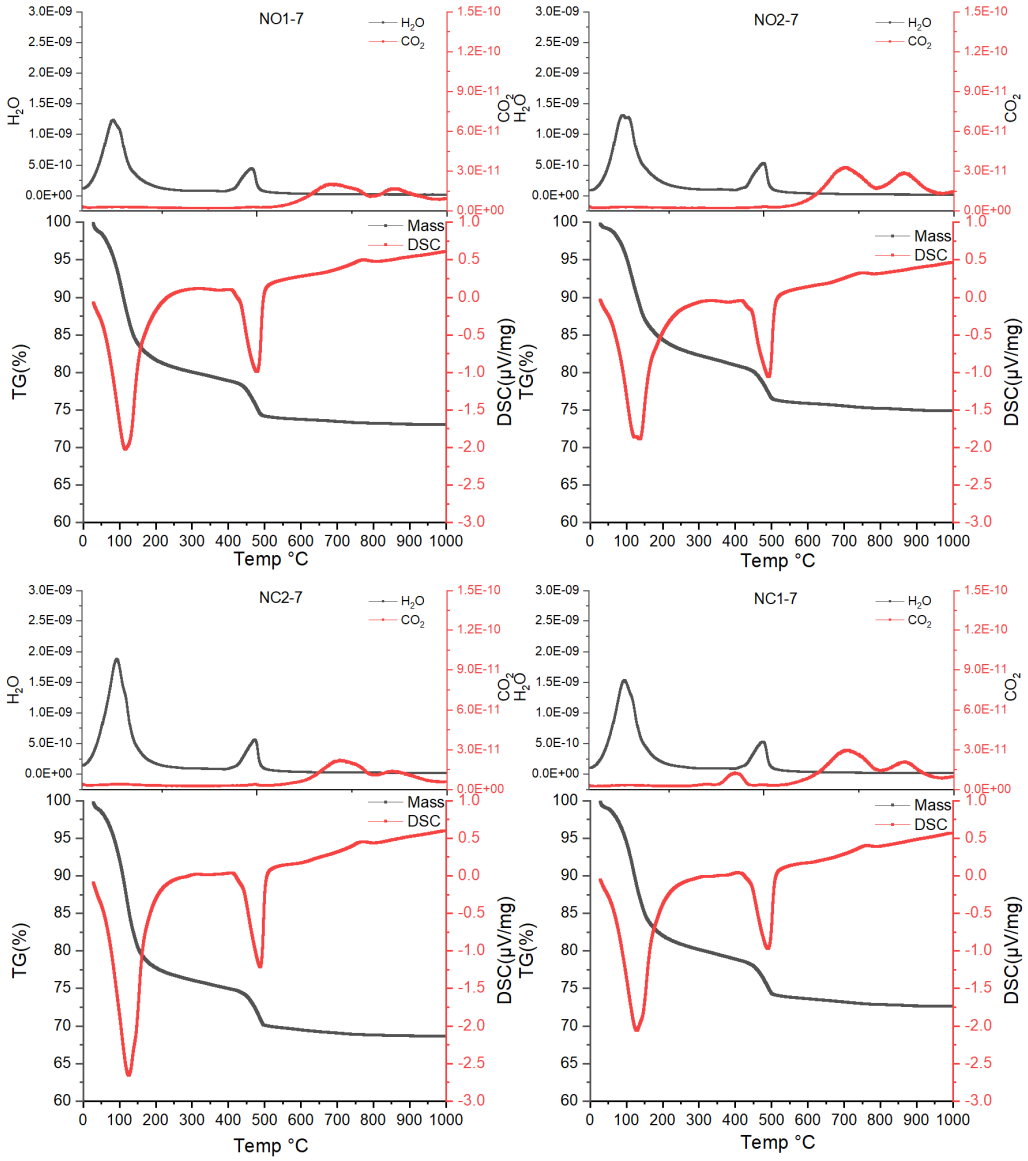

Figure 4-8 DSC/TG and Mass spectra of neat samples. N (Neat), O (No calcium source), 1 (No superplasticizer), C (Calcium source), 2(Superplasticizer).

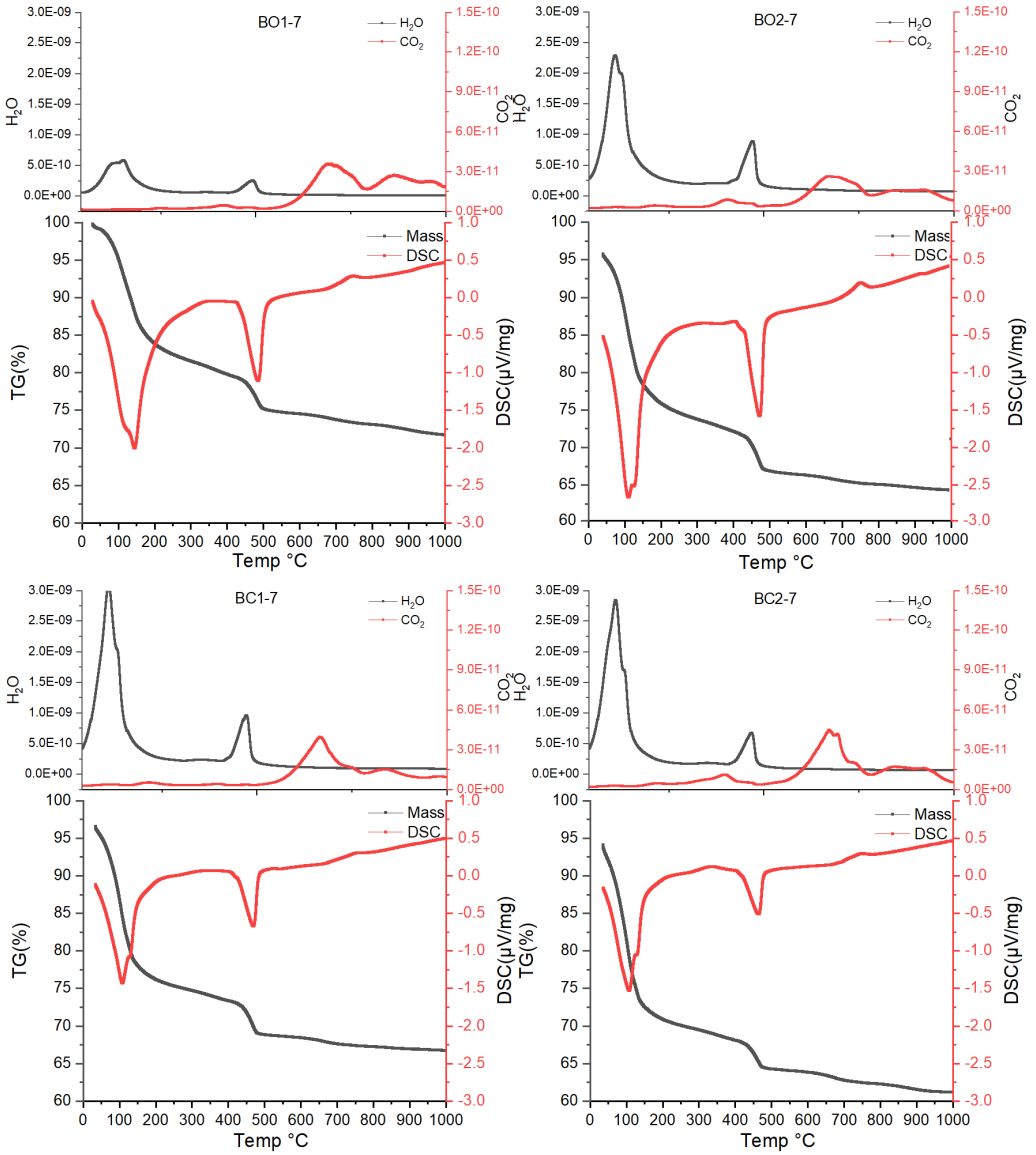

Figure 4-9 DSC/TG and Mass spectra of neat samples. B (Bacterial), O (No calcium source), 1 (No superplasticizer), C (Calcium source), 2(Superplasticizer).

4.3.2 Deconvolution of the ^{29}Si NMR

Figure 4-10 and Figure 4-11 show the ^{29}Si MAS NMR spectra and the deconvolution of all hydration products for 7 day samples. The peaks related to the possible silicate structures with different shifts and intensities were assigned to these blends. The assigned peaks included monomers (alite and belite) Q^0 at ≈ -71.3, dimers (Q^1) at ≈ -79.2, and middle chains at ≈ -81.5 for Q^2(1Al) or ≈ -85.2 ppm for Q^2(0Al) (5,6,131). Additionally, a small peak related to monomers in γ-C_2S was present throughout all the blends and samples, which originally is from the raw white Portland cement. Table 5-1 shows the percentage of each Q^n units in 7 day samples.

Table 4-1 Q^n unit percentage for all samples at 7 days.

	NO1	NO2	NC1	NC2	BO1	BO2	BC1	BC2
Q^0(H)	2.9%	2.4%	2.8%	3.3%	3.8%	3.7%	3.1%	2.9%
Q^1	44%	42.4%	42.8%	44.3%	45%	46.1%	43.8%	48.4%
Q^2(1Al)	8.7%	9.7%	9%	8.4%	8.7%	7.2%	7%	7.5%
Q^2	10.5%	12.2%	11.9%	12.1%	10.2%	11%	10.6%	11.7%

The comparison of 7 days neat samples showed a broader peak at ~78 ppm for neat samples with an added calcium source. The presence of a broader peak with no shoulders would increase the possible deconvolution errors and peak fitting. However, after careful calculations, it seemed that the addition of calcium nitrate had slightly increased the Q^2(1Al) peak at 81.5 ppm. Q^2(1Al) is the result of Al atoms replacing bridging tetrahedra structure, which as a result should increase the Ca/Si ratio of the structure after further substitution.

According to Plusquellec et al. [199] addition of calcium nitrate will increase the calcium concentration and lower the pH value. It will also change the surface properties of C-S-H and aluminium will be able to be incorporated in the structure.

Addition of bacteria at 7 days showed no change in the ^{29}Si MAS NMR spectra apart from lower Q^2(1Al) compared to the neat samples.

The comparison of the ^{29}Si MAS NMR spectra for both control and bacterial groups showed a slight change in the quantities of the C-S-H phases. These differences can be neglected and concluded as a similarity between hydrated wPC and hydrated bacterial wPC.

Further comparison of the NMR analysis are presented in section 5.7.

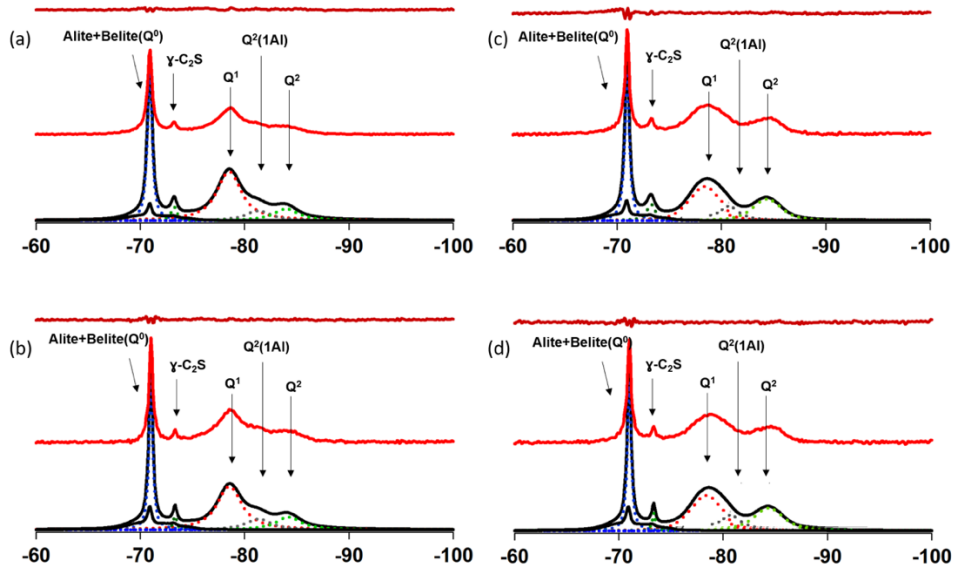

Figure 4-10 ^{29}Si NMR spectra of neat 7days, including experimental spectrum (middle, red), residual (top, red) and the individual frequencies. (a) neat, (b) with superplasticizer, (c) with calcium nitrate, (d) with calcium nitrate and superplasticizer.

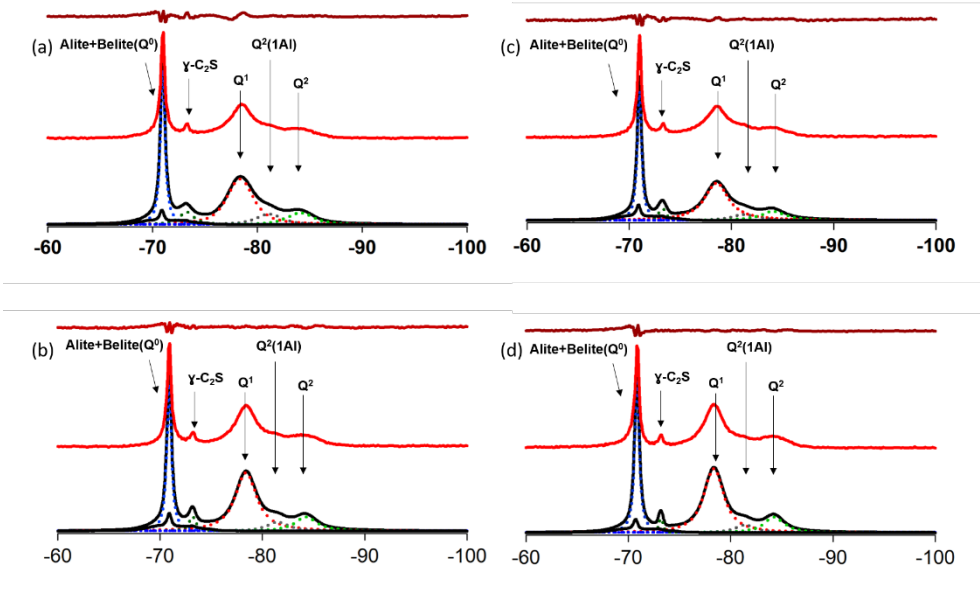

Figure 4-11 ^{29}Si NMR spectra of bacterial 7days, including experimental spectrum (middle, red), residual (top, red) and the individual frequencies. (a) bacterial, (b) with superplasticizer, (c) with calcium nitrate, (d) with calcium nitrate and superplasticizer.

4.4 28 day samples

4.4.1 STA

Figure 4-12 is representing TGA data for control samples at 28 day age. The TG and emission curves suggested that all 4 samples had a CH% content ranging between 15% - 18% and indicated a very small amount of calcium carbonate ranging from 0.25% - 0.45%. The highest amount CC% in control samples was again related to NC1-28 and NC2-28 which had the initial calcium nitrate source added during the mix.

TGA data for bacterial samples at 28 days age is represented in Figure 4-13. Noting the TG and emission curves, the CH content present in the samples were in a range of 12% - 16%, whereas, the amount of calcium carbonate available in the samples was in the range of 5% - 6%. The highest amount of CC% in 28 day old bacterial samples was related to BC2-28 which had the initial

calcium nitrate source added during the mix. It is also possible to conclude that the samples with higher amounts of calcium carbonate are showing lower amounts of calcium hydroxide.

As expected, calcium carbonate content in bacterial samples at 28 days was still showing more increase (almost 100% increase compared to 7 days bacterial samples), whereas for reference samples the only indication of an increase in CC% was for samples with added calcium nitrate. The jump in CC% of the bacterial samples is correlated with the previous finding of high enzyme activity of bacteria at early ages in presence of nutrient [27]. Meanwhile, it is in agreement with Amiri .et .al [118] for the possibility of using viable bacteria strains for biomineralization applications in cement-based materials.

Once again the CH percentage was following a trend regarding the presence of calcium source and samples with the initial addition of calcium nitrate for bacterial samples, were showing less drop in the CH content. The addition of calcium nitrate as calcium source for bacteria strain was preventing the bacteria from using calcium hydroxide for urease enzyme activity hence the smaller decrease in CH percentage. However, another factor affecting the CH% was the added superplasticizer. The addition of superplasticizer in samples resulted in less calcium hydroxide for all systems and also resulted in a higher calcium carbonate percentage for bacterial samples[200]. The decrease in CH content by the addition of superplasticizer can be due to retarding characteristics of superplasticizer and longer availability of calcium ions for bacteria to form calcium carbonate.

Further comparison of the STA, XRD analysis are presented in section 5.6.2.

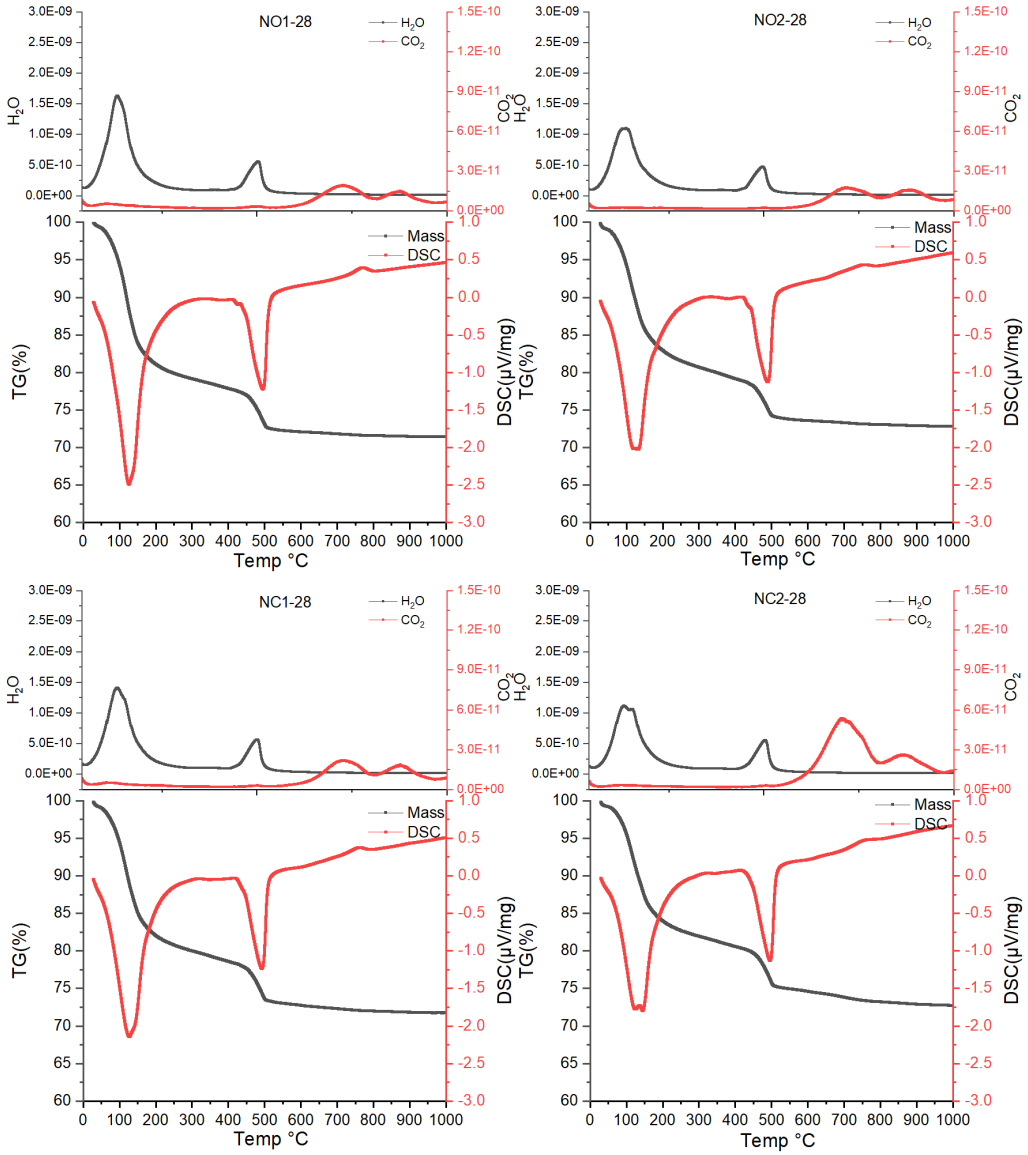

Figure 4-12 DSC/TG and Mass spectra of neat samples. N (Neat), O (No calcium source), 1 (No superplasticizer), C (Calcium source), 2(Superplasticizer).

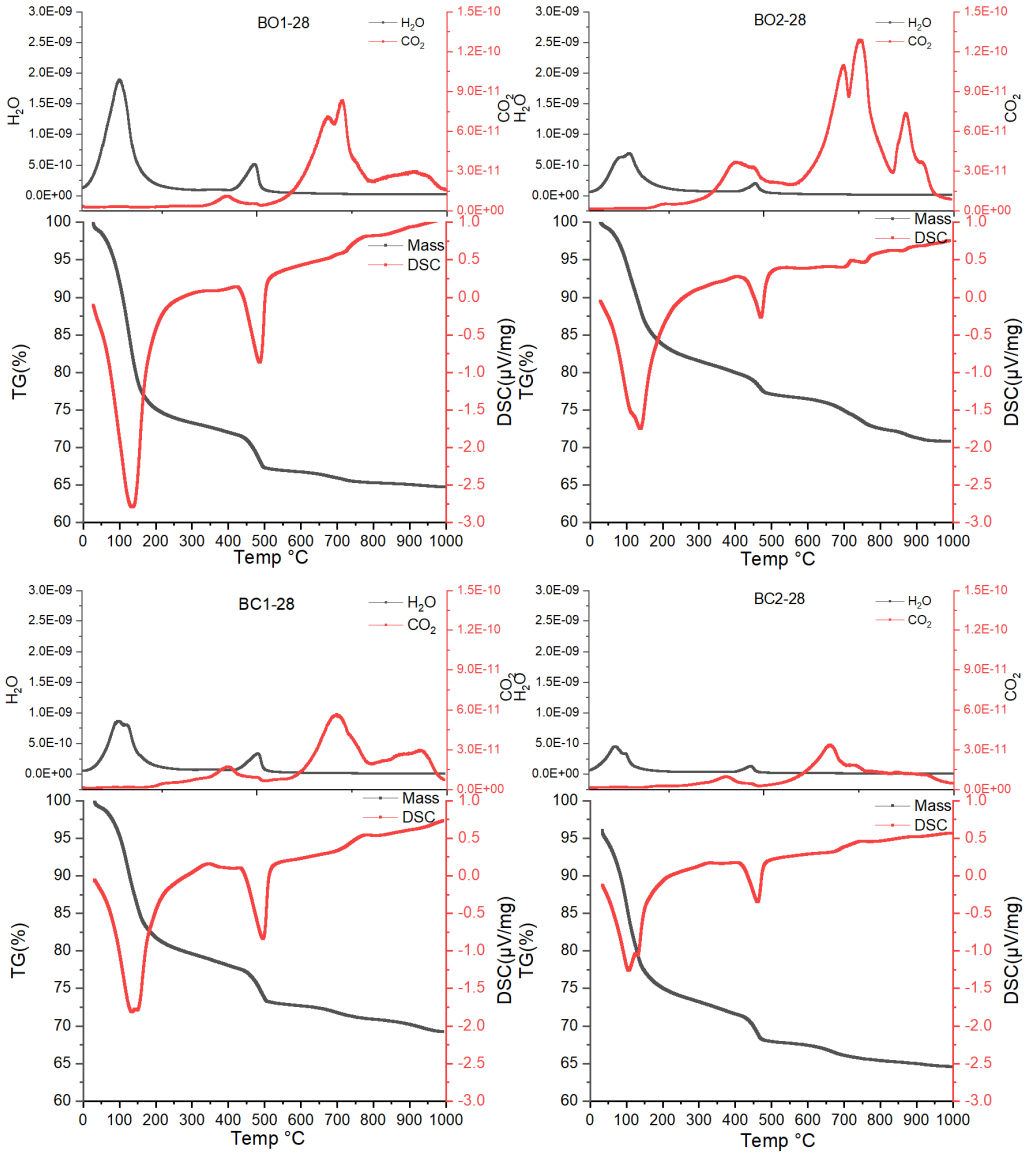

Figure 4-13 DSC/TG and Mass spectra of neat samples. B (Bacterial), O (No calcium source), 1 (No superplasticizer), C (Calcium source), 2(Superplasticizer).

4.4.2 Deconvolution of the ^{29}Si NMR

The ^{29}Si MAS NMR spectra and the deconvolution of all hydration products for 28 day samples are shown in Figure 4-14 and Figure 4-15. All the samples showed peaks at -71 ppm for Q^0, -79 ppm and -85 ppm for Q^1 and Q^2 and -82 ppm for $Q^2(1Al)$ indicating incorporation of aluminium in the silicate chain.

The NMR spectra for 28 days neat samples did not show any differences between the neat samples and the neat samples with additional calcium nitrate. The Q^1 value for neat samples was around 43% changing to 44% in bacterial paste, $Q^2(1Al)$ for neat paste was around 10% compared to 9% in bacterial samples and very similar Q^2 range at 22% for neat samples and 20% for bacterial wPC paste at 28 days. Table 5-2 is representing the Q^n species and their percentages in each sample at 28 days which is calculated through NMR deconvolution.

Table 4-2 Q^n unit percentage for all samples at 28 days.

	NO1	**NO2**	**NC1**	**NC2**	**BO1**	**BO2**	**BC1**	**BC2**
$Q^0(H)$	2.3%	2.1%	2.5%	1.9%	2.6%	2.8%	2.8%	2.8%
Q^1	43.1%	43.9%	42.1%	45%	43.8%	45.8%	44.3%	44.7%
$Q^2(1Al)$	10.4%	9.3%	9.6%	11.3%	9.4%	8.6%	9.5%	9.7%
Q^2	22.2%	22.2%	21.5%	22.8%	19%	18.1%	20.1%	20%

Both sample groups showed the expected mean chain length (MCL) of 3.5 ~ 3.7 and Al/Si ratio of ~ 0.07. The formation of C-S-H and C-A-S-H in

bacterial and neat wPC pastes experienced a degree of stability in the amount of Q^1 and an increase in $Q^2(1Al)$ and Q^2 compared to 7 day samples.

After the early hours and the acceleration characteristics of calcium nitrate, the two systems showed almost the same trend in NMR spectra and it can be summarized as the addition of bacterial culture to wPC paste has no (or negligible) differences. Therefor, the use of biomineralization should not have any early age implications on the structural integrity of the C-S-H.

Further comparisons of the NMR analysis are presented in section 5.7.

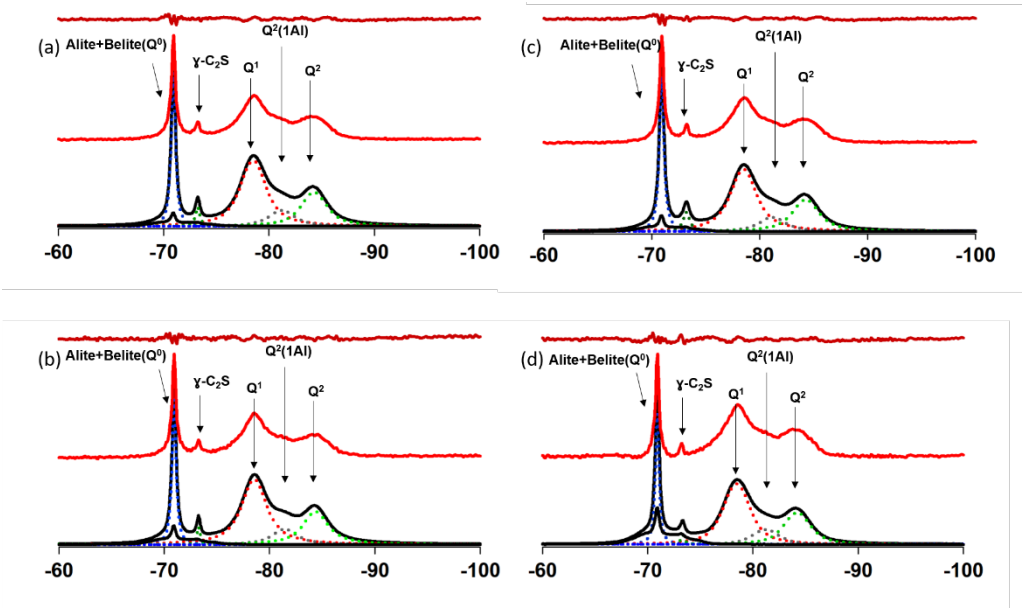

Figure 4-14 ^{29}Si NMR spectra of neat 28days, including experimental spectrum (middle, red), residual (top, red) and the individual frequencies. (a) neat, (b) with superplasticizer, (c) with calcium nitrate, (d) with calcium nitrate and superplasticizer.

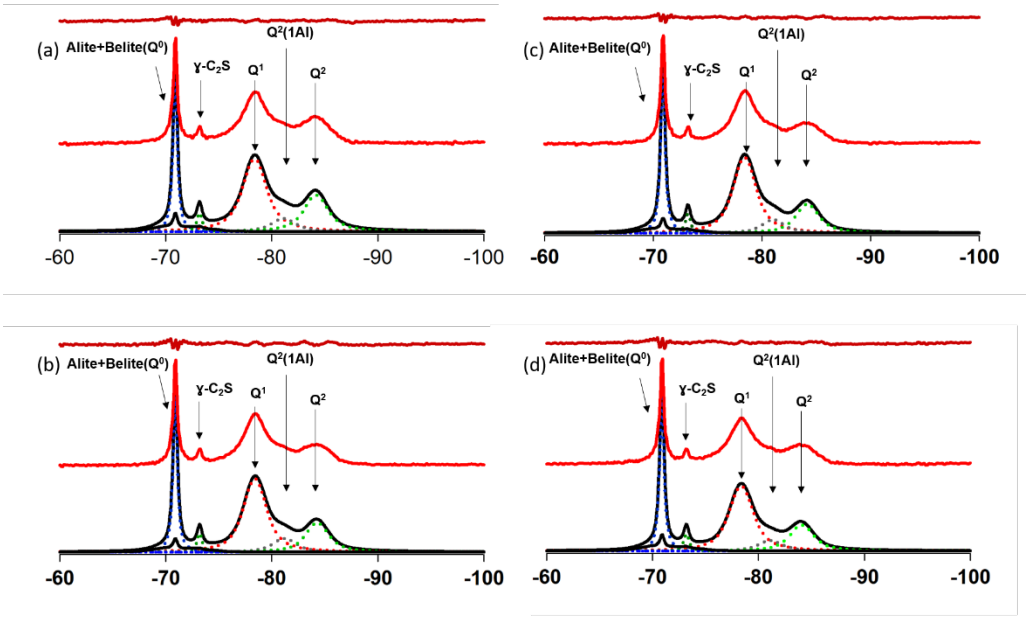

Figure 4-15 ^{29}Si NMR spectra of bacterial 28days, including experimental spectrum (middle, red), residual (top, red) and the individual frequencies. (a) neat, (b) with superplasticizer, (C) with calcium nitrate, (d) with calcium nitrate and superplasticizer.

4.5 45 day samples

4.5.1 STA

The TG and emission curves for 45 day old control samples are presented in Figure 4-16. The calcium hydroxide available in the wPC samples was in a range of 17% - 19% and the amount of calcium carbonate for all control samples was less than 0.6%. As expected the highest percentage of calcium carbonate available in the samples related to the control samples with added calcium nitrate source during the mix which resulted in higher CH and CC content. Table 5-3 is showing the STA results for portlandite and calcium carbonate percentage for both bacterial and neat wPC paste at 7, 28 and 45 days.

Table 4-3 Portlandite and calcium carbonate percentage from STA analysis for both bacterial and neat wPC paste at 7, 28 and 45 days. N (Neat), B(Bacterial), O (No calcium source), 1 (No superplasticizer), C (Calcium source), 2(Superplasticizer).

	7 days		28 days		45 days	
	CH%	$CaCO_3$%	CH%	$CaCO_3$%	CH%	$CaCO_3$%
NO1	12.33	0.23	15.62	0.23	18.09	0.23
NO2	11.92	0.23	13.16	0.23	17.68	0.23
NC1	14.46	0.68	17.27	0.45	18.71	0.45
NC2	14.80	0.45	16.86	0.45	18.09	0.68
BO1	8.63	2.95	13.16	5.03	14.80	6.36
BO2	10.11	2.73	11.10	5.91	12.33	6.82
BC1	13.16	2.73	16.86	5.45	15.21	6.82
BC2	12.05	3.07	14.39	6.14	13.98	7.50

As for 45 day old bacterial samples, the percentage of calcium carbonate raised to around 6% . Bacterial samples with initial calcium nitrate source (BC1-45 and BC2-45) experienced the highest percentage of calcium carbonate. Whereas calcium hydroxide content of samples was lower than the control samples ranging from 12% to 16%.

The 45 day samples also showed the same result as early age samples with a change in the calcium carbonate content of bacterial samples. At 45 days the increase of calcium carbonate in bacterial samples was similar to 28 days

samples and this is due to the depletion of nutrients available in the sample and the only source of nutrient is through the medium which the sample was submerged. The porosity of the cement paste samples was less than mortar and concrete resulting in restricted access to nutrients through the porosity and submersion environment. As for calcium hydroxide in bacterial samples, graphs show the same percentages as for 28 days samples which again could be due to a lack of calcium ion in the matrix which can initiate the use of calcium hydroxide as a calcium source at 45 days.

The small increase in calcium carbonate content is suggesting the viability of bacteria at 45 days whereas minimal changes in Calcium hydroxide percentages (less than 1%) even with a decrease in CH percentage (BC2-45) suggest a lack of calcium ion source and the initiation of using calcium hydroxide as the calcium source for biomineralization.

Further comparison of the STA, XRD analysis are presented in section 5.6.2.

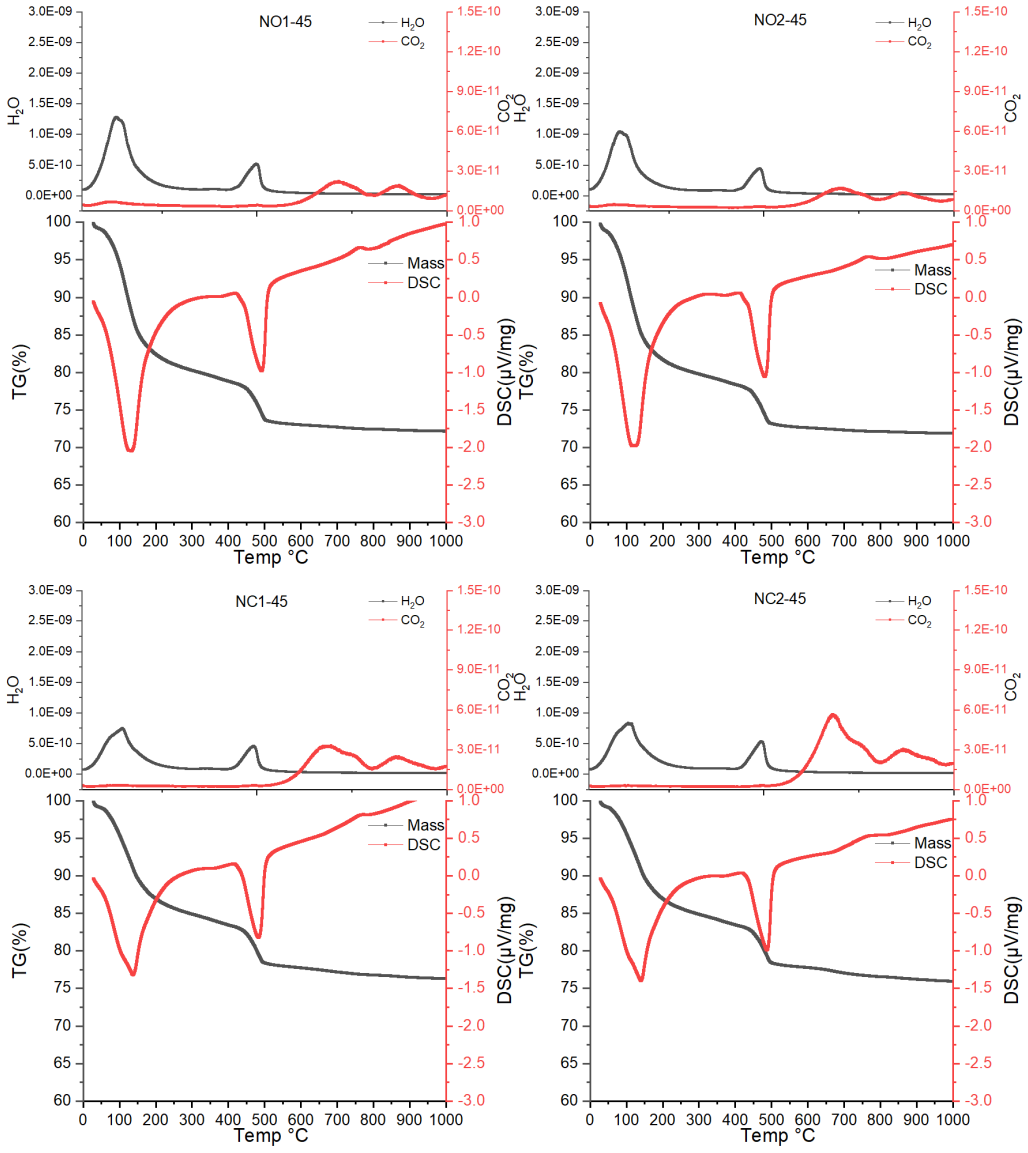

Figure 4-16 DSC/TG and Mass spectra of neat samples. N (Neat), O (No calcium source), 1 (No superplasticizer), C (Calcium source), 2(Superplasticizer).

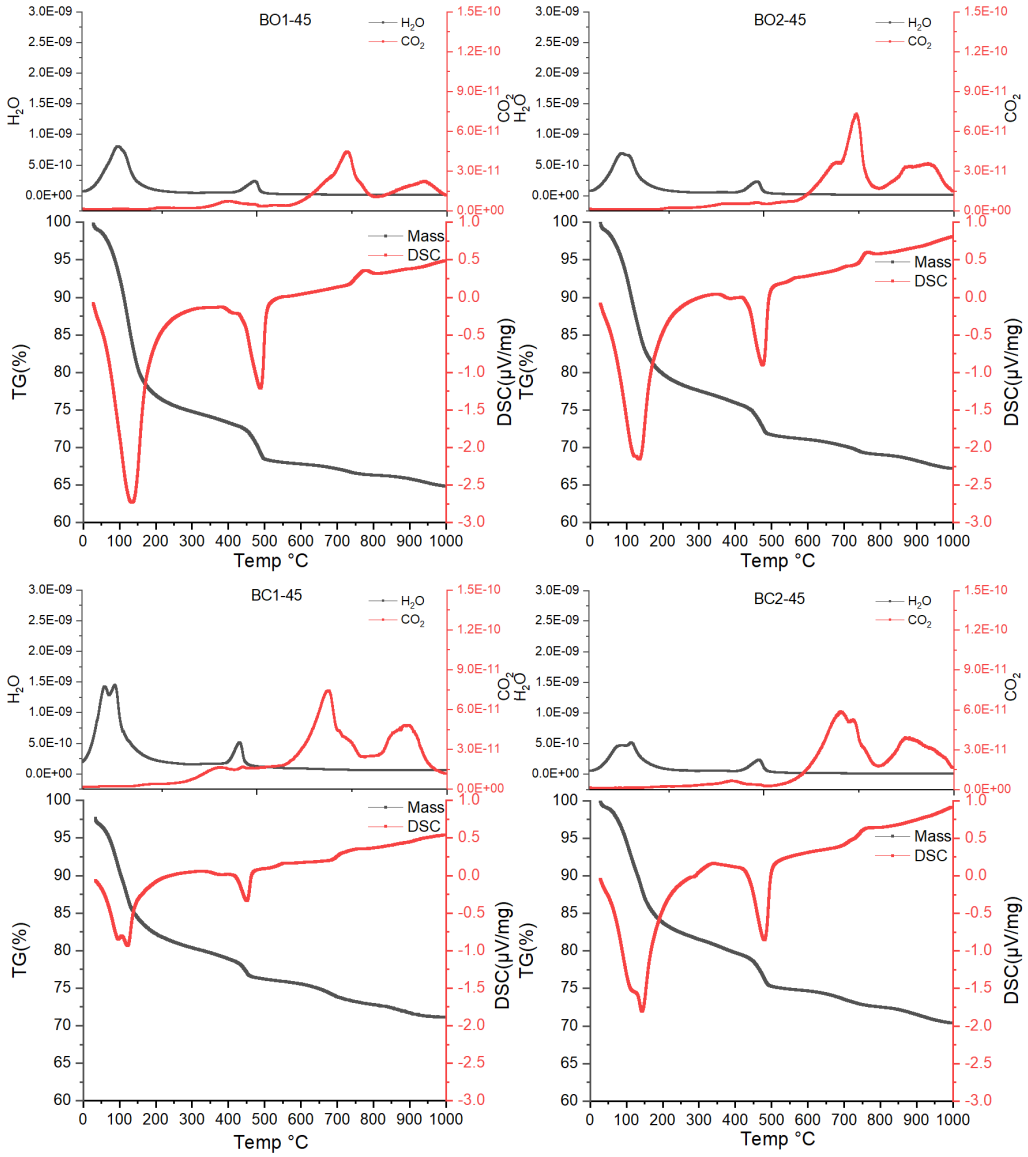

Figure 4-17 DSC/TG and Mass spectra of neat samples. B (Bacterial), O (No calcium source), 1 (No superplasticizer), C (Calcium source), 2(Superplasticizer).

4.5.2 Deconvolution of the ^{29}Si NMR

The ^{29}Si MAS NMR spectra and the deconvolution of all hydration products for 45 day samples are shown in Figure 4-18 and Figure 4-19.

The NMR spectra for 45 days neat samples did not show any significant differences between the neat samples and the neat samples with additional calcium nitrate. The similarity between these two systems at 45 days again can provide proof of the negligible effect of biomineralization on the C-S-H structure.

At 45 days, MCL values for bacterial and neat wPC were approximately 3.8 and there was an increase in Al/Si ratio (45 day~ 0.08) compared to 28 day sample (28 day ~0.07). The replacement of the bridging tetrahedra structures by Al atoms at 45 days could be concluded.

The calculated value of Q^1 for 45 day samples was similar to 28 and 7 day samples indicating that the initially formed C-S-H chains were stable. The values for Q^2(1Al) and Q^2 at 45 days showed a slight increase compared to 28 day samples. These changes were similar for both bacterial and neat wPC pastes.

Table 4-4 Q^n unit percentage for all samples at 45 days.

	NO1	**NO2**	**NC1**	**NC2**	**BO1**	**BO2**	**BC1**	**BC2**
Q^0(H)	1.6%	1.7%	1.2%	1.6%	2.5%	2.4%	2.6%	2.6%
Q^1	44.3%	42.3%	43.2%	44.6%	44.7%	45.3%	42.7%	44.9%
Q^2(1Al)	12%	12.2%	12.1%	12.5%	11.7%	12.6%	12.6%	12.6%
Q^2	23.8%	24.2%	23.1%	24.2%	22%	21.2%	22.6%	20.9%

Table 5-4 is representing the Q^n species and their percentages in each sample at 45 days which is calculated through NMR deconvolution.

After the early ages and the acceleration characteristics of calcium nitrate, two systems experienced a very similar trend in NMR spectra and it can be summarized as the addition of bacterial culture to wPC paste has no (or negligible) differences. Therefor, the use of biomineralization should not have any early age implications on the structural integrity of the C-S-H. Further comparison of the NMR analysis are presented in section 5.7.

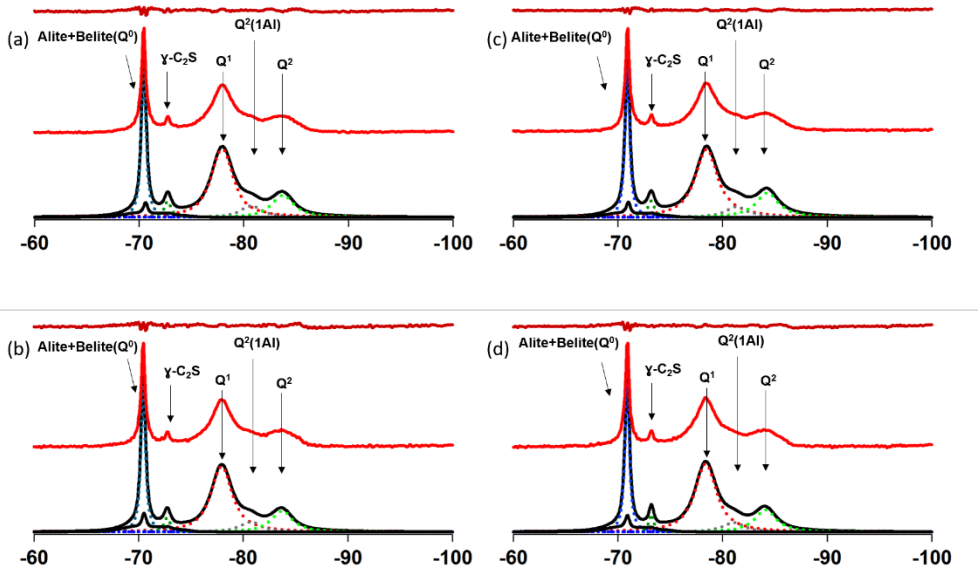

Figure 4-18 ^{29}Si NMR spectra of neat 45days, including experimental spectrum (middle, red), residual (top, red) and the individual frequencies. (a) neat, (b) with superplasticizer, (c) with calcium nitrate, (d) with calcium nitrate and superplasticizer.

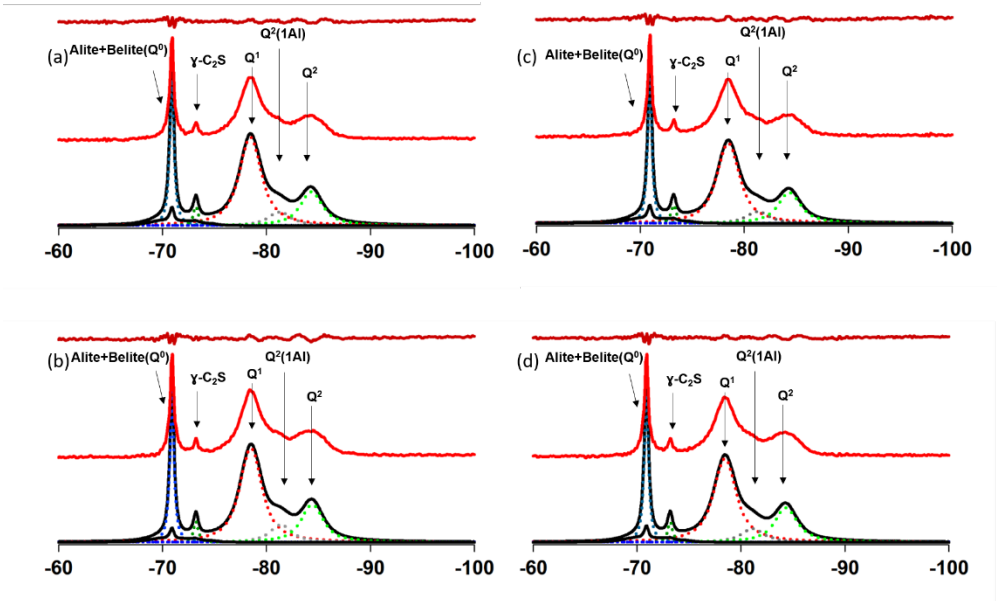

Figure 4-19 ^{29}Si NMR spectra of bacterial 45days, including experimental spectrum (middle, red), residual (top, red) and the individual frequencies. (a) neat, (b) with superplasticizer, (c) with calcium nitrate, (d) with calcium nitrate and superplasticizer.

4.6 STA, XRD and NMR Summary in regards with ageing

4.6.1 Comparison of the X-ray diffraction patterns

Figure 4-20 to Figure 4-23 are representing the XRD analysis for both control and bacterial wPC paste at 7, 28 and 45 days. Excluding the corundum peaks, the samples showed the trace of Portlandite, Ettringite, alite, belite and calcium carbonate. The double peaks around 32° 2θ represent the belite and the reduction of belite by ageing.

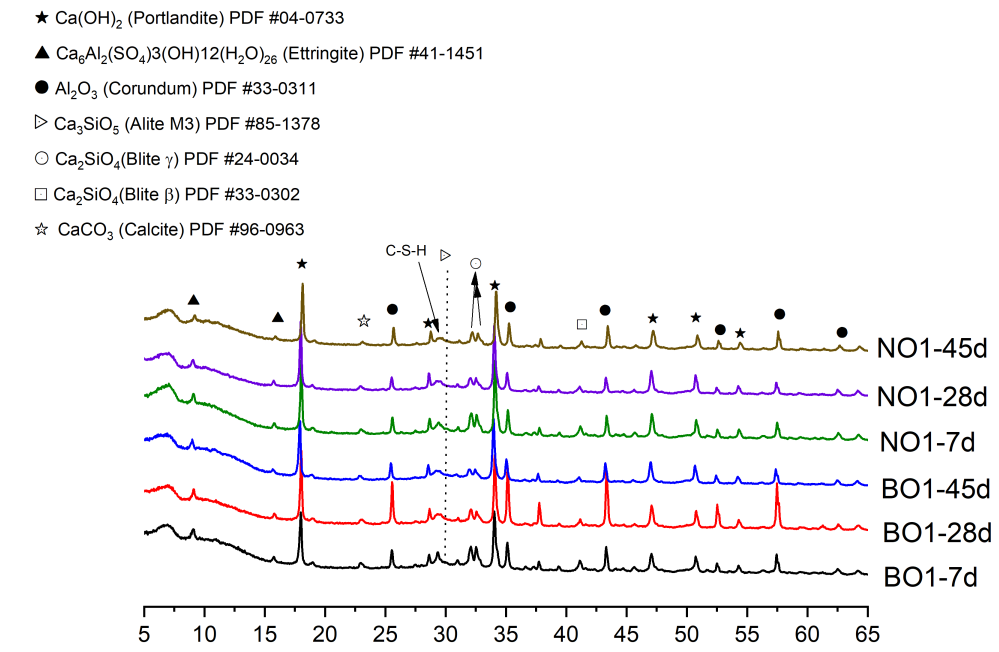

Figure 4-20 X-Ray diffraction for control and bacterial samples without superplasticizer, N (wPC), B (Bacteria), O (No calcium source), 1 (No superplasticizer).

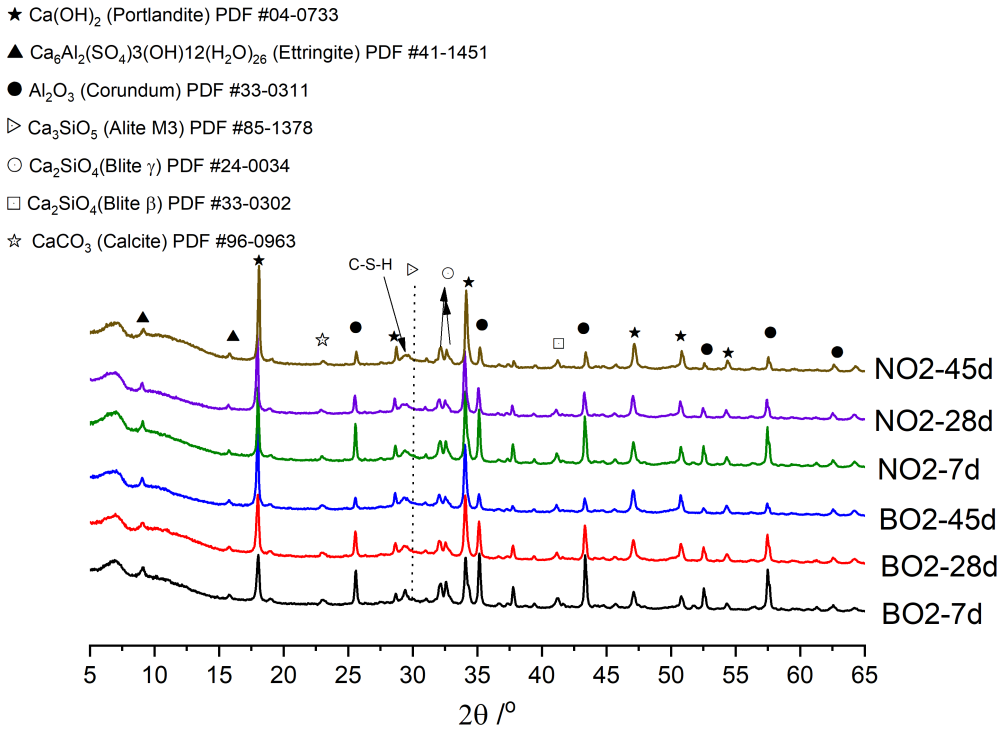

Figure 4-21 X-Ray diffraction for control and bacterial samples with superplasticizer, N (wPC), B (Bacteria), O (No calcium source), 2(Superplasticizer).

The same behaviour also presented itself with a peak around 41° 2θ. As for alite and the broad peak around 30° 2θ, the changes were very slim. This was due to the early reaction of alite before 7 days and also overlapping peaks at the same 2θ angle related to the presence of calcite which led to presence of a broad peak rather than a sharper peak for alite. However the peak at this angle had a sharper shape at 7 days compared to older samples.

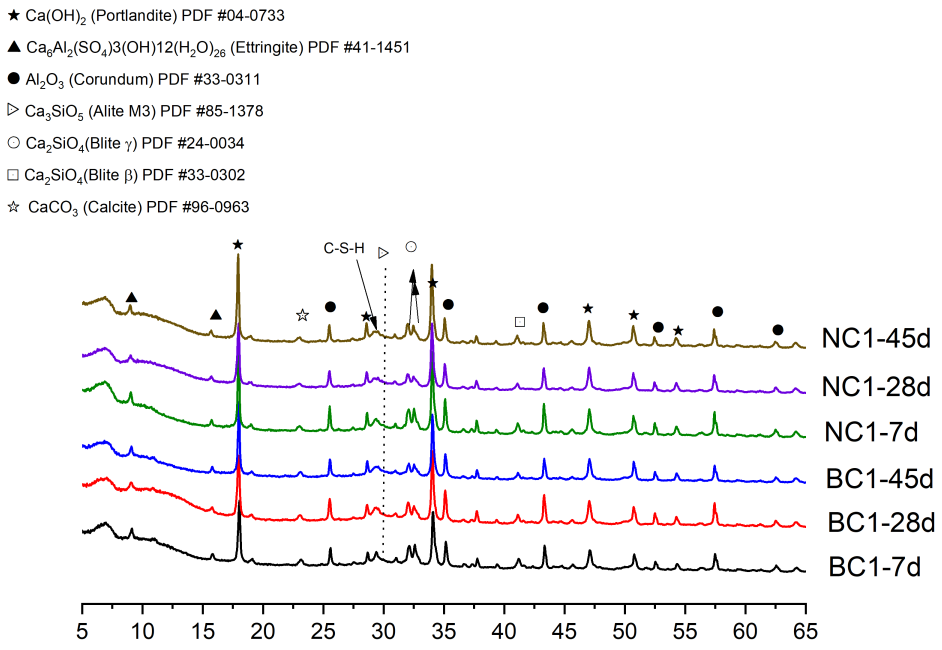

Figure 4-22 X-Ray diffraction for control and bacterial samples containing Ca^{2+} without superplasticizer, N (wPC), B (Bacteria), 1 (No superplasticizer), C (Calcium source).

The sharp peaks at 17° and 34° 2θ represented the presence of portlandite in samples and the peaks showed a higher intensity at later ages.

The peak present at 23° 2θ was related to the presence of the calcite in samples, however, the shape and the size of the peaks between different samples seemed similar and an indication of the very minor changes by the

ageing process. The amount of portlandite and calcium carbonate are discussed in more detail in section 5.6.2.

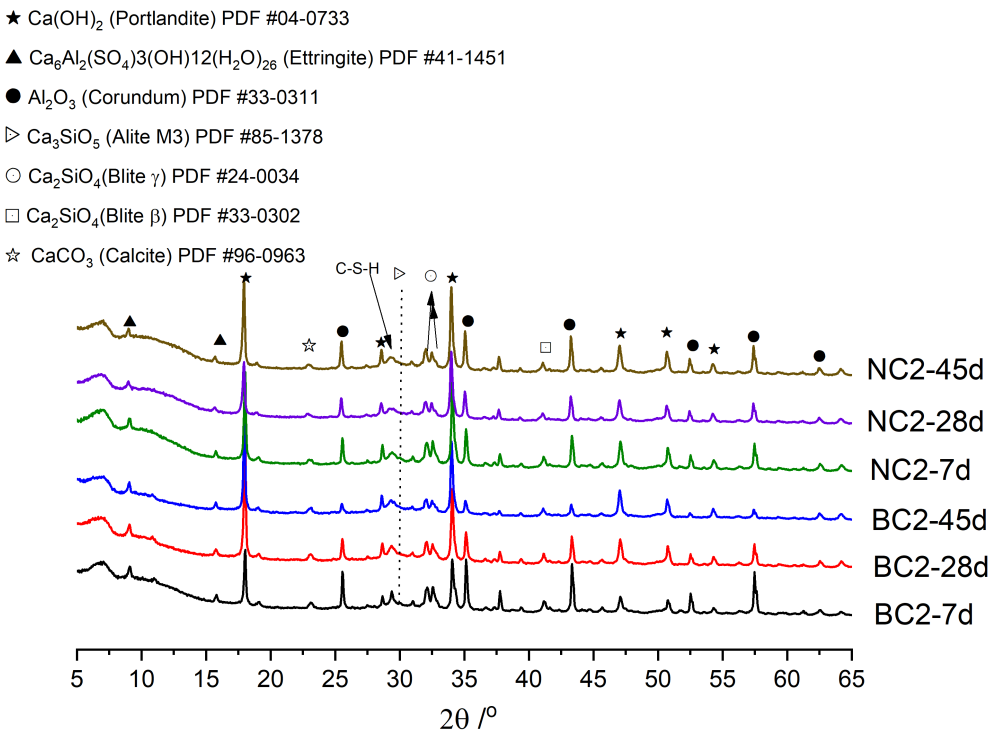

Figure 4-23 X-Ray diffraction for control and bacterial samples containing Ca^{2+} with superplasticizer, N (wPC), B (Bacteria), , C (Calcium source), 2(Superplasticizer).

4.6.2 Comparison of the CH and CC content

The calculated amount of calcium carbonate and calcium hydroxide from QXRD and STA analysis are represented in Figure 4-24 and Figure 4-25 for both control and bacterial wPC paste. The comparison of the QXRD and STA data showed a similar behaviour for CH formation in samples with slightly larger traces of CH content in STA calculations.

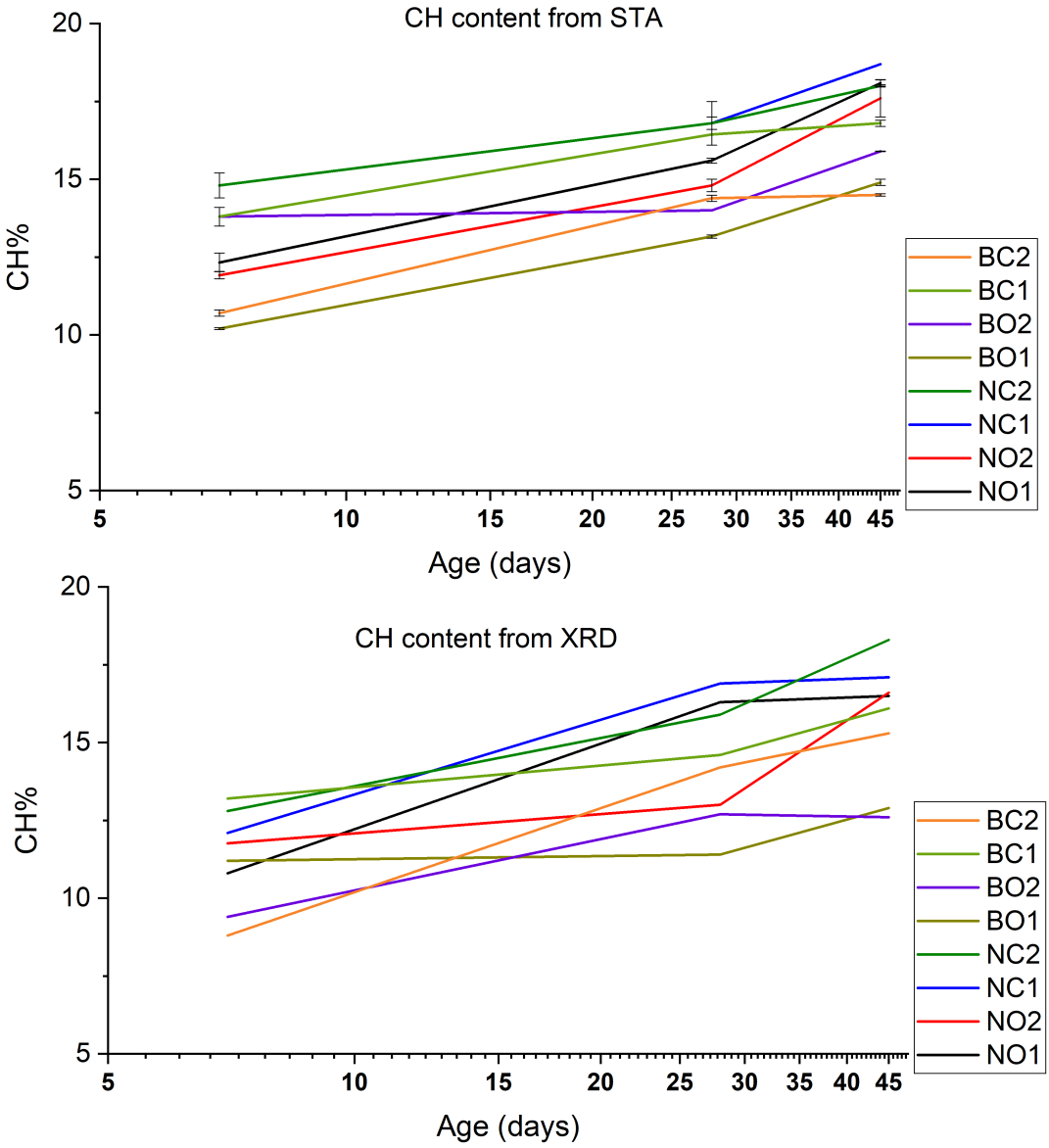

Figure 4-24 Calcium hydroxide content calculated from STA analysis and QXRD analysis, N (wPC), B (Bacteria), O (No calcium source), 1 (No superplasticizer), C (Calcium source), 2(Superplasticizer)*.

*Error bars represent the standard deviation for STA samples only. XRD test results were collected for one sample per type per age.

In general, the bacterial wPC paste samples resulted in lower CH content at all ages, whereas the absence of calcium ion source increase the consumption of CH as a calcium source and the addition of calcium nitrate would

help the early age CH formation but the decrease in porosity by ageing will again accelerate the calcium hydroxide consumption by bacteria. The bacterial samples with added calcium ion source showed a lower portlandite content compare to other samples at 45 days. This behaviour could be due to higher amounts of calcium carbonate precipitation inside and on the surface of the sample. The increase in calcium carbonate precipitation after 28 days resulting in lower porosity ratio which will then restrict the access to the available calcium and nutrient source available in the submersion medium[201]. As a result of restricted access to further calcium ion source and availability of the calcium hydroxide as soluble material inside the sample, bacteria would possibly use calcium hydroxide as secondary calcium source.

According to Chen et al. [202], biomineralization in cement-based materials can consume the available calcium hydroxide and it can be closely related to hydration process in absence of calcium ion source. The possibility of consumption of calcium hydroxide by bacteria has been discussed. Meanwhile, the direct relationship between the depth of targeted area with the consumption rate of calcium hydroxide and calcium carbonate precipitation in cement paste system have been proven by Chen et al. [202].

Figure 4-25 is representing the calculated calcium carbonate content form QXRD and STA techniques for all samples at 7, 28, and 45 days.

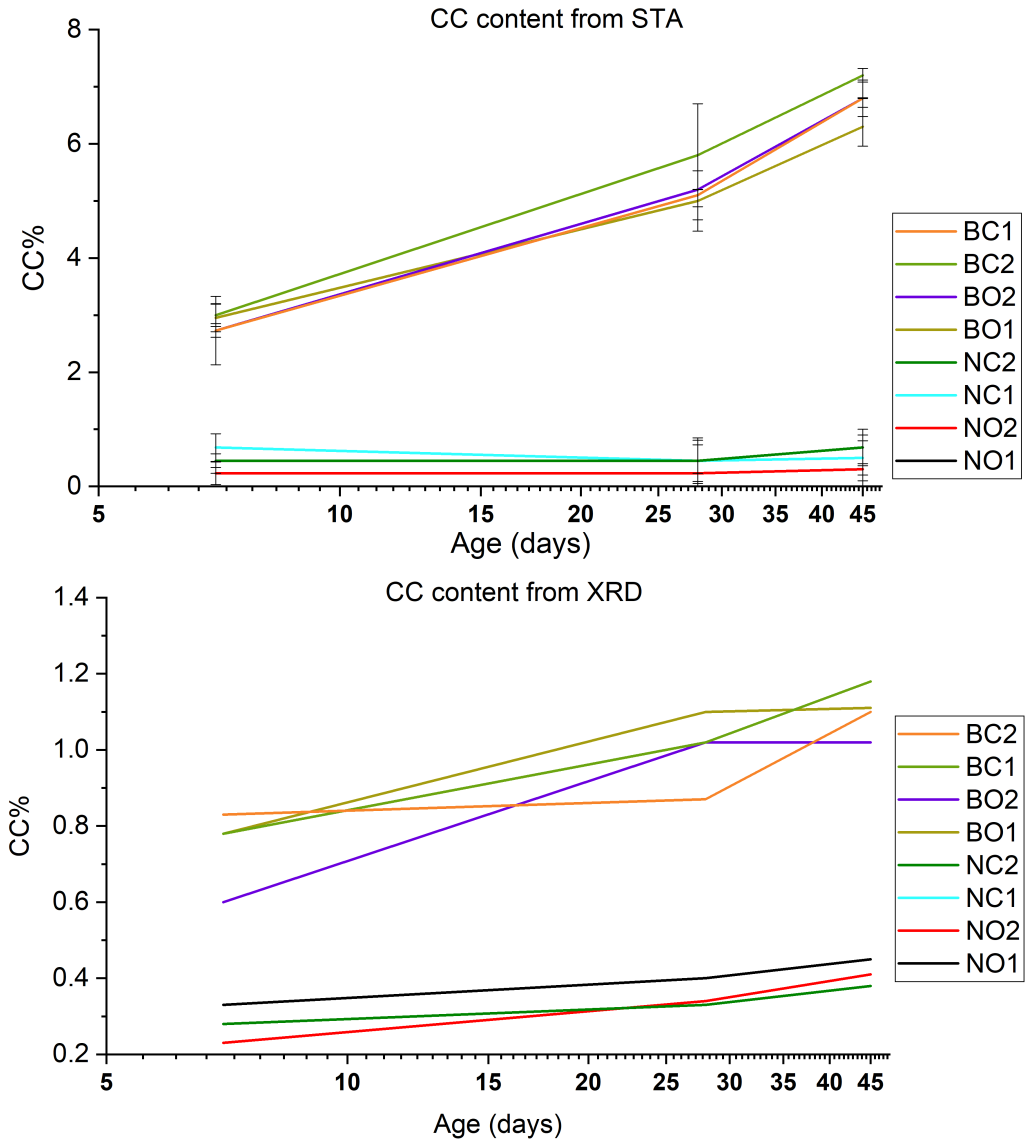

Figure 4-25 Calcium carbonate content calculated from STA analysis and QXRD analysis, N (wPC), B (Bacteria), O (No calcium source), 1 (No superplasticizer), C (Calcium source), 2(Superplasticizer)*.

*Error bars represent the standard deviation for STA samples only. XRD test results were collected for one sample per type per age

According to the results from STA technique, the calcium carbonate content of samples showed a significant increase for bacterial samples at different ages compared to reference samples. This increase was more

pronounced up to 28 days and at 45 days the $CaCO_3$ showed a slight change which can be explained by the lack of sufficient nutrition for bacteria. However, another factor affecting the slow rate of calcium carbonate increase at 45 days could be the nature of the cement paste sample having less porosity and restricted access to submersion media nutrient.

As it can be interpreted from the collected data, superplasticizer addition into the mix favours the formation of more calcium carbonate. Previously the effect of superplasticizer has been proven to favour the calcite formation in biomineralization in cement-based materials, However, in some cases, the addition of superplasticizer experienced a slight drop in the percentage of available $CaCO_3$[118]. Addition of the calcium ion source (Calcium nitrate in this study) is another reason for the increase in $CaCO_3$ percentage especially at 28 days age samples.

With the comparison of the QXRD data, it is obvious that the calcium carbonate content calculated through quantitative XRD analysis is showing far less difference between wPC paste and bacterial wPC paste.

This difference in calcium carbonate content from thermal analysis and QXRD techniques is an indication of the poor crystallinity of the calcium carbonate in bacterial samples.

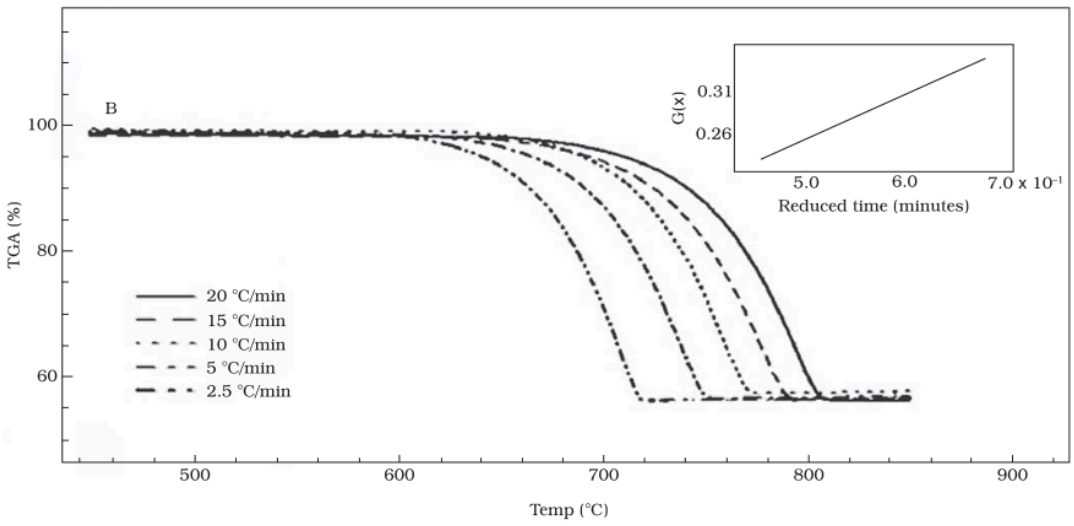

Figure 4-26 TG curve of industrial calcium carbonate obtained at different heating rates[203]**.**

According to Murakami et al.[203], calcium carbonate indication drop in the TG curve in the thermal analysis could be affected by many factors. In Murakami's study, it has been shown that the stability of calcium carbonate at temperatures higher than 600 °C is directly related to the morphology of the crystal and the crystal size. The larger crystal size results in a differential thermogravimetry (DTG) peak at temperatures after 800 °C and the smaller crystal result in peaks around 700°C. Another factor affecting the position of the calcium carbonate peak is the heating steps (Figure 4-26) in thermal analysis and higher heating rates tend to shift the decomposition of calcium carbonate to higher temperatures.

According to Villain et al. [204] presence of a calcium carbonate DTG peaks after 800 °C can be interpreted as calcite crystals. Figure 4-27 shows the result of thermal analysis for a mortar sample.

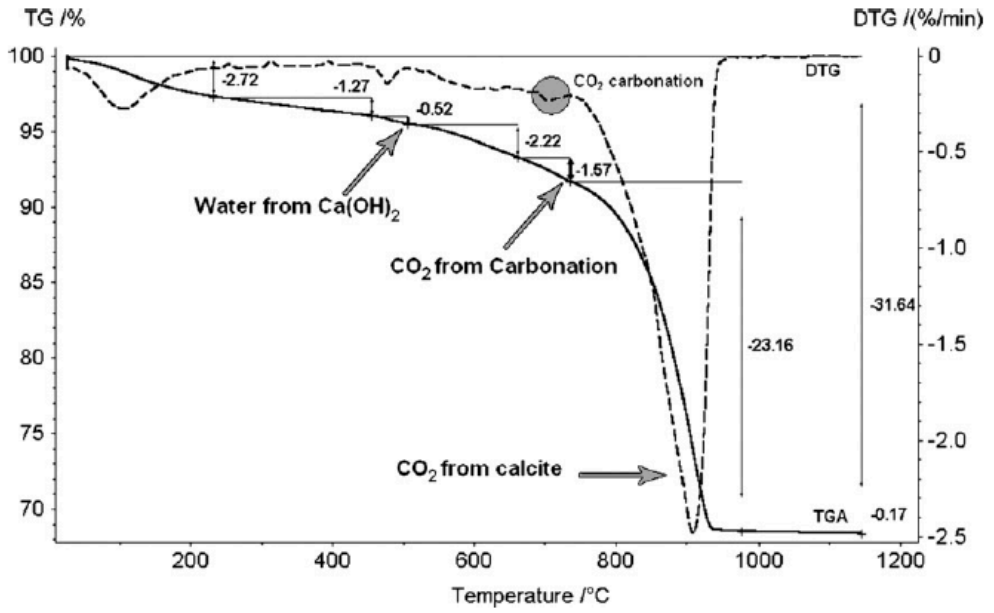

Figure 4-27 TG and DTG curve for Dissociation of a carbonated sample of crushed concrete mortar during a TGA test: concrete containing limestone aggregates[204]**.**

As shown in this TG/DTG graph in Figure 4-27, the calcium carbonate DTG peak for carbonation in the mortar sample is present at 730°C and the sharp DTG peak for calcite from aggregates is at a temperature of 900 °C.

According to Rodha et. al. [205], amorphous calcium carbonate produced through biomineralization is a metastable phase. This amorphous calcium carbonate transforms into a less hydrated phase by ageing and heating and over time the dehydrated amorphous calcium carbonate crystallizes to calcite or aragonite. The transformation and crystallization of amorphous calcium carbonate have been widely studied using differential scanning calorimetry [205]–[208].

Koga et. al [208] has investigated the crystallization of amorphous calcium carbonate due to heating and the DSC work in this study showed 2 separate

steps of calcium carbonate crystallization at 320 °C and 700 °C which is also observed in biogenic calcium carbonate studies. These two crystallization steps observed through exothermic peaks in DSC result have also been investigated by other researchers [205]. It has also been mentioned that the low water content in the biogenic amorphous calcium carbonate (0.25 mol of water) could be considered anhydrous and is a transient phase which can easily crystallize into calcite. This crystallization enthalpy measured for amorphous calcium carbonate has been proven to be similar to that seen in DSC measurement around 320 °C for dehydrated amorphous calcium carbonate.

Considering the DSC results for both bacterial and neat wPC paste at different ages presented in section 5.3, the presence of 2 peaks at around 300 °C and 700 °C might be an indication of crystallization of the amorphous calcium carbonate during TG heating. This would help with the explanation of second calcium carbonate decomposition seen in STA result after 800 °C.

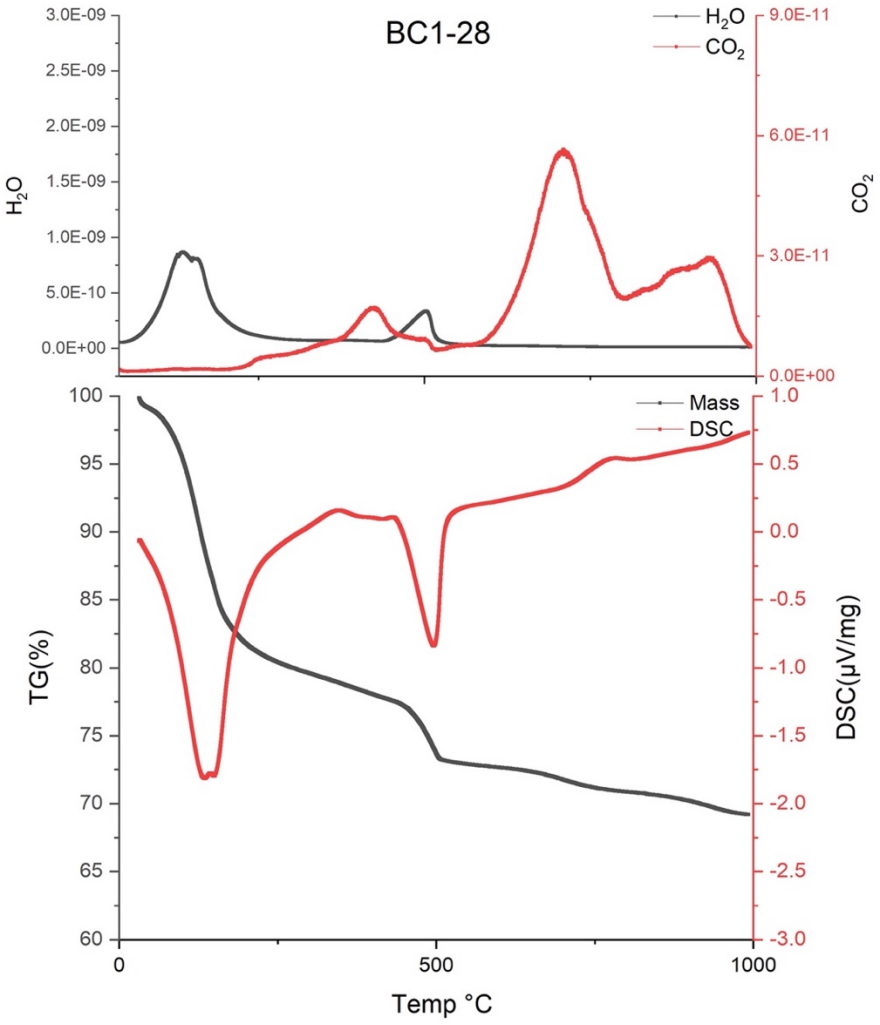

Figure 4-28 STA and gas emission results for BC1-28, Bacterial sample with added calcium source at 28 days.

Figure 4-28 is a representative STA and gas emission analysis for bacterial samples. Sample BC1-28 is the bacterial wPC paste with added calcium carbonate source cured for 28 days and then grinded (without hydration stopping) for thermal analysis.

The gas emission for thermal analysis was recorded for H_2O and CO_2 emission. The CO_2 emission showed separate peaks at 700 °C and 900 °C. From the literature it can be proven that both these peaks are related to calcium

carbonate decomposition[204]. It is also viable that the temperature differences for these two peaks is an indication of the calcium carbonate morphology, crystal structure and stability. Hence, the smaller peak before 900 °C could be marked as a more stable crystal of calcium carbonate known as calcite and earlier peak at 700 °C indicates a less stable and possibly amorphous calcium carbonate.

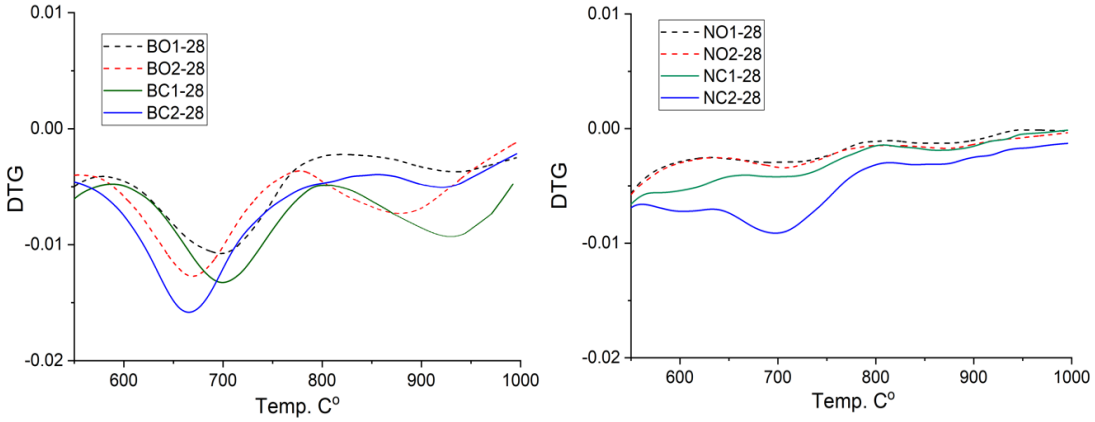

Figure 4-29 DTG curves for bacterial and neat wPC paste after 28 days of curing and tested with thermal analysis to up to 1000°C, N (wPC), B (Bacteria), O (No calcium source), 1 (No superplasticizer), C (Calcium source), 2(Superplasticizer).

Figure 4-31 is showing the thermal analysis results for bacterial and neat wPC pastes at 28 day age. The differential TG curves for bacterial samples showed 2 separate peaks before 700 °C and after 900 °C, whereas the neat wPC samples showed smaller traces of these peaks and specifically the peak around 700 °C. The differences of DTG curve between bacterial and neat wPC paste is a result of bacterial biomineralization calcium carbonate precipitation after 28 days.

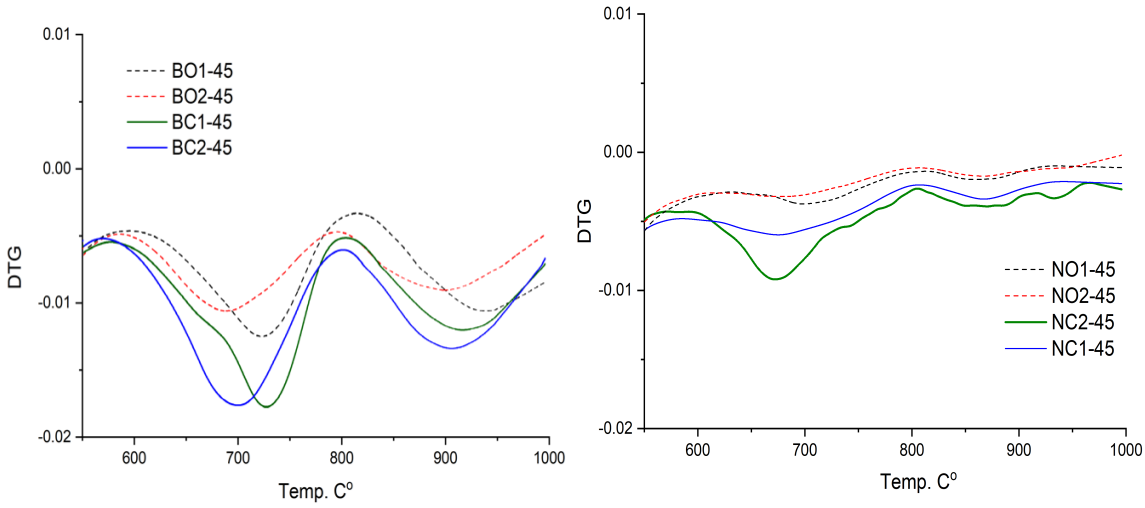

Figure 4-30 DTG curves for bacterial and neat wPC paste after 45 days of curing and tested with thermal analysis to up to 1000°C, N (wPC), B (Bacteria), O (No calcium source), 1 (No superplasticizer), C (Calcium source), 2(Superplasticizer).

Figure 4-30 shows the thermal analysis results for bacterial and neat wPC pastes at 45 day age. At 45 days we can observe more pronounced differences in calcium carbonate content between bacterial and neat wPC paste. Furthermore, the samples containing calcium ion source (added during the sample mixes) showed higher amounts of calcium carbonate at both 700 and 900 °C. This behaviour in bacterial samples was also been observed in the literature, where the addition of the calcium ion source into bacterial culture results in a higher amount of calcium carbonate precipitations[190]. The same behaviour can also be observed in 28 days aged samples.

Further analysis of calcium carbonate decomposition has been done by focusing on DTG curves for bacterial samples at 600 °C – 1000 °C. The DTG curves were used to evaluate separate peaks at around 700 °Cand 900 °C by curve fitting and area calculation by Gaussian method. Figure 4-31 is an

example of the fitted curves and Table 5-5 is representing the comparison of these different peaks in DTG curves.

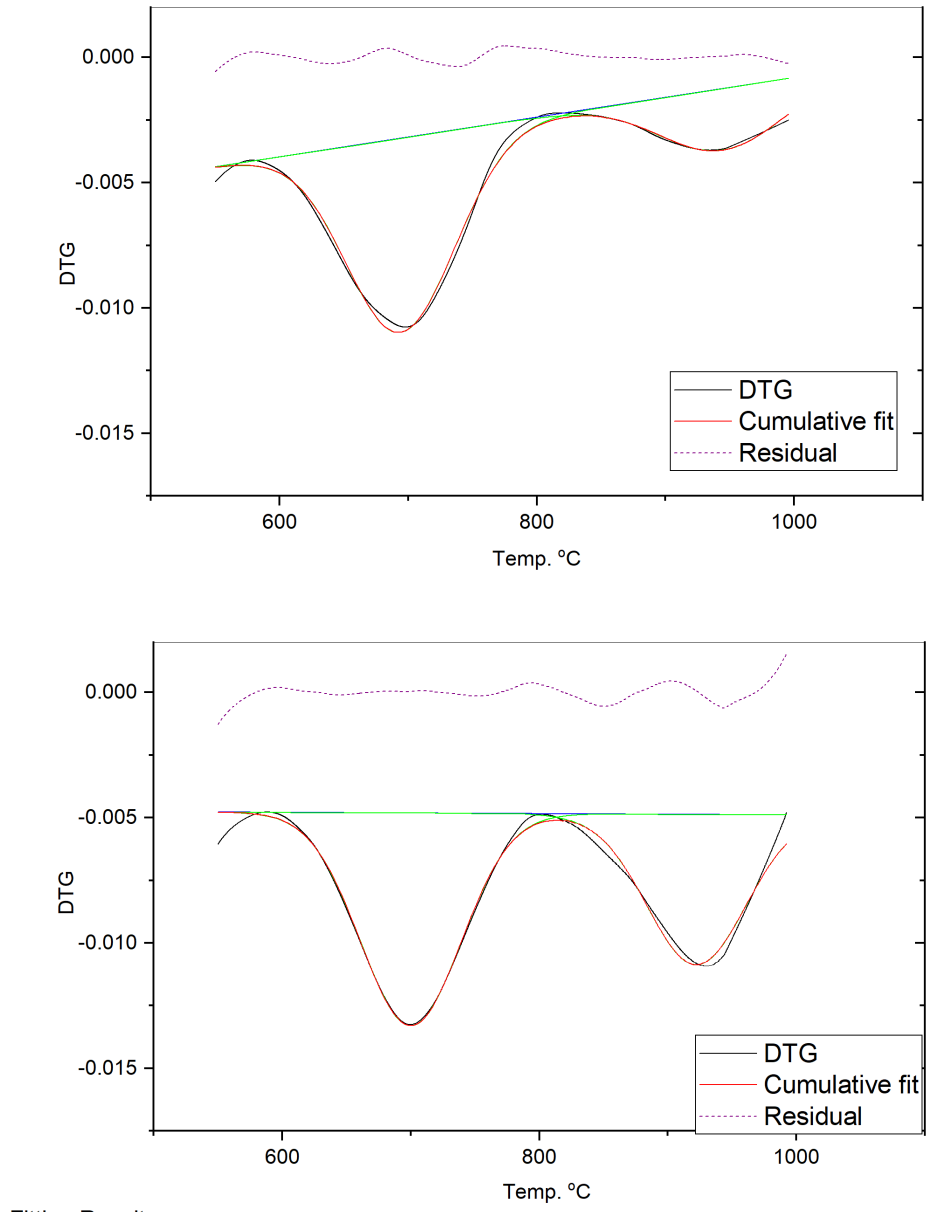

Figure 4-31 DTG curve analysis and curve fitting for BO1 (Top), BC1 (Bottom) at 28 days.

The aim of DTG curve fitting and area calculation was to investigate the ratio of poor crystalline calcium carbonate with well structured calcite content of each sample. For this purpose, the percentage of area under the curve for each

peak in each sample from DTG curve concerning calcium carbonate decomposition for bacterial samples at 28 and 45 days is available in Table 5-5. As discussed previously in this section, the temperature that calcium carbonate decomposes is a well established evaluation for crystallinity and its structure. The curve fitting figures for all the samples at 28 and 45 days ranging from 600 °C to 1000 °C is presented in Appendix F.

Table 4-5 Percentage of area under the curve for each peak for DTG curve fitting analysis for calcium carbonate decomposition in each sample.

Peak at	Age	BO1	BO2	BC1	BC2
~700 °C	28	76.2%	57%	56%	79.6%
	45	57.6%	47.3%	56.4%	54.2%
~900 °C	28	23.8%	43%	44%	21.4%
	45	42.4%	52.7%	43.6%	45.6%

As presented in the Table 5-5, Calculation was carried out to achieve a ratio between the initial peak at around 700 °C and second phase at around 900 °C for bacterial samples. All the samples apart from BC at 28 days showed an increase in the percentage of the second decomposition peak area by addition of superplasticizer and promoting the calcite formation [118]. Another point of interest was related to ratio changes in regards with ageing process, where in all the samples at 45 days showed an increase in the ratio of the area under the

second peak at ~ 900 °C. The age related change was in line with the literature and agreed with the increase of the crystallinity in ACC structure over time.

The overall trend of calcium carbonate content in bacterial and wPC paste samples calculated from STA and QXRD, resulted in the difference in the calcium carbonate content of bacterial samples compared to neat samples. As mentioned earlier, the calcium carbonate quantities measured by STA analysis are much higher than the QXRD measurements. This is another indication of the presence of poorly crystalline or amorphous calcium carbonate in the bacterial wPC paste.

According to Basaran et al.[118], the presence of superplasticizer and calcium ion source in bacterial culture leads to calcite precipitation. In their study, the direct addition of the superplasticizer and calcium ion source to the bacterial culture (17 hours incubated *S.pasteruii* in the nutrient medium) resulted in the calcite precipitation. However, from the discussion provided in this section, it can be concluded that the presence of calcite crystals is far less than in other studies with bacterial cement paste. This can be due to the low porosity ratio in white Portland cement paste compared to mortar samples used in Basaran et al. [118] study.

The low porosity ratio in our bacterial wPC paste can lead to volume restriction to form calcite crystals by bacteria. Also, the access to the nutrient solution used to submerge samples can be limited in a less porous paste.

Another possible explanation for changes in thermogravimetry graphs at higher temperatures at 810°C has been given by Skevi et.al. [31] where they have incorporated dead and live bacteria cells into the mix. Based on their findings, the compressive strength of the samples were observed to increase for

both samples containing dead or alive cell. Based on this work, the changes in TGA graphs after 810°C are related to the decomposition of C-S-H to wollastonite and is assumed to be an increase in the amount of C-S-H for samples that contained bacteria cell regardless of their viability. They have also observed an increase in all other hydration product when bacteria cells were incorporated and showed a higher degree of hydration. Skevi et.al. [31] has concluded that the impact of bacterial cell on hydration product is a more complex interaction and depends on many factors such as type and amount of bacteria, type of the cement clinker and its fineness, and amount of water.

4.6.3 FTIR analysis

Figure 4-32 is showing the FTIR results for samples collected from the gaps introduced on bacterial wPC paste specimens after 45 days. The collected samples tested with FTIR technique showed some sharp peaks.

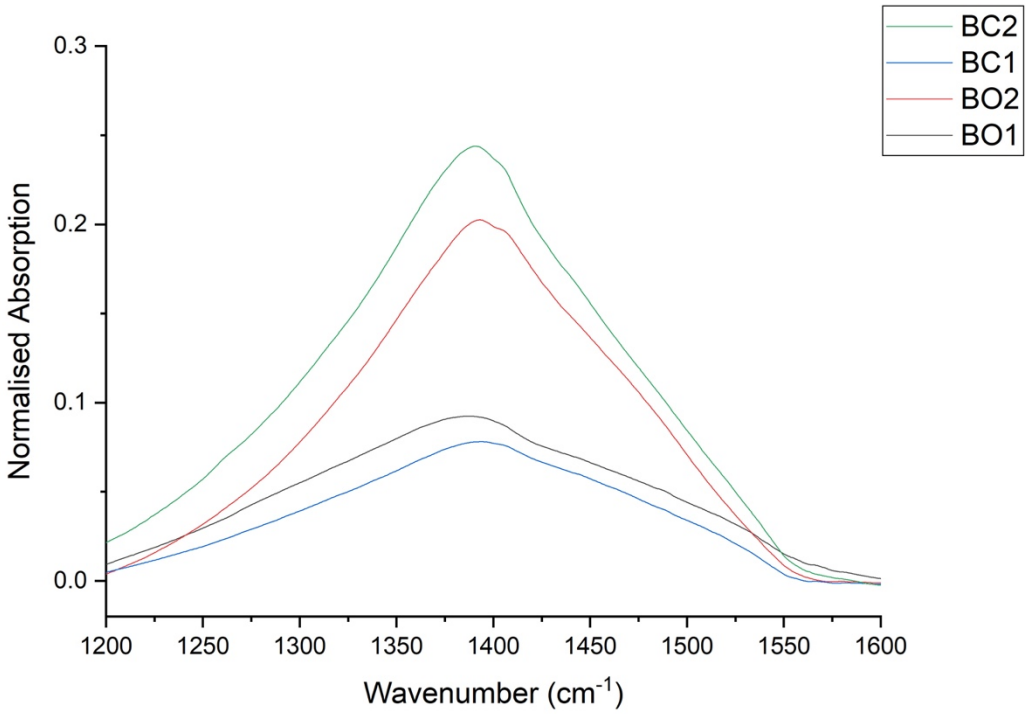

Figure 4-32 FTIR analysis of the collected precipitation inside the gap on bacterial wPC paste specimens, B (Bacteria), O (No calcium source), 1 (No superplasticizer), C (Calcium source), 2(Superplasticizer).

The figure represented here is focused on the peaks present at 1390 cm^{-1}. According to Wiktor et al. [23], because of different crystal structures related to calcium carbonate and their morphology, they can be discriminated by using FT-IR technique. The major vibration band for calcite is identified in Figure 4-32: C-O stretching vibration. This vibration peak is centred at 1390 cm^{-1}.

Considering the FT-IR analysis for 4 different bacterial wPC paste, it is apparent that the precipitation by bacteria should result in large amounts of calcite. However, comparison of the FT-IR, STA and QXRD data indicates the lack of calcite content inside the bacterial samples must have been prevented by another factor.

All the materials and bacteria used for preparation of the samples were kept constant. Samples were cured in the same environment and conditions. The pH value of the nutrient media solution used for submerging the samples was controlled. Considering all these factors and consistency of the environmental factors, the only possible explanation can related to the provided gap volume differences in samples.

The samples prepared for FTIR analysis were altered by cutting a small gapped area on samples and the precipitations collected in these gaps were used for FTIR analysis. However, the samples used for STA and XRD analysis were collected from the broken samples with no cracks or artificially made gaps. It can be argued that the smaller sized pores inside the wPC paste samples were also restricting the required space for *S.pasteruii* strains to produce a well structured calcium carbonate formations.

4.7 ^{27}Al and ^{29}Si MNR

^{27}Al NMR can be used when aluminium is incorporated in the calcium sulfoaluminate phases or as a guest ion in C-S-H which produces resonance for octahedral AFt and AFm and tetrahedral C-S-H locations. Peaks at ≈9ppm and ≈13ppm indicate the presence of Al in AFm phases and Aft phases respectively.

Figure 4-33 and Figure 4-34 represent ^{27}Al NMR spectrum for 28 days and 45 days old samples respectively. The only difference in the spectrums for both 28 and 45 days samples was the smaller peak at 9ppm for samples containing bacteria with no addition of calcium nitrate. The smaller peak at 9ppm indicated less amount of AFm in these samples. As discussed in section 2.5, according to Jones et al.[87], the AFm family have a layered structure and the basic foundation unit is $[Ca_4Al_2(OH)_{12}]^{2+}$. The number of interlayers balancing anions are affected by the size and polarization of these anions and control the interlayer water contents and directly control the layer stacking sequence.

It could be argued that the addition of bacteria with no calcium source results in prevention of AFt transition into AFm. This can be due to decomposition of the calcium hydroxide and consequently the changes in the available anions in the interlayer water and pH.

Also depending on the nature of AFt and AFm in these samples, if the phases were carbon baring structures, it might be possible that the initiated biomineralization in absence of calcium nitrate favoured the MICP and preventing the AFm formation due to decreased amount of carbonate ions.

Another explanation can be derived due to the presence of calcium nitrate in the samples showing higher AFm phases. According to Balonis et al. [88], presence of nitrate ions in the mixture will result in formation of nitrate baring AFm (NO_3-AFm). Hence the only drop in the AFm content is when there is no addition of calcium nitrate.

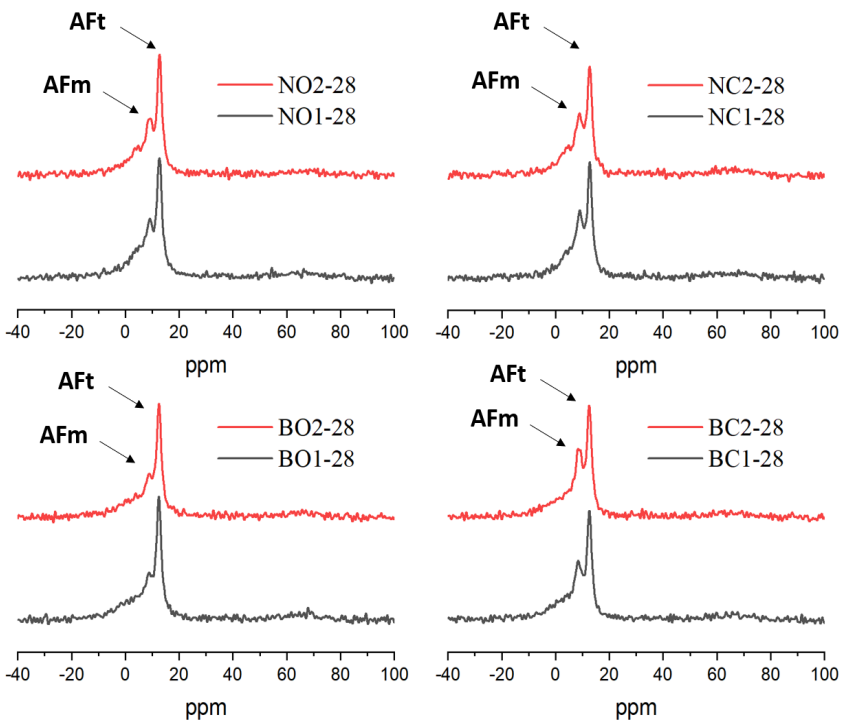

Figure 4-33 ^{27}Al NMR spectra of 28days samples. N (Neat), C(Calcium nitrate), B (Bacteria), O (No calcium addition), 1(No additive), 2(Superplasticizer).

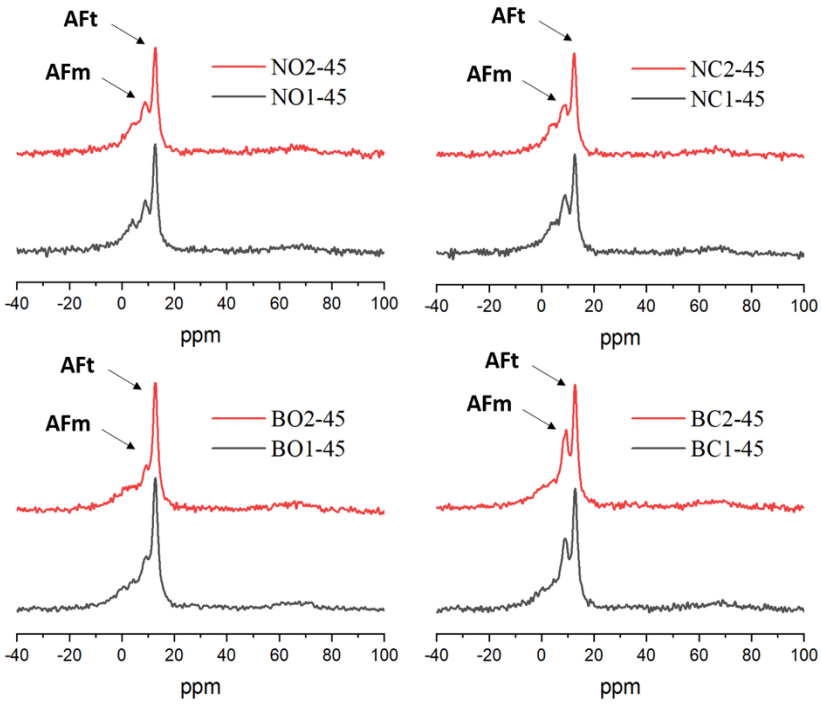

Figure 4-34 ^{27}Al NMR spectra of 45days samples. N (Neat), C(Calciumnitrate), B(Bacteria), O (No calcium addition), 1(No additive), 2(Superplasticizer).

Moreover, it has been observed that with addition of 5-10% calcium nitrate in calcium aluminate cements, NO_3-AFm is dominating phase at 28 days [89]. In the presence of calcium nitrate, NO_3-AFm and NO_3-Aft are more preferred.

Further evaluation of AFt phases present in the samples at 7, 28 and 45 days has been done by QXRD analysis and presented in Figure 4-35. The amount of AFt and its evolution in all the samples followed a similar trend where there was a negligible change from 7 days to 45 days. However, the amount of AFt in BC2 and BC1 samples (Bacterial wPC with addition of calcium ion source) was lower than of that in the other samples at all different ages. This was also in agreement with ^{27}Al NMR results as the bacterial samples with added calcium source showed a higher AFm content that can be the result of AFt transition to AFm.

The presence of calcium nitrate in samples can also affect the AFm formation and result in nitrate AFm crystallisation in which the water content of the nitrate-AFm is very dependent on environmental conditions such as humidity[88]. The presence of nitrite and nitrates can displace the sulfate, hydroxide and carbonates from AFM structure (see section 2.5).

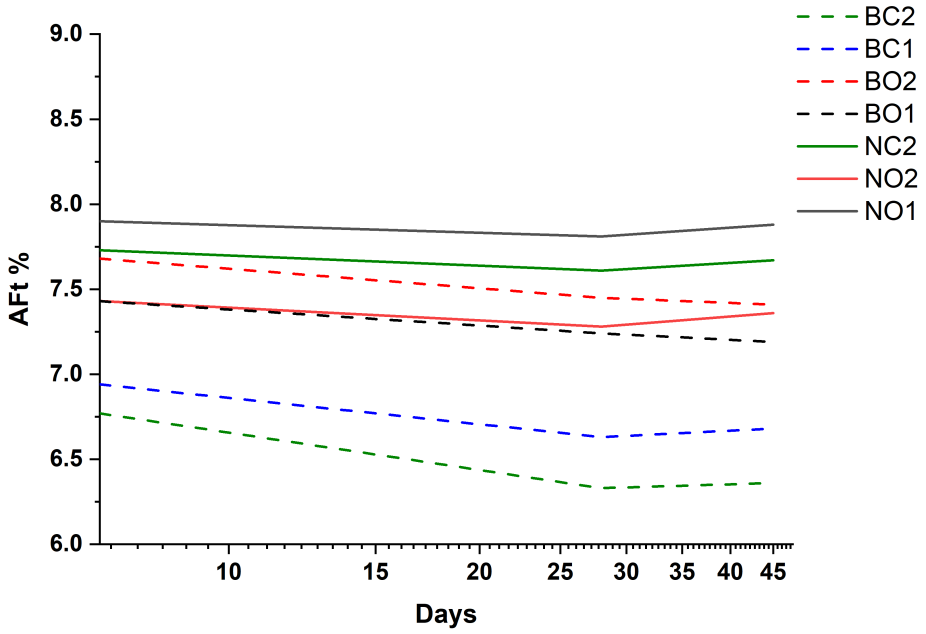

Figure 4-35 AFt% calculated for all samples from quantitative XRD analysis, N (wPC), B (Bacteria), O (No calcium source), 1 (No superplasticizer), C (Calcium source), 2(Superplasticizer).

^{29}Si NMR technique is used for comprehensive understanding of the silicate anion structure and the coordination of aluminium in C-S-H. After the deconvolution of the spectrum for each sample, the Al/Si ratio was calculated using this equation:

$$\frac{Al}{Si} = \frac{\frac{1}{2}Q^2(1Al)}{Q^1 + Q^2 + Q^2(1Al)}$$

Considering the equation above , increase and decrease in the Al/Si value could be directly to the value of the Q^2(1Al) peak.

Figure 4-36 and Figure 4-37 are presenting the Al/Si ratio calculated from ^{29}Si NMR for bacterial wPC and neat wPC paste samples at three different ages of 7, 28 and 45 days.

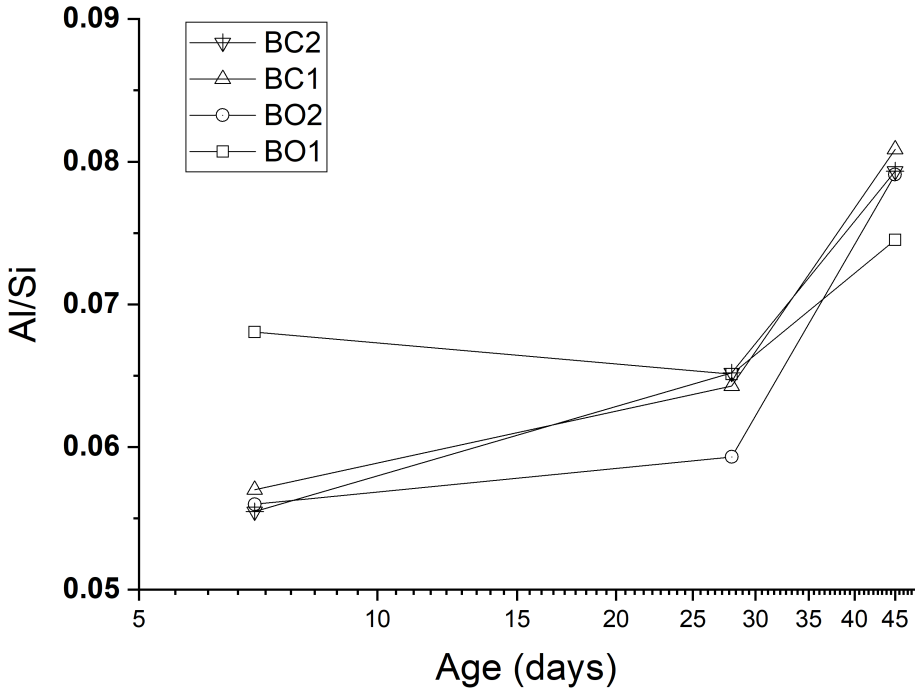

Figure 4-36 Al/Si ratio for bacterial samples at 7, 28 and 45 days, calculated from NMR deconvolution, B (Bacteria), O (No calcium source), 1 (No superplasticizer), C (Calcium source), 2(Superplasticizer).

Increasing the polymerization of silicate tetrahedra will result in up field chemical shifts in ^{29}Si NMR spectrum [209]. According to previous studies [209]–[211] Q^2 tetrahedra has a up field moving chemical shift compared to Q^1 groups (≈ -79 ppm) in NMR spectra by 6 ppm. The characteristics of chemical environments surrounding silicate tetrahedra could be affected by the displacement of Si atoms by Al at bridging positions in the aluminosilicate chain and will initiate a down field chemical shift of ≈ 3-5 ppm [45]. Hence, Q^2(1Al) has been assigned to the peak at ≈ -82 ppm in ^{29}Si MAS NMR spectra throughout relative studies[212], [213].

Comparing the Al/Si ratio of bacterial and neat wPC paste over 45 days, showed a similar trend in the changes of the Al/Si values ranging from 0.06 to 0.8 and the stability of the Q^2(1Al) in the samples. However, considering that there were no additional aluminium in the samples, it should be noted that bacterial samples have lower starting point with a value around 0.06.

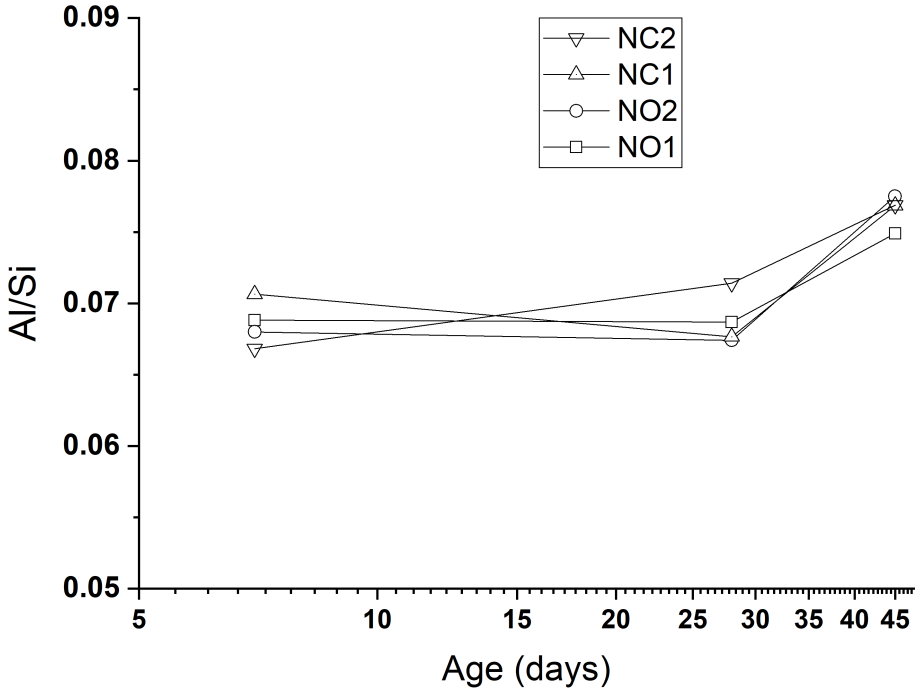

Figure 4-37 Al/Si ratio for neat samples at 7, 28 and 45 days, calculated from NMR deconvolution, N (wPC), O (No calcium source), 1 (No superplasticizer), C (Calcium source), 2(Superplasticizer).

The lower value of the Al/Si ratio for bacterial samples at only 7 days is a result of less substitution of the bridging tetrahedra with aluminium in the chain. Lower Al/Si ratio at 7 and 28 days was observed for bacterial pastes. Once again it was observed that the addition of the bacteria and calcium ion source had a small effect on positioning of the aluminium in silicate chain. This could also be linked with the changes in pH value of bacterial samples and addition of the

calcium ion source and the consumption of the carbonate anion in the system by bacteria. According to Hopital et. al.[214], increase in the alkalinity, increases the aluminium uptake in C-S-H which is in agreement with 45 day samples where the most carbonate content consumption were achieved.

According to the literature [143], the mean chain length (MCL) increases with the degree of hydration and it has been observed that the MCL value could range between 2-5 for early age samples up to 5 years. The amount of silicate species in C-S-H varies as a result of hydration. In C_3S, the isolated silicate tetrahedra are converted to disilicate ions, and with time, a higher degree of polymerization occurs. Rather than sheets or 3D networks, polymerization occurs in chains. As there is no Q^3 in the samples, the MCL value is related to Q^2/Q^1 and $Q^2(1Al)/Q^1$ ratios of the samples and these ratios could be used as an indication of reaction in terms of MCL.

Furthermore, the increase in the MCL value is also an indication of the stability of C-S-H chains[137], it has been observed that addition of 6% nanosilica increases the C-S-H stability and MCL in calcium leaching experiments [215].

The main chain length of all bacterial and neat wPC paste are given in Figure 4-38 and Figure 4-39 at 3 different ages of 7, 28 and 45 days. All the values have been calculated after the NMR spectrum deconvolution using the equation:

$$MCL = 2\left(1 + \frac{Q^2}{Q^1} + \frac{3Q^2(1Al)}{2Q^1}\right)$$

The MCL value for bacterial samples changed from 3 at 7 days to 3.4 at 28 days and 3.6 at 45 days and indicated polymerization of initial dimer units. As for neat wPC past, the MCL started at around 3.2 at 7 days and changed to 3.6 at 28 days and 3.8 at 45 days. The higher MCL value for neat samples compared to bacterial wPC paste can be interpreted as higher volumes of Al substitution and/or polymerization.

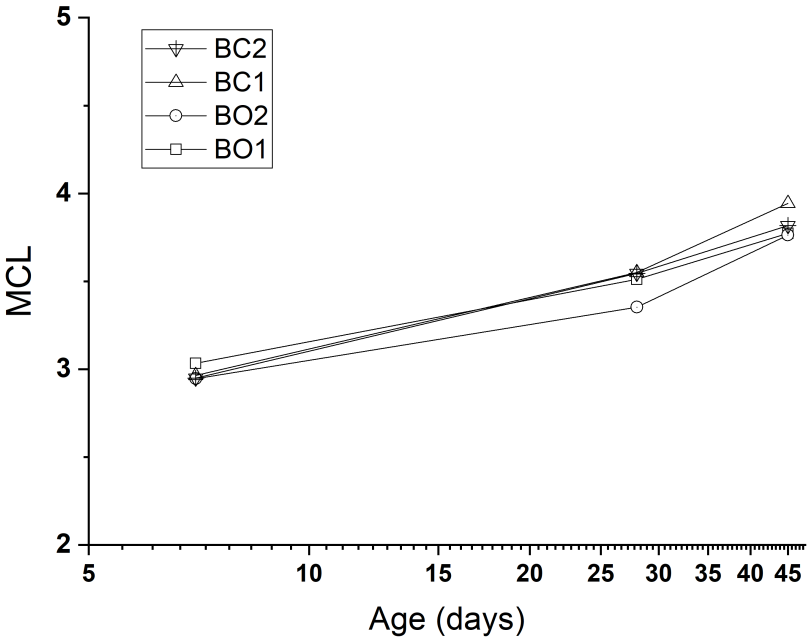

Figure 4-38 Main chain length (MCL) for bacterial samples at 7, 28 and 45 days, calculated from NMR deconvolution, B (Bacteria), O (No calcium source), 1 (No superplasticizer), C (Calcium source), 2(Superplasticizer).

The comparison of the MCL for all systems showed a similarity between bacterial and neat wPC paste at different ages. The MCL values for both bacterial wPC and neat wPC at 7, 28 and 45 days ranged from 3 at 7 days to 4 at 45 days after hydration. This was also in agreement with the literature on the increase of MCL value by ageing and further hydration of the cement phases.

Another means to evaluate the hydration rate and effect of ageing is related to the consumption of alite and blite. The amount of alite and blite was calculated by ^{29}Si NMR and QXRD. The peak related to monomers at ≈ -71.3 ppm in NMR deconvolutions corresponding to Q^0 was calculated for all samples. Isolated tetrahedra available in alite and blite produces this resonance in ^{29}Si NMR spectrum (Q^0). Figure 4-40 is showing the total of Q^0 and γ-C_2S for all the samples at 7, 28 and 45 days.

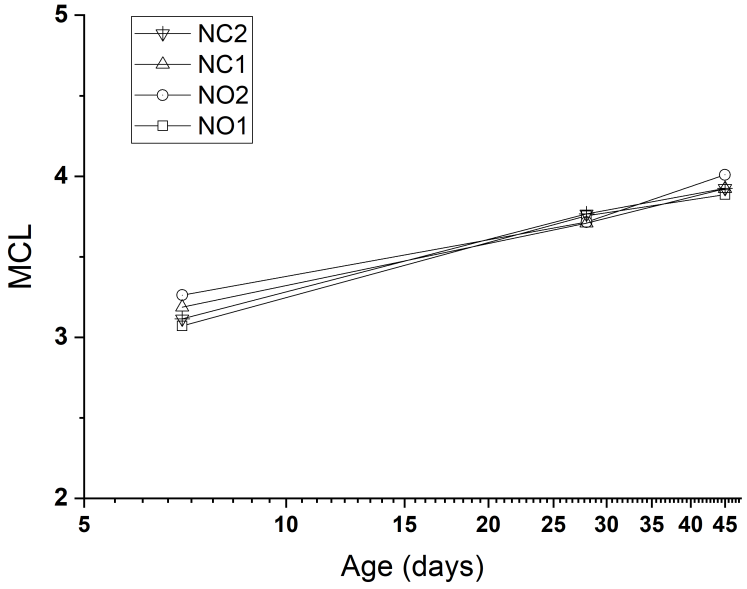

Figure 4-39 Main chain length (MCL) for neat samples at 7, 28 and 45 days, calculated from NMR deconvolution, N (wPC), O (No calcium source), 1 (No superplasticizer), C (Calcium source), 2(Superplasticizer).

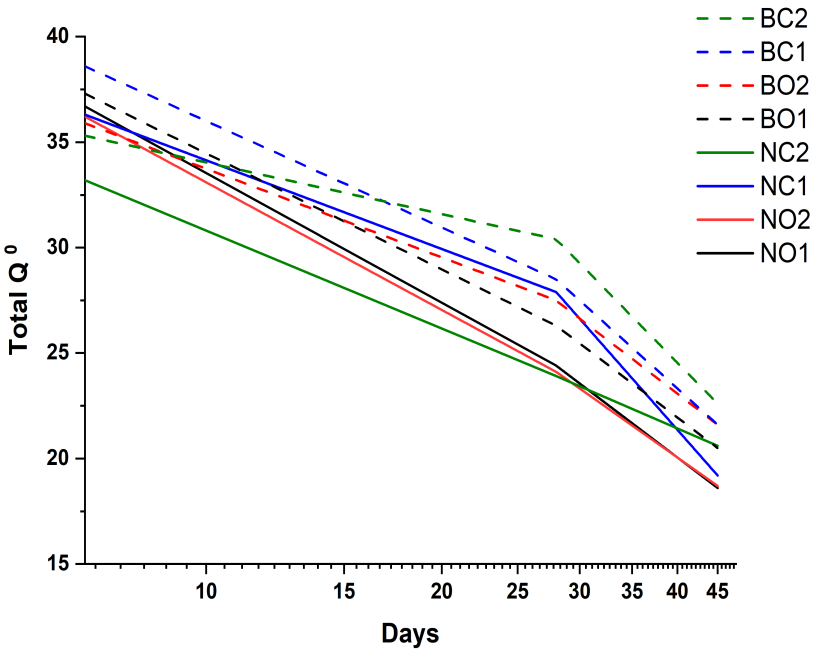

Figure 4-40 Total Q^0 + γ-C_2S percentage for bacterial and neat wPC at 7, 28 and 45 days calculated from ^{29}Si NMR deconvolutions, N (wPC), B (Bacteria), O (No calcium source), 1 (No superplasticizer), C (Calcium source), 2(Superplasticizer).

The deconvolution of NMR spectrum aims to obtain total integrals for the Q species instead of investigating the sites of each connectivity. The frequencies used for the deconvolution are not directly related to the structural meaning, but to evaluate the best fit for the total inclusion of each connectivity.

Lippmma et al. [216] has shown that at early hours of C_3S hydration, the main peaks present in ^{29}Si NMR spectra are related to monosilicate groups (Q^0) which range from -66.5 to 73.5 ppm. Only after 6 hours of hydration, the appearance of a new peak at -79 ppm was reported which is related to the end group Q^1 units ranging from -77.9 to -82.6 ppm. The comparison carried out in Lippmma et al. [216] work, showed that the hydrated products tend to have a broader signal and lower crystallinity.

The estimation of the monosilicate units (Q^0) and γ-C_2S in samples can also be used as an indication of the. hydration evolution by ageing as this value declines over time. The conversion of Q^0 species into other Q^n units and production of longer silica chains is in agreement with the MCL values calculated through ^{29}Si NMR for all samples.

The degree of hydration can be calculated through ^{29}Si NMR and QXRD analysis in which the determination of hydration degree is related to consumption level of alite and belite at any age. Subtraction of the remaining volume fraction of anhydrous materials at specific time from the initial volume before the hydration process starts [66], [217], [218].

$$\text{Degree of hydration } \% = \frac{Q^1+Q^2}{Q^0+Q^2+Q^3}$$

Where Q^n is silicate unit calculate from ^{29}Si NMR deconvolution.

$$Degree\ of\ hydration\ \% = \frac{V_{anhy.t_o} - V_{anhy.t_t}}{V_{anhy.t_o}}$$

Where $V_{anhy.}\ t_n$ is volume fraction of anhydrous material at time n (prior to hydration n = 0)

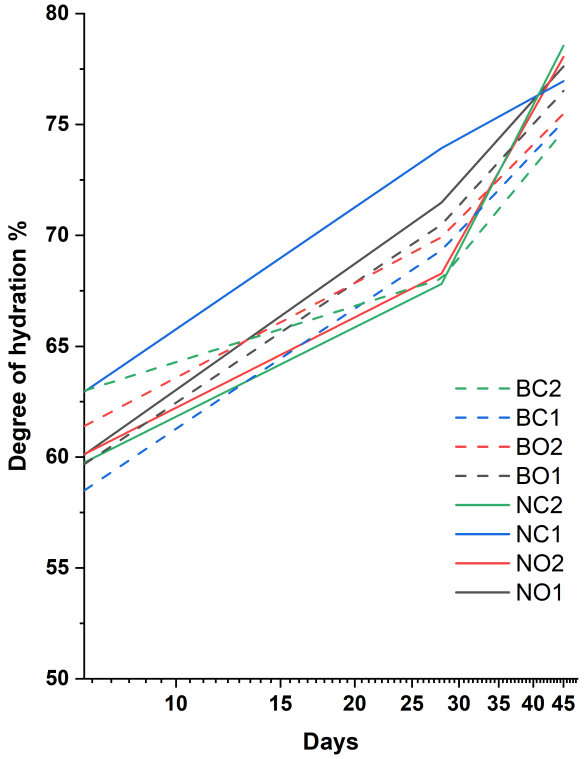

Figure 4-41 DoH calculated from ^{29}Si NMR deconvolution for all samples at 7, 28 and 45 days, N (wPC), B (Bacteria), O (No calcium source), 1 (No superplasticizer), C (Calcium source), 2(Superplasticizer).

Figure 4-41 and Figure 4-42 are showing the degree of hydration calculated for alite and blite crystals available in all samples at 7, 28 and 45 days through ^{29}Si NMR and quantitative XRD respectively. The peaks related to alite and belite respectively at around 30 and 32 2θ were recognized and the available percentage of each crystal structure was calculated by Rietveld refinement method. The degree of hydration of alite and blite in regards with confirmed total present phases was calculated. Comparison of Figure 4-41and Figure 4-42 shows that the calculated consumption of anhydrous material from ^{29}Si NMR for bacterial and neat wPC paste at different ages is in agreement with degree of hydration estimated by QXRD.

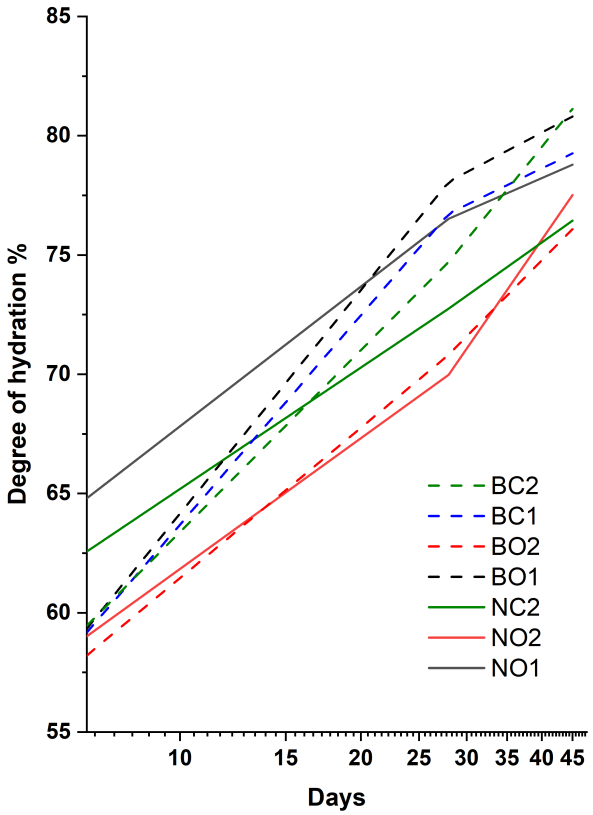

Figure 4-42 DoH calculated for all samples at 7, 28 and 45 days from quantitative XRD analysis, N (wPC), B (Bacteria), O (No calcium source), 1 (No superplasticizer), C (Calcium source), 2(Superplasticizer).

From the calculated degree of hydration for bacterial and neat samples, it can be concluded that the addition of bacterial culture acts as a retarder at an early age (7 days), especially when mixed with superplasticizer and this is in line with the isothermal calorimetry results and also the previous studies in the literature. After 45 days all the samples experience a similar DoH of around 75%.

Figure 4-43 to Figure 4-46 are representing the results from the deconvolution of the ^{29}Si NMR for all samples at 7, 28 and 45 days. The peaks related to each structural silicate formation were assigned to these results. These peaks included monomers (Q^0) at ≈ -71.3, dimers (Q^1) at ≈ -79.2, and middle chains at ≈ -81.5for Q^2(1Al) or ≈ -85.2 ppm for Q^2(0Al) [76], [219].

Additionally a small peak relating to monomers present in γ-C_2S was assigned in all samples and originated from raw wPC.

Moreover, another small peak was assigned to Q^{0H} at the chemical shift close to γ-C_2S and has been ignored due to its small value. For the deconvolution process, the line width and shape in all samples were relaxed to achieve the best fit for the total integral connectivity of each site. Furthermore, when there was an overlap between the frequencies of different units, the shape of the with was also relaxed for a better fit.

The Figures presented here, give the distribution of silicate units in different blends at 7-46 days after hydration. The data for each Q^n(mAl) are normalized to 100% and indicate the silicate unit changes more

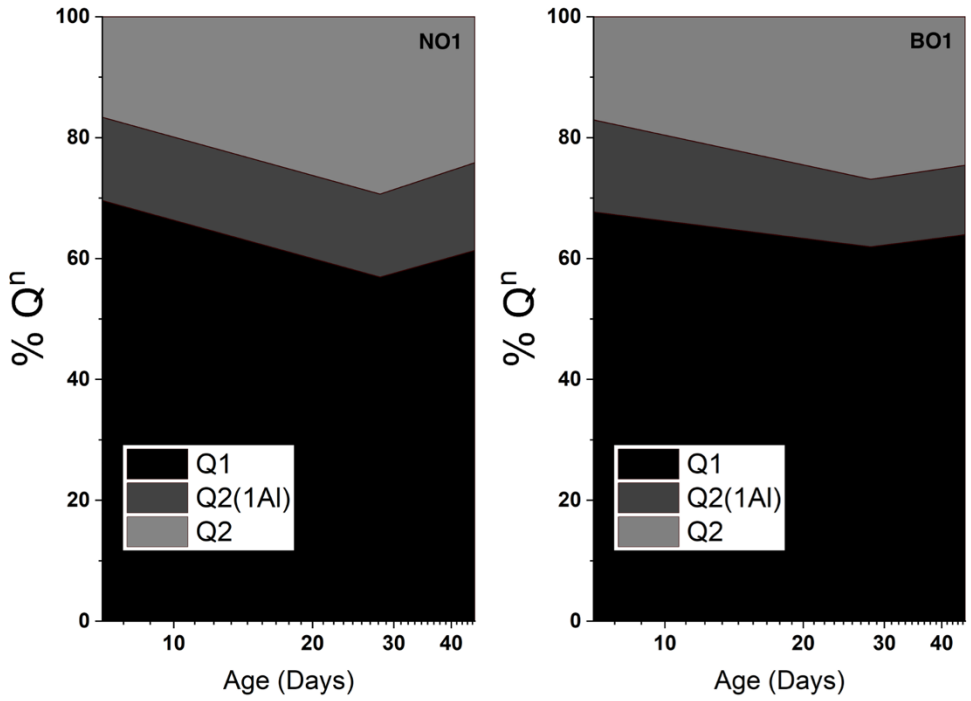

Figure 4-43 %Q^n quantities calculated from NMR spectrum at 7, 28 and 45 days for neat cement paste (left) and bacterial cement paste (Right).

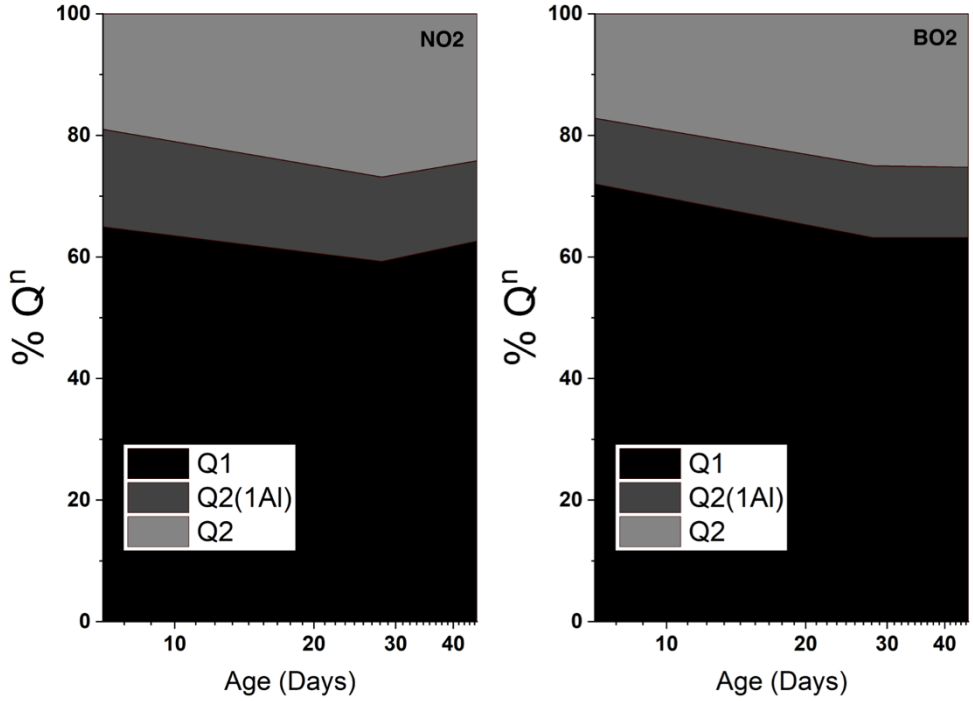

Figure 4-44 %Q^n quantities calculated from NMR spectrum at 7, 28 and 45 days for neat cement paste with superplasticizer (left) and bacterial cement paste with superplasticizer (Right).

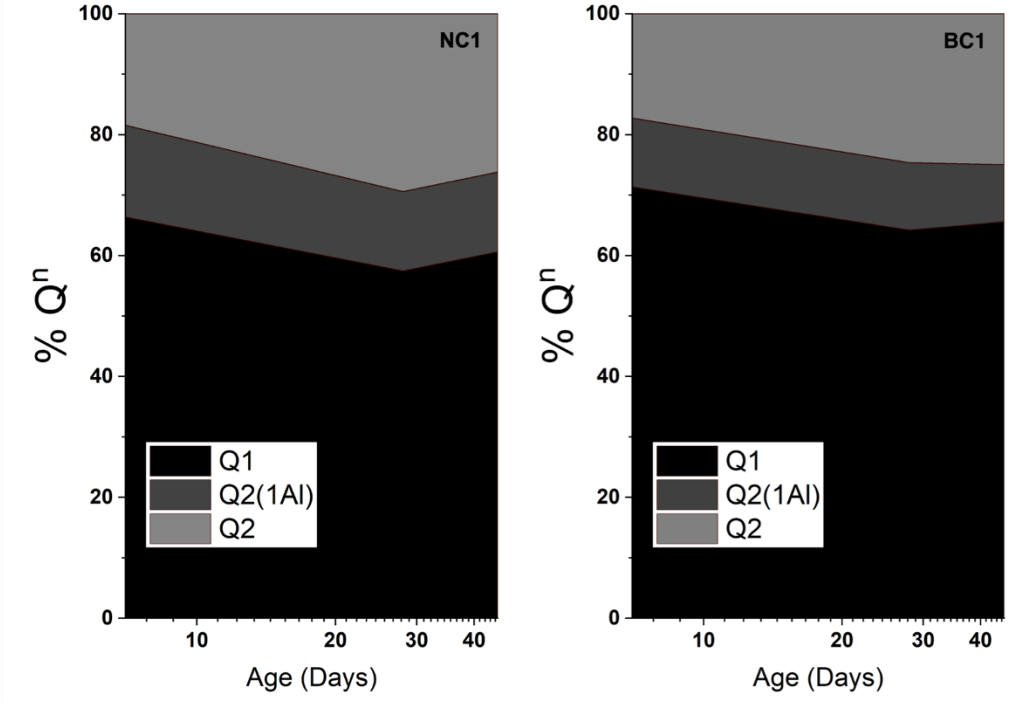

Figure 4-45 %Q^n quantities calculated from NMR spectrum at 7, 28 and 45 days for neat cement paste with calcium ion source (left) and bacterial cement paste with calcium ion source (Right).

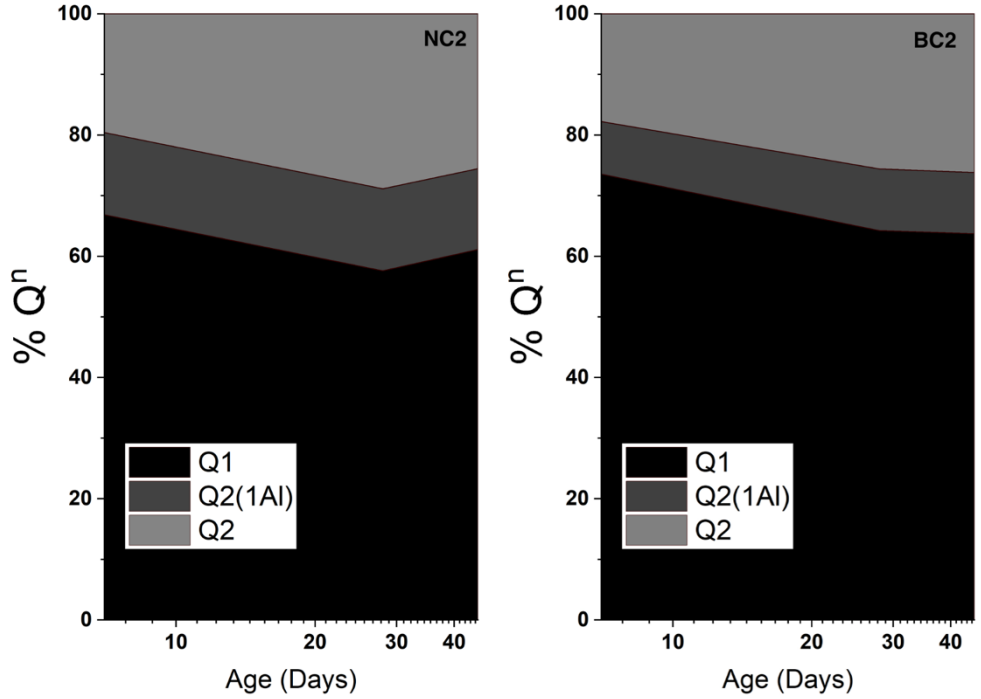

Figure 4-46 %Q^n quantities calculated from NMR spectrum at 7, 28 and 45 days for neat cement paste with calcium ion source and superplasticizer (left) and bacterial cement paste with calcium ion source and superplasticizer (Right).

Comparing both target groups, the obvious difference was related to the slight decrease in the amount of Q^2(1Al) in the bacterial sample after 45 days. It can be discussed that the addition of the bacteria into wPC paste had an effect on the value of Q^2(1Al) tetrahedra in the system and silicon replacement by aluminium. Apart from Q^2(1Al) tetrahedra, other silicon units were experiencing similar behaviour.

4.8 SEM

Bacterial wPC and neat wPC samples prepared with superplasticizer and calcium ion source were subjected to SEM examination. Sample preparation process is described in previous chapter. All samples were tested at 28 and 45 days after the hydration.

The initial proposed approach was to use EDX point analysis to investigate and find the target areas for higher carbon and calcium concentration in order to locate the calcium carbonate rich points on the sample testing surface. However, due to limited time and access, point analysis was only used on some samples to find the interest areas for mapping analysis. Figure 4-47 and Figure 4-48 are representing the point analysis for four different samples at 45 days which concluded the porosity gaps and areas are more likely to yield higher concentration of calcium carbonate in presence of bacteria indicating the microbially induced calcium carbonate precipitation.

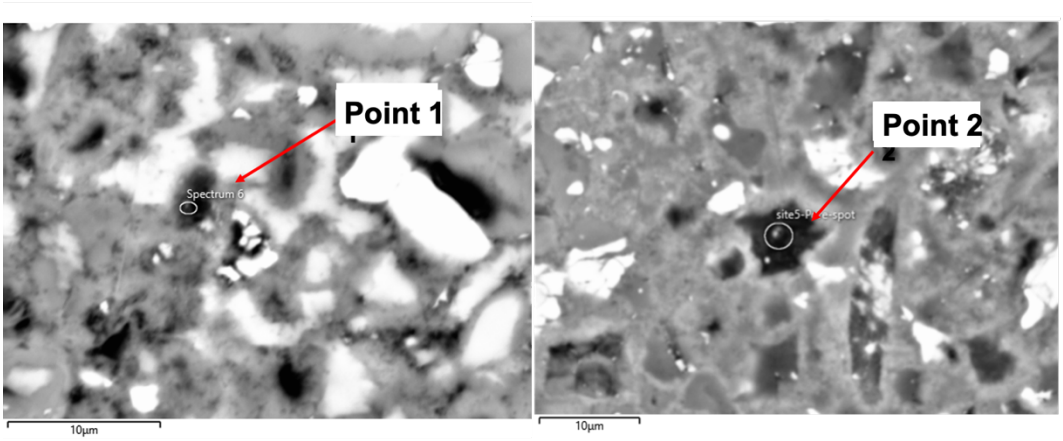

Figure 4-47 SEM-EDX point analysis for NO1 (right) and NC1(left) at 45 days.

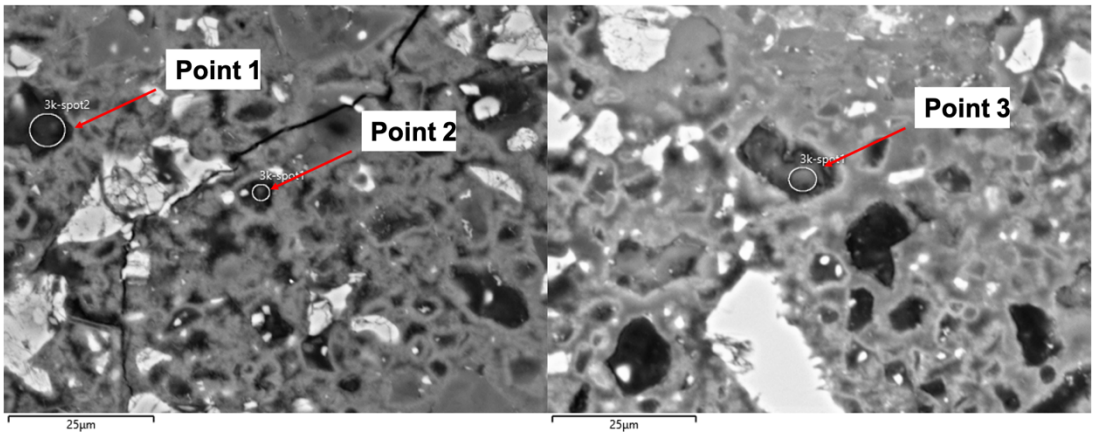

Figure 4-48 SEM-EDX point analysis for BO1 (left) and BO2 (right) at 45 days.

The similar target points have been marked on point analysis and the comparison of the EDX analysis is presented in Table 5-6. Comparison of material composition from these areas points out the strong possibility of calcium carbonate formation inside the porosity gaps for bacterial samples. Bacterial samples showed higher carbon and calcium concentration and lower Al% and Si% content in these areas.

Table 4-6 Material composition of target points from SEM-EDX analysis for bacterial and neat wPC paste samples.

		C%	*O%*	*Al%*	*Si%*	*Ca%*
Figure 4-46	Point 1	1.46	19.24	0.38	1.67	12.47
	Point 2	2.42	22.04	0.36	1.37	18.49
Figure 4-47	Point 1	18.61	15.37	0.08	0.27	12.46
	Point 2	13.34	12.62	0.12	0.06	15.01
	Point 3	16.38	12.58	0.21	0.17	24.04

The examination included secondary (SE) and backscattered(BSE) imaging of the exposed surface to the electron beam. After surface examination of the samples with SEM where multiple areas were chosen for SE and BSE imaging, Energy Dispersive X-ray analysis (EDX) was used for evaluation of the carbon concentration in samples. The carbon concentration was used in order to investigate the presence of calcium carbonate. Theoretically, areas with higher volume of calcium carbonate should experience higher carbon concentrations when inspected with EDX analysis.

Figure 4-49 to Figure 4-52 are representing the carbon mapping and backscattered imaging for the neat wPC paste at 45 days. As it can be observed, there were no unusual carbon concentration in wPC paste without the bacteria. The consistent carbon mapping layer of the neat white Portland cement samples could be considered as lack of high concentration of calcium carbonate in these samples.

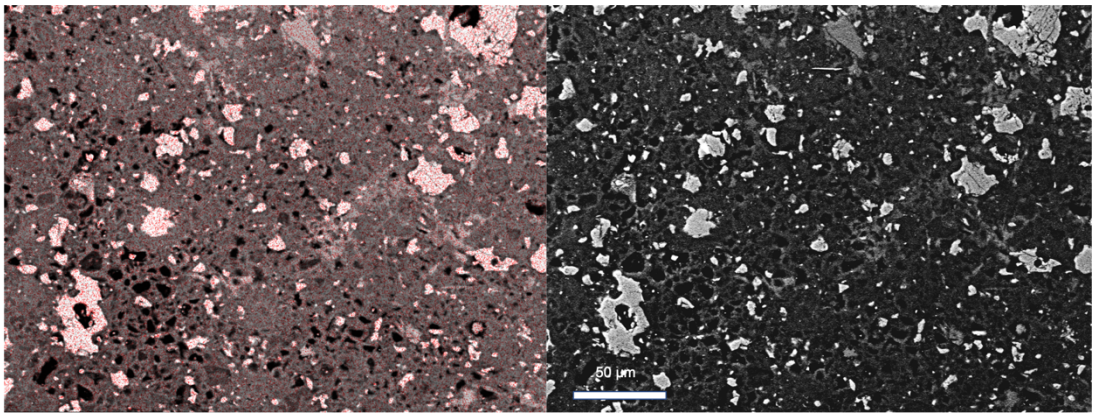

Figure 4-49 Scanning electron microscopy imaging of NO1 at 45 days EDX mapping of Carbon concentration (left) and backscattered image of the same region (Right). Carbon mapping points are covered with the red layer of the EDX analysis (Image on the left).

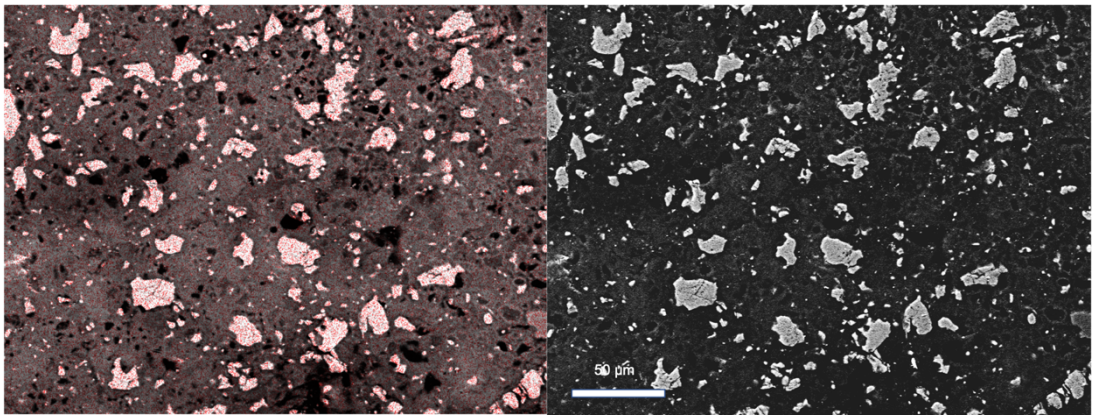

Figure 4-50 Scanning electron microscopy imaging of NO2 at 45 days EDX mapping of Carbon concentration (left) and backscattered image of the same region (Right). Carbon mapping points are covered with the red layer of the EDX analysis (Image on the left).

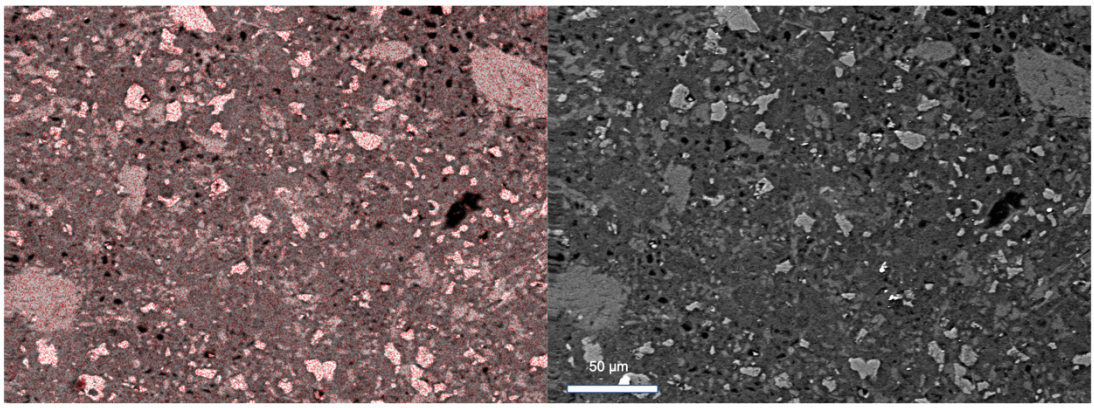

Figure 4-51 Scanning electron microscopy imaging of NC1 at 45 days EDX mapping of Carbon concentration (left) and backscattered image of the same region (Right). Carbon mapping points are covered with the red layer of the EDX analysis (Image on the left).

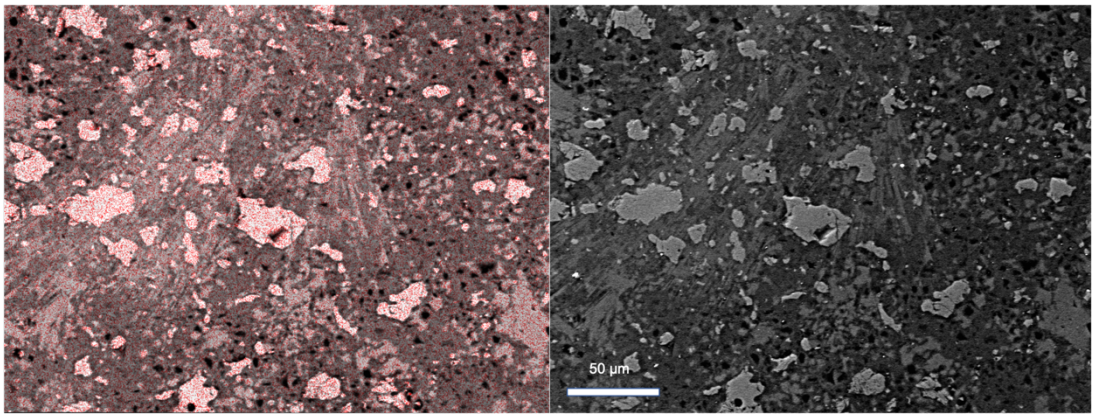

Figure 4-52 Scanning electron microscopy imaging of NC2 at 45 days EDX mapping of Carbon concentration (left) and backscattered image of the same region (Right). Carbon mapping points are covered with the red layer of the EDX analysis (Image on the left).

Further SE, BSE and EDX analysis of the bacterial wPC paste are shown in Figure 4-53 to Figure 4-60 at 28 and 45 days.

The EDX technique for bacterial white Portland cement pastes revealed some high concentrations of calcium carbonate in 28 and 45 days old samples. These areas are marked with white circles in the images. The backscattered imaging was used to eliminate the possibility of external objects being the main source of these calcium carbonate concentrated areas. As it can be expected, the handling of the samples after the hardening of the epoxy resin and during the grounding of the examination surface could lead to the deposition of the external materials. Since carbon is one of the most abundant materials, these external materials would result in false carbon concentration areas for EDX technique.

Figure 4-59, is one of the examples showing a foreign object on the examination surface where it appears with a white shade on the images. For this

reason, the comparison of the SE and BSE images for carbon EDX analysis in this study was essential.

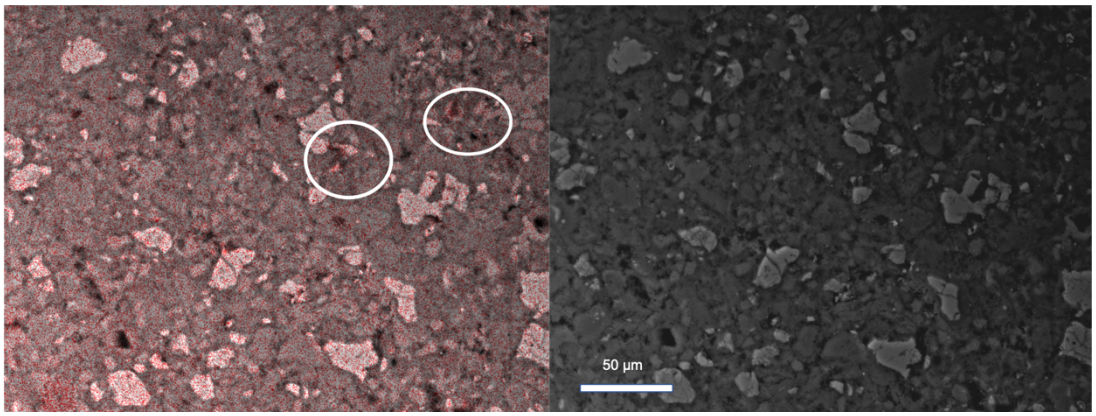

Figure 4-53 Scanning electron microscopy imaging of BC1 at 28 days EDX mapping of Carbon concentration (left) and backscattered image of the same region (Right). Carbon mapping points are covered with the red layer of the EDX analysis (Image on the left). Carbon concentrated areas are marked with circles.

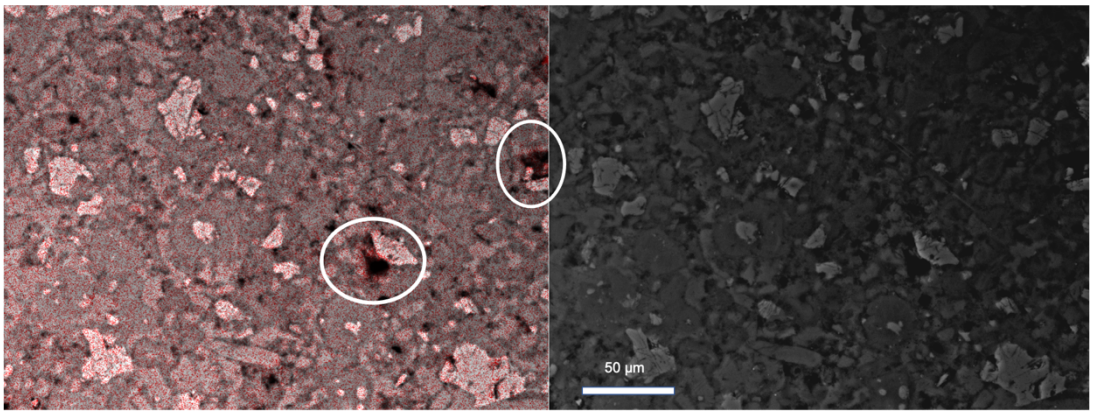

Figure 4-54 Scanning electron microscopy imaging of BC2 at 28 days EDX mapping of Carbon concentration (left) and backscattered image of the same region (Right). Carbon mapping points are covered with the red layer of the EDX analysis (Image on the left). Carbon concentrated areas are marked with circles.

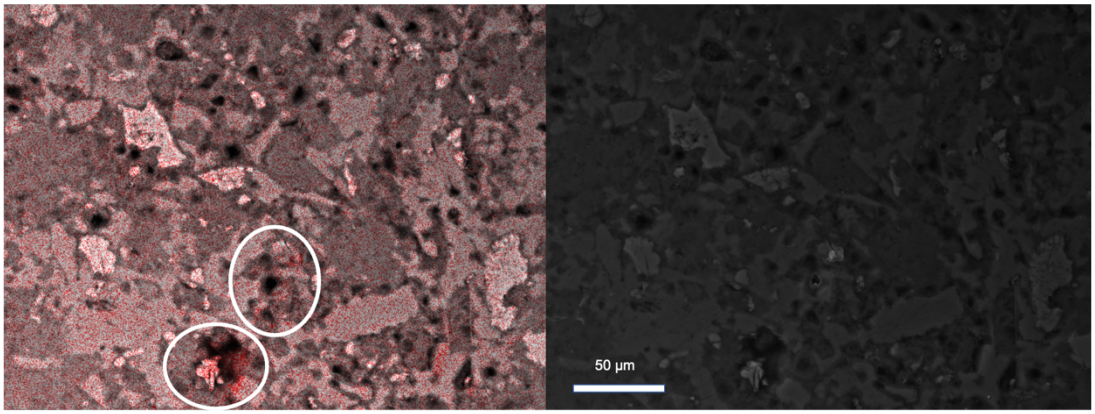

Figure 4-55 Scanning electron microscopy imaging of BO1 at 28 days EDX mapping of Carbon concentration (left) and backscattered image of the same region (Right). Carbon mapping points are covered with the red layer of the EDX analysis (Image on the left). Carbon concentrated areas are marked with circles.

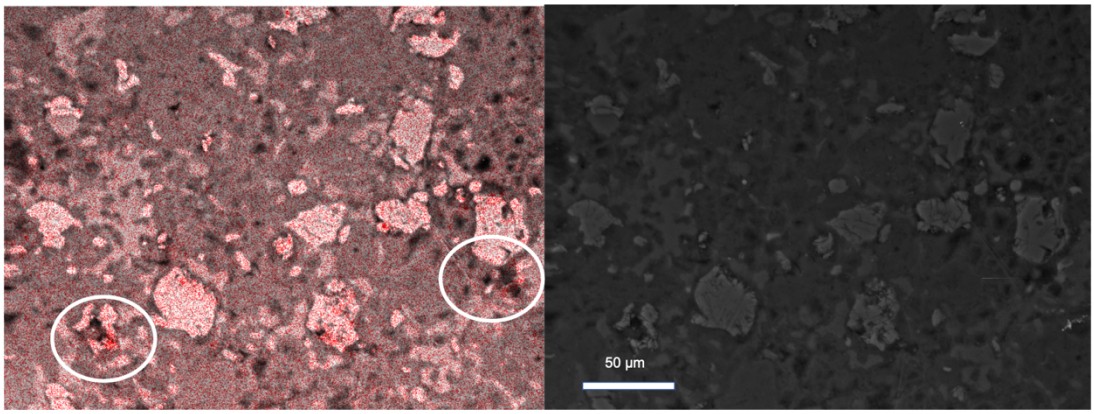

Figure 4-56 Scanning electron microscopy imaging of BO2 at 28 days EDX mapping of Carbon concentration (left) and backscattered image of the same region (Right). Carbon mapping points are covered with the red layer of the EDX analysis (Image on the left). Carbon concentrated areas are marked with circles.

The interest point of this study regarding high carbon concentration and consequently presence of calcium carbonate in these samples was observed with SEM-EDX technique used for bacterial white Portland cement paste samples. Interestingly, all the areas marked for calcium carbonate presence are in or near the vicinity of the available pores inside the samples.

The restriction of calcium carbonate presence in samples only to available gaps in the wPC paste system is in line with the initial hypothesis of the

formation of microbial induced calcium carbonate requires sufficient space volume. This result has also been seen from comparison of the STA and QXRD data where (as discussed in section 5.6.2) the calcium carbonate content in bacterial samples was mainly seen as none/poor crystalline structure. The effects of micro-crack sizes on biomineralization in cement-based materials has been extensively studied and in most of the case and shown that the available space volume has a direct effect on the microbial induced calcium carbonate precipitation [190], [220]. This is further proof of the behaviour of bacterial induced biomineralization in cement-based materials and the effects of porosity on its applications.

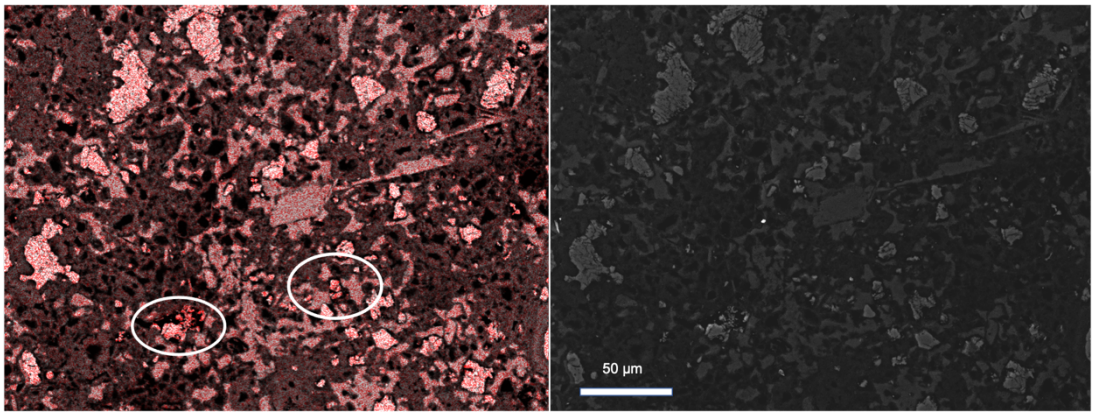

Figure 4-57 Scanning electron microscopy imaging of BC1 at 45 days EDX mapping of Carbon concentration (left) and backscattered image of the same region (Right). Carbon mapping points are covered with the red layer of the EDX analysis (Image on the left). Carbon concentrated areas are marked with circles.

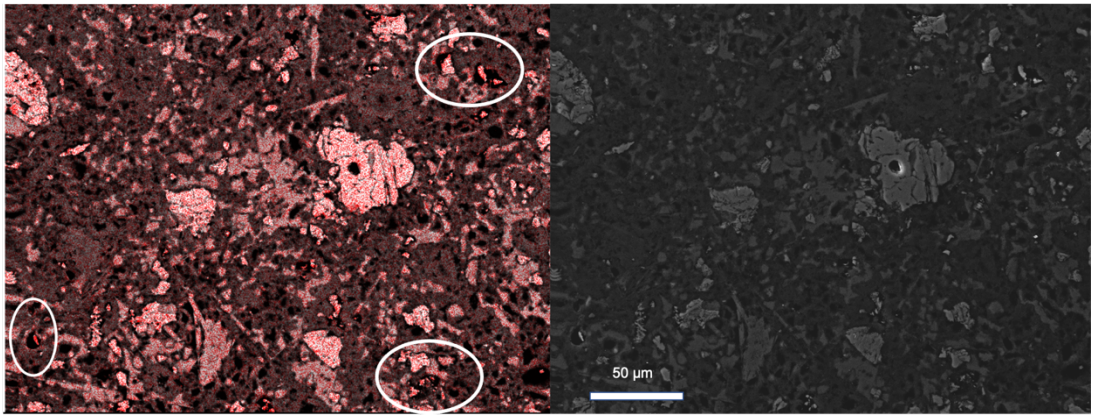

Figure 4-58 Scanning electron microscopy imaging of BC2 at 45 days EDX mapping of Carbon concentration (left) and backscattered image of the same region (Right). Carbon mapping points are covered with the red layer of the EDX analysis (Image on the left). Carbon concentrated areas are marked with circles.

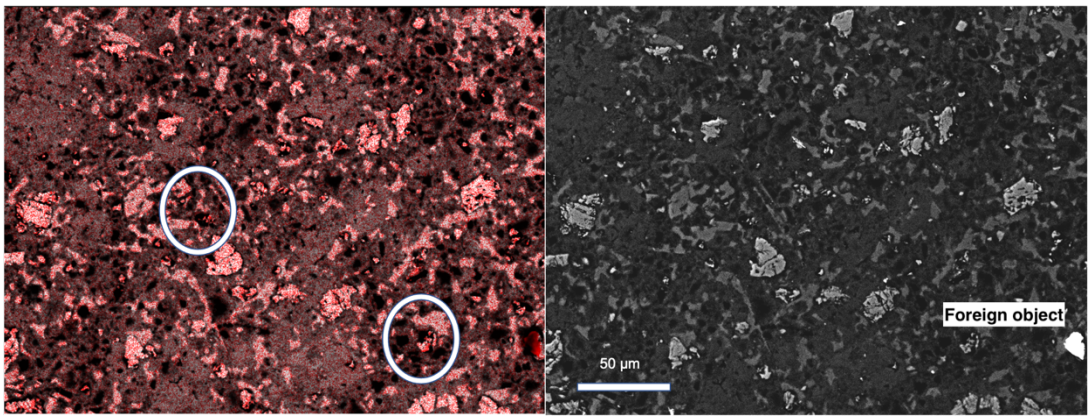

Figure 4-59 Scanning electron microscopy imaging of BO1 at 45 days EDX mapping of Carbon concentration (left) and backscattered image of the same region (Right). Carbon mapping points are covered with the red layer of the EDX analysis (Image on the left). Carbon concentrated areas are marked with circles.

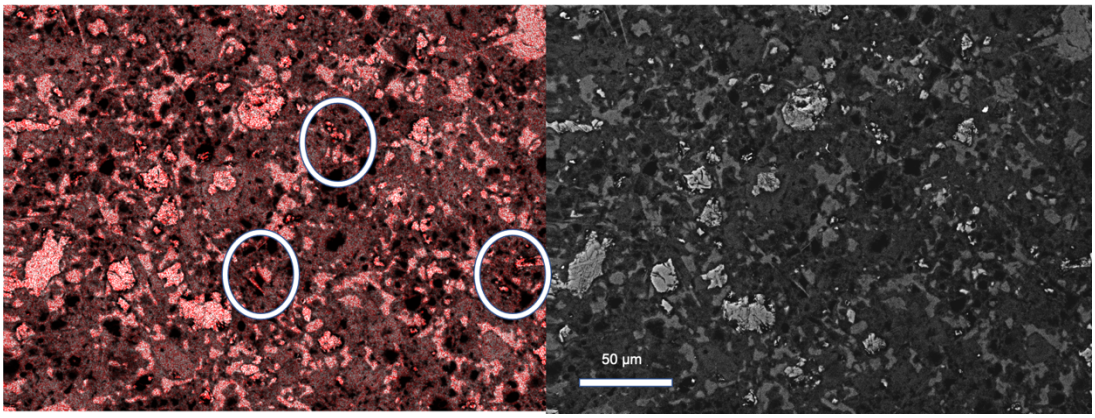

Figure 4-60 Scanning electron microscopy imaging of BO2 at 45 days EDX mapping of Carbon concentration (left) and backscattered image of the same region (Right). Carbon mapping points are covered with the red layer of the EDX analysis (Image on the left). Carbon concentrated areas are marked with circles.

Chapter 5
Conclusion and Future work

The effects of vegetative *S. pasteruii* grown in corn steep liquor medium added to the white Portland cement with and without calcium ion source addition on C-S-H structure has been investigated. With the results obtained from this work, the mechanism of biomineralization was better understood and more specifically the limitation of this application was obtained. Figure 5-1 represents the findings of the current work based on the outlined objectives and as a result of experimental work programme.

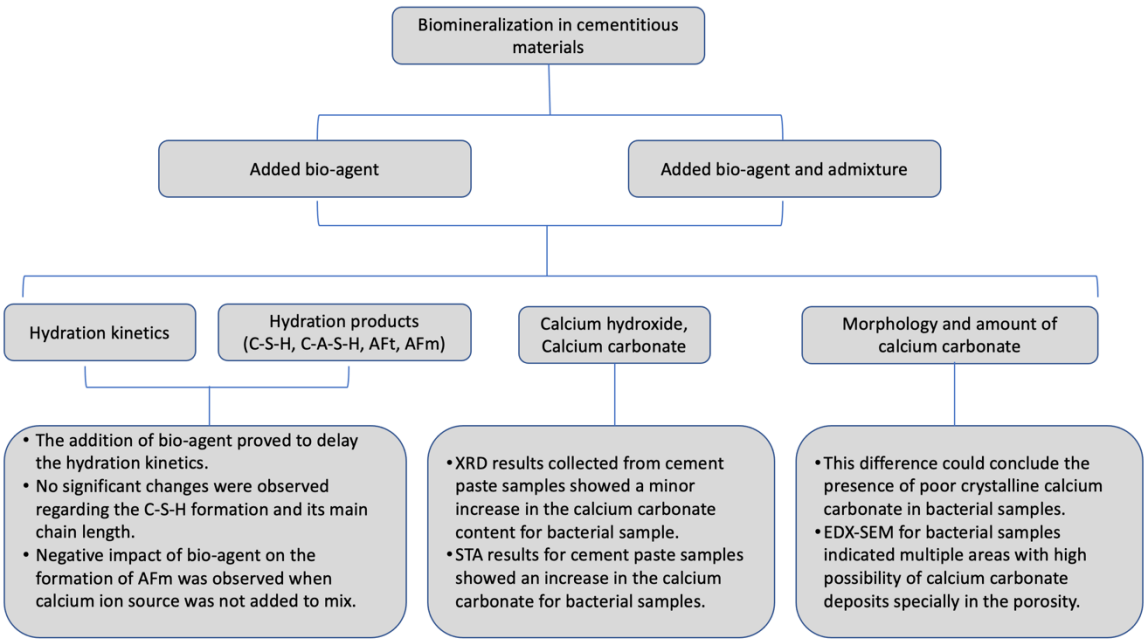

Figure 5-1 Schematic general overview of the findings as a result of work programme for the study.

The corn steep liquor was proven to be affective in bacterial culture as the nutrient source. The specific CSL used in this work has been provided by the fish food industry and it is widely available in the market. The use of CSL was proven

to be effective on *S. pasteruii* strain cells and achieved the expected colony formed per unit in studies where yeast extract was the main nutrient source.

The influence of superplasticizer added to viable bacterial culture was investigated by the XRD technique. The precipitation collected from the aquas bacterial culture with added superplasticizer was proven to yield a larger amount of calcite compared to samples collected from the culture with no additional chemical materials. Furthermore, the precipitation collected from artificial crack introduced in bacterial white Portland cement and tested by FT-IR techniques was also in line with calcite formation with bacteria and added superplasticizer.

The isothermal calorimetry investigation showed that the addition of bacterial culture to the white Portland cement acts as a retarder and delays the setting time of the paste.

Meanwhile, the ^{29}Si NMR investigation showed no significant changes in the structure of the C-S-H polymers tested after 7 days. The MCL for all the samples ranges between 3-4 and Al/Si ratio is from 0.06 to 0.08. However, results from ^{27}Al NMR suggest there is a negative effect on the formation of the AFm in bacterial samples with no additional calcium ion source. Further investigation of AFm formation in cement-based materials with biomineralization application would be advantageous.

Results acquired through STA and XRD techniques showed a significant difference in the calculated calcium carbonated content between two analyses. The STA data regarding calcium carbonate content proves the MICP in cement-based materials when compared to neat wPC paste. However, The quantified XRD data does not show a significant difference between bacterial and neat wPC paste at 7, 28 and 45 days. This difference could be due to the formation of

amorphous/poor crystalline calcium carbonate in the bacterial samples. This formation of amorphous calcium carbonate in bacterial wPC pastes can be explained by the low porosity ratio and high density of the cement paste samples. This theory was proven by SEM imaging and the observation of high calcium carbonate concentration in close proximity of gaps and porosity in the samples.

Using SEM imaging analysis, all samples were tested at 28 and 45 days after the hydration and bacterial incorporation. SE and BSE techniques were used for acquired images and EDX analysis was done to inspect the carbon concentration areas. With the assumption of appropriate sample handling and elimination of any foreign objects on the surface after polishing the samples, it is safe to hypothesize that the high carbon concentration in EDX analysis is an indication for the possible calcium carbonate presence in the samples. With all the test procedure during SEM technique, the samples containing bacteria showed areas with high calcium carbon concentration. It should be mentioned that all these calcium carbonate present were concentrated in close proximity of the available gaps. This finding through SEM imaging is also further prove to the necessity of higher porosity ratio in samples for calcium carbonate precipitation in bacterial wPC paste.

5.1 Future work

The effect of bacterial biomineralization on cement hydration at early ages need better understanding and investigation. The existing studies are mainly focused on self-healing applications at later ages. However, according to this

study there are no significant changes after 7 days on hydration products apart from calcium carbonate and calcium hydroxide content of the wPC paste.

Furthermore, the influence of biomineralization on Si substitution by Al requires extensive work to investigate the possible outcomes of different ratios of bacteria and calcium ion sources. Also, the early formation of AFt and AFm could yield interesting information of biomineralization influence on cement hydration. These could also be investigated with extra addition of Al into the system in different ratios. This could also include the investigation of possible decomposition of calcium hydroxide by bacteria to continue the biomineralization by investigating a more comprehensive sampling and testing regimes where the curing process would include wet and dry conditions.

Another aspect of this study which could help the future work is the fact that porosity ratio in samples has a direct effect on the morphology of the precipitated calcium carbonate. Using this knowledge, it should be considered that instead of cement-paste samples, mortar samples (with lower density) or artificial porosity generator materials (such as light weight aggregates) could be used.

The ability of microbially induced calcium carbonate to bond with cement-based materials is one of the key concerns. The bonding ability of microbially induced calcium carbonate and cement, on the other hand, has yet to be studied. The findings of a study looking into the bonding capacity between the precipitate and the cement-based material would reveal details about the microorganism's ability to heal and the application's resilience. Endospores need time to regenerate before they can become metabolically active viable cells, causing a pause in the healing process. The conditions needed for endospore

recovery, as well as the time delay caused by reformation, are still unknown. Furthermore, the effects of endospores on the properties of cement-based materials are poorly understood.

List of References

[1] R. Siddique, V. Nanda, E. Kadri, M. I. Khan, M. Singh, and A. Rajor, “Influence of bacteria on compressive strength and permeation properties of concrete made with cement baghouse filter dust,” *Constr. Build. Mater.*, vol. 106, pp. 461–469, 2016, doi: 10.1016/j.conbuildmat.2015.12.112.

[2] W. De Muynck, N. De Belie, and W. Verstraete, “Microbial carbonate precipitation in construction materials: A review,” *Ecol. Eng.*, vol. 36, pp. 118–136, 2010, doi: 10.1016/j.ecoleng.2009.02.006.

[3] N. Tarun, “Sustainability of concrete construction,” *Pract. Period. Struct. Des. Constr.*, vol. 13, no. 2, 2008.

[4] M. B. Ali, R. Saidur, and M. S. Hossain, “A review on emission analysis in cement industries,” *Renew. Sustain. Energy Rev.*, vol. 15, no. 5, pp. 2252–2261, 2011, doi: 10.1016/j.rser.2011.02.014.

[5] M. Khan and S. Ahmad, “CAUSES AND EVALUATION OF CRACKS IN CONCRETE STRUCTURES,” *Int. J. Tech. Res. Appl.*, vol. 2, no. 5, pp. 29–33, 2014.

[6] E. Ghafari, M. Arezoumandi, H. Costa, and E. Júlio, “Influence of nano-silica addition in the durability of UHPC,” *Constr. Build. Mater.*, vol. 94, pp. 181–188, 2015, doi: 10.1016/j.conbuildmat.2015.07.009.

[7] N. De Belie, “Microorganisms versus stony materials: a love–hate relationship,” *Mater. Struct.*, vol. 43, pp. 1191–1202, 2010, doi: 10.1617/s11527-010-9654-0.

[8] W. De Muynck, K. Cox, N. De Belie, and W. Verstraete, “Bacterial carbonate precipitation as an alternative surface treatment for concrete,” *Constr. Build. Mater.*, vol. 22, pp. 875–885, 2008, doi: 10.1016/j.conbuildmat.2006.12.011.

[9] Y. C. Ersan, “Microbial nitrate reduction induced autonomous self-healing in concrete,” Thesis, Delt university of technology, Thesis, 2016.

[10] K. Van Tittelboom and N. De Belie, “Self-healing in cementitious materials-a review,” *Materials (Basel).*, vol. 6, no. 6, pp. 2182–2217, 2013, doi: 10.3390/ma6062182.

[11] M. Wu, B. Johannesson, and M. Geiker, “A review: Self-healing in cementitious materials and engineered cementitious composite as a self-healing material,” *Constr. Build. Mater.*, vol. 28, no. 1, pp. 571–583, 2012.

[12] D. Talham, “Biomineralization: Principles and Concepts in Bioinorganic Materials Chemistry,” *Cryst. Growth Des.*, vol. 2, no. 6, p. 675, 2002.

[13] K. Sarayu, N. R. Iyer, and a. R. Murthy, “Exploration on the biotechnological aspect of the ureolytic bacteria for the production of the cementitious materials - A review,” *Appl. Biochem. Biotechnol.*, vol. 172, pp. 2308–2323, 2014, doi: 10.1007/s12010-013-0686-0.

[14] J. Y. Wang, N. De Belie, and W. Verstraete, “Diatomaceous earth as a protective vehicle for bacteria applied for self-healing concrete,” *J. Ind.*

Microbiol. Biotechnol., vol. 39, pp. 567–577, 2012, doi: 10.1007/s10295-011-1037-1.

[15] C. Rodriguez-Navarro, F. Jroundi, M. Schiro, E. Ruiz-Agudo, and M. T. González-Muñoz, “Influence of substrate mineralogy on bacterial mineralization of calcium carbonate: Implications for stone conservation,” *Appl. Environ. Microbiol.*, vol. 78, no. 11, pp. 4017–4029, 2012, doi: 10.1128/AEM.07044-11.

[16] L. S. Wong, “Microbial cementation of ureolytic bacteria from the genus Bacillus: A review of the bacterial application on cement-based materials for cleaner production,” *J. Clean. Prod.*, 2015, doi: 10.1016/j.jclepro.2015.01.019.

[17] D. Sarda, H. S. Choonia, D. Sarode, and S. Lele, “Biocalcification by Bacillus pasteurii urease : a novel application,” *J. Ind. Microbiol.*, vol. 36, pp. 1111–1115, 2009, doi: 10.1007/s10295-009-0581-4.

[18] V. Achal, X. Pan, and N. Özyurt, “Improved strength and durability of fly ash-amended concrete by microbial calcite precipitation,” *Ecol. Eng.*, vol. 37, no. 4, pp. 554–559, 2011, doi: 10.1016/j.ecoleng.2010.11.009.

[19] H. M. Jonkers, A. Thijssen, G. Muyzer, O. Copuroglu, and E. Schlangen, “Application of bacteria as self-healing agent for the development of sustainable concrete,” *Ecol. Eng.*, vol. 36, pp. 230–235, 2010, doi: 10.1016/j.ecoleng.2008.12.036.

[20] P. Ghosh, S. Mandal, S. Pal, G. Bandyopadhyaya, and B. D. Chattopadhyay, “Development of bioconcrete material using an enrichment culture of novel thermophilic anaerobic bacteria,” *Indian J. Exp. Biol.*, vol. 44, no. April, pp. 336–339, 2006.

[21] H. M. Jonkers and E. Schlangen, “Development of a bacteria-based self healing concrete,” *Proc. int. FIB Symp.*, vol. 1, pp. 425–430, 2008, doi: 978-1-4398-2841-0.

[22] H. M. Jonkers, “Self-healing concrete : a biological approach,” pp. 195–204, 2007.

[23] V. Wiktor and H. M. Jonkers, “Quantification of crack-healing in novel bacteria-based self-healing concrete,” *Cem. Concr. Compos.*, vol. 33, no. 7, pp. 763–770, 2011, doi: 10.1016/j.cemconcomp.2011.03.012.

[24] S. Bang, J. Lippert, U. Yerra, S. Mulukutla, and V. Ramakrishnan, “Microbial calcite, a bio-based smart nanomaterial in concrete remediation,” *Int. J. Smart Nano Mater.*, vol. 1, no. 1, pp. 28–39, 2010, doi: 10.1080/19475411003593451.

[25] J. Y. Wang, H. Soens, W. Verstraete, and N. De Belie, “Self-healing concrete by use of microencapsulated bacterial spores,” *Cem. Concr. Res.*, vol. 56, pp. 139–152, 2014, doi: 10.1016/j.cemconres.2013.11.009.

[26] J. Y. Wang, D. Snoeck, S. Van Vlierberghe, W. Verstraete, and N. De Belie, “Application of hydrogel encapsulated carbonate precipitating bacteria for approaching a realistic self-healing in concrete,” *Constr. Build. Mater.*, vol. 68, pp. 110–119, 2014, doi: 10.1016/j.conbuildmat.2014.06.018.

[27] Z. Basaran, “Biomineralization in cement based materials : inoculation of vegetative cells,” university of Texas at Austin, 2013.

[28] Z. B. Bundur, M. J. Kirisits, and R. D. Ferron, “Biomineralized cement-based materials: Impact of inoculating vegetative bacterial cells on hydration and strength,” *Cem. Concr. Res.*, vol. 67, pp. 237–245, 2015, doi: 10.1016/j.cemconres.2014.10.002.

[29] N. K. Dhami and S. M. Reddy, “Biofilm and microbial applications in biomineralized concrete,” *Adv. Top. Biominer.*, no. 2, p. 174, 2012.

[30] V. S. Whiffin, L. a. van Paassen, and M. P. Harkes, “Microbial carbonate precipitation as a soil improvement technique,” *Geomicrobiol. J.*, vol. 24, no. 918547867, pp. 417–423, 2007, doi: 10.1080/01490450701436505.

[31] L. Skevi, B. Reeksting, T. Hoffmann, S. Gebhard, and K. Paine, “Incorporation of bacteria in concrete : The case against MICP as a means for strength improvement,” *Cem. Concr. Compos.*, vol. 120, no. 104056, 2021.

[32] T. D. Hoffmann;, B. J. Reeksting;, and S. Gebhard, “Bacteria-induced mineral precipitation: a mechanistic review,” *Microbiol. Soc.*, vol. 167, no. 4, 2021, doi: https://doi.org/10.1099/mic.0.001049.

[33] R. F. Feldman, “Concrete Science,” *Concr. Admixtures Handb.*, pp. 1–66, Jan. 1996, doi: 10.1016/B978-081551373-5.50005-2.

[34] H. F. . Taylor, *Cement chemistry*, 2nd ed. Thomas Telford, 1997.

[35] J. P. Skalny, *Materials science of concrete 1*. 1989.

[36] D. Ménétrier, I. Jawed, and J. Skalny, “Effect of gypsum on C_3S hydration,” *Cem. Concr. Res.*, no. 10, pp. 697–701, 1980.

[37] G. C. Bye, *Portland cement: composition production and properties*. Published on behalf of the Institute of Ceramics by Pergamon Press, 1999.

[38] P. D. Tennis; and J. I. Bhatty, “Characteristics of portland and blended cements: results of a survey of manufacturers,” 2006.

[39] J. J. Thomas, S. A. FitzGerald, D. A. Neumann, and R. A. Livingston, “State of water in hydrating tricalcium silicate and Portland cement pastes as measured by Quasi-elastic neutron scattering,” *J. Am. Ceram. Soc.*, vol. 84, pp. 1811–1816, 2001.

[40] P. Hewlett, *Chemistry of cement and concrete*, 4th ed. 2003.

[41] D. Stephan and S. Wistuba, “Crystal structure refinement and hydration behaviour of $3CaO{\cdot}SiO_2$ solid solutions with MgO, Al_2O_3 and Fe_2O_3,” *J. Eur. Ceram. Soc.*, no. 26, pp. 141–148, 2006.

[42] D. Stephan, S. N. Dikoundou, and G. Raudaschl-Sieber, “Hydration characteristics and hydration products of tricalcium silicate doped with a combination of MgO, Al_2O_3 and Fe_2O_3,” *Thermochim. Acta*, no. 472, pp. 64–73, 2008.

[43] L. Fernandez, C. Alonso, A. Hidalgo, and C. Andrade, “The role of magnesium during the hydration of C_3S and CSH formation. Scanning electron microscopy and mid-infrared studies,” *Adv. Cem. Res.*, no. 17, pp. 9–21, 2005.

[44] I. G. Richardson and G. W. Groves, “Microstructure and microanalysis of hardened ordinary Portland cement pastes,” *J. Mater. Sci.*, no. 28, pp. 265–277, 1993.

[45] I. G. Richardson, A. R. Brough, R. Brydson, G. W. Groves, and C. M. Dobson, “Location of Aluminum in Substituted Calcium Silicate Hydrate (C-S-H) Gels as Determined by ^{29}Si and ^{27}Al NMR and EELS,” *, J. Am. Ceram. Soc.*, no. 27, pp. 2285–2286, 1993.

[46] J. B. Ings, P. W. Brown, and G. Frohnsdorff, “Early hydration of large single crystals of tricalcium silicate,” *Cem. Concr. Res.*, no. 13, pp. 843–848, 1983.

[47] E. M. Gartner, “Hydration mechanisms,” *J. Am. Ceram. Soc.*, pp. 95–125, 1989.

[48] K. Wieslaw, *Cement and concrete chemistry*. Springer Science, 2014.

[49] A. K. Chatterjee, “High belite cements—Present status and future technological options,” *Cem. Concr. Res.*, vol. 26, pp. 1213–1225, 1996.

[50] J. G. Jang and H. K. Lee, “Microstructural densification and CO_2 uptake promoted by the carbonation curing of belite-rich Portland cement,” *Cem. Concr. Res.*, vol. 82, pp. 50–57, 2016.

[51] R. Taylor, “Characterization of C-S-H in early and late age systems containing admixtures,” University of Leeds, Thesis, 2010.

[52] K. Fukuda and N. Wakamatsu, “Improvement in hydration reactivity of α-phase belite by remelting reaction,” *J. Am. Ceram. Soc.*, vol. 84, pp. 639–641, 2001.

[53] R. Trettin, G. Oliew, C. Stadelmann, and W. Wieker, “Very early hydration of dicalcium silicate-polymorphs,” *Cem. Concr. Res.*, no. 21, pp. 757–764, 1991.

[54] I. Jelenić, A. Bezjak, and M. Bujan, “Hydration of B_2O_3-stabilized α′-and βmodifications of dicalcium silicate,” *Cem. Concr. Res.*, no. 8, pp. 173–180, 1978.

[55] L. Nicoleau, A. Nonat, and D. Perrey, “The di- and tricalcium silicate dissolutions,” *Cem. Concr. Res.*, no. 47, pp. 14–30, 2013.

[56] J. W. Bullard, H. M. Jennings, R. A. Livingston, A. Nonat, G. W. Scherer, and J. J. T. Schweitzer, K.L. Scrivener, “Mechanisms of cement hydration,” *Cem. Concr. Res.*, pp. 1208–1223, 2011.

[57] P. Juilland, E. Gallucci, R. Flatt, and K. Scrivener, “Dissolution theory applied to the induction period in alite hydration,” *Cem. Concr. Res.*, pp. 831–844, 2010.

[58] F. A. Steele and W. P. Davey, “The crystal structure of tricalcium aluminate,” *J. Am. Chem. Soc.*, vol. 51, pp. 2283–2293, 1929.

[59] P. Mondal and J. W. Jeffery, “The crystal structure of tricalcium aluminate,” *Acta Cryst*, vol. 31, pp. 689–697, 1975.

[60] E. Breval, “C_3A hydration,” *Cem. Concr. Res.*, vol. 6, pp. 129–137, 976.

[61] R. Wonnemann and I. Odler, “Effect of alkalies on portland cement hydration. I. Alkali oxides incorporated into the crystalline lattice of clinker

minerals," *Cem. Concr. Res*, vol. 13, no. 4, pp. 477–482, 1983.

[62] J. J. Beaudoin and V. Ramachandran, "A new perspective on the hydration characteristics of cement phases," *Cem. Concr. Res.*, no. 22, pp. 689–694, 1992.

[63] I. Odler, *Hydration, setting and hardening of Portland cement*, 4th ed. Elsevier Ltd, 2003.

[64] N. L. Thomas and D. D. Double, "The hydration of Portland cement, C_3S and C_2S in the presence of a calcium complexing admixture," *Cem. Concr. Res.*, pp. 391–400, 1983.

[65] H. F. W. Taylor *et al.*, "The hydration of tricalcium silicate," *Matériaux Constr.*, vol. 7, pp. 457–468, 1984.

[66] I. G. Richardson, "Model structures for C-(A)-S-H(I)," *Acta Crystallogr. Sect. B Struct. Sci. Cryst. Eng. Mater.*, vol. 70, no. 6, pp. 903–923, 2014, doi: 10.1107/S2052520614021982.

[67] P. Barret and D. Ménétrier, "Filter dissolution of C3S as a function of the lime concentration in a limited amount of lime water," *Cem. Concr. Res.*, pp. 521–534, 1980.

[68] S. Mindess, J. F. Young, and D. Darwin, *Concrete*. Prentice Hall PTR, 2003.

[69] K. L. Scrivener and A. Nonat, "Hydration of cementitious materials, present and future," *Cem. Concr. Res.*, vol. 41, no. 7, pp. 651–665, 2011, doi: 10.1016/j.cemconres.2011.03.026.

[70] K. L. Scrivener, "The development of microstructure during the hydration of Portland cement.," University of London, Thesis, 1984.

[71] I. G. Richardson, "Tobermorite/jennite-and tobermorite/calcium hydroxide-based models for the structure of C-S-H: applicability to hardened pastes of tricalcium silicate, β-dicalcium silicate, Portland cement, and blends of Portland cement with blast-furnace slag, metakaoli," *Cem. Concr. Res.*, vol. 34, no. 9, pp. 1733–1777, 2004.

[72] J. J. Chen, "The nanostructure of calcium silicate hydrate," Northwestern University USA, Thesis, 2003.

[73] E. Bonaccorsi, S. Merlino, and H. F. W. Taylor, "The crystal structure of jennite, $Ca_9Si_6O_{18}(OH)_6\ 8H_2O$," *Cem. Concr. Res.*, vol. 34, no. 9, pp. 1481–1488, 2004.

[74] N. Hara and N. Inoue, "Formation of jennite from fumed silica," *Cem. Concr. Res.*, vol. 10, pp. 667–682, 1980.

[75] E. L'Hôpital, B. Lothenbach, D. A. Kulik, and K. Scrivener, "Influence of calcium to silica ratio on aluminium uptake in calcium silicate hydrate," *Cem. Concr. Res.*, vol. 85, pp. 111–121, 2016, doi: 10.1016/j.cemconres.2016.01.014.

[76] I. G. Richardson, "Nature of C-S-H in hardened cements," *Cem. Concr. Res.*, vol. 29, no. 8, pp. 1131–1147, 1999, doi: 10.1016/S0008-8846(99)00168-4.

[77] P. J. P. G. and A. M. Fernando Pelisser, "Effect of the Ca/Si Molar Ratio

on the Micro/nanomechanical Properties of Synthetic C-S-H Measured by Nanoindentation," *J. Phys. Chem.*, vol. 116, no. 32, pp. 16815–17306, 2012.

[78] T.C. Powers, "Structure and physical properties of hardened Portland cement paste," *J. Am. Ceram. Soc.*, vol. 41, no. 1, pp. 1–6, 1958.

[79] R. F. Feldman and P. J. Sereda, "A New model for hydrated Portland cement and its practical implications," *Eng. J. Canada*, vol. 53, no. 8/9, pp. 53–59, 1970.

[80] H. F. W. Taylor, "Proposed structure for calcium silicate hydrate gel," *Am. Ceram. Soc.*, vol. 69, no. 6, pp. 464–467, 1986.

[81] I. G. Richardson and G. W. Groves, "Models for the composition and structure of calcium silicate hydrate (CSH) gel in hardened tricalcium silicate pastes," *Cem. Concr. Res.*, vol. 22, no. 6, pp. 1001–1010, 1992.

[82] I. G. Richardson and G. W. Groves, "The incorporation of minor and trace elements into calcium silicate hydrate gel in hardened cement pastes," *Cem. Concr. Res.*, vol. 23, pp. 4793–4802, 1993.

[83] R. J. Pellenq *et al.*, "A realistic molecular model of cement hydrates," in *Proceedings of the National Academy of Sciences of the United States of America*, 2009, pp. 16102–16107.

[84] I. G. Richardson, "The importance of proper crystal-chemical and geometrical reasoning demonstrated using layered single and double hydroxides," *Acta Crystallogr. Sect. B Struct. Sci. Cryst. Eng. Mater.*, vol. 69, no. 2, pp. 150–162, 2013.

[85] H. Minard, "Mechanisms and parameters controlling the tricalcium aluminate reactivity in the presence of gypsum," *Cem. Concr. Res.*, vol. 37, no. 10, pp. 1418–1426, 2007.

[86] I. G. Richardson, "Nature of the hydration products in hardened cement pastes," *Cem. Concr. Compos.*, vol. 22, no. 2, pp. 97–113, 2000, doi: 10.1016/S0958-9465(99)00036-0.

[87] M. R. Jones *et al.*, "Studies using ^{27}Al MAS NMR of AFm and AFt phases and the formation of Friedel's salt," *Cem. Concr. Res.*, vol. 33, no. 2, pp. 177–182, 2003, doi: 10.1016/S0008-8846(02)00901-8.

[88] M. Balonis, M. Mędala, and F. P. Glasser, "Influence of calcium nitrate and nitrite on the constitution of AFm and AFt cement hydrates," *Adv. Cem. Res.*, vol. 23, no. 3, pp. 129–143, 2011, doi: 10.1680/adcr.10.00002.

[89] H. Wang, G. Diao, G. Liu, H. Wang, L. Gao, and G. Liu, "The effect of calcium nitrate on the hydration of calcium aluminate cement at different curing temperatures," *6th Int. Conf. Durab. Concr. Struct. ICDCS 2018*, vol. 02, no. Icc, pp. 295–302, 2018.

[90] V. S. Ramachandran, *Concrete Admixtures Handbook: Properties, Science and Technology,*. Noyes Publications, Saddle River, NJ.

[91] S. K. Ghosh, *Self-healing materials: fundamentals, design strategies and applications*. Weinheim: Wiley-VCH, 2009.

[92] V. S. Whiffin, "Microbial CaCO3 Precipitation for the Production of

Biocement," *Murdor Univ. Repos.*, vol. PhD, no. September, pp. 1–162, 2004, doi: http://researchrepository.murdoch.edu.au/399/2/02Whole.pdf.

[93] V. Achal, A. Mukherjee, and M. S. Reddy, "Effect of calcifying bacteria on permeation properties of concrete structures," *J. Ind. Microbiol. Biotechnol.*, vol. 38, no. 9, pp. 1229–1234, 2011, doi: 10.1007/s10295-010-0901-8.

[94] J. Wang, "Self-healing concrete by means of immobilized carbonate precipitating bacteria," University of Ghent, Thesis, 2012.

[95] S. Stocks-Fischer, J. K. Galinat, and S. S. Bang, "Microbiological precipitation of $CaCO_3$," *Soil Biol. Biochem.*, vol. 31, pp. 1563–1571, 1999, doi: 10.1016/S0038-0717(99)00082-6.

[96] F. Hammes and W. Verstraete, "Key roles of pH and calcium metabolism in microbial carbonate precipitation," *Rev. Environ. Sci. Biotechnol.*, vol. 1, no. 1, pp. 3–7, 2002, doi: 10.1023/A:1015135629155.

[97] F. Hammes, N. Boon, J. De Villiers, W. Verstraete, S. D. Siciliano, and J. De Villiers, "Strain-specific ureolytic microbial calcium carbonate precipitation," *Appl. Environ. Microbiol.*, vol. 69, no. 8, pp. 4901–4909, 2003, doi: 10.1128/AEM.69.8.4901.

[98] L. Addadi, S. Raz, and S. Weiner, "Taking advantage of disorder: Amorphous calcium carbonate and its roles in biomineralization," *Adv. Mater.*, vol. 15, no. 12, pp. 959–970, 2003, doi: 10.1002/adma.200300381.

[99] B. M. Mortensen, M. J. Haber, J. T. Dejong, L. F. Caslake, and D. C. Nelson, "Effects of environmental factors on microbial induced calcium carbonate precipitation," *J. Appl. Microbiol.*, vol. 111, no. Kohnhauser 2007, pp. 338–349, 2011, doi: 10.1111/j.1365-2672.2011.05065.x.

[100] H. Roy, R ; Rossi, E ; Silfwerbrand, J; Jonkers, "Encapsulation techniques and test methods of evaluating the bacteria-based self-healing efficiency of concrete," *Nord. Concr. Res.*, vol. 62, no. 1, pp. 63–85, 2020.

[101] X. Wang, S. Chen, and Z. Ang, "Self-healing concrete incorporating mineral additives and encapsulated lightweight aggregates: Preparation and application," *Constr. Build. Mater.*, vol. 301, no. 124119, 2021.

[102] J. Wang, K. Van Tittelboom, N. De Belie, and W. Verstraete, "Use of silica gel or polyurethane immobilized bacteria for self-healing concrete," *Constr. Build. Mater.*, vol. 26, no. 1, pp. 532–540, 2012, doi: 10.1016/j.conbuildmat.2011.06.054.

[103] N. Huynh, K. Imamoto, C. Kiyohara, and N. Huyen, "Mechanism analysis and improvement of bacterial bio-mineralization for self-healing concrete Using bacillus subtilis natto immobilized in Lightweight aggregate," *CIGOS 2021, Emerg. Technol. Appl. GREEN Infrastruct.*, vol. 203, pp. 763–771, 2022.

[104] Ruoting Pei *et al.*, "Use of bacterial cell walls to improve the mechanical performance of concrete," *Cem. Concr. Compos.*, vol. 39, pp. 122–130, 2013, doi: https://doi.org/10.1016/j.cemconcomp.2013.03.024.

[105] C. S. S. Durga, Nerella Ruben, M. S. R. Chand, and C. Venkatesh., "Performance studies on rate of self healing in bio concrete.," *Today proc.*,

vol. 27, pp. 158–162, 2019, [Online]. Available: https://doi.org/10.1016/j.%0Amatpr.2019.09.151.

[106] Wasim Khaliq, Muhammad Basit Ehsan, “Crack healing in concrete using various bio influenced self-healing techniques,” *Constr. Build. Mater.*, 2016.

[107] Nidhi Naina; R.Surabhia; YathishN.V; V.Krishnamurthy; T.Deepa; SeemaTharann, “Enhancement in strength parameters of concrete by application of Bacillus bacteria,” *Constr. Build. Mater.*, vol. 202, pp. 904–908, 2019.

[108] P. Jagannathan, K. S. S. Narayanan, K. devi Arunachalam, and S. kumar Annamalai, “Studies on the mechanical properties of bacterial concrete with two bacterial species,” *Mater. Today Proc.*, 2018, doi: 0.1016/ j.matpr.2017.12.320.

[109] B. M. S. Reddy and D. Revathi, “An experimental study on effect of Bacillus Sphaericus bacteria in crack filling and strength enhancement of concrete.,” *Mater. Today Proc.*, vol. 19, pp. 803–809, 2019, doi: https://doi.org/10.1016/j.matpr.2019.08.135.

[110] N. Chahal, R. Siddique, and A. Rajor, “Influence of bacteria on the compressive strength, water absorption and rapid chloride permeability of concrete incorporating silica fume,” *Constr. Build. Mater.*, vol. 37, no. 1, pp. 645–651, 2012, doi: 10.1016/j.conbuildmat.2012.07.029.

[111] R. Andalib *et al.*, “Optimum concentration of Bacillus Megaterium for strengthening structural concrete,” *Constr. Build. Mater.*, vol. 118, pp. 180–193, 2016.

[112] V. Nagarajan, T. K. Prabhu, M. G. Shankar, and P. Jagadesh, “A study on the strength of the bacterial concrete embedded with bacillus megaterium,” *Int. Res. J. Eng. Technol.*, vol. 4, no. 12, 2017.

[113] J. S. Dickson and M. Koohmaraie, “Cell surface charge characteristics and their relationship to bacterial attachment to meat surfaces.,” *Appl. Environ. Microbiol.*, vol. 55, no. 4, pp. 832–6, Apr. 1989, Accessed: Mar. 09, 2017. [Online]. Available: http://www.ncbi.nlm.nih.gov/pubmed/2499255.

[114] Z. B. Bundur, A. Amiri, Y. C. Ersan, N. Boon, and N. De Belie, “Impact of air entraining admixtures on biogenic calcium carbonate precipitation and bacterial viability,” *Cem. Concr. Res.*, vol. 98, no. January, pp. 44–49, 2017, doi: 10.1016/j.cemconres.2017.04.005.

[115] S. Liu, Z. Basaran, J. Zhu, and R. Douglas, “Evaluation of self-healing of internal cracks in biomimetic mortar using coda wave interferometry,” *Cem. Concr. Res.*, vol. 83, pp. 70–78, 2016, doi: 10.1016/j.cemconres.2016.01.006.

[116] V. Achal, a. Mukherjee, P. C. Basu, and M. S. Reddy, “Lactose mother liquor as an alternative nutrient source for microbial concrete production by Sporosarcina pasteurii,” *J. Ind. Microbiol. Biotechnol.*, vol. 36, pp. 433–438, 2009, doi: 10.1007/s10295-008-0514-7.

[117] V. Achal, A. Mukherjee, and M. S. Reddy, “Biocalcification by Sporosarcina pasteurii using corn steep liquor as the nutrient source,” *Orig. Reseacr Ind. Biotechnol.*, no. October 2015, pp. 170–174, 2010, doi:

10.1089/ind.2010.6.170.

[118] A. Amiri and Z. B. Bundur, “Use of corn-steep liquor as an alternative carbon source for biomineralization in cement-based materials and its impact on performance,” *Constr. Build. Mater.*, vol. 165, pp. 655–662, 2017, doi: 10.1016/j.conbuildmat.2018.01.070.

[119] R. W. Liggett and H. Koffler, “Corn steep liquor in microbiology,” *Bacteriol. Rev.*, vol. 12, no. 4, pp. 297–311, 1948.

[120] A. Fahmi, H. Katebi, M. H. Bonab, and H. S. Kafil, “Microbial sand stabilization using corn steep liquor culture media and industrial calcium reagents in cementation solutions,” *Ind. Biotechnol.*, vol. 14, no. 5, 2018.

[121] A. B. Amini, M. Faraji, S. Babakhani, H. Samadi, and A. Fahmi, “Improvement of mortar samples using the bacterial suspension cultured in the industrial corn steep liquor media,” *Ind. Biotechnol.*, vol. 18, no. 3, pp. 162–167, 2022.

[122] M. S. R. Sumit Joshi, Shweta Goyal, “Corn steep liquor as a nutritional source for biocementation and its impact on concrete structural properties,” *Ind. Microbiol. Biotechnol.*, vol. 45, no. 8, pp. 657–667, 2018.

[123] V. S. Whiffin, “Microbial $CaCO_3$ Precipitation for the production of Biocement,” Murdoch University, Thesis, 2004.

[124] K. Paine, “Bacteria-based self-healing of concrete: effects of environment, exposure and crack size,” in *Proceedings of the RILEM Conference on Microorganisms-Cementitious Materials Interactions*, 2016, vol. 10, no. 1, pp. 97–114.

[125] J. T. Dejong, M. B. Fritzges, and K. Nüsslein, “Microbially induced cementation to control sand response to undrained shear,” *J. Geotech. Geoenvironmental Eng.*, no. November, pp. 1381–1392, 2006.

[126] S. K. Ramachandran, V. Ramakrishnan, and S. S. Bang, “Remediation of concrete using microorganisms,” *ACI Mater. J.*, no. 98, pp. 3–9, 2001.

[127] V. Achal, A. Mukerjee, and M. Sudhakara Reddy, “Biogenic treatment improves the durability and remediates the cracks of concrete structures,” *Constr. Build. Mater.*, vol. 48, pp. 1–5, Nov. 2013, doi: 10.1016/j.conbuildmat.2013.06.061.

[128] F. Bravo, D. Silva, N. Boon, W. Verstraete, and N. De Belie, “Screening of bacteria and concrete compatible protection materials,” *Contruction Build. Mateirlas*, vol. 88, pp. 196–203, 2015, doi: 10.1016/j.conbuildmat.2015.04.027.

[129] K. Paine *et al.*, “Microencapsulated spores and growth media for self-healing mortars,” in *Life-Cycle Analysis and Assessment in Civil Engineering: Towards an Integrated Vision - Proceedings of the 6th International Symposium on Life-Cycle Civil Engineering, IALCCE 2018*, 2018, pp. 2247–2253.

[130] A. Amiri, “Use of biomineralization in self-healing cement-based materials,” Özyeğin University, Thesis, 2017.

[131] B. J. Reeksting, T. D. Hoffmann, L. Tan, K. Paine, and S. Gebhard, “In-depth profiling of calcite precipitation by environmental bacteria reveals

fundamental mechanistic differences with relevance to application," *Appl. Environ. Microbiol.*, vol. 86, no. 7, pp. 1–16, 2020, doi: 10.1128/AEM.02739-19.

[132] A. Bentur, "Effect of gypsum on the hydration and strength of C_3S pastes," *Am. Ceram. Soc.*, no. 59, pp. 210–213, 1976.

[133] I. Pane and W. Hansen, "Investigation of blended cement hydration by isothermal calorimetry and thermal analysis," *Cem. Concr. Res.*, no. 35, pp. 1155–1164, 2005.

[134] E. Berodier and K. Scrivener, "Understanding the filler effect on the nucleation and growth of C-S-H," *J. Am. Ceram. Soc.*, no. 97, pp. 3764–3773, 2014.

[135] I. Wadsö and L. Wadsö, "Systematic errors in isothermal micro-and nanocalorimetry," *J. Therm. Anal. Calorim.*, no. 82, pp. 553–558, 2005.

[136] L. Wadsö, "Operational issues in isothermal calorimetry," *Cem. Concr. Res.*, no. 40, pp. 1129–1137, 2010.

[137] E. Tajuelo Rodriguez, K. Garbev, D. Merz, L. Black, and I. G. Richardson, "Thermal stability of C-S-H phases and applicability of Richardson and Groves' and Richardson C-(A)-S-H(I) models to synthetic C-S-H," *Cem. Concr. Res.*, vol. 93, pp. 45–56, 2017, doi: 10.1016/j.cemconres.2016.12.005.

[138] V. S. Ramachandran and J. J. Beaudoin, *Handbook of analytical techniques in concrete science and technology*. Elsevier, 2000.

[139] M. Thiery, G. Villain, P. Dangla, and G. Platret, "Investigation of the carbonation front shape on cementitious materials: Effects of the chemical kinetics," *Cem. Concr. Res.*, vol. 37, pp. 1047–1058, 2007.

[140] S. Vinnakota, "Understanding the long-term evolution of C-S-H phases present in cement backfills," Civil engineering Department, University of Leeds, Thesis, 2019.

[141] B. K. Marsh and D. R.L., "Pozzolanic and cementitious reactions of fly ash in blended cement pastes," *Cem. Concr. Res*, pp. 301–310, 1988.

[142] A. K. Chatterji, "X-Ray diffraction," *Anal. Tech. Concr. Sci. Technol.*, pp. 275–332, 1958.

[143] E. T. Rodriguez, "Relation between composition, structure and morphology in C-S-H," Leeds, 2015.

[144] K. Scrivener, R. Snellings, B. Lothenbach, and Eds, *A practical guide to microstructural analysis of cementitious materials*. Crc press, 2016.

[145] N. V. Y. Scarlett and I. C. Madsen, "Quantification of phases with partial or no known crystal structures," *Powder Diffr.*, no. 64, pp. 89–98, 2006.

[146] R. Snellings, A. Salze, and K. L. Scrivener, "Use of X-ray diffraction to quantify amorphous supplementary cementitious materials in anhydrous and hydrated blended cements," *Cem. Concr. Res.*, no. 64, pp. 89–98, 2014.

[147] D. L. Bish and S. Howard, "Quantitative phase analysis using the Rietveld method," *J. Appl. Crystallogr.*, no. 21, pp. 86–91, 1988.

[148] H. Rietveld, “A profile refinement method for nuclear and magnetic structures,” *J. Appl. Crystallogr.*, no. 2, pp. 65–71, 1969.

[149] K. L. Scrivener, T. Füllmann, E. Gallucci, G. Walenta, and E. Bermejo, “Quantitative study of Portland cement hydration by X-ray diffraction/Rietveld analysis and independent methods,” *Cem. Concr. Res.*, no. 34, pp. 1541–1547, 2004.

[150] L. McCusker, R. Von Dreele, D. Cox, D. Louer, and P. Scardi, “Rietveld refinement guidelines,” *J. Appl. Crystallogr.*, no. 32, pp. 36–50, 1999.

[151] D. Jansen, C. Stabler, F. Goetz-Neunhoeffer, S. Dittrich, and J. Neubauer, “Does Ordinary Portland Cement contain amorphous phase? A quantitative study using an external standard method,” *, Powder Diffr.*, no. 26, pp. 31–38, 2011.

[152] F. H. Chung, “Quantitative interpretation of X-ray diffraction patterns of mixtures. I. Matrix-flushing method for quantitative multicomponent analysis,” *J. Appl. Crystallogr.*, no. 7, pp. 519–525, 1974.

[153] F. H. Chung, “Quantitative interpretation of X-ray diffraction patterns of mixtures. III. Simultaneous determination of a set of reference intensities,” *J. Appl. Crystallogr.*, no. 8, pp. 17–19, 1975.

[154] D. Jansen, F. Goetz-Neunhoeffer, C. Stabler, and J. Neubauer, “A remastered external standard method applied to the quantification of early OPC hydration,” *Cem. Concr. Res.*, no. 41, pp. 602–608, 2011.

[155] P. M. Suherman, A. van Riessen, B. O’Connor, D. Li, D. Bolton, and H. Fairhurst, “Determination of amorphous phase levels in Portland cement clinker,” *Powder Diffr.*, no. 17, pp. 178–185, 2002.

[156] G. Le Saout and K. Scrivener, “Early Hydration of Portland Cement with Corundum Addition,” in *16 Internationale Baustofftagung (ibausil)*, 2006, pp. 409–416.

[157] A. D. La Torre, S. Bruque, and M. Aranda, “Rietveld quantitative amorphous content analysis,” *J. Appl. Crystallogr.*, no. 34, pp. 196–202, 2001.

[158] I. C. Madsen, N. V. Scarlett, and A. Kern, “Description and survey of methodologies for the determination of amorphous content via X-ray powder diffraction,” *Cryst. Mater.*, no. 226, pp. 944–955, 2011.

[159] B. H. O’Connor and M. D. Raven, “Application of the Rietveld refinement procedure in assaying powdered mixtures, Powder Diffraction,” *Powder Diffr.*, no. 3, pp. 2–6, 1988.

[160] R. Von Dreele, “Quantitative texture analysis by Rietveld refinement,” *J. Appl. Crystallogr.*, no. 30, pp. 517–525, 1997.

[161] L. McCusker, R. Von Dreele, D. Cox, D. Louer, and P. Scardi, “Rietveld refinement guidelines, Journal of Applied Crystallography,” *J. Appl. Crystallogr.*, no. 32, pp. 36–50, 1999.

[162] M. Ben Haha, K. De Weerdt, and B. Lothenbach, “Quantification of the degree of reaction of fly ash,” *Cem. Concr. Res.*, no. 40, pp. 1620–1629, 2010.

[163] V. Kocaba, E. Gallucci, and K. L. Scrivener, “Methods for determination of degree of reaction of slag in blended cement pastes,” *Cem. Concr. Res.*, no. 42, pp. 511–525, 2012.

[164] K. L. Scrivener, “Backscattered electron imaging of cementitious microstructures: Understanding and quantification,” *Cem. Concr. Compos.*, vol. 26, no. 8, pp. 935–945, 2004, doi: 10.1016/j.cemconcomp.2004.02.029.

[165] W. Reusch, “Nuclear Magnetic Resonance Spectroscopy,” Michigan State Univ., 2013.

[166] M. Smith and K. Mackenzie, “Multinuclear solid-state NMR of inorganic materials,” *Multinucl. Solid-State NMR Inorg. Mater.*, vol. 6, pp. 5–7, 2002.

[167] J. A. Iggo, *NMR spectroscopy in inorganic chemistry*. Oxford University Press, 2001.

[168] M. Mägi, E. Lippmaa, A. Samoson, G. Engelhardt, and A. R. Grimmer, “Solid-state high-resolution silicon-29 chemical shifts in silicates,” *Phys. Chem.*, vol. 88, no. 8, pp. 1518–1522, 1984.

[169] J. Hirljac, Z. Q. Wu, and J. F. Young, “Silicate polymerization during the hydration of alite,” *Cem. Concr. Res.*, vol. 13, pp. 877–886, 1983.

[170] J. Francis, “Investigations of calcium silicate hydrate structure using silicon-29 Nuclear Magnetic Resonance Spectroscopy,” *Am. Ceram. Soc.*, vol. 120, pp. 118–120, 1988.

[171] J. A. Herterich, “Microstructure and phase assemblage of low-clinker cements during early stages of carbonation,” University of Leeds, Thesis, 2017.

[172] I. G. Richardson and G. W. Groves, “The structure of the calcium silicate hydrate phases present in hardened pastes of white Portland cement/blast-furnace slag blends,” *J. Mater. Sci.*, vol. 32, pp. 4793–4802, 1997.

[173] I. G. Richardson, A. R. Brough, R. Brydson, G. W. Groves, and C. M. Dobson, “Location of aluminium in substituted calcium silicate hydrate (C-S-H) gels as determined by Si-29 and Al-27 NMR and EELS,” *Am. Ceram. Soc.*, vol. 76, pp. 2285–2288, 1993.

[174] S. Thomas, K. Meise-Gresch, W. Müller-Warmuth, and I. Odler, “MAS NMR studies of partially carbonated Portland cement and tricalcium silicate pastes,” *J. Am. Ceram. Soc.*, vol. 76, no. 8, pp. 1998–2004, 1993, doi: 10.1111/j.1151-2916.1993.tb08323.x.

[175] T. F. Sevelsted and J. Skibsted, “Carbonation of C-S-H and C-A-S-H samples studied by 13C, 27Al and 29Si MAS NMR spectroscopy,” *Cem. Concr. Res.*, vol. 71, pp. 56–65, 2015, doi: 10.1016/j.cemconres.2015.01.019.

[176] Y. Tong, H. Du, and L. Fei, “Comparison between the hydration processes of tricalcium silicate and beta-dicalcium silicate,” *Cem. Concr. Res.*, vol. 21, no. 4, pp. 509–514, 1991, doi: 10.1016/0008-8846(91)90100-V.

[177] I. G. Richardson, A. V. Girão, R. Taylor, and S. Jia, “Hydration of water- and alkali-activated white Portland cement pastes and blends with low-

calcium pulverized fuel ash," *Cem. Concr. Res.*, vol. 83, pp. 1–18, 2016, doi: 10.1016/j.cemconres.2016.01.008.

[178] E. Tajuelo Rodriguez, K. Garbev, D. Merz, L. Black, and I. G. Richardson, "Thermal stability of C-S-H phases and applicability of Richardson and Groves' and Richardson C-(A)-S-H(I) models to synthetic C-S-H," *Cem. Concr. Res.*, vol. 93, pp. 45–56, 2017, doi: 10.1016/j.cemconres.2016.12.005.

[179] J. Skibsted, H. J. Jakobsen, and C. Hall, "Direct observation of aluminum guest ions in the silicate phases of cement minerals by ^{27}Al MAS NMR spectroscopy," *J. Chem. Soc. Trans.*, vol. 90, no. 14, pp. 2095–2098, 1994.

[180] K. Van Tittelboom, N. De Belie, W. De Muynck, and W. Verstraete, "Use of bacteria to repair cracks in concrete," *Cem. Concr. Res.*, vol. 40, no. 1, pp. 157–166, 2010, doi: 10.1016/j.cemconres.2009.08.025.

[181] Z. B. Bundur, A. Amiri, Y. C. Ersan, N. Boon, and N. De Belie, "Impact of air entraining admixtures on biogenic calcium carbonate precipitation and bacterial viability," *Cem. Concr. Res.*, vol. 98, no. July 2016, pp. 44–49, 2017, doi: 10.1016/j.cemconres.2017.04.005.

[182] V. Achal, A. Mukherjee, S. Goyal, and M. S. Reddy, "Corrosion prevention of reinforced concrete with microbial calcite precipitation," *ACI Mater. J.*, vol. 109, no. 109, pp. 157–164, 2012.

[183] V. Achal, a. Mukherjee, and M. S. Reddy, "Effect of calcifying bacteria on permeation properties of concrete structures," *J. Ind. Microbiol. Biotechnol.*, vol. 38, pp. 1229–1234, 2011, doi: 10.1007/s10295-010-0901-8.

[184] Y. Fujita, F. G. Ferris, R. D. Lawson, F. S. Colwell, and R. W. Smith, "Subscribed Content Calcium Carbonate Precipitation by Ureolytic Subsurface Bacteria," *Geomicrobiol. J.*, vol. 17, no. January 2012, pp. 305–318, 2000, doi: 10.1080/782198884.

[185] G. Le Saoût, V. Kocaba, and K. Scrivener, "Application of the Rietveld method to the analysis of anhydrous cement," *Cem. Concr. Res.*, no. 41, pp. 133–148, 2011.

[186] L. Mitchell, P. Whitfield, and J. Beaudoin, "The effects of particle statistics on quantitative Rietveld analysis of cement," in *12th International congress on the Chemistry of Cement*, 2007, pp. 1–12.

[187] R. Snellings, A. Bazzoni, and K. Scrivener, "The existence of amorphous phase in Portland cements: Physical factors affecting Rietveld quantitative phase analysis," *Cem. Concr. Res.*, no. 59, pp. 139–146, 2014.

[188] D. Jansen, F. Goetz-Neunhoeffer, B. Lothenbach, and J. Neubauer, "The early hydration of Ordinary Portland Cement (OPC): An approach comparing measured heat flow with calculated heat flow from QXRD," *Cem. Concr. Res.*, no. 42, pp. 134–138, 2012.

[189] S. T. Bergold, F. Goetz-Neunhoeffer, and J. Neubauer, "Influence of the reactivity of the amorphous part of mechanically activated alite on its hydration kinetics," *Cem. Concr. Res.*, no. 88, pp. 73–81, 2016.

[190] C. Stuckrath, R. Serpell, L. M. Valenzuela, and M. Lopez, “Quantification of chemical and biological calcium carbonate precipitation: Performance of self-healing in reinforced mortar containing chemical admixtures,” *Cem. Concr. Compos.*, vol. 50, pp. 10–15, 2014, doi: 10.1016/j.cemconcomp.2014.02.005.

[191] Adu-amankwah, “Relationship between microstructure, durability and performance of CEM X composite cements,” University of Leeds, Thesis, 2016.

[192] M. J. Duer, *Solid-state NMR spectroscopy principles and applications*. Oxford Blackwell Science Ltd, 2002.

[193] J. Xu and W. Yao, “Multiscale mechanical quantification of self-healing concrete incorporating non-ureolytic bacteria-based healing agent,” *Cem. Concr. Res.*, vol. 64, pp. 1–10, 2014, doi: 10.1016/j.cemconres.2014.06.003.

[194] T. Ogino, T. Suzuki, and K. Sawada, “The formation and transformation mechanism of calcium carbonate in water,” *Geochim. Cosmochim. Acta*, vol. 51, pp. 2757–2767, 1987, doi: 10.1016/0016-7037(87)90155-4.

[195] K. L. Scrivener, “The development of microstructure during the hydration of Portland cement.,” Imperial College of Science and Technology University of London, Thesis, 1984.

[196] V.S. Ramachandran and M. S. Lowery, “Conduction calorimetric investigation of the effect of retarders on the hydration of Portland cement,” *Thermochim. Acta*, vol. 195, pp. 373–387, 1991.

[197] F. Massazza, “Admixtures in Concrete,” *Adv. Cem. Technol.*, pp. 569–648, 1983.

[198] S. Mwaluwing, T. Ayano, and K. Sakata, “Influence of urea in concrete,” *Cem. Concr. Res.*, pp. 733–745, 1997.

[199] G. Plusquellec and A. Nonat, “Interactions between calcium silicate hydrate (C-S-H) and calcium chloride, bromide and nitrate,” *Cem. Concr. Res.*, vol. 90, pp. 89–96, 2016, doi: 10.1016/j.cemconres.2016.08.002.

[200] A. M. Grabiec, “Contribution to the knowledge of melamine superplasticizer effect on some characteristics of concrete after long periods of hardening,” *Cem. Concr. Res.*, 1999, doi: 10.1016/S0008-8846(99)00024-1.

[201] A. M. Rashad, “Effects of ZnO_2, ZrO_2, Cu_2O_3, CuO, $CaCO_3$, SF, FA, cement and geothermal silica waste nanoparticles on properties of cementitious materials - A short guide for Civil Engineer,” *Constr. Build. Mater.*, vol. 48, pp. 1120–1133, 2013, doi: 10.1016/j.conbuildmat.2013.06.083.

[202] Y. Chen and C. Qian, “Characterization Methods for the Effect of Microbial Mineralization on the Microstructure of Hardened C3S Paste,” *Adv. Mater. Sci. Eng.*, 2020.

[203] F. S. Murakami, P. O. Rodrigues, C. M. T. De Campos, and M. A. S. Silva, “Physicochemical study of $CaCO_3$ from egg shells,” *Cienc. e Tecnol. Aliment.*, vol. 27, no. 3, pp. 658–662, 2007, doi: 10.1590/S0101-

20612007000300035.

[204] G. Villain, M. Thiery, and G. Platret, “Measurement methods of carbonation profiles in concrete: Thermogravimetry, chemical analysis and gammadensimetry,” *Cem. Concr. Res.*, vol. 37, no. 8, pp. 1182–1192, 2007, doi: 10.1016/j.cemconres.2007.04.015.

[205] A. V. Radha, T. Z. Forbes, C. E. Killian, P. U. P. A. Gilbert, and A. Navrotsky, “Transformation and crystallization energetics of synthetic and biogenic amorphous calcium carbonate,” *Proc. Natl. Acad. Sci. U. S. A.*, vol. 107, no. 38, pp. 16438–16443, 2010, doi: 10.1073/pnas.1009959107.

[206] G. Wolf and C. Günther, “Thermophysical investigations of the polymorphous phases of calcium carbonate,” *J. Therm. Anal. Calorim.*, vol. 65, no. 3, pp. 687–698, 2001, doi: 10.1023/A:1011991124181.

[207] L. M. Barcina, A. Espina, M. Suárez, J. R. García, and J. Rodríguez, “Characterization of monumental carbonate stones by thermal analysis (TG, DTG and DSC),” *Thermochim. Acta*, vol. 290, no. 2, pp. 181–189, 1997, doi: 10.1016/S0040-6031(96)03074-2.

[208] N. Koga and Y. Yamane, “Thermal behaviors of amorphous calcium carbonates prepared in aqueous and ethanol media,” *J. Therm. Anal. Calorim.*, vol. 94, no. 2, pp. 379–387, 2008, doi: 10.1007/s10973-008-9110-3.

[209] E. Lippmma, “Structural studies of silicates by solid-state high-resolution silicon-29 NMR,” *Am. Ceram. Soc.*, no. 102, pp. 4889–4893, 1980.

[210] E. Lippmma, “A high resolution ^{29}Si NMR study of the hydration of tricalciumsilicate.,” *Cem. Concr. Res.*, no. 29, pp. 45–56, 1982.

[211] X. Cong and R. J. Kirkpatrick, “^{29}Si MAS NMR study of the structure of calcium silicate hydrate.,” *Adv. Cem. Based Mater.*, no. 3, pp. 144–156, 1996.

[212] I. G. Richardson and G. W. Groves, “The structure of the calcium silicate hydrate phases present in hardened pastes of white portland cement GGBFS,” *J. Mater. Sci.*, no. 32, pp. 4793–4802, 1997.

[213] I. G. Richardson and J. G. Cabrera, “The nature of C-S-H in model slag-cements,” *Cem. Concr. Compos.*, no. 22, pp. 259–266, 2000.

[214] E. L’Hôpital, B. Lothenbach, G. Le Saout, D. Kulik, and K. Scrivener, “Incorporation of aluminium in calcium-silicate-hydrates,” *Cem. Concr. Res.*, vol. 75, pp. 91–103, 2015, doi: 10.1016/j.cemconres.2015.04.007.

[215] J. J. Gaitero, W. Zhu, and I. Campillo, “Multi-scale study of calcium leaching in cement pastes with silica nanoparticles,” *Nanotechnol. Constr. Springer*, no. 3, pp. 193–198, 2009.

[216] E. Lippmaa, M. Mägi, M. Tarmak, W. Wieker, and A. R. Grimmer, “A high resolution ^{29}Si NMR study of the hydration of tricalciumsilicate.,” *Cem. Concr. Res.*, vol. 12, no. 5, pp. 597–602, 1982, doi: 10.1016/0008-8846(82)90020-5.

[217] V. Kocaba, “Development and evaluation of methods to follow microstructural development of cementitious systems including slags,” École Polytechnique Federale de Lausanne.

[218] I. G. Richardson and G. W. Groves, “Models for the composition and structure of calcium silicate hydrate (C-S-H) gel in hardened tricalcium silicate pastes.,” *Cem. Concr. Res.*, no. 22, pp. 1101–1110, 1992.

[219] I. G. Richardson, “The calcium silicate hydrates,” *Cem. Concr. Res.*, no. 38, pp. 137–158, 2008.

[220] V. Wiktor and H. M. Jonkers, “Quantification of crack-healing in novel bacteria-based self-healing concrete,” *Cem. Concr. Compos.*, vol. 33, pp. 763–770, 2011, doi: 10.1016/j.cemconcomp.2011.03.012.

Appendix A

Igor Pro Code used for ^{29}Si NMR deconvolution

.IPF code:

```
#pragma rtGlobals=1                    // Use modern global access method.
function (filename) //filename of the form filename="name.txt" for e.g
string filename
NewPath/O Path1 "M:lab folder:NMR:" //Here you need to change path name please do not forget the colon at the end!
Loadwave/G/D/N=temp/O/P=path1 filename
//wave N278_spect
//infotochange=waveinfo(N278_spect,0)
duplicate/O temp1,N278_spect
wave temp0
variable a=temp0[0] //First point of x wave
variable np=numpnts(temp0)
variable b=temp0[(np-1)] //Last point of x wave
//variable delta = b-a
setscale x, a, b, N278_spect //a=first x value and b=last x value
killwaves/Z temp0, temp1
//wave temp0
//variable a=temp0[0]
//variable b=temp0[1]
//variable/G delta = b-a
//waveinfo
End
```

First cycle of curve fitting followed by relaxation of shape, width and intensity:

•Initialize(59.5561921333)

General binary file load from "data" (16384 total bytes)

Data length: 2048, waves: temp0, temp1

2048

Applying 10 Hz exponential linebroadening to N278

Transforming N278 ; 8192 pnts; -938.888 ppm to 740.199 ppm.

Autophasing N278

V_npnts= 8192; V_numNaNs= 0; V_numINFs= 0; V_avg= 2.79556e+16;

V_Sum= 2.29012e+20; V_sdev= 1.77347e+17; V_rms= 1.79527e+17;

V_adev= 4.9778e+16; V_skew= 7.96939; V_kurt= 65.5367;

V_minloc= -903.014; V_maxloc= -80.9975; V_min= 1.02941e+14;

V_max= 1.74051e+18; V_startRow= 0; V_endRow= 8191;

•SetAxis/A

•Save/C N278_spect as "N278_spect.ibw"

•N278_wt(46.507,21.498)=0

•N278_wt(-40.819,-113.18)=0

•N278_wt(-183.9,-212.4)=0

•make /n=4 coef

•edit coef

•FuncFit baselineSi coef N278_spect /W=N278_wt /I=1 /D=N278_fitted /R

Fit converged properly

N278_fitted= baselineSi(coef,x)

Res_N278_spect= N278_spect - (baselineSi(coef,x))

coef={-2.3275e+07,-3253,51.976,0.011111}

V_chisq= 5.74305e+18; V_npnts= 7575; V_numNaNs= 0; V_numINFs= 0;

V_startRow= 0; V_endRow= 8191; V_startCol= 0; V_endCol= 0;

W_sigma={0.0182,5.72e-05,5.59e-08,1.24e-10}

• N278_fitted= baselineSi(coef,x)

• Res_N278_spect= N278_spect - (baselineSi(coef,x))

•make /o/n=28 coef6

•edit coef6

•make /o/n=28 coef6

•FuncFit/H="111" v7nossb coef6

Appendix B

SEM images of the bacterial samples at 45 days

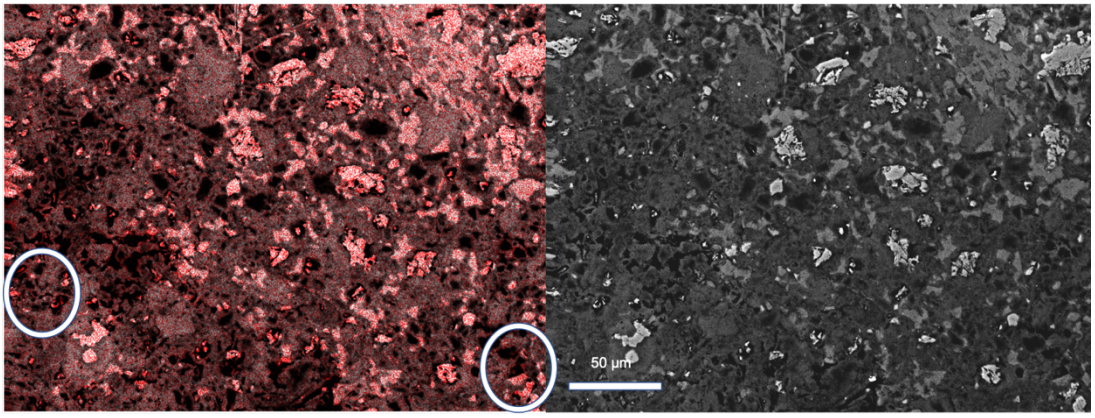

a)Scanning electron microscopy imaging of BO1 at 45 days EDX mapping of Carbon concentration (left) and backscattered image of the same region (Right). Carbon mapping points are covered with the red layer of the EDX analysis (Image on the left).

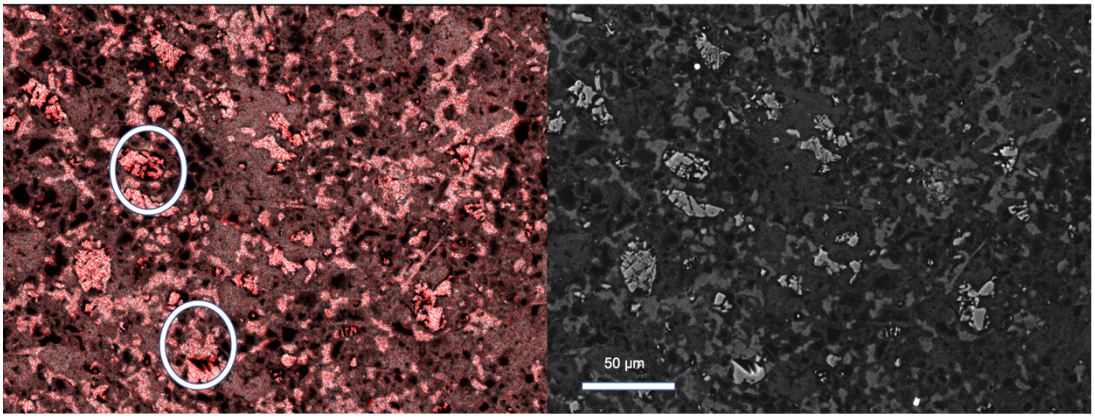

b)Scanning electron microscopy imaging of BO1 at 45 days EDX mapping of Carbon concentration (left) and backscattered image of the same region (Right). Carbon mapping points are covered with the red layer of the EDX analysis (Image on the left).

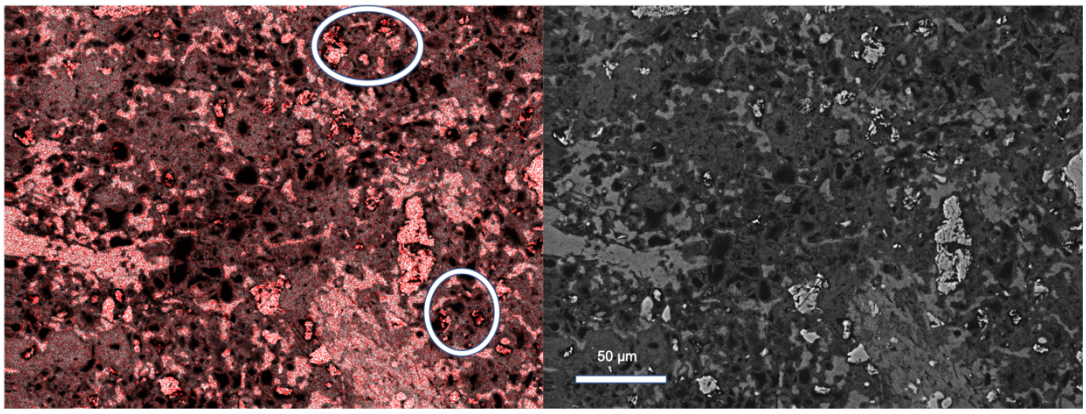

c)Scanning electron microscopy imaging of BO2 at 45 days EDX mapping of Carbon concentration (left) and backscattered image of the same region (Right). Carbon mapping points are covered with the red layer of the EDX analysis (Image on the left).

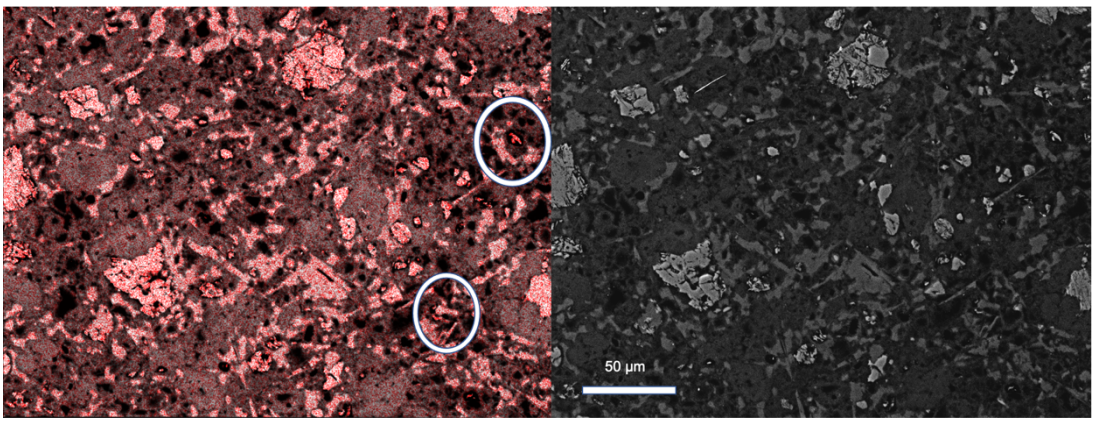

d)Scanning electron microscopy imaging of BO2 at 45 days EDX mapping of Carbon concentration (left) and backscattered image of the same region (Right). Carbon mapping points are covered with the red layer of the EDX analysis (Image on the left).

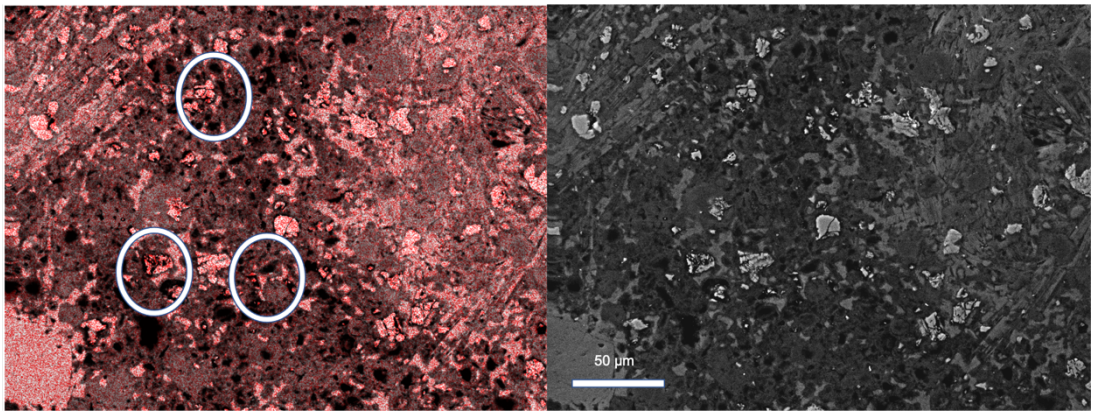

e)Scanning electron microscopy imaging of BC1 at 45 days EDX mapping of Carbon concentration (left) and backscattered image of the same region (Right). Carbon mapping points are covered with the red layer of the EDX analysis (Image on the left).

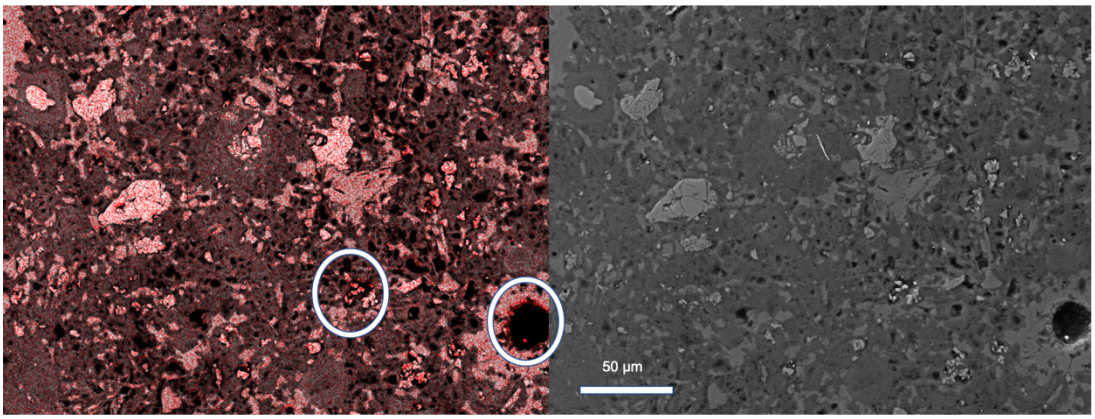

f)Scanning electron microscopy imaging of BC1 at 45 days EDX mapping of Carbon concentration (left) and backscattered image of the same region (Right). Carbon mapping points are covered with the red layer of the EDX analysis (Image on the left).

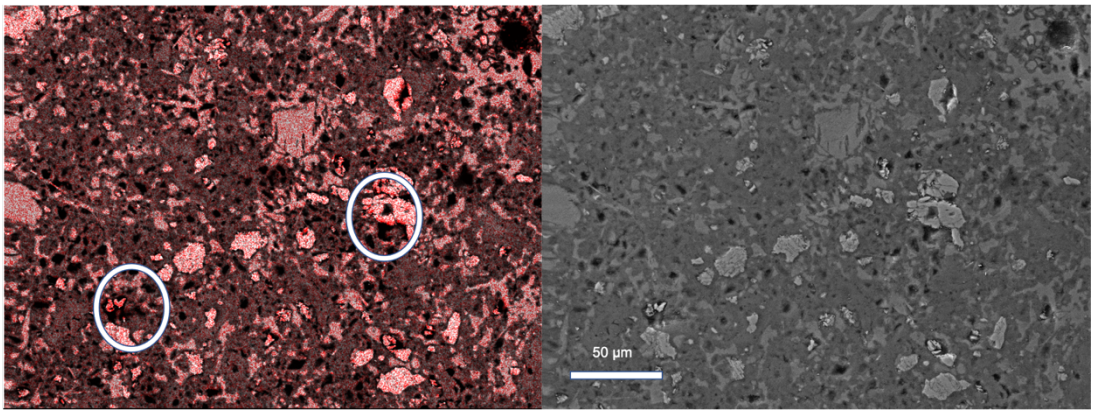

g)Scanning electron microscopy imaging of BC2 at 45 days EDX mapping of Carbon concentration (left) and backscattered image of the same region (Right). Carbon mapping points are covered with the red layer of the EDX analysis (Image on the left).

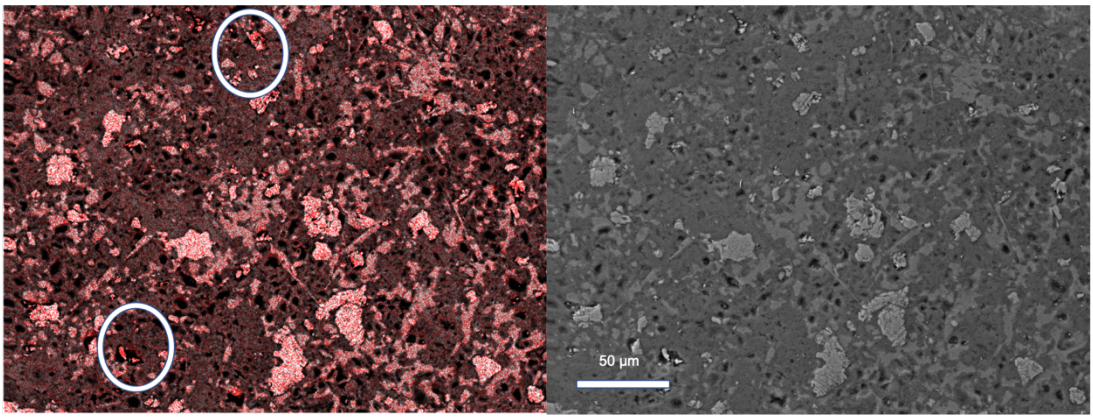

h)Scanning electron microscopy imaging of BC2 at 45 days EDX mapping of Carbon concentration (left) and backscattered image of the same region (Right). Carbon mapping points are covered with the red layer of the EDX analysis (Image on the left).

Appendix C

FT-IR graph for collected precipitation from artificial gap in bacterial samples(Samples contain hydrated wPC paste residue)

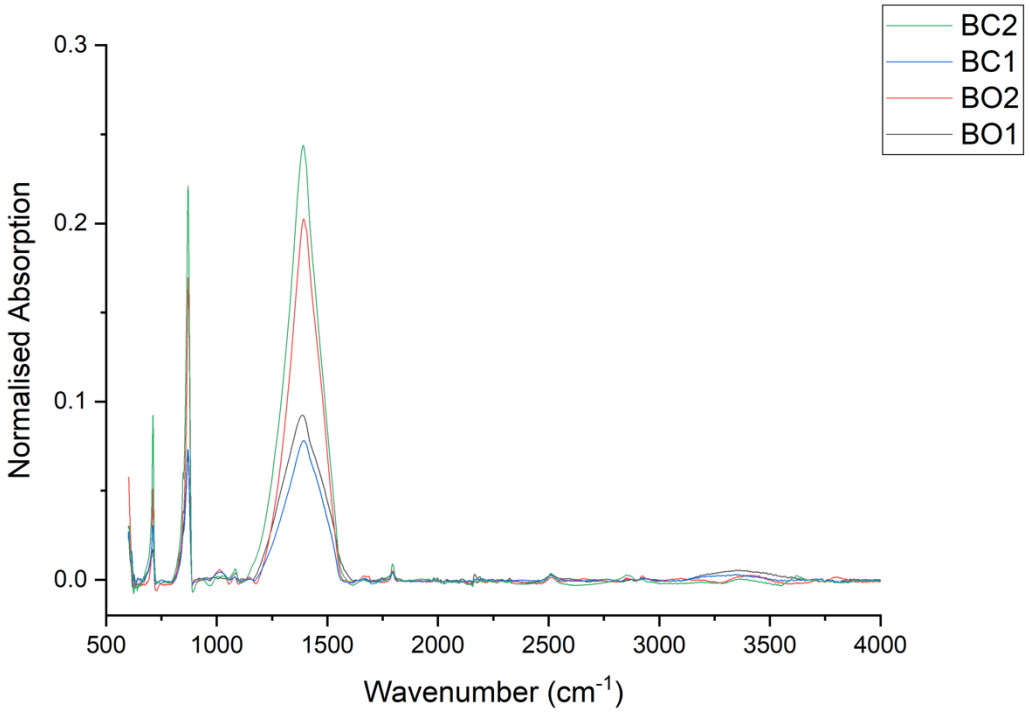

Appendix D

Bacteria strain and data sheet

Sporosarcina pasteurii

DSM 33

BACTERIA

Name:

Sporosarcina pasteurii (Miquel 1889) Yoon et al. 2001

Synonym(s):

Bacillus S. pasteurii (Miquel 1889) Chester 1898

DSM No.: 33, Type strain

Strain designation:

22, Gibson 22

Other collection no. or WDCM no.:

ATCC 11859, CCM 2056, NCIB 8841, NCTC 4822

Isolated from:

soil

Country:

country of origin unknown

Date of sampling:

before 22.08.1990

Nagoya Protocol Restrictions:

There are NO known Nagoya Protocol restrictions for this strain.

History:

<- ATCC <- F.F. Lombard <- T. Gibson, 22

Cultivation conditions:

Medium 220 + urea (20g/l), 30°C

Summary and additional information:

<- ATCC <- F.F. Lombard <- T. Gibson, 22. Soil. Type strain. Taxonomy/description (63, 1300, 3768, 8102). Produces urease (948), urease (80). (Medium 220 + urea (20g/l), 30°C).

Risk group:

1 (classification according to German TRBA)

Appendix E

BASF MasterGlenium 52 superplasticizer

EN 934-2: T3.1 & T3.2

www.master-builders-solutions.com/en-gb

Product Data	
Appearance:	Brown liquid
Specific gravity @ 20°C:	1.10 ± 0.03 g/cm³
pH-value:	7.0 ± 1
Alkali content (%):	≤ 5.00 by mass
Chloride content (%):	≤ 0.10 by mass
Corrosion behaviour:	Contains only components according to BS EN 934-1:2008, Annex A.1
Air Content:	Fulfilled
Water reduction:	≥ 112% of Reference mix
Increase in consistence:	Increase of ≥ 120mm from initial slump or ≥ 160mm from initial flow
Retention of consistence:	At 30 mins ≥ Reference mix at initial
Compressive strength:	Fulfilled
Durability:	NPD
Dangerous substances:	NPD

Appendix F

DTG curves and fitted peaks for bacterial samples at 28 and 45 days

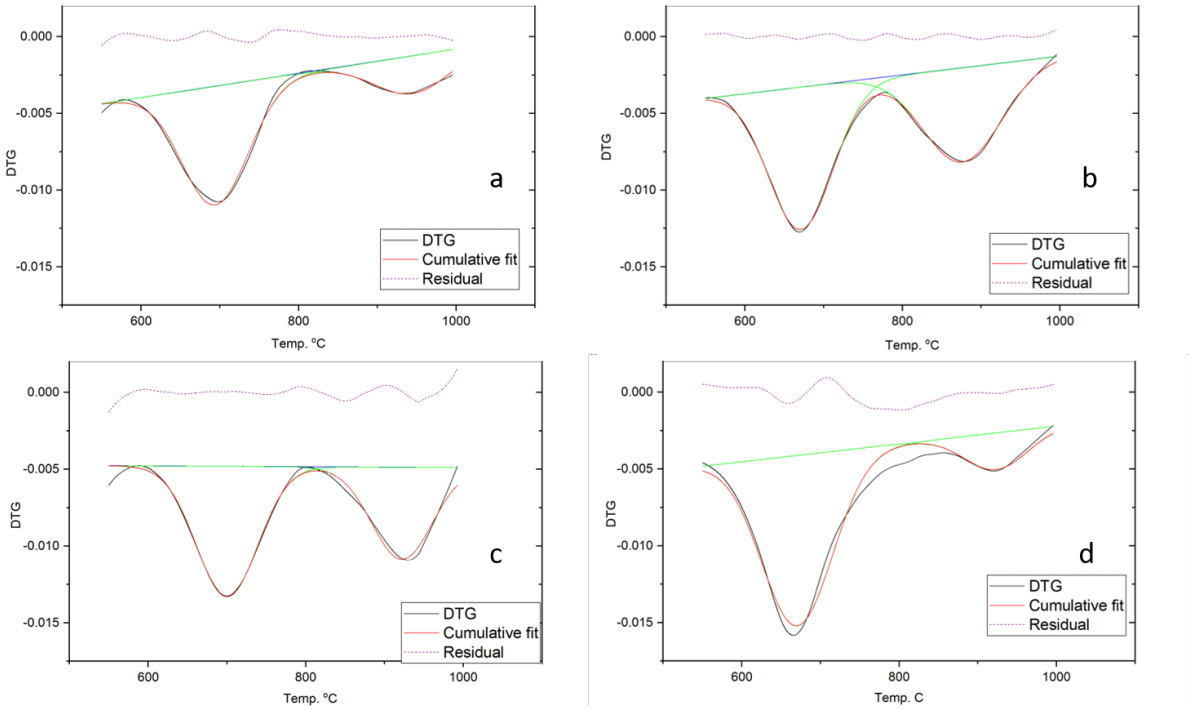

DTG curves, fitted peaks and residue for 28 day sample. (a) BO1, (b) BO2, (c) BC1, (d) BC2. Range : 600 °C to 900 °C.

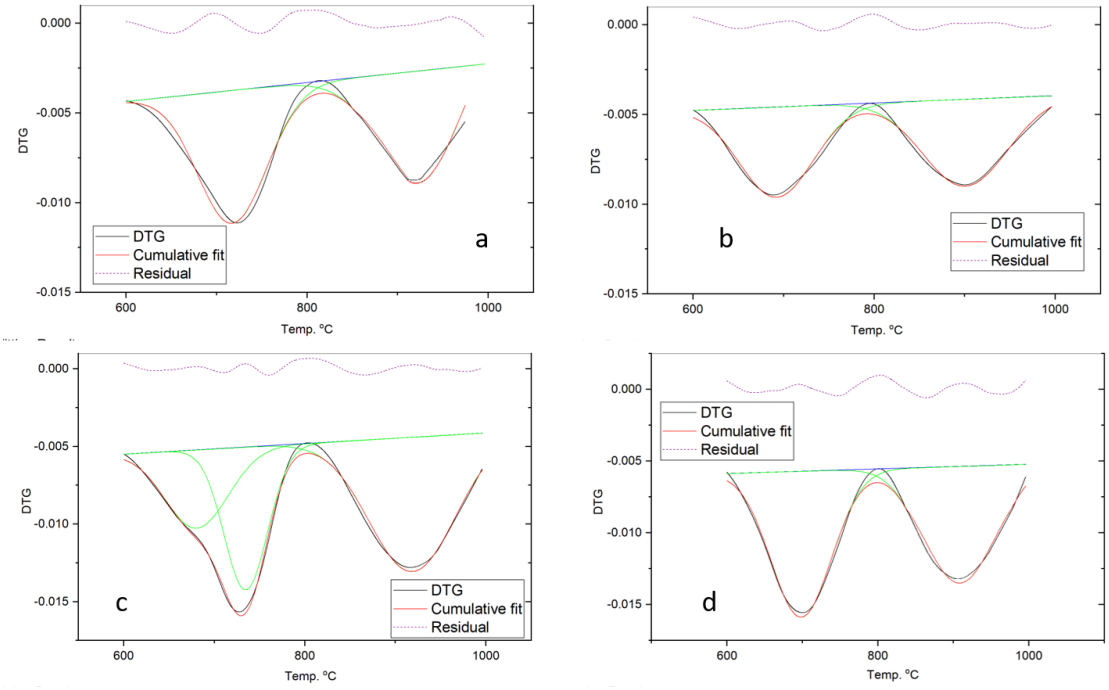

DTG curves, fitted peaks and residue for 45 day sample. (a) BO1, (b) BO2, (c) BC1, (d) BC2. Range : 600 °C to 900 °C.

Appendix G

Quantitative XRD and phase fitting

For all the graphs:

Experiment pattern	———
Fit pattern	———
Residual	———

1) NO1-7

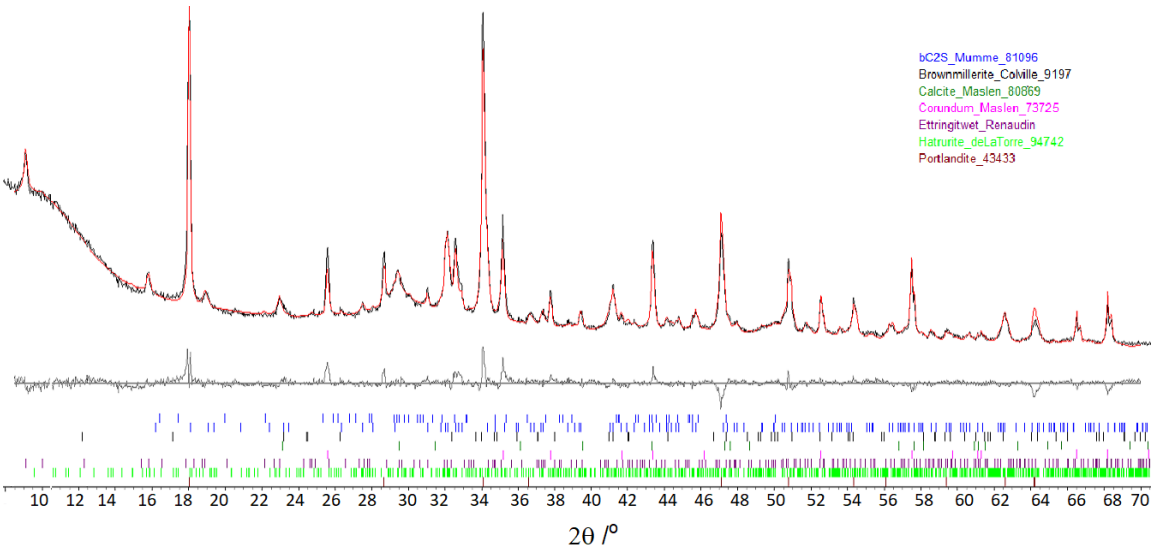

2) NO1-28

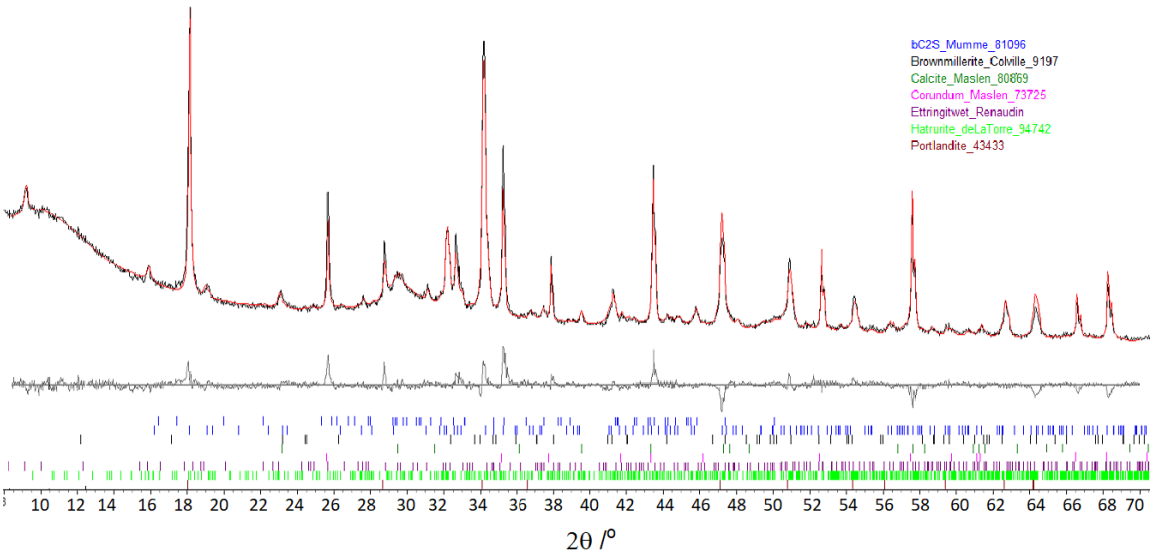

3) NO1-45

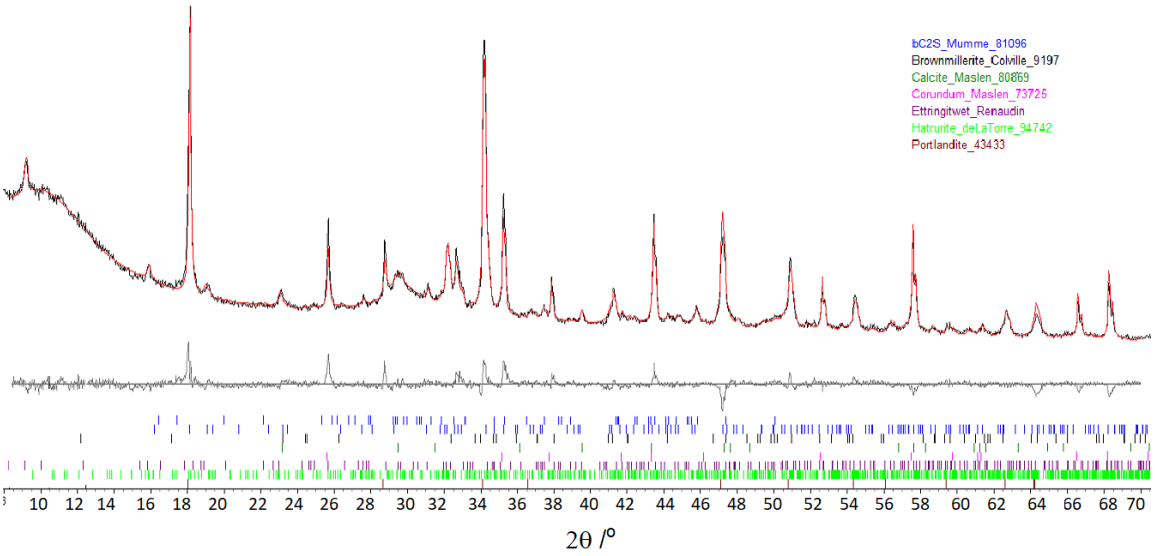

4) NO2-7

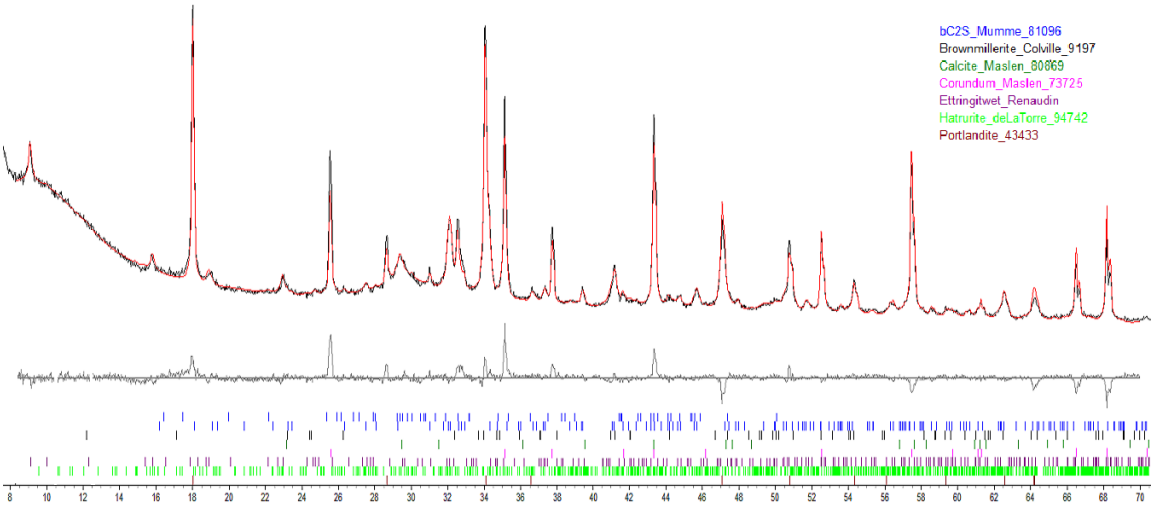

5) NO2-28

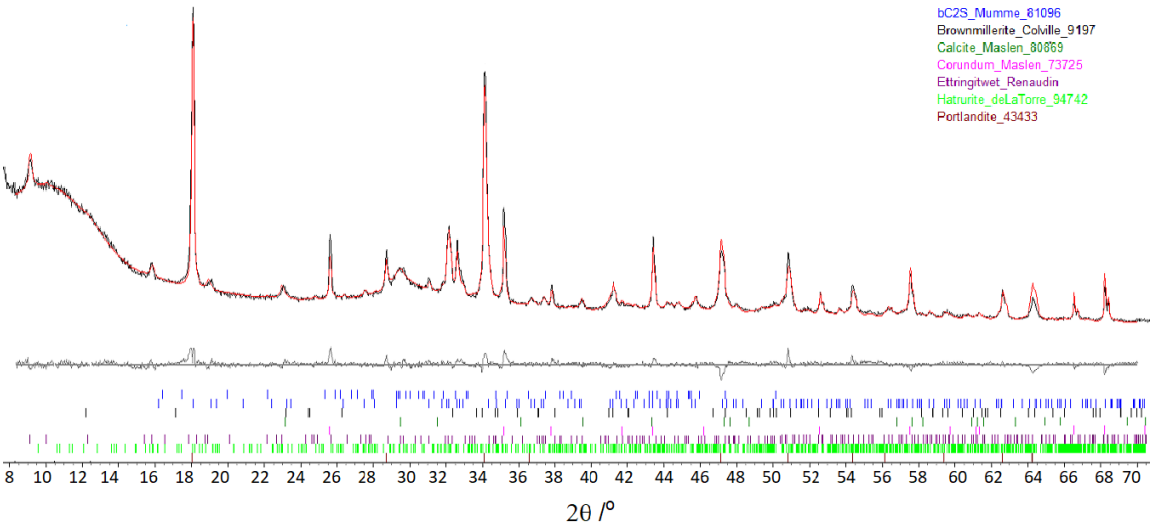

6) NO2-45

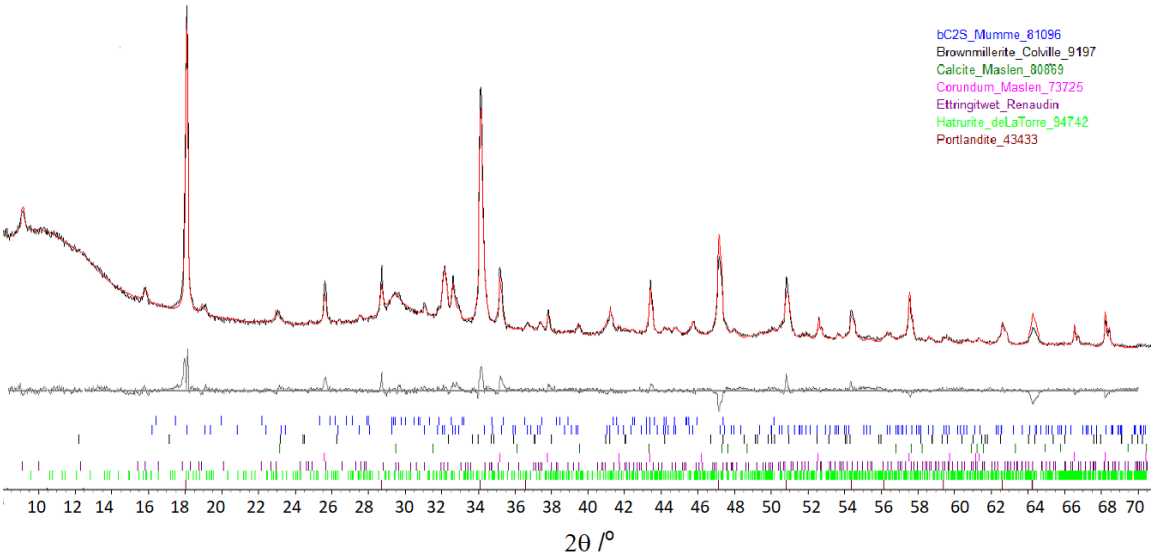

7) NC1-7

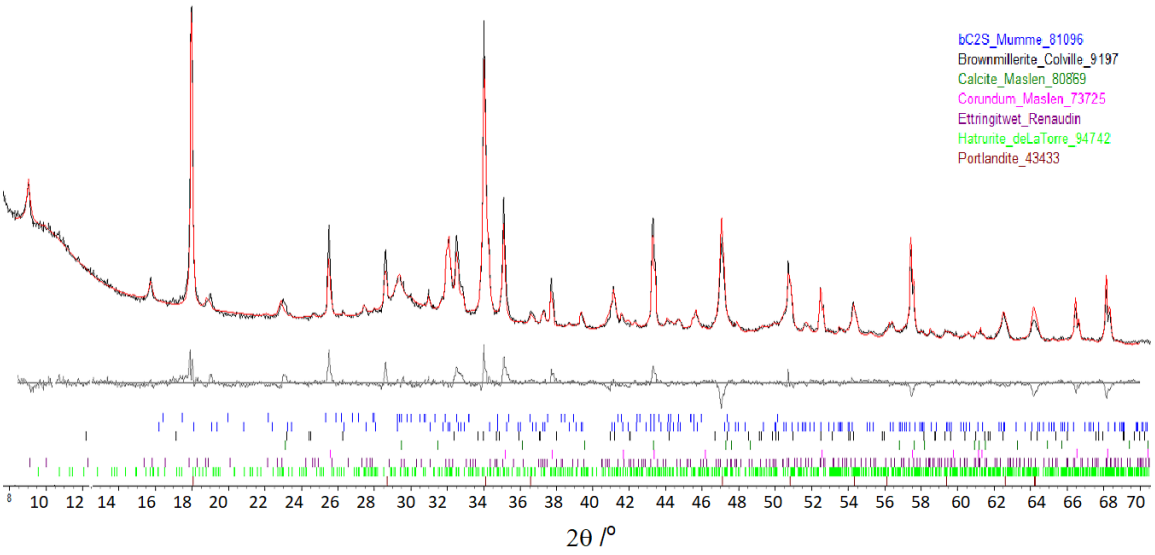

8) NC1-28

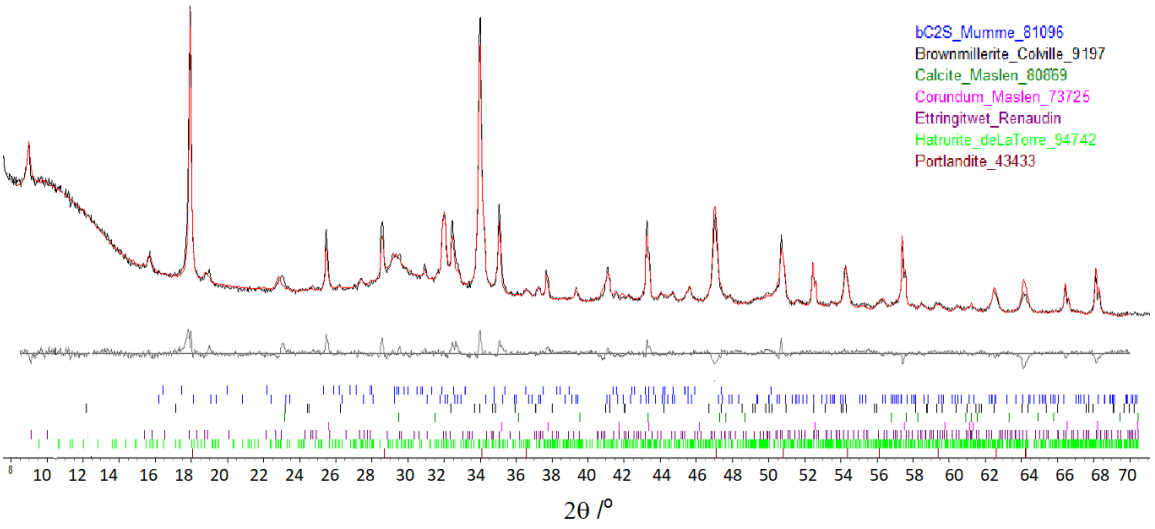

9) NC1-45

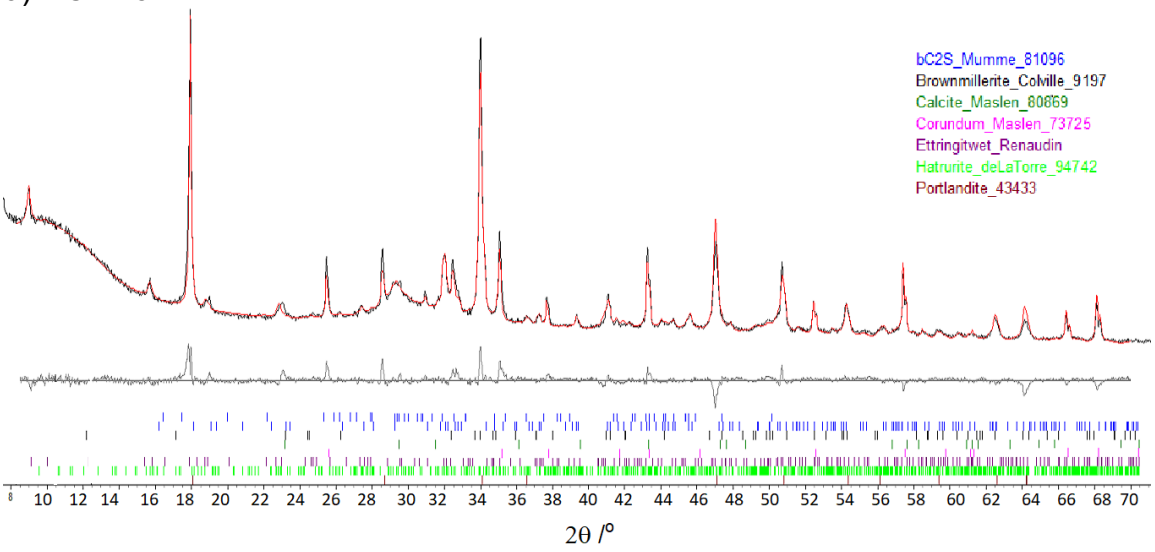

10) NC2-7

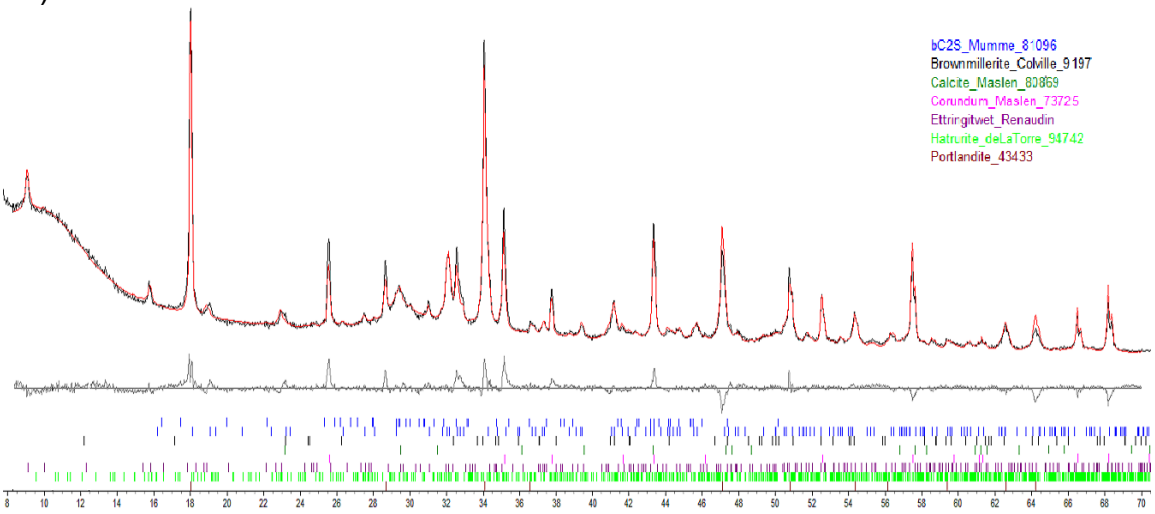

11) NC2-28

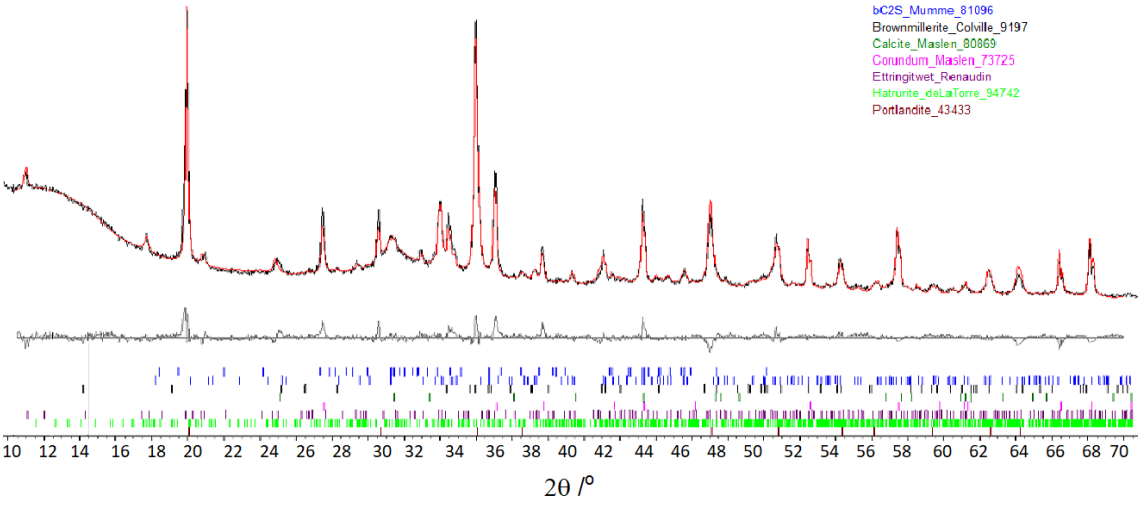

12) NC2-45

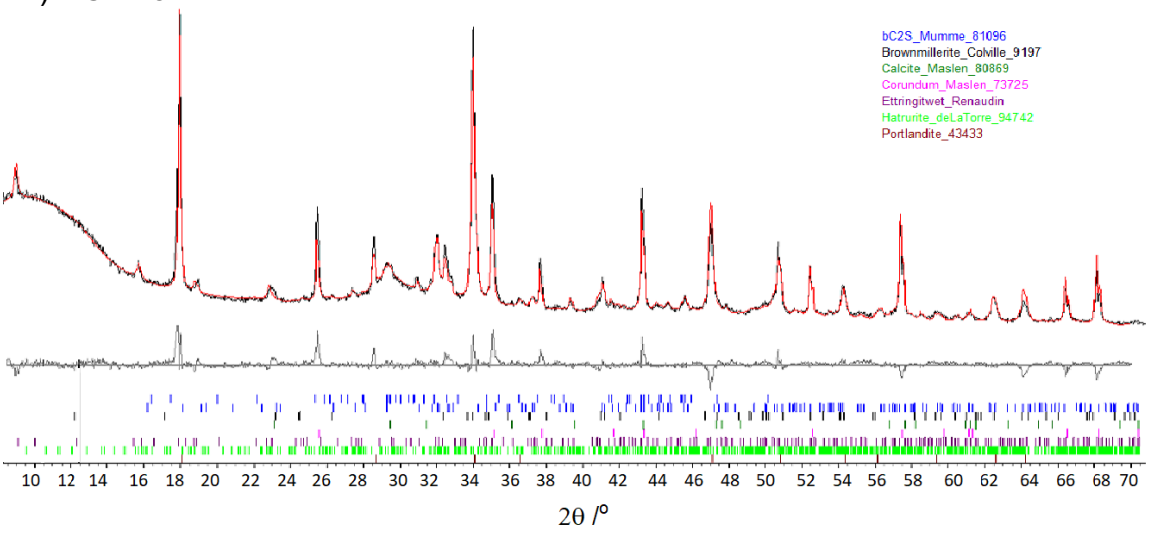

13) BO1-7

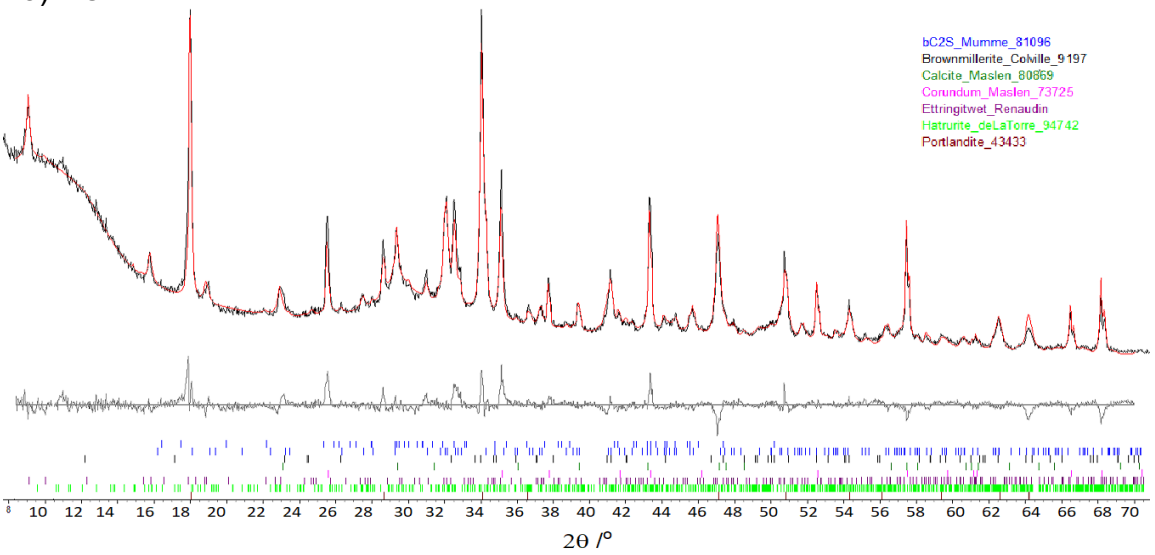

14) BO1-28

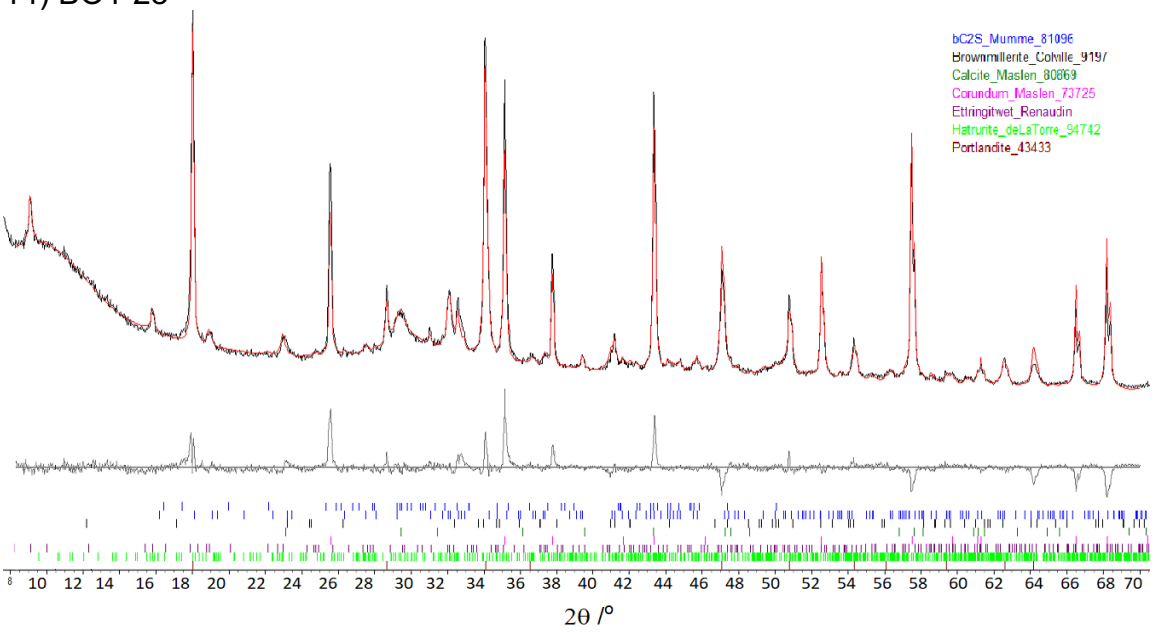

15) BO1-45

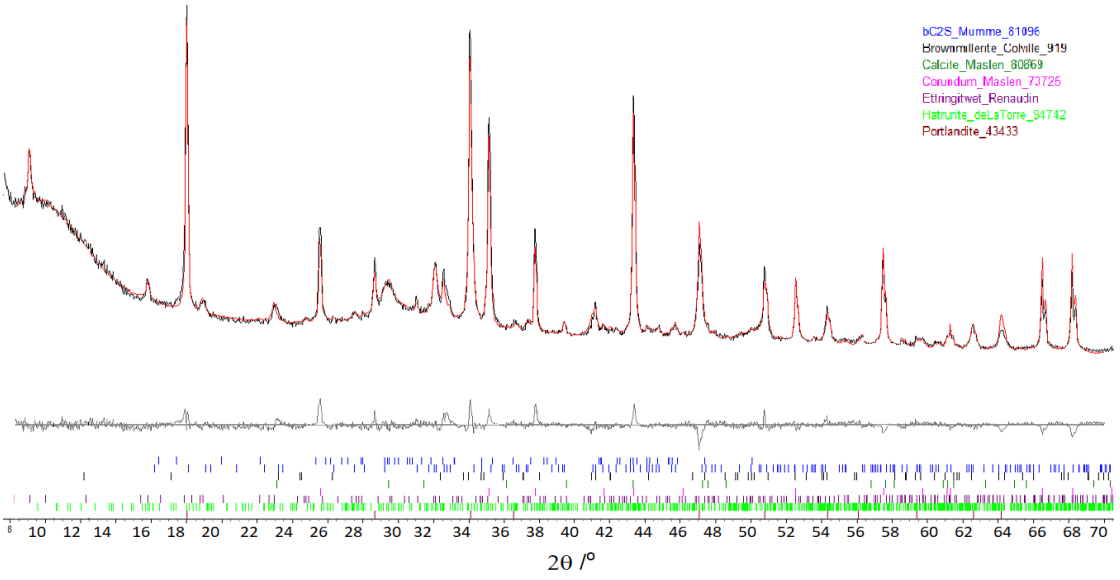

16) BO2-7

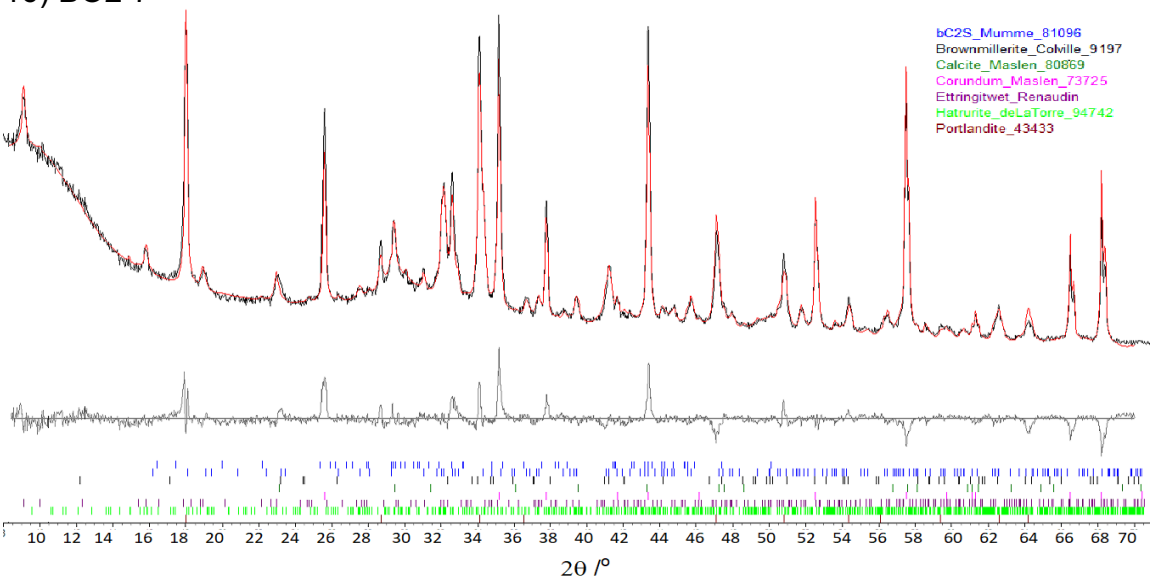

17) BO2-28

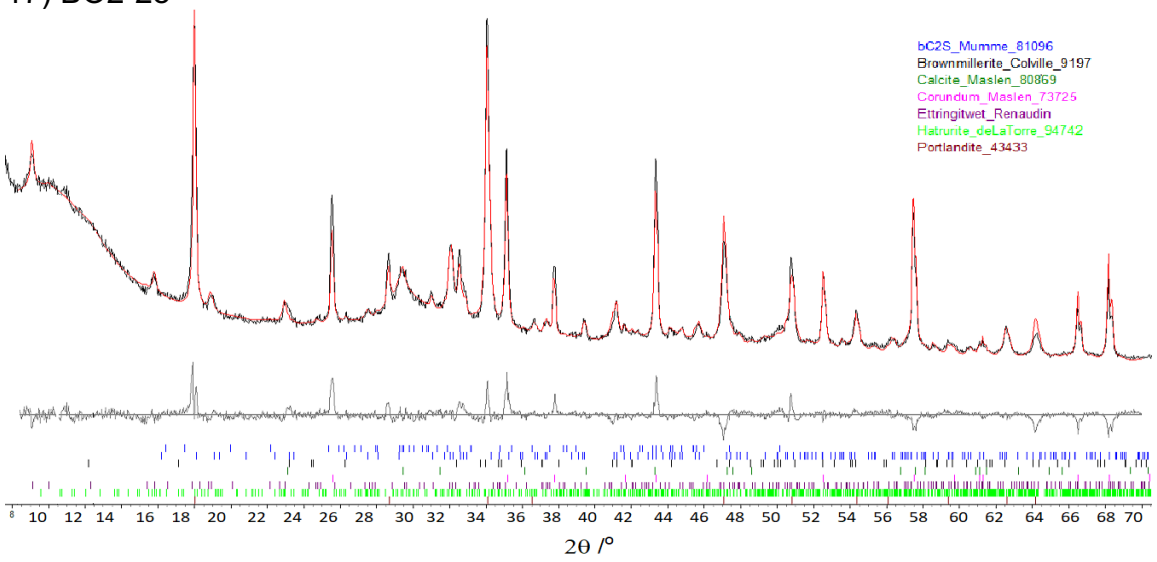

18) BO2-45

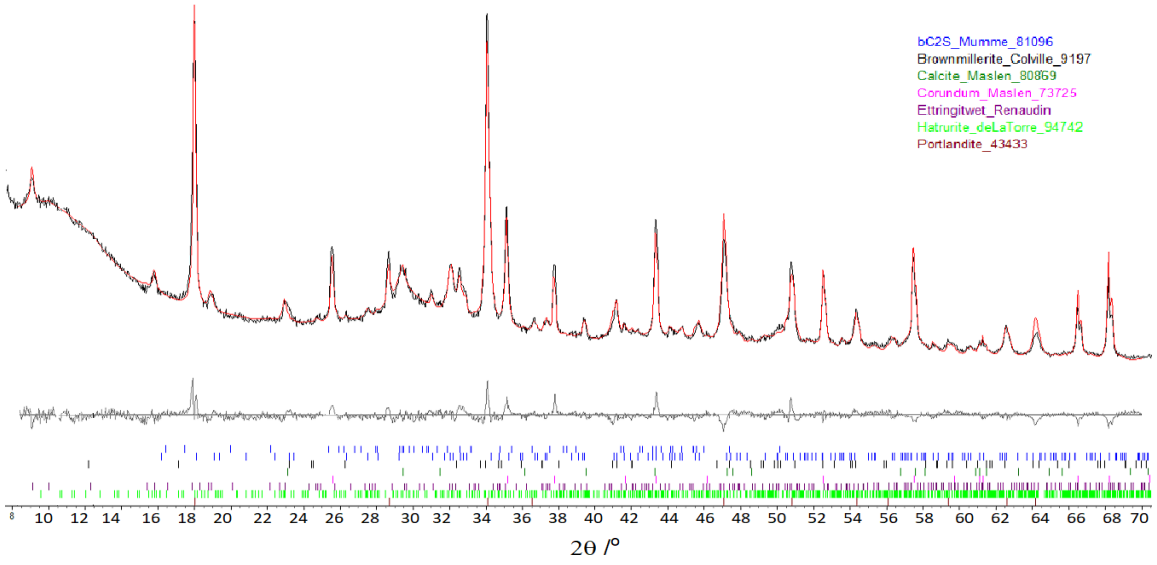

19) BC1-7

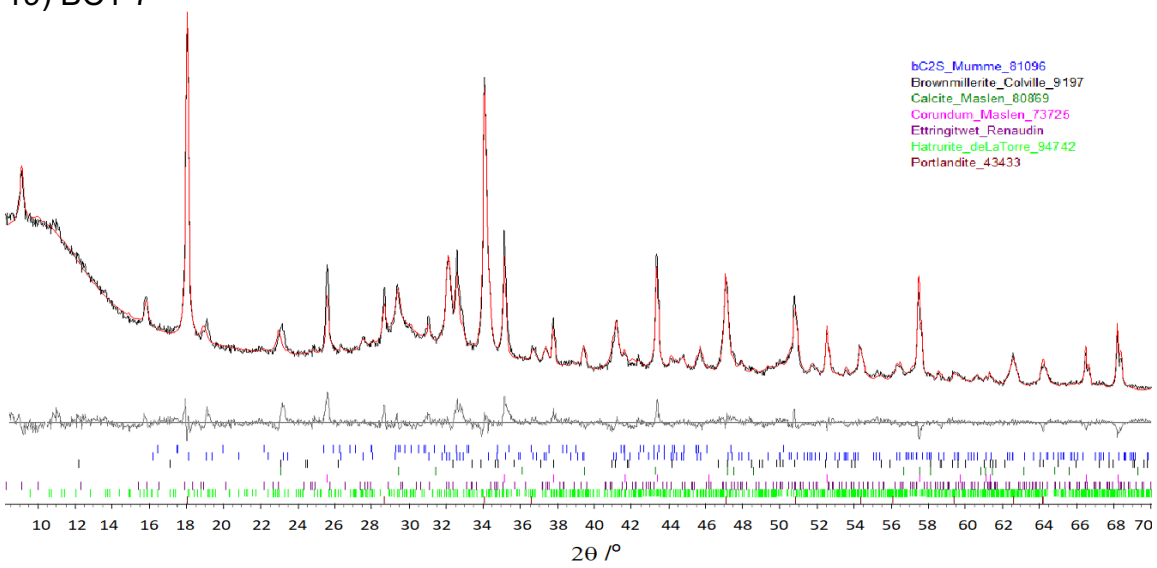

20) BC1-28

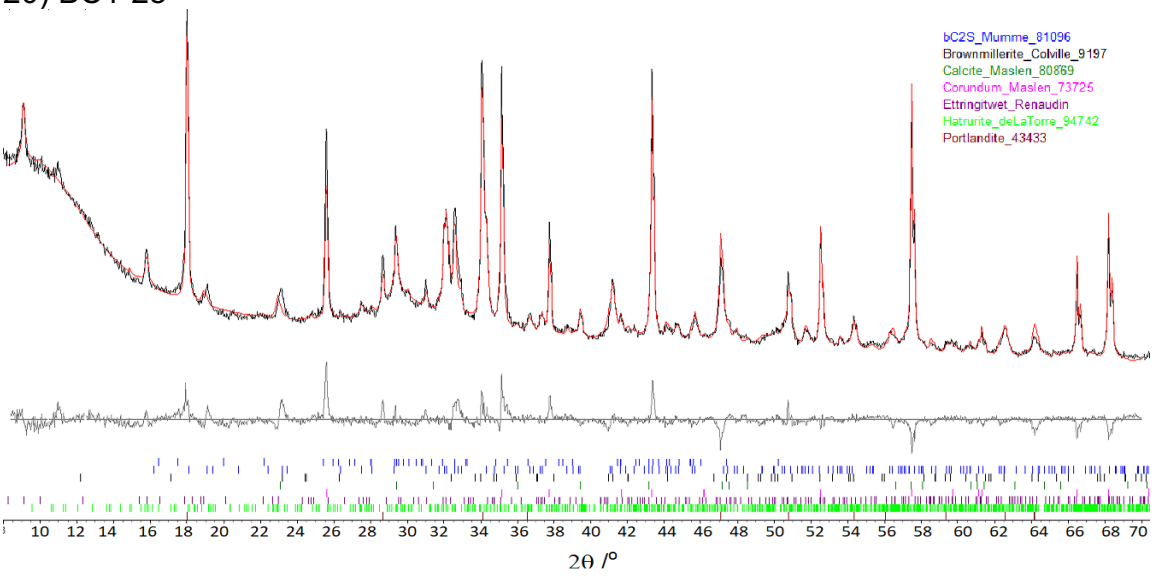

21) BC1-45

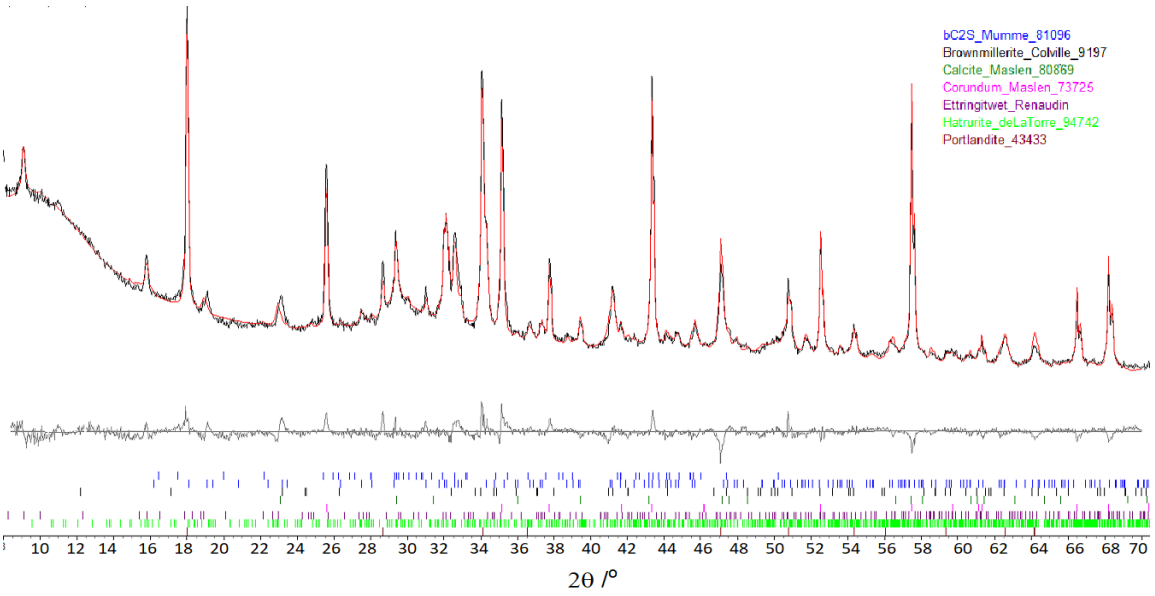

22) BC2-7

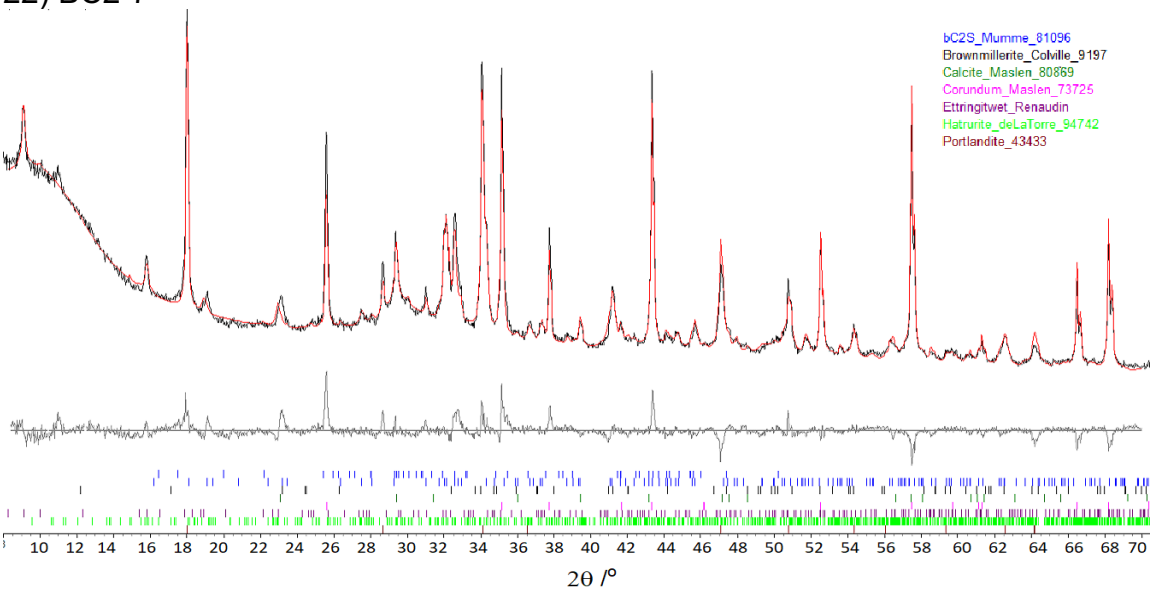

23) BC2-28

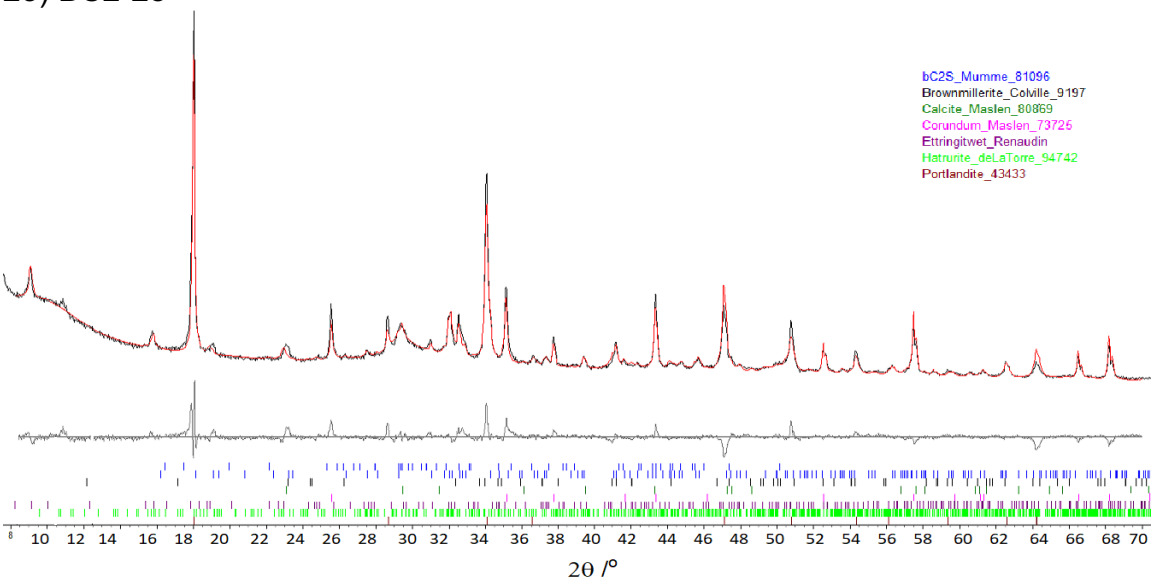

24) BC2-45

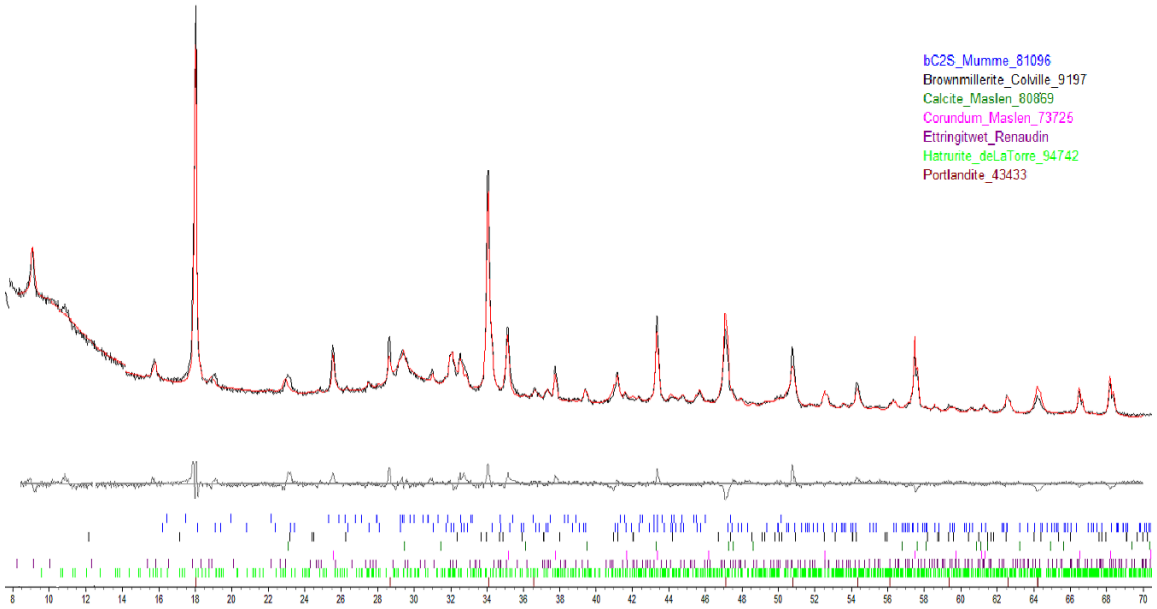
bC2S_Mumme_81096
Brownmillerite_Colville_9197
Calcite_Maslen_80869
Corundum_Maslen_73726
Ettringitwet_Renaudin
Hatrurite_deLaTorre_94742
Portlandite_43433
8 10 12 14 16 18 20 22 24 26 28 30 32 34 36 38 40 42 44 46 48 50 52 54 56 58 60 62 64 66 68 70